EARTH-ABUNDANT TRANSITION METAL CHALCOGENIDE ELECTROCATALYSTS FOR RENEWABLE ENERGY APPLICATIONS

by

MATTHEW SCOTT FABER

A dissertation submitted in partial fulfillment of

the requirements for the degree of

DOCTOR OF PHILOSOPHY

(CHEMISTRY)

at the

UNIVERSITY OF WISCONSIN–MADISON

2014

Date of final oral examination: June 19, 2014

The dissertation is approved by the following members of the Final Oral Committee:

Song Jin, Professor – Chemistry (Materials)
John C. Wright, Professor – Chemistry (Physical)
Kyoung-Shin Choi, Professor – Chemistry (Materials & Analytical)
Daniel C. Fredrickson, Assistant Professor – Chemistry (Inorganic)
Ive Hermans, Associate Professor – Chemistry (Organic & Inorganic)

© COPYRIGHT BY MATTHEW S. FABER 2014

ALL RIGHTS RESERVED

PREFACE

EARTH-ABUNDANT TRANSITION METAL CHALCOGENIDE ELECTROCATALYSTS FOR RENEWABLE ENERGY APPLICATIONS

MATTHEW SCOTT FABER, PHD

UNIVERSITY OF WISCONSIN–MADISON

2014

Energy sustainability is perhaps the greatest ongoing challenge facing humanity. Our need to replace fossil fuel-based sources of energy with environmentally friendly, secure, and renewable alternatives continues to grow, and although this fact has been long realized by the scientific community and beyond, no present-day solution effectively competes with fossil fuels from an economic or performance standpoint. Although several renewable energy technologies, including photovoltaic solar cells and fuel cell systems, can efficiently supply usable power with little or no environmental impact, they often suffer from high costs due to the expensive raw materials and complex processing steps required to produce high performance devices. These costs ultimately limit the scalability of such technologies and, consequently, their potential to address our looming energy concerns. However, the viability of many renewable energy technologies—particularly those rooted in electrochemistry—could be substantially increased by replacing expensive and scarce materials (such as noble metals) with low-cost, earth-abundant alternatives that exhibit comparable performance. My research has primarily focused on

identifying and developing such alternative electrocatalysts, generally within the family of transition metal chalcogenides, and assessing their utility in electrochemical energy conversion applications.

Chapter 1 reviews both electrochemical energy conversion and alternative earth-abundant electrocatalyst materials, and in so doing lays the foundation for the following chapters. First, I outline the need to reduce our reliance on fossil fuels by transitioning to more sustainable sources of energy, with particular attention toward to solar energy conversion. The challenges facing these technologies, mainly in terms of their cost and scalability, are presented and used to motivate the search for alternative, low-cost, earth-abundant materials that could be leveraged to increase the economic feasibility of such technologies. Many of the key concepts related to electrochemical energy conversion that appear in later chapters are introduced here. Most importantly, the fundamental role of electrocatalysts in facilitating electrochemical reactions is detailed, with the discussion framed around the specific energy conversion applications where there exist clear opportunities for earth-abundant materials to reduce or eliminate the need for costly noble metal electrocatalysts: specifically, the hydrogen evolution reaction (HER), the oxygen reduction reaction (ORR), and the redox processes that enable the regenerative operation of liquid-junction photoelectrochemical solar cells, such as dye- and quantum dot-sensitized solar cells (DSSCs and QDSSCs, respectively). Following this general review of electrocatalysis, the various classes of alternative, earth-abundant electrocatalysts presently under investigation are surveyed, concentrating mainly on the inorganic transition metal compounds. Then, the primary obstacles facing such earth-abundant inorganic electrocatalysts are detailed, as are current and emerging strategies for increasing their performance. Lastly, I provide a general

perspective on the current state and near future of earth-abundant electrocatalyst development, with the goal of inspiring more directed studies that could accelerate our rate of advance.

Chapter 2 follows up on the groundwork laid in Chapter 1 by providing a complete example of the development and implementation of an earth-abundant electrocatalyst material for use in an alternative solar energy conversion device. Specifically, I describe the facile synthesis of metallic cobalt pyrite (cobalt disulfide, CoS_2; cattierite) thin films on insulating glass substrates and demonstrate their use as robust, high-performance counter electrodes in QDSSCs that employ the sulfide/polysulfide redox electrolyte as the hole-transporting medium. In this application, these CoS_2 thin film counter electrodes replace the platinum-containing cathodes that have historically been used as QDSSC counter electrodes, despite the high cost and low terrestrial abundance of platinum. Further discouraging their use, platinum electrodes suffer from instability due to chemical incompatibility with the sulfide/polysulfide redox electrolyte, resulting in low QDSSC performance. Importantly, these cobalt pyrite counter electrodes enable QDSSC solar light-to-electricity power conversion efficiencies as high as 4.16%, with average efficiency improvement of 54 (±14)% over equivalent devices assembled with a traditional platinum counter electrode. Detailed electrochemical characterization of these CoS_2 thin film electrodes shows that CoS_2 possesses higher intrinsic electrocatalytic activity toward polysulfide reduction than platinum, rationalizing the observed increase in QDSSC performance. Furthermore, CoS_2 exhibits exceptional stability in the sulfide/polysulfide redox electrolyte, in contrast to platinum, enabling highly reproducible and stable QDSSC performance. This work clearly demonstrates that low-cost, earth-abundant electrocatalysts can indeed compete with their noble metal counterparts, inspiring further investigation of such alternative materials for energy

conversion applications.

In Chapter 3, I establish the generality of CoS_2 as high-performance earth-abundant electrocatalyst by showing its high intrinsic activity toward the HER. Here, I demonstrate that thin films of CoS_2 prepared on graphite efficiently catalyze the HER to generate molecular $H_2(g)$ fuel. Furthermore, by synthesizing CoS_2 in controlled micro- or nanowire morphologies, its HER electrocatalytic performance can be enhanced. The increase in effective electrode surface area that accompanies CoS_2 micro- and nanostructuring substantially boosts its performance. Moreover, micro- and nanostructuring of the CoS_2 material has the synergistic effect of increasing its operational stability, cyclability, and maximum achievable rate of hydrogen generation by promoting the release of evolved gas bubbles from the electrode surface. The benefits of electrocatalyst micro- and nanostructuring are further demonstrated by the increased activity of CoS_2 nanowire electrodes over planar film electrodes toward both polysulfide and triiodide reduction, suggesting a simple and straightforward way to improve the performance of QDSSCs and DSSCs, respectively. Extension of this micro- and nanostructuring strategy to other earth-abundant materials could similarly enable inexpensive electrocatalysts that lack the high intrinsic activity of the noble metals.

Chapter 4 builds upon the discovery of CoS_2 as an exceptional HER electrocatalyst by exploring the HER activity of other pyrite-phase earth-abundant transition metal disulfides and alloys thereof. Remarkably, the high intrinsic electrocatalytic activity of CoS_2 toward the HER is not unique among the various members of the pyrite family, with thin films of iron pyrite (iron disulfide, FeS_2; “fool’s gold”) and nickel pyrite (nickel disulfide, NiS_2; vaesite) also catalyzing the HER at low overpotential. I have also prepared and characterized pyrite-phase transition

metal disulfide alloy electrocatalyst thin films, which exhibit enhanced HER electrocatalytic performance as compared to the binary pyrites. The structural disorder that results from alloying could increase the areal density of active sites for catalysis, boosting their performance. Additionally, the incorporation of cobalt into these pyrite-phase transition metal dichalcogenide HER electrocatalysts consistently enhances their performance, suggesting a special role for cobalt in facilitating the HER. It is actually binary NiS_2, however, that shows the highest intrinsic electrocatalytic activity toward the HER, despite its relatively low performance, encouraging the further exploration of alloying and controlled synthesis strategies to improve its performance. Additionally, expanding upon the work in Chapter 2, I demonstrate the high activity of other pyrite-phase transition metal disulfides toward polysulfide reduction and highlight the particularly high intrinsic activity of NiS_2 (consistent with its high activity toward the HER). Together, these results establish the transition metal pyrites as a rich family of electrocatalytic materials worthy of further investigation.

The appendices that follow either present work complementary to the main chapters or describe the results of collaborations and/or works in progress. Specifically, Appendix 1 provides additional experimental details and data pertaining to Chapter 2. Similarly, Appendix 2 contains extensive experimental details, discussion, and supplementary data relating to Chapter 3. In Appendix 3, I show the direct vapor-phase synthesis of both CoS_2 and pyrite-phase cobalt diselenide ($CoSe_2$), the selenium analogue of cobalt disulfide, for electrocatalysis applications, particularly the HER. Unlike the conversion syntheses for CoS_2 reported in Chapters 2–4, which yield polycrystalline products with poorly defined surface structure, this new direct synthesis route enables the preparation of phase-pure, high-quality, faceted, micron-scale crystals of CoS_2

and $CoSe_2$ on a variety of compatible substrates, including graphite. Although the electrocatalytic activity of CoS_2 and $CoSe_2$ toward the HER is known, as described in Chapters 1, 3 and 4, its precise origin remains elusive. Such faceted electrocatalyst particles could enable the study of facet-dependent electrocatalytic activity, which could be correlated to the pyrite crystal structure to yield insights about the potential mechanism of catalysis. To this end, I have characterized the HER electrocatalytic activity of these faceted CoS_2 and $CoSe_2$ particles, and preliminary results indicate improved activity relative to their corresponding polycrystalline materials. This suggests that certain crystalline facets may exhibit particularly high electrocatalytic activity, and by tuning the synthesis to selectively favor exposure of these high-activity facets, the electrocatalytic performance of CoS_2 and $CoSe_2$ (and potentially other pyrite-phase materials) in a variety of energy conversion applications could be substantially enhanced.

Lastly, Appendix 4 presents the results of a collaborative effort to generalize the high electrocatalytic activity of the metallic 1T-phase of the layered transition metal dichalcogenide (TMDs). Nanosheets of both molybdenum disulfide (MoS_2) and tungsten disulfide (WS_2) can be synthesized through chemical vapor deposition on a variety of compatible substrates, and upon conversion from their as-synthesized, thermodynamically-favored, semiconducting 2H polymorph to their metastable, metallic 1T polymorph, their intrinsic activity toward the HER is greatly enhanced. In the same way that the pyrite-phase transition metal disulfides effectively catalyze both the HER and polysulfide reduction, we anticipated that the 1T-phase layered TMDs would also show high activity toward polysulfide reduction. To test this hypothesis, we deposited 1T-MoS_2 or 1T-WS_2 nanosheets onto glass-supported CoS_2 thin film electrodes (which are shown in Chapter 2 to be highly compatible with the sulfide/polysulfide electrolyte), which

were then assembled into symmetrical electrochemical cells filled with sulfide/polysulfide redox electrolyte. These 1T-phase layered TMD electrocatalysts enable enhanced electrode performance as compared to the unmodified CoS_2 electrodes, owing to their higher intrinsic electrocatalytic activity, while still maintaining high electrode stability. To demonstrate this high activity in working devices, I incorporated various counter electrodes modified with 1T-MoS_2 nanosheet electrocatalysts into QDSSCs and characterized their performance. The highest-performing device exhibits an overall solar light-to-electricity power conversion efficiency of 2.80%, more than double that previously reported for QDSSCs employing a MoS_2-based counter electrode. These results suggest the general electrocatalytic activity of the 1T-phase layered TMDs toward a variety of redox reactions relevant to energy conversion, and further support previous observations that the specific phase of these materials can dramatically affect their intrinsic electrocatalytic activity.

The body of work presented here represents substantial progress toward the development of earth-abundant transition metal chalcogenide electrocatalysts for renewable energy applications. The discovery of cobalt pyrite's exceptional electrocatalytic activity toward polysulfide reduction, resulting in enhanced QDSSC performance, was just the first step toward establishing the pyrite-phase transition metal disulfides as a new class of effective electrocatalysts for energy conversion. The fact that their performance can be greatly improved through the introduction of micro- and nanostructuring indicates that their controlled synthesis in nanoscale morphologies should be further developed and implemented. Additionally, the trends in their performance that have emerged suggest potential pathways toward enhancing both their intrinsic activity and overall electrocatalytic performance. While the work here mostly focuses

on the pyrite-phase transition metal disulfides, the lessons learned should translate to other materials systems, offering simple strategies for improving the performance of a wide variety of earth-abundant inorganic electrocatalyst materials with the goal of enabling the various renewable energy technologies that promise to reduce our reliance on fossil fuels.

ACKNOWLEDGMENTS

At the culmination of my greatest academic accomplishment, I would be remiss in not recognizing the contributions of all those who helped enable my success. Were it not for the support of so many, I almost certainly would not be where I am today.

First and foremost, I must credit my family for creating a warm, loving environment that promotes achievement. My parents, Jeffrey A. and Debra D. Faber, and my two sisters, Dr. Meredith L. Faber and Melissa A. Faber, were always there for me, no matter what the circumstances, and have collectively been the most influential people in my life. Thanks to them, I will never underestimate the power of family: among their many roles, they have been a bottomless well of encouragement, a net to catch me should I fall, and a receptive audience to my lame jokes.

My parents got the ball rolling early. Some of my earliest memories are of my parents trying to sate my eagerness to learn. I still remember my mother taking the time to write multiplication problems on a sheet of loose-leaf paper, my infant sister in the crib nearby, and then proceeding to blow my mind by telling me that "any number multiplied by one equals itself." Not many four-year-olds are so casually hit with mathematical axioms. Such interactions built the foundation of my academic career. From the very beginning, my parents instilled in me the belief that I was capable of succeeding in whatever pursuit at the highest level. It was this self-confidence that drove me to always strive for excellence. It helped that, as the middle child, I had the advantage of watching Meredith pave the way through school; later, I had the pleasure of seeing Melissa uphold the "Faber Legacy." Mom and Dad, clearly your seemingly unorthodox *laissez-faire* parenting style works, as it has now yielded two kids with PhDs and one with

enough sense to find better ways to spend her time.

I must also acknowledge the many teachers and mentors I've had along my journey, and none more than my PhD adviser, Professor Song Jin, whose boundless and unbridled enthusiasm ensured that I was always excited about science and the prospect of discovery. If my family shaped me as a person, my graduate school experience shaped me as a scientist, and Professor Jin's influence was a big part of that. Professor Jin was never lacking in creative ideas or suggestions, but more importantly, he graciously granted me the freedom to work on the research problems that I found most interesting. Over the last five years, I've grown as a scientist in ways that I never anticipated. In equal measure, however, I must thank Professor Kenneth J. Balkus Jr. at The University of Texas at Dallas and his then graduate student Dr. Jose A. Losilla for giving me my first exposure to research. Knowing little of my capabilities in the laboratory (or lack thereof), Professor Balkus allowed me to undertake a new project tailored to my specific interests, with Jose there to provide guidance and prevent me from blowing myself up. These initial research experiences played a vital role in setting me on the path toward a PhD in Chemistry.

When I first arrived at the University of Wisconsin–Madison in 2009, I was immediately attracted to the Jin Group, not only because of the fascinating and important work they were (and still are) doing, but also because of the people doing that work. I am indebted to all members of the Jin Group, past and present, for making my graduate school experience so rewarding and fun. I would especially like to thank those group members and friends with whom I worked most closely, including Dr. Mark A. Lukowski, Dr. Jeremy M. Higgins, Dr. Rachel S. Selinsky, Nicholas S. Kaiser, Qi Ding, and Dr. Kwangsuk Park. In particular, I must thank classmates

Miguel Cabán-Acevedo and Fei Meng for being great friends and sources of inspiration throughout my time in the Jin Group. I also had the pleasure of mentoring two outstanding undergraduate co-workers, Rafal Dziedzic and Michael L. Stone. It was a great boon to have Rafal and Mickey as sounding boards for my research ideas and as diligent laboratory workers to try out those few that held water.

I was also fortunate to collaborate with many colleagues outside of the Jin Group, both at the University of Wisconsin–Madison and elsewhere. In particular, I worked closely with various members of the Solar Group, especially Dr. Yizheng Tan and Dr. Ryan Franking. It was through this collaboration that I formed working relationships with Professors Robert J. Hamers and John C. Wright and their respective research groups, and these interactions served to greatly enrich my graduate studies. Furthermore, I must thank Dr. Pralay K. Santra and Professor Prashant V. Kamat from the University of Notre Dame for teaching me in the ins and outs of liquid-junction solar cell fabrication—were it not for their kind assistance, I would still be languishing down around two percent.

I would also like to recognize the entire support staff of the Department of Chemistry, who constantly do their best to prevent the wheels from falling off, despite what a building full of students and academics throw at them. It was always a great relief to know that, whatever the crisis of the day, the folks in Chemistry would be happy to help me out. In particular, Sue Martin Zernicke and the other Divisional Coordinators were always there in the background making sure things actually got done. I'd also like to thank the various shop staff members, particularly Kendall Schneider and Rick Pfeifer in the Machine Shop for quietly tolerating my utter mechanical incompetence, and Tracy Drier in the Glass Shop for always giving me the

"borosilicate hook-up." In addition, Analytical Laboratory Director Dr. Robert L. McClain was an immensely valuable resource, as he was always willing to lend his knowledge or equipment to help solve a problem.

Of course, I must also thank the many friends—both in Madison and elsewhere—that constantly encouraged me to keep at it, no matter how much I may have complained. Aside from being a source of support, these folks are responsible for making my time in Madison perhaps my best so far. To those new friends, I am endlessly grateful for making sure that I took the time to enjoy everything Madison has to offer. In particular, I owe a great debt of gratitude to Laura S. Phillips, who, among so many other things, made it her personal duty to make sure I got out of the Chemistry building at least once per week to enjoy myself. She has so clearly enriched my life that I can definitively say I would be a different person had I not met her.

And lastly, I'd like to thank you, kind reader, for taking the time to read this distilled version of five years' work. It is my genuine hope that you will find it engaging, informative, and—with any luck—inspiring.

MATTHEW SCOTT FABER JUNE 12, 2014

TABLE OF CONTENTS

PREFACE i
ACKNOWLEDGMENTS ix
TABLE OF CONTENTS xiii
LIST OF FIGURES xvii
LIST OF TABLES xxi
LIST OF SCHEMES xxii

CHAPTER 1 EARTH-ABUNDANT INORGANIC ELECTRO-CATALYSTS AND THEIR NANOSTRUCTURES FOR ENERGY CONVERSION APPLICATIONS

1.1. ABSTRACT 1
1.2. BROADER CONTEXT 2
1.3. INTRODUCTION 3
1.4. ELECTROCATALYSIS AND ITS CENTRAL ROLE IN ELECTROCHEMICAL ENERGY CONVERSION 8
1.5. EARTH-ABUNDANT INORGANIC ELECTROCATALYSTS 17
1.5.1. Homogeneous and Supported Molecular Systems 19
1.5.2. Transition Metals and Their Alloys 20
1.5.3. Transition Metal Oxides 23
1.5.4. Transition Metal Chalcogenides 24
1.5.4.1. Layered Materials 26
1.5.4.2. Pyrite-Phase Materials 33
1.5.4.3. Amorphous Materials 41
1.5.4.4. Other Phases 43
1.5.5. Transition Metal Nitrides 44
1.5.6. Transition Metal Phosphides 47
1.5.7. Transition Metal Carbides 51
1.5.8. Transition Metal Silicides 53
1.5.9. Transition Metal Borides 54
1.5.10. Transition Metal Compound Alloys and Mixed-Anion Compounds 55
1.6. CHALLENGES FACING EARTH-ABUNDANT INORGANIC ELECTROCATALYSTS .. 56
1.7. STRATEGIES FOR ENHANCING EARTH-ABUNDANT INORGANIC ELECTRO-CATALYST PERFORMANCE AND STABILITY 58
1.7.1. Nanostructuring 58
1.7.2. Chemical Modification 61
1.7.3. Structural Modification 61

1.7.4. Composite Materials 64
1.8. SUMMARY AND PERSPECTIVES 66
1.9. REFERENCES 69

CHAPTER 2 EARTH-ABUNDANT COBALT PYRITE (CoS_2) THIN FILM ON GLASS AS A ROBUST, HIGH-PERFORMANCE COUNTER ELECTRODE FOR QUANTUM DOT-SENSITIZED SOLAR CELLS

2.1. ABSTRACT 99
2.2. INTRODUCTION 100
2.3. EXPERIMENTAL METHODS 103
2.3.1. CoS_2 Film Synthesis 103
2.3.2. Materials Characterization 104
2.3.3. Mesoscopic TiO_2 Photoanode Preparation and Sensitization by Successive Ionic Layer Adsorption and Reaction (SILAR) 104
2.3.4. Thin-Layer Liquid-Junction QDSSC Fabrication 104
2.3.5. Electrochemical and Photoelectrochemical Characterization 106
2.4. RESULTS AND DISCUSSION 107
2.5. CONCLUSIONS 124
2.6. REFERENCES 124

CHAPTER 3 HIGH-PERFORMANCE ELECTROCATALYSIS USING METALLIC COBALT PYRITE (CoS_2) MICRO- AND NANOSTRUCTURES

3.1. ABSTRACT 131
3.2. INTRODUCTION 132
3.3. MATERIALS AND METHODS 134
3.3.1. Materials Synthesis 134
3.3.2. Materials Characterization 136
3.3.3. Electrochemical Characterization of Catalytic Activity Toward the HER 137
3.3.4. Symmetrical Cell Fabrication and Measurement 137
3.4. RESULTS AND DISCUSSION 138
3.5. CONCLUSIONS 161
3.6. REFERENCES 161

CHAPTER 4 EARTH-ABUNDANT METAL PYRITES (FeS_2, CoS_2, NiS_2, AND THEIR ALLOYS) FOR HIGHLY EFFICIENT HYDROGEN EVOLUTION AND POLYSULFIDE REDUCTION ELECTROCATALYSIS

4.1. ABSTRACT 168
4.2. INTRODUCTION 169
4.3. EXPERIMENTAL METHODS 172

4.3.1. Materials Synthesis 172
4.3.2. Materials Characterization 174
4.3.3. Electrochemical Characterization of Electrocatalytic Activity Toward the HER 174
4.3.4. Symmetrical Cell Fabrication and Electrochemical Characterization 175
4.4. RESULTS AND DISCUSSION 176
4.4.1. Pyrite Thin Film Synthesis and Structural Characterization 176
4.4.2. Electrocatalytic Performance of Pyrite Thin Films Toward the HER 185
4.4.3. Electrocatalytic Performance of Pyrite Thin Films Toward Polysulfide Reduction 191
4.5. SUMMARY AND PERSPECTIVES 196
4.6. REFERENCES 197

APPENDIX 1 SUPPORTING INFORMATION FOR CHAPTER 2

A1.1. EXPERIMENTAL DETAILS 205
A1.1.1. Mesoscopic TiO_2 Photoanode Preparation 205
A1.1.2. TiO_2 Film Sensitization by Successive Ionic Layer Adsorption and Reaction (SILAR) 207
A1.1.3. Long-Term Measurement of Short-Circuit Photocurrent Density Stability 208
A1.1.4. Measurement of Incident Photon-to-Electron Conversion Efficiency Action Spectra 209
A1.2. REFERENCES 218

APPENDIX 2 SUPPORTING INFORMATION FOR CHAPTER 3

A2.1. EXPERIMENTAL DETAILS 219
A2.1.1. Glass and Graphite Substrate Preparation 219
A2.1.2. Cobalt Film Preparation 220
A2.1.3. β-$Co(OH)_2$ Microwire Synthesis 220
A2.1.3.1. *β*-$Co(OH)_2$ Microwire "Flower" Synthesis 222
A2.1.4. $Co(OH)(CO_3)_{0.5}$•xH_2O ("CHCH") Nanowire Synthesis 222
A2.1.5. Thermal Sulfidation of Co Films, β-$Co(OH)_2$ Microwires, and CHCH Nanowires 223
A2.1.6. Determination of CoS_2 Micro- or Nanowire Mass Loading on Graphite Disk Substrates 223
A2.1.7. Electrochemical Characterization of Catalytic Activity Toward the Hydrogen Evolution Reaction (HER) 224
A2.1.8. IR and Background Correction of Current Density–Voltage (J–V) Data 225
A2.1.9. Estimate of Effective Electrode Surface Area 227

A2.1.10. Fabrication and Electrochemical Characterization of Symmetrical Cells 228
A2.2. REFERENCES 242

APPENDIX 3 VAPOR PHASE SYNTHESIS OF THE COBALT DICHALCOGENIDES AND CHARACTERIZATION OF THEIR ACTIVITY TOWARD THE HYDROGEN EVOLUTION REACTION

A3.1. INTRODUCTION 243
A3.2. EXPERIMENTAL METHODS 245
A3.2.1. Graphite Substrate Preparation 245
A3.2.2. Direct Synthesis of CoS_2 and $CoSe_2$ 245
A3.2.3. Chemical Vapor Deposition of CoS_2 and $CoSe_2$ 247
A3.2.4. Materials Characterization 247
A3.2.5. Electrochemical Characterization 247
A3.3. RESULTS AND DISCUSSION 248
A3.4. PRELIMINARY CONCLUSIONS AND FUTURE WORK 257
A3.5. REFERENCES 260

APPENDIX 4 METALLIC 1T LAYERED TRANSITION METAL DICHALCOGENIDE ELECTROCATALYSTS FOR ENHANCED POLYSULFIDE REDUCTION IN QUANTUM DOT-SENSITIZED SOLAR CELLS

A4.1. INTRODUCTION 263
A4.2. EXPERIMENTAL METHODS 265
A4.2.1. Materials Synthesis 265
A4.2.2. Materials Characterization 268
A4.2.3. Electrochemical Characterization 268
A4.3. RESULTS AND DISCUSSION 270
A4.4. CONCLUSIONS 282
A4.5. REFERENCES 283

List of Figures

Figure 1.1. Trends in the Electrocatalytic Activity of Various Transition Metals Toward the HER and the ORR 16

Figure 1.2. Identification of the Edge-Site Activity of MoS_2 Toward the HER, and an Example of the Engineering Strategies Used to Maximize the Exposure of These Edge Sites 28

Figure 1.3. Enhancement of the Electrocatalytic Activity of Layered Transition Metal Dichalcogenide Nanosheets Toward the HER Through Chemical Exfoliation 31

Figure 1.4. Structural and Electrochemical Characterization of a Metallic CoS_2 Thin Film Synthesized on Glass and Used as the Counter Electrode in a QDSSC 35

Figure 1.5. Scanning Electron Microscopy (SEM) and Electrochemical Characterization of CoS_2 Film, Microwire, and Nanowire Electrodes, and Schematic Depictions of CoS_2 Microwires and Nanowires Facilitating Hydrogen Gas Bubble Release 38

Figure 1.6. Comparison of the Performance of Various Pyrite-Phase Transition Metal Disulfide and Diselenide HER Electrocatalysts 40

Figure 1.7. Tafel Plot Comparing the Intrinsic Activity of Various Molybdenum Sulfide Electrocatalysts Toward the HER 42

Figure 1.8. Polarization Curves Comparing the Relative Activity of Selected Binary and Ternary Transition Metal Nitride HER Electrocatalysts 46

Figure 1.9. Electron Microscopy and Electrochemical Characterization of Selected Nanostructured Transition Metal Phosphide HER Electrocatalysts 49

Figure 1.10. Schematic Illustrations and Performance Characterizations of MoS_2/Reduced Graphene Oxide, MoS_x/N-Doped Carbon Nanotube, and Biomass-Derived "MoSoy" Composite HER Electrocatalysts 65

Figure 2.1. Structural Characterization of an As-Synthesized CoS_2 Film on Borosilicate Glass 111

Figure 2.2. Current Density–Voltage (J–V) Characterization of QDSSC Devices Assembled with CoS_2, Pt, and RGO–Cu_2S Counter Electrodes 115

FIGURE 2.3. ELECTROCHEMICAL CHARACTERIZATION OF THE CoS_2 ON GLASS AND Pt ON FTO/GLASS ELECTRODES IN SYMMETRICAL ELECTROCHEMICAL CELLS 121

FIGURE 3.1. STRUCTURAL CHARACTERIZATION OF A CoS_2 FILM, MICROWIRE ARRAY, AND NANOWIRE ARRAY ON GRAPHITE AND THEIR CORRESPONDING PRECURSORS 143

FIGURE 3.2. ELECTROCHEMICAL CHARACTERIZATION OF CoS_2 FILM, MICROWIRE ARRAY, AND NANOWIRE ARRAY ELECTRODES FOR HER ELECTRO-CATALYSIS 146

FIGURE 3.3. CHARACTERIZATION OF CoS_2 STABILITY DURING HER ELECTRO-CATALYSIS AND SCHEME ILLUSTRATING ENHANCED HYDROGEN GAS BUBBLE RELEASE FROM CoS_2 NANO- AND MICROSTRUCTURES 153

FIGURE 3.4. STRUCTURAL AND ELECTROCHEMICAL CHARACTERIZATION OF A HIERARCHICAL CoS_2 MICROWIRE "FLOWER" ELECTRODE 156

FIGURE 3.5. ELECTROCHEMICAL CHARACTERIZATION OF CoS_2 FILM AND NANOWIRE ELECTRODE SYMMETRICAL CELLS 159

FIGURE 4.1. X-RAY DIFFRACTION (XRD) PATTERNS OF PYRITE-PHASE TRANSITION METAL DISULFIDE THIN FILMS OVER A CoS_2 THIN FILM ON GLASS 177

FIGURE 4.2. RAMAN SPECTRA OF VARIOUS PYRITE-PHASE TRANSITION METAL DISULFIDE THIN FILMS ON GRAPHITE 180

FIGURE 4.3. X-RAY PHOTOELECTRON SPECTRA (XPS) OF VARIOUS PYRITE-PHASE TRANSITION METAL DISULFIDE ALLOY THIN FILMS ON GRAPHITE 182

FIGURE 4.4. SEM IMAGES OF REPRESENTATIVE PYRITE-PHASE TRANSITION METAL DISULFIDE THIN FILMS ON GRAPHITE 184

FIGURE 4.5. ELECTROCHEMICAL CHARACTERIZATION OF THE CATALYTIC ACTIVITY OF VARIOUS PYRITE-PHASE TRANSITION METAL DISULFIDE THIN FILMS ON GRAPHITE TOWARD THE HER 186

FIGURE 4.6. ELECTROCHEMICAL CHARACTERIZATION OF THE CATALYTIC ACTIVITY OF PYRITE-PHASE TRANSITION METAL DISULFIDE THIN FILMS TOWARD POLYSULFIDE REDUCTION 192

FIGURE A1.1. CYCLING STABILITY OF QDSSCS ASSEMBLED WITH EITHER A CoS_2 OR Pt COUNTER ELECTRODE 211

FIGURE A1.2. INCIDENT PHOTON-TO-ELECTRON CONVERSION EFFICIENCY (IPCE) ACTION SPECTRA FOR QDSSCS EMPLOYING EITHER A CoS_2 OR Pt COUNTER ELECTRODE 213

FIGURE A1.3. LONG-TERM OPERATIONAL STABILITY OF QDSSCS EMPLOYING A CoS_2 THIN FILM COUNTER ELECTRODE 214

FIGURE A1.4. SHORT-CIRCUIT PHOTOCURRENT DENSITY (J_{SC}) RESPONSE AND STABILITY UNDER CHOPPED SIMULATED SUNLIGHT FOR A QDSSC ASSEMBLED WITH EITHER A CoS_2 OR Pt COUNTER ELECTRODE 215

FIGURE A1.5. OPEN-CIRCUIT VOLTAGE (V_{OC}) RISE AND DECAY UNDER APPLICATION AND REMOVAL OF SIMULATED SUNLIGHT FOR A QDSSC ASSEMBLED WITH EITHER A CoS_2 OR Pt COUNTER ELECTRODE 216

FIGURE A1.6. CYCLIC VOLTAMMETRY OF CoS_2 AND Pt SYMMETRICAL ELECTRO-CHEMICAL CELLS FILLED WITH AQUEOUS SULFIDE/POLYSULFIDE ELECTROLYTE 217

FIGURE A2.1. SEM IMAGES OF PRECURSOR FILM, MICROWIRE, AND NANOWIRE SAMPLES ON GLASS BEFORE AND AFTER THERMAL SULFIDATION TO CoS_2 231

FIGURE A2.2. LOW-MAGNIFICATION SEM IMAGE OF A CoS_2 FILM PREPARED ON GRAPHITE 233

FIGURE A2.3. XRD PATTERNS FOR β-$Co(OH)_2$ MICROWIRE AND CHCH NANOWIRE PRODUCTS PREPARED ON GRAPHITE DISK SUBSTRATES 234

FIGURE A2.4. METHOD OF *IR* AND BACKGROUND CORRECTION OF *J–V* DATA 235

FIGURE A2.5. STRUCTURAL, SPECTROSCOPIC, AND ELECTROCHEMICAL CHARACTER-IZATION OF A CoS_2 FILM ON GRAPHITE ELECTRODE BEFORE AND AFTER ELECTROCHEMICAL TESTING FOR HER CATALYTIC ACTIVITY 236

FIGURE A2.6. CYCLIC VOLTAMMETRIC (CV) DETERMINATION OF THE DOUBLE LAYER CAPACITANCE FOR A CoS_2 NW ELECTRODE 238

FIGURE A2.7. FULL CV CHARACTERIZATION OF THE HER ELECTROCATALYTIC PERFORMANCE OF CoS_2 MW AND NW ELECTRODES 239

FIGURE A2.8. DIGITAL PHOTOGRAPHS OF CoS_2 FILM AND MW ARRAY ELECTRODES EVOLVING HYDROGEN GAS 240

FIGURE A2.9. FULL CV CHARACTERIZATION OF SYMMETRICAL ELECTROCHEMICAL CELLS FILLED WITH IODIDE/TRIIODIDE REDOX ELECTROLYTE 241

FIGURE A3.1. STRUCTURAL CHARACTERIZATION OF COBALT DISULFIDE (CoS_2) PRODUCTS PREPARED DIRECTLY ON GRAPHITE 250

FIGURE A3.2. STRUCTURAL CHARACTERIZATION OF COBALT DISELENIDE ($CoSe_2$) PRODUCTS PREPARED DIRECTLY ON GRAPHITE 253

FIGURE A3.3. ELECTROCHEMICAL CHARACTERIZATION OF CoS_2 AND $CoSe_2$ ELEC-TRODES FOR HER ELECTROCATALYSIS 255

FIGURE A3.4. SEM IMAGES OF FACETED MICRORODS AND PARTICLES OF CoS_2 PRE-PARED ON GRAPHITE FROM A SODIUM SULFIDE–SULFUR FLUX 259

FIGURE A4.1. ELECTROCHEMICAL CHARACTERIZATION OF CoS_2, 1T-WS_2/CoS_2, AND 1T-MoS_2/CoS_2 ELECTRODES IN SYMMETRICAL ELECTROCHEMICAL CELLS FILLED WITH SULFIDE/POLYSULFIDE ELECTROLYTE 272

FIGURE A4.2. REPRESENTATIVE SEM IMAGES OF 1T-MoS_2 NANOSHEETS PREPARED DIRECTLY ON GRAPHITE AND GLASSY CARBON SUPPORTS 277

FIGURE A4.3. ELECTROCHEMICAL CHARACTERIZATION OF CoS_2, 1T-WS_2/CoS_2, AND 1T-MoS_2/CoS_2 ELECTRODES IN SYMMETRICAL ELECTROCHEMICAL CELLS FILLED WITH SULFIDE/POLYSULFIDE ELECTROLYTE 279

List of Tables

Table 2.1. Photovoltaic Device Characteristics of Quantum Dot-Sensitized Solar Cells Measured with Different Counter Electrodes 118

Table 3.1. Summary of the Electrochemical Properties of CoS_2 Electrodes with Different Morphologies 150

Table 4.1. Summary of the Electrochemical Properties of the Different Pyrite-Phase Thin Film Electrocatalysts for the Hydrogen Evolution Reaction 189

Table 4.2. Summary of the Electrochemical Properties of the Different Pyrite-Phase Thin Film Electrocatalysts for Polysulfide Reduction 195

Table A1.1. Comparison of the Photovoltaic Device Characteristics Measured with Representative Photoanodes from Different Batches Assembled with a CoS_2 (or Pt) Counter Electrode 212

Table A4.1. Summary of the Electrochemical Properties of CoS_2, 1T-WS_2/CoS_2, and 1T-MoS_2/CoS_2 Symmetrical Electrochemical Cells ... 274

Table A4.2. Photovoltaic Device Characteristics of Quantum Dot-Sensitized Solar Cells Measured with Different Counter Electrodes 281

List of Schemes

Scheme 1.1. Schematic Illustration of Selected Energy Conversion Applications for Earth-Abundant Inorganic Electrocatalysts 7

Scheme 1.2. Schematic Illustrations of the Respective Roles of the Electrocatalyst at the Counter Electrode of DSSCs and QDSSCs 11

Scheme 2.1. Schematic Depictions of the Preparation of a CoS_2 Film Electrode and a Liquid-Junction QDSSC Device 109

Scheme 3.1. Schematic Depictions of the Preparation of a CoS_2 Film, Microwire Array, or Nanowire Array on a Graphite Disk (or Glass) Substrate 140

CHAPTER 1

Earth-Abundant Inorganic Electrocatalysts and Their Nanostructures for Energy Conversion Applications †

1.1. Abstract

Electrocatalysis plays a key role in the energy conversion processes central to several renewable energy technologies that have been developed to lessen our reliance on fossil fuels. However, the best electrocatalysts for these processes—which include the hydrogen evolution reaction (HER), the oxygen reduction reaction (ORR), and the redox reactions that enable regenerative liquid-junction photoelectrochemical solar cells—often contain scarce and expensive noble metals, substantially limiting the potential for these technologies to compete with fossil fuels. The considerable challenge is to develop robust electrocatalysts composed exclusively of low-cost, earth-abundant elements that exhibit activity comparable to that of the noble metals. In this review, we summarize recent progress in the development of such high-performance earth-abundant inorganic electrocatalysts (and nanostructures thereof), classifying

---

† This chapter was prepared in collaboration with S. Jin and submitted as an invited Review Article in *Energy & Environmental Science* before being adapted here.

these materials based on their elemental constituents. We then detail the most critical obstacles facing earth-abundant inorganic electrocatalysts and discuss various strategies for further improving their performance. Lastly, we offer our perspectives on the current directions of earth-abundant inorganic electrocatalyst development and suggest pathways toward achieving performance competitive with their noble metal-containing counterparts.

1.2. Broader Context

Renewable energy technologies will necessarily grow in importance if we are to meet our future energy demands. The goal is for these environmentally-friendly, alternative sources of energy to become cost competitive with fossil fuels, reducing our reliance on such limited resources. For this to happen, though, the precious noble metal (or noble metal-containing) electrocatalysts used in these renewable energy technologies should be replaced with low-cost, earth-abundant substitutes that exhibit comparable catalytic activity and long-term stability. In this review, we first provide a broad overview of electrocatalysis and its role in several important renewable energy technologies, including water splitting to generate hydrogen fuel, the reduction of oxygen in fuel cell devices, and the regenerative operation of photoelectrochemical solar cells. We then discuss the various classes of earth-abundant electrocatalysts presently under investigation, highlighting important advances, emerging trends in their development, and the challenges facing them, before finally offering our perspectives on how to most effectively advance the development of earth-abundant inorganic electrocatalysts.

1.3. Introduction

In recent decades, there has been a growing need to replace fossil fuels with environmentally-friendly, secure, and sustainable alternative sources of energy. Renewable energy technologies generally rely on harvesting and storing energy from our most readily exploitable and only truly limitless source: the Sun. Mankind has developed a multitude of ways for accomplishing this task, ranging from simple agriculture to wind turbines to advanced photovoltaics, but due to issues of overall efficiency, scalability, and the intermittence of solar irradiation, no single renewable energy technology has emerged as an apparent long-term solution. Instead, several promising technologies remain under development in hopes that their collective contributions will eliminate—or at least substantially reduce—our reliance on fossil fuels.

The primary argument in favor of transitioning to renewable sources of energy is indeed quite compelling: with the amount of energy received from solar insolation vastly exceeding that consumed globally, capturing and utilizing a mere fraction could significantly offset or even obviate our need for fossil fuels.[1] Inspired by this highly attractive prospect, researchers have spent decades developing materials and devices capable of converting sunlight into electricity. Device designs ranging from completely solid-state single-crystalline photovoltaics[2] to liquid-junction photoelectrochemical solar cells[3] have been explored and shown to operate at varying (yet steadily improving) levels of solar light-to-electricity power conversion efficiency.[4] Silicon is perhaps the most studied solar absorber,[2] with high-efficiency photovoltaic modules already commercialized; however, costly processing and manufacturing hinders their large-scale deployment.[5,6] Consequently, there has been a push toward the development of high-efficiency

solution-processed photovoltaics,[7] with dye-[8] and quantum dot-sensitized,[9–11] colloidal quantum dot,[12] organic,[13] copper-indium-gallium-selenide and copper-zinc-tin-sulfide,[14] and, most recently, organic/inorganic perovskite[15,16] solar cells already demonstrating impressive conversion efficiencies.

While inexpensive and efficient photovoltaic devices would mark a great advance toward reducing our reliance on fossil fuels, the intermittent nature of sunlight necessitates the storage of the photogenerated electricity. The performance of rechargeable lithium ion batteries has advanced considerably over recent years, but further improvements in energy density and cycling stability together with lower overall cost are still needed to meet our ever-increasing power demands.[17,18] An attractive alternative solution would be to store the energy from sunlight in the chemical bonds of portable molecular fuels,[19] such as hydrogen gas[1,20–22] or simple hydrocarbons.[23–25] These molecular fuels could then be stored, transported, and ultimately consumed on demand using a light-weight fuel cell device to efficiently generate electricity with few harmful byproducts.[26,27] Hydrogen is perhaps the most attractive molecular fuel, as it can be produced through the environmentally-benign electrochemical splitting of water and consumed in the presence of oxygen (from air) to yield electrical power and water as its only products.[27] In particular, hydrogen fuel obtained by water electrolysis is free of the contaminants found in hydrogen gas from reformed hydrocarbons that can poison traditional fuel cell electrocatalysts, reducing their efficiency and lifetime.[26] Furthermore, by coupling a semiconducting light absorber with suitable electrocatalysts for hydrogen and oxygen evolution, it becomes possible to mimic photosynthesis by using solid, inorganic materials to convert sunlight into hydrogen fuel.[20,22,28–30]

Given the considerable attention that they have already received from the research community, both photovoltaic energy conversion and water electrolysis are fairly mature technologies, and one could imagine pairing the best solar cell devices with the best electrocatalysts to efficiently produce solar fuels; however, as is similarly the case for photovoltaics, issues of scalability and economic feasibility preclude such a simple solution.[31] Moreover, these technologies face constant competition from relatively inexpensive, well-established, and energy-dense fossil fuels.[1] To become economically competitive, solar fuel devices and liquid-junction photoelectrochemical solar cells must operate efficiently using low-cost and earth-abundant materials. This requirement is not met by present energy conversion technologies, which often rely on noble metal or noble metal-containing electrocatalysts to drive their relevant redox reactions. For example, platinum has long been a favored electrocatalyst for several important electrochemical reactions due to its versatility, high activity, and chemical inertness,[32] but its low abundance in the Earth's crust cannot support large-scale application.[33] Therefore, contemporary renewable energy technologies that rely on noble metal and noble metal-containing electrocatalysts ideally should transition to low-cost, earth-abundant alternatives if they hope to become cost competitive with fossil fuel-based energy sources.[34]

In this review, we seek to first provide a high-level overview of electrocatalysis and its central role in various renewable energy technologies. Due to the broad scope of this topic, we will largely limit our discussion to inorganic heterogeneous electrocatalysts and the cathodic reactions where there are clear opportunities for earth-abundant electrocatalysts: the hydrogen reduction reaction (HER), the oxygen reduction reaction (ORR), and the redox reactions in regenerative liquid-junction photoelectrochemical solar cells (Scheme 1.1). Carbon dioxide and

monoxide reduction are relatively nascent fields of heterogeneous electrocatalysis that could similarly benefit from the development of highly selective earth-abundant inorganic electrocatalysts, but they have been thoroughly reviewed elsewhere,[23–25] and because noble metal-containing electrocatalysts are generally not employed in these applications, they will not be discussed in detail here.

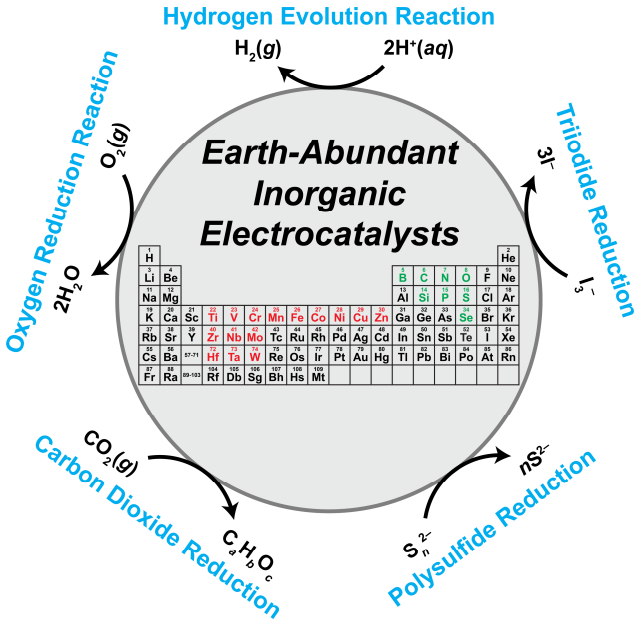

Scheme 1.1. Schematic illustration of selected energy conversion applications for earth-abundant inorganic electrocatalysts. The earth-abundant transition metal elements primarily considered in this review are indicated in red in the periodic table, while the non-metal elements in green define the specific families of electrocatalytic inorganic transition metal compounds that are discussed here.

We will then survey recent work toward developing new high-performance, earth-abundant inorganic electrocatalysts, focusing our discussion on promising classes of materials as defined by their chemical compositions. Although carbonaceous electrocatalysts, such as graphene and graphene derivatives,[35] carbon nanotubes (CNTs),[36,37] and conductive polymers,[38,39] have recently emerged as effective electrocatalysts, they lie outside the scope of this review. Homogeneous molecular catalysts have also witnessed significant development in recent years, but they have been thoroughly reviewed elsewhere[34,40–46] and will not be emphasized here. For each class of materials, we will try to highlight major advances and the prevailing trends in development. The key challenges facing earth-abundant electrocatalysts will then be detailed, along with a discussion of current and emerging strategies for improving the performance of such catalysts. Lastly, we will offer our perspectives on the development of earth-abundant electrocatalysts in hopes of lighting a path toward achieving performance competitive with their noble metal-containing analogues. Because of the tremendous progress and accelerating rate of publication in this rapidly emerging research field, we cannot ensure that this review encompasses the full body of work related to this topic, particularly those works most recently published; instead, we seek to highlight the key themes and seminal advances that have influenced the primary directions of research.

1.4. Electrocatalysis and Its Central Role in Electrochemical Energy Conversion

Any process that involves a chemical transformation induced by the transfer of electrical charge to a substrate molecule can proceed efficiently only if the rates of charge transfer and

chemical reaction are high. To maximize the efficiency of such transformations, catalysts are commonly employed to facilitate both charge transfer and subsequent chemical reaction, accelerating their respective rates. In addition to these kinetic considerations, optimized catalysts must be thermodynamically matched to the redox potential of the reaction of interest such that charge transfer can occur with minimal energy loss. The specific forms of these catalysts, as well as their methods of integration and utilization, often vary, as discussed later, but their function is always to minimize the energy cost associated with a chemical transformation reaction.

As a result, when developing electrochemical systems for efficient energy conversion based on solid/liquid or solid/gas interfaces, electrocatalysis is a key consideration.[32] Electrode materials are chosen primarily based on their ability to drive the redox reactions of interest with low energy loss, which demands minimization of the electrochemical cell voltage, V, generally given by

$$V = \Delta E_{eq} - \eta_a + \eta_c - IR \qquad (1)$$

where ΔE_{eq} is the difference between the equilibrium electrode potentials; η_a and η_c represent the overpotentials at the anode and cathode, respectively; and IR is the voltage drop across all current-carrying components of the electrochemical cells, as determined by Ohm's law. An effective electrocatalyst reduces the cell voltage by minimizing the electrode overpotential, η, defined as the deviation of the applied potential from the equilibrium potential, which is related to the current density, J, by the Tafel equation,

$$|\eta| = \frac{2.3RT}{\alpha nF} \log \frac{J}{J_0}. \qquad (2)$$

In this relationship, η is minimized by a low Tafel slope ($b = 2.3RT/\alpha nF$, often expressed in mV

decade^{-1}, where R is the ideal gas constant, T is the absolute temperature, α is the electrochemical transfer coefficient, n is the number of electrons involved in the electrode reaction, and F is the Faraday constant), which gives the applied overpotential necessary to change the current density by an order of magnitude, and a large exchange current density (J_0), which indicates the electrode kinetics toward the redox reaction of interest. Therefore, electrocatalysts with high intrinsic activity toward a specific redox process are characterized by a low Tafel slope and a high exchange current density.

Consequently, electrocatalysts and electrocatalytic electrode materials are primarily selected based on their ability to reduce overpotentials, regardless of the specific application. For example, in liquid-junction photoelectrochemical dye- and quantum dot-sensitized solar cell (DSSC and QDSSC, respectively) devices, the counter electrode material and/or electrocatalyst must be carefully selected based on its intrinsic activity toward the redox couple in solution that facilitates hole transport and the regenerative flow of photocurrent. In the case of DSSCs, the counter electrode must maximize the rate of triiodide (I_3^-) reduction (Scheme 1.2a); for QDSSCs, polysulfide species (S_n^{2-}) in solution must be efficiently reduced at the counter electrode (Scheme 1.2b).

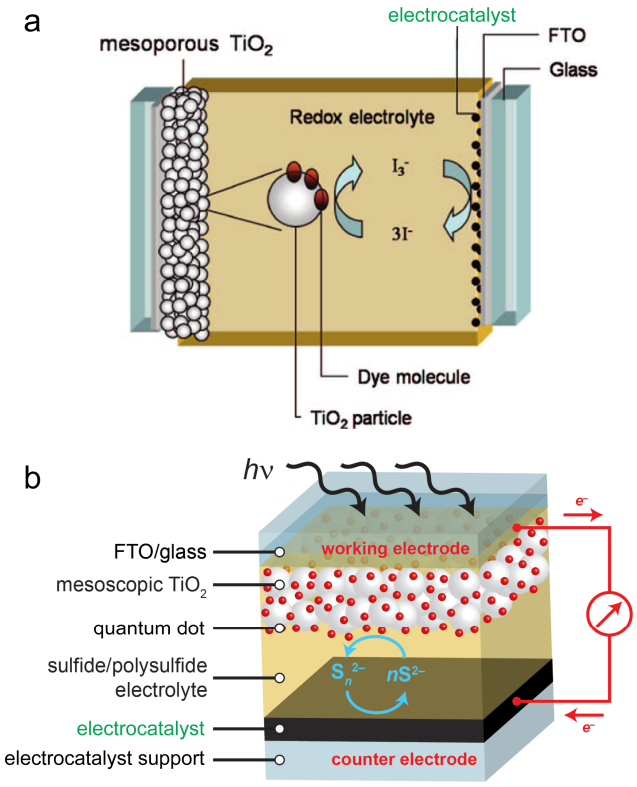

Scheme 1.2. Schematic illustrations of the respective roles of the electrocatalyst at the counter electrode of (a) dye- and (b) quantum dot-sensitized solar cells. Panels (a) and (b) adapted from Refs. 8 and 137, respectively, with permission from the American Chemical Society.

For the generation of hydrogen fuel through water electrolysis, summarized by the equation

$$2H^+(aq) + 2e^- \rightarrow H_2(g) \quad (3)$$

the cathode must be sufficiently active toward the HER to reduce protons at low overpotentials. In the case of the HER, in-depth mechanistic studies have determined the relationship between the Tafel slope and the rate-limiting step of electrocatalysis.[47] Specifically, a Tafel slope of approximately 120 mV decade^{-1} indicates that the discharge step (Volmer reaction),

$$H^+(aq) + e^- + * \rightarrow H^*_{ad} \quad (4)$$

where a free proton in solution adsorbs to an active site at the electrocatalyst surface (denoted here by an asterisk) with the transfer of an electron, is rate limiting. A Tafel slope of about 40 mV decade^{-1} suggests that the electrochemical desorption step (Heyrovský reaction),

$$H^*_{ad} + H^+(aq) + e^- \rightarrow H_2(g) + * \quad (5)$$

where a free proton in solution is simultaneously reduced and reacted with an adsorbed hydrogen atom to form $H_2(g)$, is rate limiting. A Tafel slope of 30 mV decade^{-1} indicates that the Tafel recombination step (Tafel reaction),

$$2H^*_{ad} \rightarrow H_2(g) + 2* \quad (6)$$

where two adjacent adsorbed hydrogen atoms combine to give $H_2(g)$, is rate limiting. Hydrogen evolution electrocatalysis typically proceeds through either reactions (4) and (5) (Volmer–Heyrovský mechanism) or (4) and (6) (Volmer–Tafel mechanism), but both can occur simultaneously, leading to intermediate Tafel slopes.

Similarly, in the proton exchange membrane fuel cells that convert hydrogen fuel to electricity, as well as in other types of fuel cells, the cathode must exhibit high activity toward

the four-electron reduction of dioxygen to water,

$$O_2(g) + 4H^+(aq) + 4e^- \rightarrow 2H_2O\,. \qquad (7)$$

In particular, achieving dioxygen reduction at low overpotentials remains a great challenge, even when using noble metal electrocatalysts, due to the strength of the O=O double bond.[27] Furthermore, ORR electrocatalysts with poor selectivity can yield hydrogen peroxide side products that are detrimental to fuel cell stability and lifetime.

When assessing the viability of a candidate electrocatalyst material, its performance is commonly compared to that of its competitors as well as to the state of the art. The Tafel slope and exchange current density of the electrocatalyst provide insights into its intrinsic activity. Furthermore, characteristics related to practical application, such as the onset potential for catalytic current or the overpotential required to achieve a certain catalytic current density (with 10 mA cm^{-2} being the most common standard used for HER electrocatalysis), are usually analyzed when evaluating electrocatalyst performance. The *IR* correction of current density–voltage data—which involves subtraction of the voltage drop due to the overall series or internal resistance, usually determined through electrochemical impedance spectroscopy or the current interrupt method[48]—prior to analysis enables a fair comparison of electrocatalyst performance. These aspects should be considered together with the electrocatalyst loading (typically expressed in mg cm^{-2}) and the effective electrochemical surface area (often determined either by probing the electrode double-layer capacitance[48–50] or through the physisorption of gas molecules) to ensure that electrocatalyst performance is accurately compared. Knowing the areal density of active sites for catalysis also permits calculation of the turnover frequency (*i.e.*, the number of chemical transformations that can be driven by a catalytic site per unit time), a measure of

intrinsic activity most commonly used to evaluate molecular catalysts. Standardization of these procedures into a common protocol for electrocatalyst benchmarking (as has recently been done for oxygen evolution electrocatalysts[51]) permits their objective comparison. Additional factors, such as cost, ease of synthesis, and mechanical and electrochemical stability under both operating and shutdown conditions, also inform the selection of electrocatalysts and/or electrode materials, but in all cases, electrocatalytic activity takes precedent.

The need for electrocatalysts to be electrically contacted can also place restrictions on their preparation, and, in a sense, this may have naturally led to the early identification of bulk noble metals as superior electrocatalysts. Although homogeneous catalysts can be freely diffusing in solution, heterogeneous electrocatalysts must be interfaced with a solid support that is sufficiently conductive to allow the passage of electrical current to the electrocatalysts. Common electrocatalyst supports include graphite, glassy carbon, metal foils, and transparent conducting oxide films on glass, but other conductive materials are suitable so long as they are inert in their respective electrochemical environments. Alternatively, sufficiently robust and metallically conducting electrocatalysts (including certain transition metals, alloys, and compounds) can double as the electrode material itself, eliminating the need for a conductive support. For this reason, the transition metals were among the first materials explored for electrode applications. Researchers quickly identified the noble metals, particularly platinum, as optimal electrode materials, due to their high electrocatalytic activity, chemical inertness, versatility, high conductivity, and resistance to oxidation.[32] Consequently, noble metal electrodes have long served as a trusted and reliable platform for electrochemical studies, with other transition metals failing to achieve comparable levels of performance and stability. For example,

in the case of triiodide reduction for regenerative liquid-junction DSSCs, platinum continues to serve as the benchmark counter electrode material, though other materials have recently been explored.[8,52–54] Similarly, the transition metals exhibit a Sabatier trend in HER electrocatalytic activity (yielding a so-called "volcano" plot), in accordance with theoretical predictions,[55] with platinum and other platinum group metals exhibiting the highest activity (Figure 1.1a).[56] Likewise, in agreement with experimental observation, calculations predict platinum to have the highest ORR activity among the transition metals (Figure 1.1b).[57] In each of these cases, the high electrocatalytic activity of platinum results from energetically favorable interactions with the relevant redox species in solution. Systematic surveys of electrocatalytic activity such as those shown in Figure 1.1 help to reveal design principles that can guide the development of alternative electrocatalysts with the potential to compete with platinum.

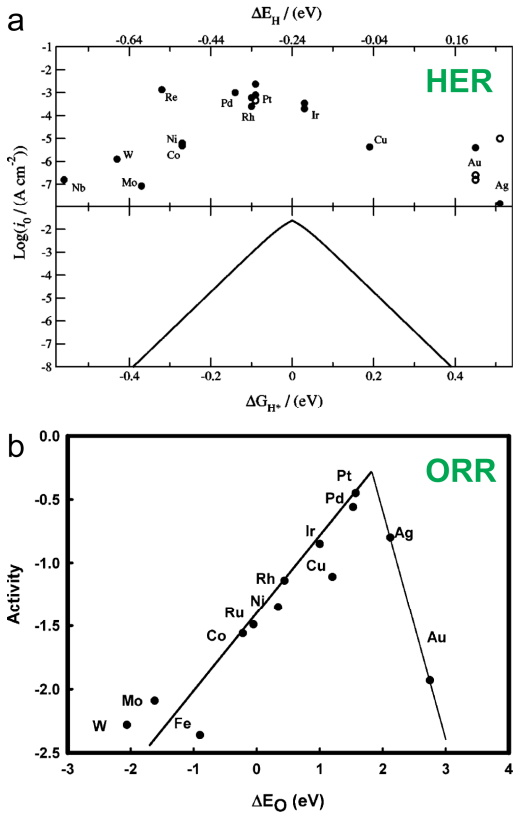

Figure 1.1. Trends in the electrocatalytic activity of various transition metals toward the hydrogen evolution reaction (HER) and oxygen reduction reaction (ORR). (a) Experimental (top) and theoretical (bottom) semi-log plots of the exchange current density for the HER at different transition metal surfaces plotted as a function of the calculated hydrogen chemisorption energy per atom (ΔE_H; top axis) and the free energy for hydrogen adsorption ($\Delta G_{H*} = \Delta E_H + 0.24$ eV; bottom axis). Reproduced from Ref. 56 with permission from The Electrochemical Society, Inc. (b) Theoretical activity of various close-packed transition metal surfaces toward the ORR plotted as a function of the oxygen binding energy (ΔE_O). Reproduced from Ref. 57 with permission from the American Chemical Society.

1.5. Earth-Abundant Inorganic Electrocatalysts

Many earth-abundant inorganic transition metal compounds have found use as heterogeneous catalysts in industrial hydrotreating and reforming processes.[58,59] For example, ruthenium-based catalysts for the hydrodesulfurization (HDS) and hydrodenitrogenation (HDN) of petroleum have been successfully replaced by sulfide catalysts containing molybdenum, cobalt, nickel, and/or tungsten.[60] Also, supported earth-abundant transition metal oxide catalysts have been implemented in a number of industrial processes and often serve as model systems to study catalytic transformations.[61] The extensive study and development of these and other industrially-relevant earth-abundant catalysts made them obvious candidate electrocatalysts for emerging energy conversion applications. Consequently, a number of the earth-abundant electrocatalysts discussed in this section have an interesting lineage that in some way traces back to alternative hydrotreating and reforming catalysts. Owing to the burgeoning interest in inexpensive electrochemical energy conversion, however, the variety of earth-abundant inorganic electrocatalysts currently under consideration has grown beyond these historical confines.

From a sustainability and scalability perspective, the need for electrocatalysts composed of elements in high terrestrial abundance is evident, but there are several other considerations that inform the selection of specific electrocatalyst materials and their methods of preparation. In addition to being low-cost and earth-abundant, we would prefer that electrocatalyst materials be environmentally benign. By using materials of low environmental impact, such as those composed primarily of rock-forming elements, disposal concerns are assuaged. Furthermore, it

would not be necessary to salvage or recycle the materials in devices containing earth-abundant electrocatalysts at the end of their lifetime, as is commonly done for devices containing noble metals. For economic and throughput reasons, the preparation of such materials should also be based on highly scalable procedures. For example, low-yield syntheses should be replaced with large-scale preparations, where possible, to ensure that electrocatalyst materials can be produced in quantities necessary to meet commercial demand. Similarly, highly specialized processing steps should be eliminated or at least minimized to avoid production bottlenecks. Lastly, the electrocatalyst support should be selected based on its capacity for both maximizing performance and minimizing cost. For example, efficient earth-abundant electrocatalysts demonstrated on metal foil, transparent conducting oxide/glass, or glassy carbon supports might instead be prepared on cheap yet highly conducting graphite substrates to reduce cost. To further boost electrocatalyst performance, high surface area supports such as carbon fiber paper could also be used.

The wide array of earth-abundant inorganic electrocatalysts that have been investigated so far can be most logically categorized based on their elemental composition. We will begin our survey by briefly discussing the molecular systems that have largely inspired the use of transition metals and their compounds as electrocatalysts. We will then outline the use of transition metals and their alloys for electrocatalytic applications, before moving on to the various classes of transition metal compounds. Note that, within this section, the phrase “transition metal” implies “non-noble transition metal” (referring to those elements indicated in red in Scheme 1.1), unless explicitly indicated otherwise. In each subsection, central themes and trends in materials development will be described, as will key demonstrations of electrocatalysis for energy

conversion.

1.5.1. Homogeneous and Supported Molecular Systems

Inspired by natural enzymes capable of efficiently catalyzing complex redox reactions, such as the photosynthetic reduction of carbon dioxide and oxidation of water to respectively produce carbohydrates and molecular oxygen,[62] great efforts have been made to design, synthesize, and characterize molecules that can split water (or other hydrogen-containing substrates) to generate hydrogen fuel.[40] Most recently, efforts have been primarily directed toward developing molecular catalysts that exclusively contain earth-abundant transition metals (*e.g.*, Fe, Co, Ni, and Mo), with particular attention toward those that can be coupled to light-absorbing semiconductors to drive the photoelectrochemical production of hydrogen fuel.[34,42–44,46] Similarly, molecular catalysts for the electrochemical reduction of carbon dioxide have been investigated.[23,45] Molecular catalysts can operate as free complexes in solution or can be covalently grafted to a conductive support.[34,42,46,63] Biomimetic incomplete cubane-type $[Mo_3S_4]^{4+}$ molecular electrocatalysts supported on highly ordered pyrolytic graphite or carbon black have been shown to exhibit high HER electrocatalytic activity.[64] When drop-cast on light-absorbing *p*-type silicon photocathodes, these cubane-like molecular clusters enable solar hydrogen evolution.[65] Despite their high intrinsic activity, such molecular catalysts often suffer from low overall performance and relatively poor stability. The possibility of unraveling the mechanisms of complex catalytic processes, however, motivates study of these molecular catalysts.[43] These insights could then lead to design principles that help guide the development of inorganic heterogeneous electrocatalysts with superior performance and long-term stability.[41] Indeed, the careful study of molecular systems has informed the development of several earth-

abundant heterogeneous electrocatalysts that will be henceforth discussed. Due to the vast body of work on molecular catalysts for alternative energy applications, we cannot provide an exhaustive overview here; instead, we refer the reader to the many review articles that summarize recent progress in this field.[34,40–46]

1.5.2. Transition Metals and Their Alloys

The superior intrinsic activity and stability of noble metal electrodes has mostly excluded the use of elemental earth-abundant transition metal electrodes for energy conversion applications. The early realization that most transition metals are reactive and/or susceptible to corrosion in many electrolytes, both aqueous and non-aqueous, has led to a strong preference for inert noble metal electrodes, even in cases where their high intrinsic activity is not needed. For example, several transition metals have been investigated as alternative counter electrode materials in DSSCs in hope of replacing platinum, including nickel, molybdenum, and tungsten, but all suffered from inferior activity and corrosion caused by the iodide species in the electrolyte.[52] Similarly, several transition metal counter electrodes have been employed in QDSSCs that employ the sulfide/polysulfide redox couple in aqueous solution. In contrast to their behavior in DSSCs, it was found that reactivity between certain transition metals and dissolved sulfur species leads to the rapid formation of a transition metal sulfide coating, which, remarkably, catalyzes polysulfide reduction more effectively than even platinum (see additional discussion in Section 1.5.4).[66]

The measurement of the HER electrocatalytic activity of the transition metals in both acidic[67] and alkaline[68] conditions has helped to guide the development of state-of-the-art earth-abundant inorganic electrocatalysts. These activities, as determined from the exchange current

density or the overpotential at a standard current density, were found to correlate with the work function of the transition metal in both acid and base, with the high work function noble metals consistently exhibiting the highest activities.[67,68] Other possible correlations between the rate of HER and the physical properties of elemental electrodes have also been investigated.[69] These results suggest that the electronic properties of a material factor heavily into its anticipated electrocatalytic activity, and that certain physical properties could predict trends in catalytic activity. Establishing such trends for redox reactions central to other energy conversion applications could similarly guide the development of improved electrocatalysts.

Noting the low activity of transition metal electrocatalysts as compared to the noble metals in most energy conversion applications, researchers began investigating the activity of transition metal alloys. In the case of hydrogen generation through electrocatalytic water splitting, "volcano" plots of transition metal activity (Figure 1.1a) suggested that there could be synergistic benefits of using alloy or multimetallic electrodes that could, through the cooperative interactions of metal species with differing hydrogen affinity, emulate or even improve upon the highly active surfaces of noble metal electrodes.[70–73] Specifically, alloying of transition metals is expected to tune the *d*-band electron filling, Fermi level energy, and interatomic spacing, all of which could impact the affinity of the alloy electrocatalyst toward the adsorbate species of interest.[32,74] One of the earliest observations of this effect was for the Ni–Mo alloys, which exhibit superb activity toward the HER in alkaline conditions.[34,75] Ni–Mo alloy coatings prepared on nickel mesh substrates have been shown to achieve a current density of 1 A cm^{-2} at a low cathodic overpotential of only 83 mV vs. the reversible hydrogen electrode (RHE).[75] Other transition metal alloys, including Ni–V, Ni–Fe, Ni–W, Co–Mo, and Fe–Mo, similarly exhibited

high activity toward the HER in alkaline conditions, although not as high as that of Ni–Mo.[76,77] Remarkably, these electrocatalytic alloy films retain their high performance for at least one year of continuous operation in alkaline conditions, with no decay in activity under shutdown conditions.[76] More recently, a synthesis for unsupported Ni–Mo nanopowders was developed, and Ni–Mo nanopowder films cast on titanium foil electrodes exhibited exceptional activity toward the HER in alkaline conditions at a substantially reduced electrocatalyst mass loading.[78] Moreover, the electrodeposition of Ni–Mo electrocatalyst particles on silicon photoelectrodes has been demonstrated, enabling an integrated photoelectrochemical system capable of storing solar energy in the form of hydrogen fuel.[79,80]

Following the observation of high HER electrocatalytic performance from Ni–Mo catalyst films, the activity of several ternary transition metal alloys was similarly investigated. Consistent with the relatively high HER activity of Ni and the Ni–Mo alloys, the highest performing ternary alloy electrocatalysts typically contain both Ni and Mo. Ternary Ni–Mo–Cd electrocatalyst films prepared on iron substrates by electrodeposition were claimed to possess very high intrinsic activity toward the HER in alkaline conditions, with Tafel slopes as low as 26–30 mV decade^{-1}.[81] Despite incorporation at only 1 at.%, the presence of cadmium in the ternary alloy was thought to facilitate hydrogen evolution by a desorptive mechanism due to adsorbed hydrogen or surface hydride species.[81] Various other ternary Ni–Mo-derived alloys have also been explored as HER electrocatalysts in alkaline conditions, including alloys containing Fe, Cu, Zn, W, Co, or Cr, with the Ni–Mo–Fe alloy exhibiting the highest performance among these.[82] To illustrate the real-world applicability of these ternary transition metal alloy HER electrocatalysts, Ni–Mo–Zn was recently integrated into a monolithic

photoelectrochemical water-splitting "artificial leaf" device.[29,83]

1.5.3. Transition Metal Oxides

Despite their prevalence as industrial catalysts,[61] the binary transition metal oxides generally do not find use as electrocatalysts due to their poor electrical conductivity and low chemical stability (particularly in acidic conditions) among transition metal compounds.[39] However, there are several successful demonstrations of transition metal oxide electrocatalysts for energy conversion.[39,84] Many transition metal oxides have decent ORR activity in alkaline media.[39] For example, manganese oxide (MnO_2) nanostructures have been shown to be effective ORR electrocatalysts in basic conditions,[85] and spinel-phase (AB_2O_4) Co–Mn–O nanoparticles have been demonstrated as bifunctional electrocatalysts for both the oxygen reduction and evolution reactions.[86] Similarly, spinel-phase lithium cobalt oxide ($LiCoO_2$) is an efficient oxygen evolution electrocatalyst, and chemically delithiated $Li_{1-x}CoO_2$ exhibits both oxygen reduction and evolution activity.[87] Interestingly, the delithiation procedure allows the $Li_{1-x}CoO_2$ electrocatalyst to be tuned for optimal bifunctional activity (which occurs for $x = 0.5$).[87] Perovskite-phase (ABO_3) oxides have also been investigated as ORR electrocatalysts, with established design principles and trends serving as predictors of electrocatalytic activity.[88] By preparing transition metal oxide electrocatalysts on a compatible conductive support, their performance and stability can often be dramatically improved.[89] For example, cobalt oxide (Co_3O_4) nanoparticles exhibit little ORR activity on their own; however, this activity is greatly enhanced when they are grown on a reduced graphene oxide (RGO) support.[90] In this case, favorable chemical and electronic coupling between RGO and the Co_3O_4 nanoparticles leads to a synergistic enhancement of electrocatalytic activity (see additional discussion in Section 1.7.4).[90]

Similarly, solution-grown magnetite (Fe_3O_4) and core/shell nickel/nickel oxide (Ni/NiO) nanoparticles anchored on metallically conducting cobalt diselenide ($CoSe_2$) nanobelts have been shown to exhibit enhanced activity toward the ORR[91] and HER,[92] respectively. Niobium oxides have also been demonstrated as stable, efficient ORR electrocatalysts in acidic conditions.[93] More recently, several niobium oxides have emerged as effective counter electrode materials in DSSCs, with tetragonal NbO_2 counter electrodes enabling power conversion efficiencies higher than that of equivalent devices assembled with a platinum counter electrode.[94] Similarly, faceted iron oxide (α-Fe_2O_3, hematite) nanoparticles were theoretically predicted to exhibit high activity toward triiodide reduction, and films thereof were subsequently demonstrated to compete with platinum counter electrodes in DSSC devices.[53]

1.5.4. Transition Metal Chalcogenides

The transition metal chalcogenides[95,96] make up the largest class of earth-abundant electrocatalysts. Initial studies on the electrocatalytic properties of metal chalcogenide electrodes mostly grew out of the investigation of single-crystalline semiconducting metal chalcogenide photoelectrodes, such as CdS, CdSe, CdTe, ZnSe, and Bi_2S_3.[97–100] More recently, these semiconducting materials have been synthesized as nanocrystalline quantum dots and used as light-absorbing inorganic sensitizers for the wide band gap semiconductor films in QDSSCs.[9–11] In these studies, it was found that the sulfide/polysulfide redox electrolyte prevented metal chalcogenide photoelectrode corrosion, thereby making it the preferred hole mediator.[98–100] Earlier works had identified platinum and gold as the most chemically stable electrode materials in the sulfide/polysulfide electrolyte, with high surface area platinum electrodes showing the best performance,[101] but it was later found that sulfur species poison platinum electrodes by

irreversibly adsorbing to their surface, substantially reducing their electrocatalytic activity.[102] It was known that sulfur species in the sulfide/polysulfide electrolyte rapidly attack non-noble transition metals such as nickel and tungsten, forming a metal sulfide surface coating,[101] but decades would pass before such high surface area metal sulfide films were discovered to possess substantially higher intrinsic activity toward the sulfide/polysulfide redox couple than platinum.[66] Cuprous sulfide (Cu_2S) spontaneously formed on copper or brass foils was identified as the most active transition metal sulfide electrocatalyst toward the sulfide/polysulfide redox couple; however, its chemical and mechanical instability in the sulfide/polysulfide electrolyte could lead to poisoning of the photoactive electrode and, eventually, complete disintegration.[66] The mechanical stability of Cu_2S-based electrodes was improved through the preparation of a Cu_2S–RGO composite,[103] which has been used as the electrocatalytic counter electrode material in liquid-junction QDSSCs to give solar light-to-electricity power conversion efficiencies as high as 6.6%.[104]

For QDSSCs, the chemical incompatibility of platinum electrodes with the sulfide/polysulfide electrolyte naturally led to the exploration of alternative, earth-abundant transition metal chalcogenide electrocatalysts for polysulfide reduction. However, in the case of DSSCs that employ the iodide/triiodide redox couple, platinum counter electrodes consistently enable the highest device performance. Here, the challenge is to identify earth-abundant electrocatalysts for triiodide reduction that can not only withstand the corrosive iodide/triiodide electrolyte, but also compete with the exceptional activity of platinum. Several transition metal chalcogenides meet these requirements. Furthermore, many transition metal chalcogenides have been investigated as replacements for noble metal electrocatalysts for the HER and ORR. Within

this section, the transition metal chalcogenides will be discussed in subgroups defined by their structure types, with most being either layered or cubic pyrite-phase materials. The emerging amorphous transition metal chalcogenide electrocatalysts—which are characterized by their *lack* of a well-defined structure—will also be briefly discussed, as will materials that do not fall into one of these three main subgroups.

1.5.4.1. Layered Materials

The layered transition metal dichalcogenide (TMD) materials,[105] with a general chemical formula of MX_2 (M being a transition metal, and X typically being S or Se), make up perhaps the most widely studied family of earth-abundant inorganic electrocatalysts.[106,107] Among the many layered TMD electrocatalysts that have recently been used for energy conversion, molybdenum disulfide (MoS_2) was one of the first to emerge, and it continues to serve as a prototypical example.[108] In 2005, a pioneering work investigating the energetics of hydrogen evolution from a [NiFe]-hydrogenase system and the FeMo cofactor active site of nitrogenase suggested MoS_2 as a possible inorganic analogue of these natural systems.[109] The electrocatalytic activity of MoS_2 nanoparticles dispersed on carbon supported the computational model, with the edge sites of the MoS_2 layers identified as being most catalytically active toward the HER (as is also the case in HDS).[109] Scanning tunneling microscopy studies performed on MoS_2 nanoparticles on a Au(111) support have served to unequivocally establish the edge sites of MoS_2 as being most active for HER (Figure 1.2a), exhibiting turnover frequencies comparable to those of high-activity noble metals.[110] The activity of these MoS_2 edge sites can also be enhanced through the introduction of cobalt "promoter" species.[111] In an effort to resolve the exact nature of the active edge sites of MoS_2, a well-defined Mo^{IV}-disulfide molecular mimic has been prepared and characterized both

structurally and electrochemically (Figure 1.2b).[112]

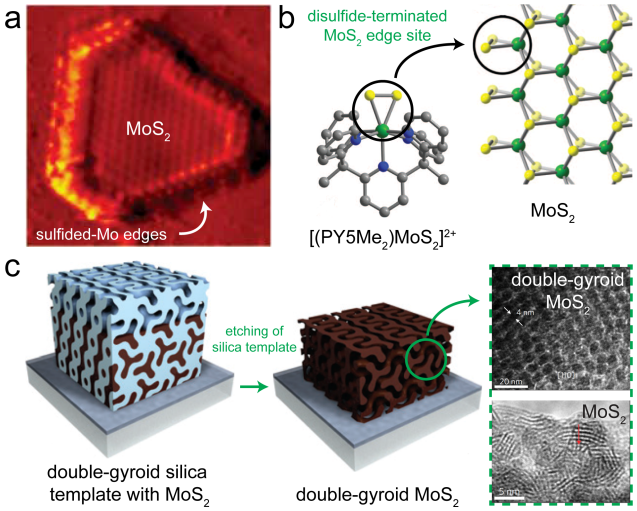

Figure 1.2. Identification of the edge-site activity of MoS_2 toward the HER, and an example of the engineering strategies used to maximize the exposure of these edge sites. (a) Atomically-resolved scanning tunneling microscopy image of a MoS_2 nanoparticle, showing the sulfided Mo-edge sites that exhibit superior HER electrocatalytic activity (60 Å by 60 Å, 1.0 nA, 300 mV). (b) Molecular analogue (left) of the triangular disulfide-terminated MoS_2 edge sites (right). (c) Abbreviated scheme for the synthesis of double-gyroid mesoporous MoS_2 engineered to preferentially expose edge sites for enhanced HER activity. Panels a and b adapted from Refs. 110 and 112, respectively, with permission from the American Association for the Advancement of Science. Panel c adapted from Ref. 124 with permission from Macmillan Publishers.

Although the layered TMDs tend to preferentially form closed fullerene-like or nanotubular structures to minimize the presence of dangling bonds at their edges,[113] various synthetic[50,114–123] and engineering[124,125] strategies have been applied to proliferate the exposed edge sites of the layered TMDs for increased electrocatalytic activity. The introduction of defects within the layered TMD crystal structure can also generate new active edge sites for catalysis, enhancing its performance.[119,120] Alternatively, the morphology of the layered TMD material can be controlled during synthesis to maximize the exposure of edge sites. For example, by engineering the synthesis of MoS_2 to yield a high surface area, mesoporous, double-gyroid morphology, the fraction of exposed MoS_2 edge sites has been increased, boosting its HER electrocatalytic performance (Figure 1.2c).[124]

Furthermore, it has recently been shown that chemical exfoliation of layered TMDs can dramatically increase the availability of active edge sites while simultaneously converting the as-synthesized MX_2 material from its thermodynamically-favored semiconducting 2H polymorph to its metallic 1T polymorph, granting enhanced electrocatalytic activity and electrical conductivity (Figure 1.3a).[50,115,116] This strategy has been employed for nanostructures of both MoS_2[115] (Figure 1.3b–c) and WS_2[50] (Figure 1.3d–e) synthesized through chemical vapor deposition (CVD). The resulting 1T-MoS_2 and 1T-WS_2 nanosheets exhibit dramatically enhanced HER electrocatalytic performance as compared to their corresponding 2H polymorphs (Figures 1.3f and 1.3g, respectively) despite the relatively low mass loading of these electrocatalyst materials. Specifically, reduced Tafel slopes are observed (43 mV decade^{-1} for the 1T-MoS_2 nanosheets, as indicated in the inset of Figure 1.3f), and low cathodic overpotentials are required to achieve an electrocatalytic current density of 10 mA cm^{-2} (187 mV and 142 mV vs. RHE for 1T-MoS_2 and

1T-WS_2, respectively). Structural characterization and electrochemical studies confirm that the metallic 1T-MoS_2 and 1T-WS_2 nanosheets exhibit facile electrode kinetics, low-loss electrical transport, and an increased density of active sites for catalysis. These distinct and previously unexploited features of 1T-MX_2 make these metallic nanosheets highly competitive earth-abundant HER electrocatalysts. Note that, in these cases, the chemical nature of the MX_2 material plays a critical role in determining its electrocatalytic activity, *i.e.*, the metallic 1T-MX_2 nanosheets are intrinsically more electrocatalytically active than the semiconducting 2H-MX_2 nanostructures. Furthermore, electrocatalytic 1T-MoS_2 has recently been coupled to a *p*-type silicon photoelectrode (Figure 1.3h) to enable hydrogen evolution driven by solar energy (Figure 1.3i).[126] Due to the exceptional HER activity of 1T-MoS_2 and the high-quality electrocatalyst–semiconductor interface enabled by the direct CVD growth of MoS_2 on silicon (followed by chemical exfoliation), a much higher photocurrent density for hydrogen evolution was achieved as compared to 2H-MoS_2 on silicon (Figure 1.3i).

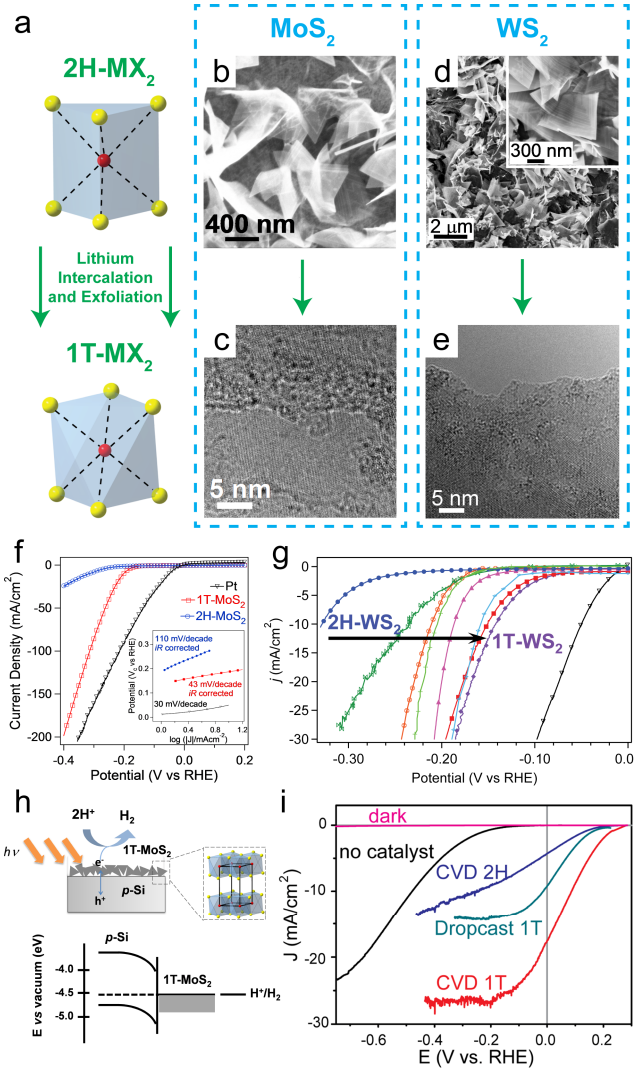

Figure 1.3. Enhancement of the electrocatalytic activity of layered TMD nanosheets toward the HER through chemical exfoliation. (a) Intercalation of lithium into semiconducting 2H-MX_2 causes a phase transition to the metallic 1T-MX_2 polymorph. This phase conversion has been demonstrated for the (b) 2H- to (c) 1T-MoS_2 and (d) 2H- to (e) 1T-WS_2 transitions, with subsequent exfoliation resulting in the formation of nanosheets. The combination of phase conversion and the exposure of additional catalytic edge sites results in a dramatic enhancement in HER electrocatalytic activity, as shown in the polarization curves for both (f) MoS_2 and (g)

WS_2. The reduced Tafel slope of 1T-MoS_2 (panel f, inset) confirms that the improved performance is due to an increase in intrinsic activity along with a proliferation of edge sites for catalysis. (h) Direct growth of 1T-MoS_2 nanosheets on a *p*-type Si photocathode enables (i) efficient hydrogen evolution driven by solar energy. Panels a–c and f adapted from Ref. 115 and panels h–i adapted from Ref. 126, both with permission from the American Chemical Society; panels d, e, and g adapted from Ref. 50 with permission from The Royal Society of Chemistry.

Similarly, vertically aligned layers of MoS_2 can be grown on glassy carbon electrodes[117] and the spacing between layers can be tuned via the electrochemical intercalation of lithium ions (along with a concomitant 2H to 1T phase transition)[118] to grant enhanced activity toward the HER. Various chemical and engineering strategies can be used to improve the electrocatalytic activity of other layered TMDs, including WS_2,[127,128] $MoSe_2$,[117,129] and WSe_2.[129] The success of layered TMD electrocatalysts has further driven research efforts toward their preparation in nanostructured morphologies in order to leverage new or improved physical and chemical properties for energy conversion (and other) applications.[130–133] Additionally, the recent success of $NbSe_2$ nanosheets[134] and $MoSe_2$ particles[135] as triiodide reduction electrocatalysts in DSSCs and petaled MoS_2 as a polysulfide reduction electrocatalyst in QDSSCs[136] suggests that the layered TMDs likely exhibit high activity toward a broad range of redox processes.

1.5.4.2. Pyrite-Phase Materials

Recently, the cubic pyrite-phase TMDs[96] (MQ_2, where M is typically Fe, Co, or Ni and Q is commonly S or Se) have emerged as a new subclass of efficient electrocatalysts. As a rich family of mineral-forming compounds, the pyrites are expected to have high chemical stability, making them attractive for electrocatalytic applications. Perhaps inspired by industrial catalysts,[58] pyrite-phase materials have been exploited in sensitized solar cells and investigated as oxygen reduction and hydrogen evolution electrocatalysts. For example, metallic cobalt pyrite (CoS_2) polycrystalline thin films synthesized on insulating glass substrates (Figure 1.4a) were shown to outperform platinum counter electrodes in QDSSCs filled with sulfide/polysulfide electrolyte, improving device performance and stability (Figure 1.4b).[137] Electrochemical characterization further confirmed that CoS_2 exhibits both enhanced stability and activity toward

polysulfide reduction as compared to platinum (Figure 1.4c).

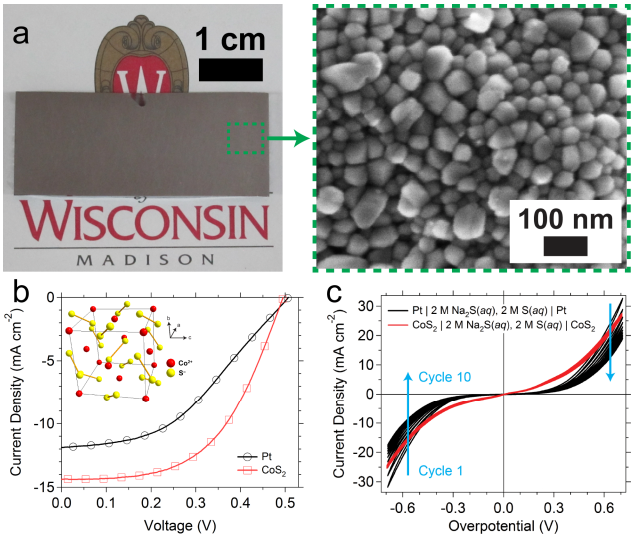

Figure 1.4. Structural and electrochemical characterization of a metallic cobalt pyrite (CoS_2) thin film synthesized on glass and used as the counter electrode in a QDSSC. (a) Digital photograph showing the opaque CoS_2 film on the glass substrate (left), and scanning electron microscopy (SEM) image depicting the small-grain polycrystalline texture of the CoS_2 film (right). (b) Current density−voltage characterization of QDSSC devices filled with an aqueous sulfide/polysulfide (2 M S^{2-}/2 M S) electrolyte solution showing the enhanced performance of devices assembled with a CoS_2 counter electrode (red trace with square markers) rather than a Pt counter electrode (black trace with circle markers). The cubic pyrite crystal structure of CoS_2 is shown in the inset. (c) Cyclic voltammetric characterization of symmetrical electrochemical cells employing either CoS_2 (red trace) or Pt (black trace) electrodes and filled with sulfide/polysulfide electrolyte. Adapted from Ref. 137 with permission from the American Chemical Society.

Metallic CoS_2 also exhibits good stability and activity toward the iodide/triiodide redox couple, particularly when prepared in a high surface area morphology[49] or as a composite with graphene.[138] Remarkably, nanorod arrays[139] and nanocrystalline thin films[140] of iron pyrite (FeS_2), the semiconducting isostructural analogue of CoS_2,[141,142] on fluorine-doped tin oxide (FTO)/glass substrates have also been shown to compete with platinum counter electrodes in DSSCs. Similarly, high surface area CoS_2 hollow spheres drop cast on FTO/glass possess high electrocatalytic activity toward the disulfide/thiolate (T_2/T^-) redox couple sometimes used in DSSCs and QDSSCs, enabling DSSC performance exceeding that achieved with a platinum counter electrode.[143] Some pyrite phase transition metal diselenides, including $CoSe_2$ and $NiSe_2$, also show high electrocatalytic activity toward triiodide reduction.[135]

The ORR activity of the pyrite-phase (and other) transition metal chalcogenides was investigated as early as the 1970s,[144] but due to their comparatively low performance and durability, their activity went mostly unappreciated. It was not until much later that pyrite-phase transition metal disulfides including FeS_2, $(Fe,Co)S_2$, and CoS_2 were again investigated as model ORR electrocatalysts.[145,146] The family of pyrite-phase ORR electrocatalysts has since been expanded to include transition metal diselenides, with carbon-supported $CoSe_2$ nanoparticles exhibiting decent ORR activity in acidic conditions.[147] These works inspired further study of the pyrites for ORR, and it was recently found that nanocrystalline CoS_2 exhibits high activity and long-term stability under ORR operating conditions,[148,149] making it a promising candidate for the replacement of platinum in fuel cell systems.

The noble metal-containing compound ruthenium disulfide (RuS_2) was one of the first pyrites identified as an active HER electrocatalyst in acidic conditions.[150] Because the pyrite

structure accommodates compositional variation as a solid solution, allowing the formation of pyrite-phase alloys,[58] the effects of cobalt or nickel substitution in the RuS_2 lattice on electrocatalytic activity were investigated and optimized.[150] Interestingly, the binary pyrite-phase compounds CoS_2 and nickel pyrite (NiS_2) were also suggested as HER electrocatalysts,[150] but it was not until very recently that their specific HER activity was investigated. The high activity of CoS_2 toward the HER in acidic conditions, confirmed using thin film electrodes (Figure 1.5a), has been further enhanced by preparing CoS_2 microwire (Figure 1.5b) and nanowire (Figure 1.5c) arrays directly on a graphite support.[49] These comparisons showed that the introduction of micro- or nanostructuring to the CoS_2 material dramatically increased its performance (Figure 1.5d) and stability (Figure 1.5e) during hydrogen evolution by synergistically increasing the effective electrode surface area (leading to proliferation of active sites for electrocatalysis) and facilitating the release of evolved gas bubbles from the electrode surface (Figure 1.5f), particularly for the microwire structures, as further discussed in Section 1.7.1.[49]

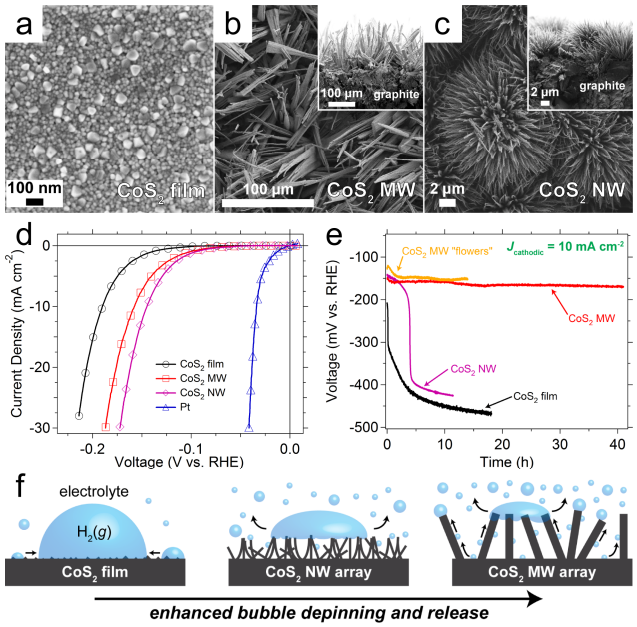

Figure 1.5. Scanning electron microscopy images of cobalt pyrite (CoS_2) (a) film, (b) microwire (MW), and (c) nanowire (NW) electrodes. (d) Polarization curves showing the relative activity of as-prepared CoS_2 materials with different morphologies on graphite electrodes (film, open circles; MW, open squares; NW, open diamonds) toward the hydrogen evolution reaction in 0.5 M $H_2SO_4(aq)$, along with that of a Pt wire standard (open triangles). (e) Long-term stability measurements for representative CoS_2 film, NW, MW, and hierarchical MW "flower" electrodes demonstrating the increased stability achieved through nanostructuring or, in particular, microstructuring. (f) Schematic depictions of CoS_2 NWs and MWs bursting the larger hydrogen gas bubbles that commonly pin at the surface of CoS_2 film electrodes, with the MWs most effectively wicking the evolved bubbles and maintaining the solid–liquid interface. Adapted from Ref. 49 with permission from the American Chemical Society.

The same micro- and nanostructuring strategy was also shown to enhance the performance of CoS_2-based electrodes toward triiodide and polysulfide reduction, suggesting their improved performance in liquid-junction DSSCs and QDSSCs, respectively.[49] Similarly, $CoSe_2$ films have been prepared on high surface area carbon fiber paper substrates to further increase their HER electrocatalytic performance.[151] Furthermore, the HER activities of various binary earth-abundant transition metal pyrites (and alloys thereof), including disulfides (Figure 1.6a) and diselenides (Figure 1.6b), were screened and compared to bring out trends in their performance. Based on a comparison of their Tafel slopes (Figure 1.6c), it was found that thin films of CoS_2, $CoSe_2$, and NiS_2 on glassy carbon exhibited the highest intrinsic activities among the pyrites.[152] These recent works serve to substantially broaden the family of pyrite-phase HER electrocatalysts and establish that their activity can be modified through alloying, suggesting a potential pathway toward improving their intrinsic activity toward the HER and perhaps other electrochemical energy conversion processes.

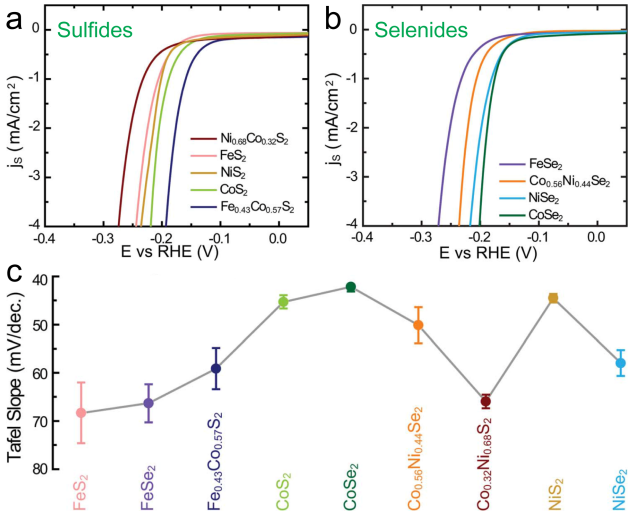

Figure 1.6. Comparison of the performance of various pyrite-phase transition metal (a) disulfide and (b) diselenide HER electrocatalysts, along with (c) a comparison of their corresponding Tafel slopes. Adapted from Ref. 152 with permission from The Royal Society of Chemistry.

1.5.4.3. Amorphous Materials

In the last few years, amorphous molybdenum sulfide (MoS_x, x = 2–3) has been identified as an effective electrocatalyst for the HER.[107,153] Despite lacking the well-defined catalytically active sites of MoS_2, amorphous MoS_x remarkably exhibits higher activity than as-synthesized crystalline MoS_2, achieving Tafel slopes as low as 40 mV decade^{-1} (Figure 1.7).[153] Furthermore, amorphous MoS_x can be deposited on conducting substrates through facile and scalable electrodeposition[153–156] or wet chemical[157–159] syntheses at room temperature and atmospheric pressure, in contrast to the harsh conditions (high temperature, low pressure, *etc.*) typically employed to synthesize high-quality crystalline MoS_2, and reduced to the more active amorphous MoS_2 under standard electrochemical operating conditions. Amorphous MoS_x exhibits high HER activity and stability over a wide range of electrolyte acidities, making it compatible with most contemporary water-splitting and fuel cell technologies.[153] Recently it has been reported that codepositing amorphous MoS_x with conductive polypyrrole yields composite electrocatalyst films with exceptional activity toward the HER.[155] Additionally, engineering strategies analogous to those employed for MoS_2 (and other earth-abundant inorganic electrocatalysts) have similarly been used to boost the HER electrocatalytic performance of amorphous MoS_x.[159,160]

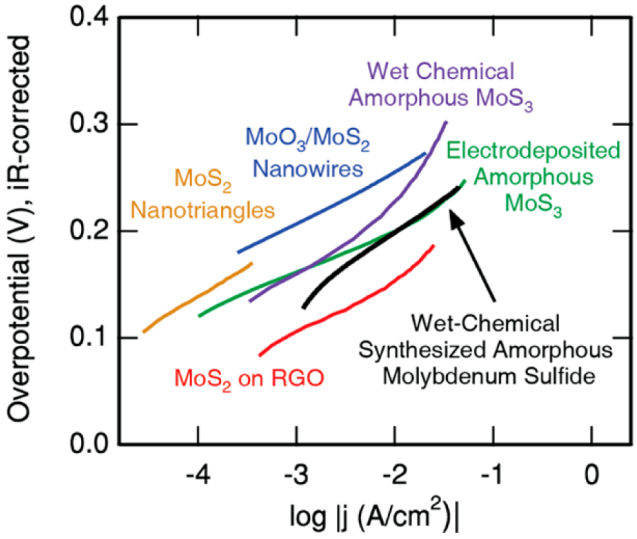

Figure 1.7. Tafel plot comparing the intrinsic activity of various molybdenum sulfide electrocatalysts toward the HER. Adapted from Ref. 157 with permission from the American Chemical Society.

Following these reports of high electrocatalytic activity and previous demonstrations of MoS_2 as an effective cocatalyst for photocatalytic hydrogen evolution driven by visible light,[161] amorphous MoS_x has also been used to catalyze the photoelectrochemical splitting of water. When deposited over a Ti/TiO_x-protected n^+p-Si photocathode, amorphous MoS_x enables an onset of photoelectrochemical hydrogen evolution at 0.33 V vs. RHE, approaching that achieved when using platinum.[154] These photoelectrodes were relatively stable, with degradation in performance caused by failure of the Ti/TiO_x protection layer (resulting in surface oxidation of the photocathode) rather than the amorphous MoS_x electrocatalyst.[154] It was later found that Mo/MoS_2 can serve as a more chemically stable silicon protection layer than Ti/TiO_x, improving long-term stability.[162] Amorphous MoS_x has also been electrochemically deposited over TiO_2-protected cuprous oxide (Cu_2O) photocathodes to enable photoelectrochemical hydrogen evolution.[156] The onsets of photocurrent for the MoS_x/n^+p-Si[154] and MoS_x/Cu_2O[156] photocathodes are more favorable than that for the 1T-MoS_2/p-Si heterojunction[126] due to a buried junction and more advantageous band bending; however, higher photocurrent density has been achieved using 1T-MoS_2/p-Si photocathodes, likely due to the high-quality semiconductor–electrocatalyst interface and the superior HER electrocatalytic activity of 1T-MoS_2. Recently, the use of amorphous transition metal chalcogenide electrocatalysts has expanded beyond just MoS_x, with amorphous cobalt sulfide (Co–S) films electrodeposited on conducting and semiconducting electrodes showing high activity toward electrochemical and photoelectrochemical hydrogen evolution in neutral or alkaline electrolytes.[163]

1.5.4.4. Other Phases

A number of other transition metal chalcogenides and their nanostructures have emerged

as promising electrocatalysts.[131] For example, sea urchin-like NiSe nanofiber assemblies exhibit HER activity comparable to supported MoS_2 electrocatalysts.[164] Additionally, CoS and Co_9S_8 have been shown to compete with platinum toward triiodide reduction in DSSCs.[165–167] Similarly, small-grain NiS films electrodeposited on FTO/glass show high electrocatalytic activity toward triiodide reduction and enable DSSC performance comparable to that achieved with conventional platinum counter electrodes.[168] Very recently, the metal selenides (including $Cu_{1.8}Se$ and PbSe) have emerged as a new class of efficient electrocatalysts for polysulfide reduction in QDSSCs.[169] Similarly, several transition metal selenides, including $Co_{0.85}Se$ and $Ni_{0.85}Se$, have also been shown to be efficient electrocatalysts for triiodide reduction in DSSCs.[170]

1.5.5. Transition Metal Nitrides

As has also been the case for the transition metal sulfides, the use of transition metal nitrides as industrial catalysts, particularly for HDN,[59,171] inspired investigation of their applicability as electrocatalytic materials. Their stability in conditions of extreme pH and under high applied electrochemical bias makes them good candidate electrocatalyst materials.[39] Transition metal nitride compounds are commonly prepared by the thermal nitridation of transition metal-containing starting materials in the presence of ammonia.[39,172] Various transition metal nitrides have been examined as electrocatalyst materials, including the tungsten nitrides (WN and W_2N), molybdenum nitrides (MoN and Mo_2N), tantalum nitrides (TaN and Ta_3N_5), and nickel molybdenum nitrides ($NiMoN_x$), as well as titanium, vanadium, and niobium nitride (TiN, VN, and NbN, respectively).[172] Due to electronic modification of the transition metal *d*-band electron density of states, the transition metal nitrides are expected to exhibit enhanced noble

metal-like activity toward those electrocatalytic transformations that involve the donation of *d* electrons, such as the HER.[171]

Noting the high activity of the Ni–Mo alloys toward the HER and the enhanced chemical stability of the transition metal nitrides over the corresponding metals, carbon-supported MoN and $NiMoN_x$ nanosheets were prepared and shown to exhibit improved HER activity and cycling stability in acidic conditions relative to carbon-supported spherical NiMo alloy nanoparticles.[173] The low Tafel slope of 35 mV $decade^{-1}$ exhibited by the $NiMoN_x$ nanosheets was rationalized by the high fraction of exposed active sites and a favorable catalytic synergism between nickel, which binds H weakly, and molybdenum, which binds H strongly.[71,173] Similarly, layered nanoparticulate cobalt molybdenum nitride ($Co_{0.6}Mo_{1.4}N_2$) has been reported as an efficient, stable HER electrocatalyst in both acidic and alkaline conditions with performance exceeding that of the $NiMoN_x$ nanosheets.[174] The improved HER electrocatalytic activity of $Co_{0.6}Mo_{1.4}N_2$ and $NiMoN_x$ relative to their binary counterparts is illustrated in Figure 1.8.

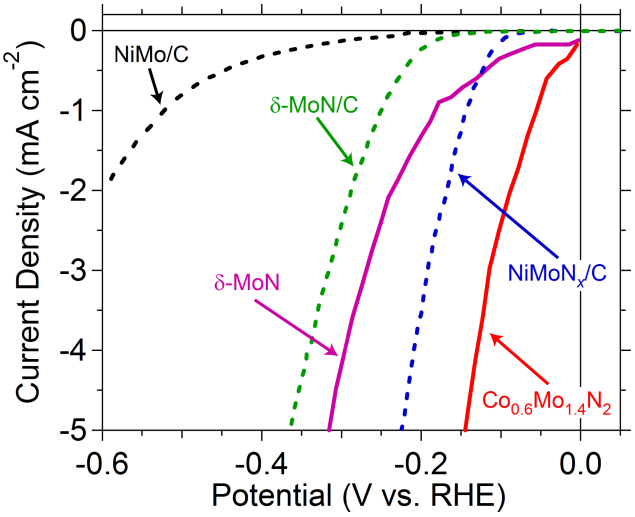

Figure 1.8. Polarization curves illustrating the relative activity of carbon-supported NiMo nanoparticles (NiMo/C, black trace), δ-MoN nanosheets (δ-MoN/C, green trace), and NiMo nitride nanosheets (NiMoN$_x$/C, blue trace), as well as nanostructured MoN (δ-MoN, violet trace) and cobalt molybdenum nitride ($Co_{0.6}Mo_{1.4}N_2$, red trace) toward the HER in $H_2(g)$-saturated 0.1 M $HClO_4(aq)$. The dashed traces show the improved activity of the transition metal nitrides relative to the corresponding transition metal alloy catalyst, with the ternary NiMoN$_x$/C catalyst exhibiting superior performance. Similarly, the solid traces show that the electrocatalytic activity of nanostructured δ-MoN can be enhanced through the incorporation of Co and the concomitant formation of the $Co_{0.6}Mo_{1.4}N_2$ phase. Data for NiMo/C, δ-MoN/C, and NiMoN$_x$/C (dashed lines) obtained from Ref. 173; data for δ-MoN and $Co_{0.6}Mo_{1.4}N_2$ (solid lines) obtained from Ref. 174.

Transition metal nitrides have also been used for ORR electrocatalysis, with TiN nanocrystals prepared on nitrogen-doped graphene showing excellent activity.[175] Additionally, the high electrocatalytic activity of the transition metal nitrides has been noted in DSSCs, where nanoparticulate MoN and WN counter electrodes enable DSSC performance approaching that of equivalent devices assembled with a platinum counter electrode.[176] The activity of TiN, VN, and MoN toward triiodide reduction is substantially enhanced when they are prepared as nanoparticles embedded in nitrogen-doped RGO, resulting in DSSC performance rivaling or even exceeding that achieved with a platinum counter electrode.[177] Similarly, the triiodide reduction performance of TiN–CNT composites greatly exceeds that of TiN nanoparticles alone due to the superior electrical conductivity of the CNT network (see additional discussion in Section 1.7.4).[178]

1.5.6. Transition Metal Phosphides

Although the catalytic activity of transition metal phosphide compounds, such as dinickel phosphide (Ni_2P), has been known for over half a century,[179] they have only recently been investigated for heterogeneous (electro)catalysis.[59,180–182] In 1995, it was shown that the performance of electrodeposited amorphous Ni–P electrodes (*ca.* 3 wt% phosphorous content) toward the HER in alkaline conditions can be orders of magnitude higher than that of Ni electrodes.[183] Perhaps because such early works did not carry out detailed structural analysis of these transition metal phosphide materials (instead referring to them simply as "metal–phosphorous alloys"[184]), it was only very recently that the transition metal phosphides have reemerged as one of the most promising classes of earth-abundant inorganic electrocatalysts. Nanoporous iron monophosphide (FeP) nanosheets (Figure 1.9a) prepared through an anion-

exchange procedure exhibit an encouraging Tafel slope of 67 mV decade^{-1} toward the HER in 0.5 M $H_2SO_4(aq)$, but their overall performance lags behind that of other earth-abundant HER electrocatalysts.[185] On the other hand, hollow and faceted Ni_2P nanoparticles (Figure 1.9b) show HER activity and stability in 0.5 M $H_2SO_4(aq)$ that is among the best for non-noble electrocatalysts.[186] More recently, cobalt phosphide (CoP) nanoparticles[187] (Figure 1.9c) and nanoporous nanowire arrays[188] (Figure 1.9d) have been reported to exhibit both superb activity toward the HER and long-term stability in acidic conditions, surpassing the performance of nanostructured Ni_2P. To highlight the recent rapid advances in transition metal phosphide HER electrocatalyst performance, the polarization data for the FeP nanosheet, Ni_2P nanoparticle, CoP nanoparticle, and CoP nanowire electrodes have been compared in Figure 1.9e.

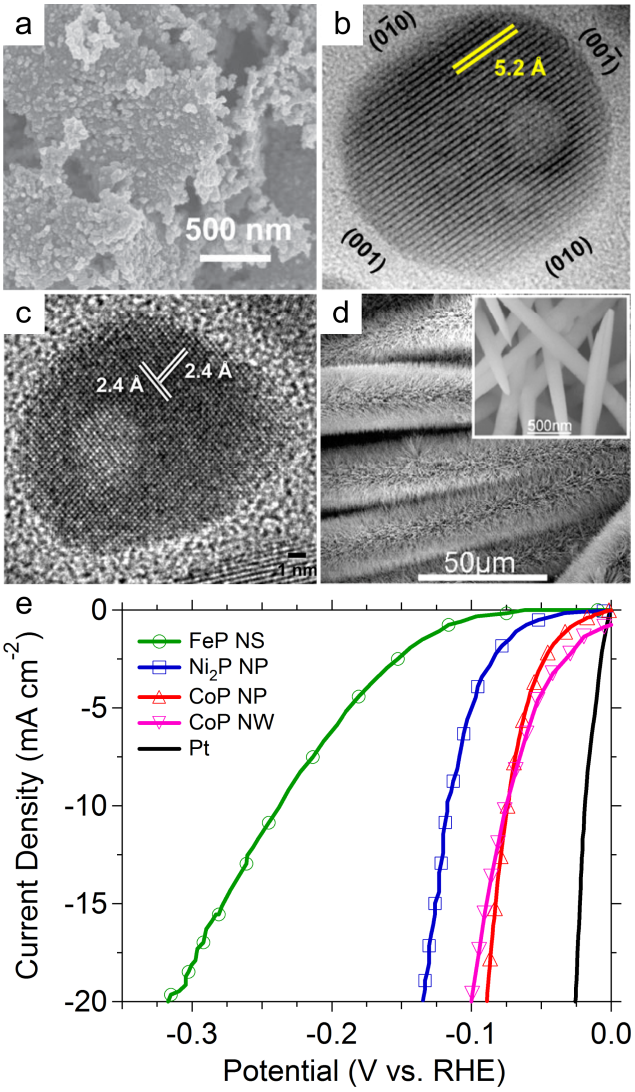

Figure 1.9. Electron microscopy characterization of (a) iron phoshide (FeP) nanosheets (NS), (b) nickel phosphide (Ni_2P) nanoparticles (NP), (c) cobalt phosphide (CoP) NP, and (d) CoP nanowires (NW) supported by carbon cloth, along with (e) polarization curves comparing their electrocatalytic activity toward the HER in 0.5 M H_2SO_4(*aq*) electrolyte in comparison with that of a Pt standard (black trace). Images and data for the FeP NS, Ni_2P NP, and CoP NW electrodes obtained from Refs. 185 (with permission from The Royal Society of Chemistry), 186, and 188 (both with permission from The American Chemical Society), respectively. Image and data for

the CoP NP and Pt standard electrodes obtained from Ref. 187 with permission from Wiley-VCH Verlag GmbH & Co. KGaA.

Besides the HER, there has also been recent interest in the use of transition metal phosphides as electrocatalysts in DSSCs.[52] For example, nickel phosphide ($Ni_{12}P_5$) has been reported as an effective triiodide reduction electrocatalyst.[189] Embedding $Ni_{12}P_5$ in graphene resulted in a synergistic enhancement of DSSC performance, with overall conversion efficiency approaching that of equivalent devices assembled with a platinum/FTO counter electrode.[189] The Ni_5P_4 phase of nickel phosphide and molybdenum phosphide (MoP) have also been demonstrated as counter electrode electrocatalysts in DSSCs, with the performance of Ni_5P_4 exceeding that of MoP.[190] As is also the case for $Ni_{12}P_5$, the preparation of Ni_5P_4 as a composite with mesoporous carbon boosts its performance nearly to the level of platinum-based counter electrodes.[190]

1.5.7. Transition Metal Carbides

Since the observation by Levy and Boudart that tungsten carbide can exhibit platinum-like behavior,[191] the catalytic activity[192] and surface properties[171,193] of many transition metal carbides have been studied in great detail. Recently, the platinum-like properties of the transition metal carbides have inspired research into their use as replacements for noble metal electrocatalysts in energy conversion applications, particularly for the HER.[172] Along with the transition metal nitrides, the transition metal carbides share the desirable attributes of corrosion resistance, stability, and mechanical strength, suggesting long electrocatalyst lifetime.[172] Tungsten monocarbide (WC) is the most widely studied transition metal carbide for electrocatalysis, due to its high activity, high electrical conductivity, and low sensitivity to the molecular compounds that can poison noble-metal electrocatalysts, such as hydrogen sulfide and carbon monoxide, making it particularly attractive for fuel cell applications.[39,172] Furthermore,

increased resistance to surface oxidation at low pH as compared to more metal-rich carbides (*e.g.*, W_2C or Mo_2C) means that WC is a more suitable HER electrocatalyst in acidic conditions.[194] Besides WC, many other transition metal carbides have been studied as electrocatalysts for the HER. Bulk Mo_2C has been shown to be an active HER electrocatalyst in both acidic and alkaline environments, achieving Tafel slopes as low as 54 mV decade^{-1}.[195] Nanoporous Mo_2C nanowires show improved HER performance in acidic electrolyte due to increased surface area and diffusion of species through the open structures.[196] It was recently demonstrated that Mo_2C nanoparticles prepared on carbon nanotubes show vastly improved activity toward the HER as compared to bulk Mo_2C or Mo_2C on a carbon black support, mostly due to favorable electronic interactions between the Mo_2C nanoparticles and the CNT support.[197] Furthermore, nanoparticles of other molybdenum carbide phases, including α-MoC_{1-x}, η-MoC, and γ-MoC, have been synthesized and shown to exhibit encouraging stability and activity toward the HER.[198]

Noting their high activity toward electrocatalytic water splitting, transition metal carbide electrocatalysts have also been used for solar energy conversion.[52] For example, tungsten semicarbide (W_2C) thin films deposited on *p*-type silicon photoelectrodes have been reported as effective catalysts for the photoelectrochemical evolution of hydrogen.[199] In addition, composite counter electrodes consisting of MoC, Mo_2C, or WC particles embedded in ordered mesoporous carbon (or other conductive additives) achieve conversion efficiencies in DSSCs employing the iodide/triiodide redox electrolyte rivaling or even exceeding that of devices assembled with a platinum counter electrode.[200] Noting the importance of high surface area to achieving high device performance, mesoporous WC films prepared on FTO/glass have been shown to serve as

effective counter electrodes for DSSCs, achieving 85% of the solar light-to-electricity power conversion efficiency that can be achieved with platinum counter electrodes in equivalent devices.[201] Similarly, various transition metal carbides have been investigated as electrocatalytic electrode materials for a variety of redox couples used in liquid-junction QDSSCs. Titanium carbide (TiC) electrodes prepared through a spray-coating method enable performance rivaling that of platinum counter electrodes in tin sulfide (SnS)-sensitized QDSSCs that employ either the iodide/triiodide, disulfide/thiolate, or sulfide/polysulfide redox couple.[202] Similarly, the performance of TiC counter electrodes in cadmium sulfide (CdS)-sensitized QDSSCs filled with the sulfide/polysulfide redox electrolyte has also been shown to exceed that of gold counter electrodes.[203]

1.5.8. Transition Metal Silicides

The transition metal silicides represent a relatively underexplored class of potential earth-abundant inorganic electrocatalysts, and, in general, their usage in catalysis has been limited. Following computational work suggesting high hydrogen sulfide tolerance for the metal silicides,[204] several first-row transition metal silicides have been investigated as HDS catalysts.[205,206] Analogous transition metal silicides have also been explored as carbon monoxide methanation catalysts.[207] However, despite most transition metal silicides possessing high electrical conductivity and good electrochemical stability, there have been few studies of their electrocatalytic activity. That said, several transition metal silicides have been previously investigated as electrocatalysts for the HER in both acidic[208] and alkaline[209] conditions, with the emerging trends in activity suggesting possible pathways toward improved silicide electrocatalysts.[210] While the performance of the earth-abundant transition metal silicides falls

far behind that of silicides containing noble metals,[210] the promising HER activity of certain earth-abundant transition metal silicides (VSi_2, Cr_3Si, FeSi, $CoSi_2$, $NiSi_2$, and Cu_5Si, among others) encourages further exploration. Indeed, even commercial molybdenum silicide ($MoSi_2$) and tungsten silicide (WSi_2) powders were recently shown to exhibit decent HER electrocatalytic activity and stability in 0.1 M $H_2SO_4(aq)$.[211] Moreover, as a rich family of materials with an ever-increasing number of controlled synthesis strategies for obtaining unique morphologies, including nanowires,[212] nanoparticles,[213] and high surface area hierarchical structures,[214] there are likely other transition metal silicides (and related intermetallic compounds) that could serve as effective earth-abundant electrocatalysts, yet remain to be investigated.

1.5.9. Transition Metal Borides

Like the transition metal phosphides, the transition metal borides represent a family of materials with known catalytic activity whose members have seldom been explored as electrocatalysts for energy conversion applications.[59,182] For electrocatalytic applications, the superior electrical conductivity (often higher than the parent metal itself) and anticipated chemical inertness of the transition metal borides make them especially attractive.[182] Although crystalline metal-rich borides such as Ni_3B and Co_2B were found to be susceptible to sulfidation when exposed to the high temperatures of industrial HDS, amorphous transition metal borides (often loosely referred to as "metal–boron alloys," as in the case of the amorphous transition metal phosphides) show enhanced stability and activity.[59,182] Various amorphous transition metal borides (and alloys thereof) can be prepared as supported and unsupported particles through the facile reaction of metal halide and borohydride salt solutions.[59,184] For example, both undoped[215] and doped[216] amorphous nickel boride (Ni_2B) have been explored as HER electrocatalysts in

alkaline electrolytes. Recently, molybdenum boride (MoB) was shown to catalyze the HER in both acidic and alkaline conditions with reasonable efficiency, but it experienced rapid corrosion at pH 14.[195] At pH 0, however, the MoB catalyst was stable over long periods of continuous operation.[195] Although surface oxides rapidly form when MoB is exposed to air, these oxides can be cathodically removed under normal HER operating conditions.[195] Commercial titanium boride (TiB_2), tungsten boride (WB), and zirconium boride (ZrB_2) powders have also been demonstrated as HER electrocatalysts in 0.1 M $H_2SO_4(aq)$, though their performance was modest and their rates of corrosion were relatively high.[211]

1.5.10. Transition Metal Compound Alloys and Mixed-Anion Compounds

Given the wide range of binary transition metal compounds that exhibit electrocatalytic activity toward redox processes central to energy conversion, and the fact that the activity of several electrocatalysts can be enhanced by mixing multiple transition metals, it is reasonable to expect that more complex transition metal compounds or compound alloys might possess further enhanced electrocatalytic activity. As has been demonstrated for the transition metal alloy electrocatalysts, the controlled introduction of additional cations (or anions) to a host compound is expected to modify its electrocatalytic activity due to changes in its electronic properties and/or the geometric arrangement of atoms. This concept has been perhaps best exemplified in the nitride system, where the ternary $NiMoN_x$ and $Co_{0.6}Mo_{1.4}N_2$ compounds exhibit significantly higher activity than δ-MoN, perhaps owing to favorable interactions between metal atoms (Figure 1.8). Similarly, other relevant properties, such as chemical stability, could also be altered through changes in composition. Many mixed-anion transition metal compounds, such as oxynitrides and carbonitrides, have been investigated as electrocatalysts, particularly for the

ORR.[39] In addition, carbon- and nitrogen-containing "N–M–C" (M = Co and/or Fe) electrocatalysts derived from polyaniline, although not strictly of a well-defined carbonitride phase, have been shown to exhibit superb activity, long-term stability, and four-electron selectivity toward the ORR (*i.e.*, low hydrogen peroxide yield).[217] Carbonitride compounds have been scarcely explored as HER electrocatalysts, but tungsten carbonitride (WCN) with a high fraction of tungsten nitride (WN) shows decent activity and high stability in both acidic and alkaline media.[218]

1.6. Challenges Facing Earth-Abundant Inorganic Electrocatalysts

For earth-abundant inorganic electrocatalysts to become competitive with those containing noble metals, there are a number of specific challenges that must be overcome. Most obvious among these is the need for comparable levels of intrinsic electrocatalytic activity. While various strategies might be employed to boost the performance of electrocatalysts with inferior intrinsic activity, materials with higher intrinsic activity will always be preferred. Indeed, when examining a new potential electrocatalyst, its intrinsic activity toward the electrochemical process of interest is usually the first property probed, as low activity can immediately render a candidate material uninteresting. Second, the electrocatalyst must be sufficiently stable in the conditions of electrocatalysis to permit long-term usage without performance decay. Typically, electrocatalyst stability is reported under continuous operating conditions. However, in such tests, the electrical bias applied to drive catalysis might suppress electrocatalyst corrosion (*e.g.*, oxidation). Ideally, earth-abundant electrocatalysts should also be highly stable under "standby" (or "shutdown") conditions, where no bias is applied, or even under conditions of current

reversal. While the strict requirements for long-term stability might be relaxed somewhat for earth-abundant electrocatalysts that can be easily replaced or regenerated, the ideal materials should be sufficiently stable as to permit indefinite operation with minimal decay in performance.

Various secondary requirements should also be met by ideal earth-abundant electrocatalysts, including superior electrical conductivity, chemical compatibility, and catalytic generality. Metallically conducting electrocatalysts ensure fast charge carrier transport and minimal electrode polarization (*i.e.*, low Ohmic losses) under operating conditions and, hence, maximum efficiency. Electrocatalytic activity (in the form of a Tafel slope) is often reported and compared after *IR* correction to ensure a fair comparison of intrinsic activity between candidate materials, particularly over regions of low to modest current densities. However, such a comparison ignores the benefits of low overall series resistance in enabling high current densities at reduced overpotentials, which is especially relevant in practical water electrolysis systems. Earth-abundant electrocatalysts should also possess high chemical compatibility with their operating environment, such that they are not poisoned during operation, nor should they contaminate or degrade other components of the electrochemical system. This requirement is particularly relevant for electrocatalysts used at the counter electrodes of photoelectrochemical solar cells, since they must maintain stable performance in the presence of the redox electrolyte while also not contaminating or otherwise altering the behavior of the light-absorbing photoelectrode. Lastly, the ideal earth-abundant electrocatalyst should be general, exhibiting high activity toward many catalytic processes. Much like the many electrocatalytic roles of the noble metals and compounds thereof, earth-abundant alternatives with sufficiently high activity

and stability would optimally catalyze a range of diverse redox reactions, thereby eliminating the need to develop new and unique earth-abundant electrocatalysts for each redox system of interest.

1.7. Strategies for Enhancing Earth-Abundant Inorganic Electrocatalyst Performance and Stability

Many chemical and engineering strategies have been shown to boost the performance and stability of earth-abundant inorganic electrocatalysts. These efforts are aimed at increasing the activity of the electrocatalyst toward the redox process of interest, the number of available sites for catalysis, or in some cases, both. Maximizing these two factors ensures that the electrocatalyst operates at the highest possible level of performance. Most earth-abundant inorganic electrocatalysts offer opportunities to enhance their performance by addressing one or both of these factors either synthetically or through post-synthetic treatments. Here, we will outline the commonly demonstrated strategies for increasing electrocatalyst performance, pointing out key examples of each.

1.7.1. Nanostructuring

It is well known that the magnitude of an electrocatalytic current will scale with the effective surface area of the electrocatalyst.[32] While modification to the chemical composition or structural phase of the electrocatalyst might increase the areal density of active sites for catalysis, morphological changes, such as nanostructuring, that increase the real surface area could also increase the number of available active sites. Without changing the per site turnover frequency, simply multiplying the number of available sites through an increase in surface rugosity will

necessarily enhance the overall electrocatalytic performance. This is perhaps the most straightforward—and commonly utilized—strategy for increasing electrocatalyst performance.

One early recognition of the role of real surface area in promoting the overall performance of an earth-abundant electrocatalyst was in the transition metal alloy system, where researchers noted that the surface roughness of alloy catalysts was commonly higher than that of pure metal systems, affording more available sites for catalysis.[75] This phenomenon was particularly relevant for the Ni–Mo alloy HER electrocatalysts, where the electrode surface rugosity was further increased by selective leeching of molybdenum.[29,75,77,81] By preparing the Ni–Mo material in a nanoparticulate morphology,[78] the real surface area (and, consequently, electrocatalytic performance) could be further increased. Similarly, nanomaterial synthesis strategies ranging from templated preparations to spontaneous solution- or gas-phase growth have been applied in most of the classes of earth-abundant inorganic electrocatalysts detailed in Section 1.5 in order to increase their electrocatalytic performance. Additionally, post-synthetic strategies for increasing real surface area, such as the chemical exfoliation of the layered TMD materials MoS_2[115] and WS_2[50,116] through a lithium intercalation treatment, have been shown to be effective in increasing electrocatalytically active surface area (Figure 1.3).

The role of electrocatalyst nanostructuring in improving electrocatalytic performance has been clearly demonstrated through the comparison of CoS_2 film, microwire, and nanowire electrode activity toward the HER.[49] Despite similar synthetic procedures for arriving at the different CoS_2 morphologies, thus leading to a consistent intrinsic activity and areal density of active sites, they exhibit vastly different levels of overall electrocatalytic performance (with the CoS_2 nanowire electrodes enabling the highest performance) owing to their different

electrochemical surface areas (Figure 1.5).[49] In this example, the relative effective electrochemical surface areas were determined by measuring the electrode double-layer capacitance,[48,49] which is proportional to the surface area. The generality of the nanostructuring strategy was also demonstrated by the improved performance of CoS_2 nanowire electrodes toward polysulfide and triiodide reduction as compared to CoS_2 film electrodes.[49] Furthermore, this work establishes that, in the electrocatalysis of gas-evolving applications such as water splitting, electrocatalysts with a micro- or nanowire morphology can effectively promote gas bubble release from the electrode surface (Figure 1.5c), simultaneously enabling high current densities at reduced overpotentials and dramatically improved electrode stability.[49]

The many demonstrations of improved electrocatalyst performance through nanostructuring motivate the preparation of earth-abundant inorganic electrocatalysts in nanoscale morphologies. With the growing number of strategies for the controlled synthesis of nanomaterials,[131,133,182,212,219,220] the opportunities for preparing earth-abundant electrocatalysts in morphologies that maximize both the fraction of exposed active sites and the long-term operational stability of the materials similarly grow. In cases where the active sites for catalysis are known and well-characterized, controlled nanomaterials synthesis could afford the opportunity to prepare the inorganic electrocatalyst material with predominant exposure of those most active facets. Similarly, high surface area electrocatalyst supports, such as conductive nanowire arrays, hierarchical structures,[219] or mesoporous film scaffolds,[160] could be employed to further enhance the real electrocatalyst surface area. It may also be the case that the intrinsic activity of a nanostructured electrocatalyst material differs from that of its bulk counterpart, perhaps due to variations in surface composition, atomic arrangement, or electronic properties at

the nanoscale, further motivating their controlled synthesis and characterization.

1.7.2. Chemical Modification

The trends in the electrocatalytic activity of the transition metals and transition metal alloys clearly establish that the electronic structures and properties of electrocatalysts play a key role in determining their activity. Similarly, the effects of "promoter" species in increasing the intrinsic activity of certain electrocatalysts has been documented.[111] Drawing on the wealth of established knowledge regarding the doping of semiconductor materials to alter their electronic properties, one could imagine incorporating "dopant" or "promoter" species into established earth-abundant electrocatalysts to enhance their activity. By including either electron-poor or electron-rich species into a host material, it may be possible to tune its Fermi level and other electrical properties for enhanced electrocatalytic activity. These "dopant" species may also alter the oxidation state of the catalytic centers, modifying their intrinsic activity. This concept has been more systematically explored through the investigation of transition metal alloys and, to a lesser extent, transition metal compound alloys (see discussion in Sections 1.5.2 and 1.5.10, respectively), but the controlled preparation and physical property characterization of other candidate materials could enable a more direct route toward high-performance earth-abundant electrocatalysts.

1.7.3. Structural Modification

In addition to chemical modification, changes in atomic arrangement may modify the physical properties of a material to improve its electrocatalytic activity. For example, the chemical exfoliation of MoS_2 and WS_2, as discussed in Section 1.5.4.1, has been noted to increase surface area and proliferate the density of catalytic edge sites.[50,115,116] More importantly,

though, this lithium intercalation and exfoliation treatment induces a phase transformation from the thermodynamically-favored semiconducting 2H polymorph to the metallically conducting 1T polymorph (Figure 1.3a), which exhibits enhanced HER activity (Figure 1.3f–g). The transfer of an electron upon lithium intercalation destabilizes the trigonal prismatic 2H-MX_2 structure and instead favors the metastable octahedrally coordinated 1T polymorph.[221] The reduced Tafel slope of 1T-MoS_2 (Figure 1.3f, inset) indicates that this phase transformation improves its intrinsic electrocatalytic activity through a modification of electronic properties. In other words, the semiconducting 2H layered TMDs become intrinsically better electrocatalysts once converted to their corresponding 1T polymorph. This is the most important benefit of the chemical exfoliation treatment. To a certain degree, then, chemical modification/electronic structure tuning (see Section 1.7.2) and structural modification may be interconnected strategies. The increase in electrocatalytic activity that accompanies the 2H to 1T transition has also been continuously tuned electrochemically and monitored using vertically aligned MoS_2 nanofilms.[118] The metallically conducting nature of the 1T polymorph also reduces Ohmic losses as compared to the 2H polymorph, further enhancing electrocatalytic performance. These benefits should also translate to improved performance in other electrocatalytic processes, such as triiodide or polysulfide reduction. While in other families of earth-abundant inorganic electrocatalysts the differences in activity between structural polymorphs mostly remain to be investigated, the case of MoS_2 serves to illustrate that the particular crystal structure and bonding environment around catalytically active sites should be carefully considered and, where possible, modified to achieve maximum activity.

Moreover, modifications of crystalline structure at the atomic level (through, for

example, the creation of lattice defects or interstitial species, grain boundaries, or dislocations) might produce sites with new or altered electrocatalytic activity.[119,120] Similarly, the recent success of amorphous HER electrocatalysts has renewed interest in studying the activity of materials that lack a well-defined crystal structure. The absence of long-range order in amorphous materials suggests that there might be new or unusual bonding arrangements (or a specific rate of occurrence thereof) that are favorable for electrocatalysis. Additionally, amorphous materials are expected to have a greater density of dangling bonds that could modify their affinity for adsorbates and, therefore, their electrocatalytic activity. Such concepts have been proposed to explain the electrocatalytic activity of amorphous transition metal alloys,[81] transition metal sulfides (particularly MoS_x),[107,153–158] Ni–P compounds,[183,184] and Ni–B compounds.[59,182,184] The precise origin of electrocatalytic activity in these amorphous materials is not fully resolved, but reports suggest the possibility of catalytic domains embedded in an amorphous matrix.[59,157] The specific oxidation state of catalytic centers (or the fact that a dispersion of oxidation states may simultaneously exist) in these amorphous electrocatalysts could also contribute to their elevated activity. Interestingly, the impressive performance of these amorphous electrocatalysts suggests that, in some instances, a well-defined crystal structure may be unnecessary—or even deleterious—in achieving high activity. Of course, the general challenge in studying amorphous electrocatalysts is the difficulty in elucidating their structural details using common materials characterization techniques (*e.g.*, X-ray and electron diffraction, electron microscopy, or infrared and Raman spectroscopy). However, we need to better understand their atomic structures using new techniques in order to advance these materials, because it is likely that under the general description of “amorphous materials” there are many

subtle structural differences that may impact catalytic activity.

1.7.4. Composite Materials

The performance of high-activity electrocatalysts—particularly those with poor electrical conductivity—can be enhanced through the preparation of a composite containing a conductive additive, such as carbon black, carbon nanofibers or microfibers, graphene, RGO, CNTs, or polymers. Integration of the electrocatalyst material with a conducting support typically leads to improvements in both performance and stability, since directly anchoring the electrocatalyst to a robust conducting support ensures a low-resistance electrical transport pathway as well as reduced likelihood of physical delamination of the electrocatalyst. Electronic coupling between the support and catalyst materials can synergistically boost intrinsic activity as well.[89,90,114,175,197,222] As an example, these effects have been clearly demonstrated for MoS_2 nanoparticles synthesized directly on RGO sheets (Figure 1.10a), which exhibit markedly enhanced intrinsic electrocatalytic activity and performance toward the HER as compared to unsupported MoS_2 particles (Figure 1.10b).[114] Similarly, amorphous MoS_x layers directly bound to vertically-aligned N-doped CNTs (Figure 1.10c) expose a particularly high density of catalytic sites and benefit from the excellent charge transport properties of the N-doped CNT supports, leading to electrocatalytic activity toward the HER approaching that of a commercial carbon-supported platinum electrocatalyst (Figure 1.10d).[159]

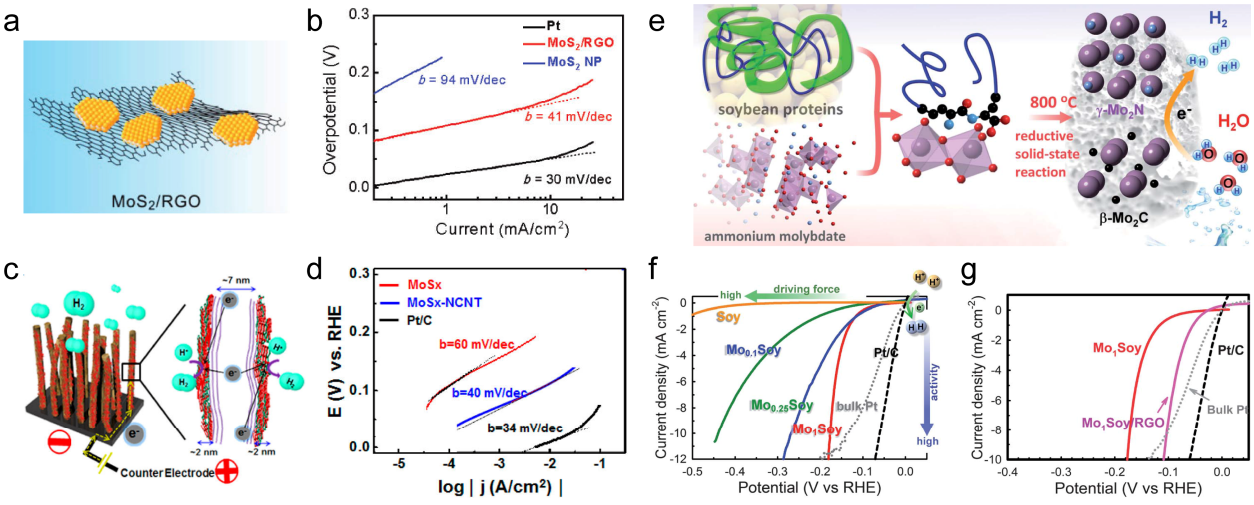

Figure 1.10. Schematic illustrations and performance characterizations of MoS_2/RGO, MoS_x/N-doped CNT, and biomass-derived "MoSoy" composite HER electrocatalysts. (a) MoS_2 nanoparticles synthesized directly on RGO sheets, which (b) exhibit dramatically increased electrocatalytic activity as compared to unsupported MoS_2 particles. (c) Amorphous MoS_x layers prepared directly on a N-doped CNT array, with (d) intrinsic electrocatalytic activity approaching that of a commercial Pt/C electrocatalyst. (e) Schematic illustration of the preparation of the "MoSoy" composite electrocatalyst, which contains both crystalline β-Mo_2C and γ-Mo_2N domains. (f) The HER electrocatalytic performance of the "MoSoy" composite varies with Mo content, with the "Mo_1Soy" composite (prepared using a 1:1 ratio of Mo precursor to soybean powder) exhibiting the highest performance. (g) The HER electrocatalytic performance of the "MoSoy" electrocatalyst can be significantly improved through preparation on a RGO conductive support. Panels a and b adapted from Ref. 114, and panels c and d adapted from Ref. 159, both with permission from the American Chemical Society; panels e–g adapted from Ref. 223 with permission from The Royal Society of Chemistry.

Electrocatalytic composites can also be prepared for the purpose of increasing robustness and long-term stability. One interesting example is the biomass-derived "MoSoy" catalyst synthesized through the solid-state reaction of ammonium molybdate with soybean powder (Figure 1.10e).[223] The resultant "MoSoy" composite consists of catalytic β-Mo_2C nanoparticles and acid-stable γ-Mo_2N nanoparticles embedded in amorphous carbon, which serves to increase the overall surface area of the composite.[223] The "MoSoy" electrocatalyst deposited on a carbon fiber paper support exhibits good activity toward the HER in 0.1 M $HClO_4(aq)$, with its performance increasing with Mo content (Figure 1.10f). This activity can be further increased by preparing the "MoSoy" material directly on a RGO support (Figure 1.10g), resulting in electrocatalytic performance competitive with the best earth-abundant HER electrocatalysts. Most importantly, the presence of the acid-stable γ-Mo_2N phase increases the long-term stability of the "MoSoy" electrocatalyst under operating conditions as compared to carbon black-supported β-Mo_2C nanoparticles. This example demonstrates that composite electrocatalysts containing catalytically active domains and domains with high chemical stability can synergistically benefit from both.

1.8. Summary and Perspectives

In this review, we have summarized recent advances in the development of earth-abundant inorganic heterogeneous electrocatalysts for energy conversion applications by examining families of materials classified by their elemental compositions. The discussion of electrocatalysis has focused on the cathodic reactions where there are clear opportunities for earth-abundant electrocatalysts, namely, the hydrogen reduction reaction, the oxygen reduction

reaction, and the redox reactions in regenerative liquid-junction photoelectrochemical cells. We have also discussed the key challenges facing such earth-abundant electrocatalysts, and enumerated several current and emerging strategies for improving their performance, including nanostructuring, chemical modification, structural modification, and the preparation of composite materials.

The field of electrocatalysis is undergoing rapid expansion, both in terms of new materials being explored and new applications being developed. The recent emergence (or reemergence) of earth-abundant materials with known catalytic activity (toward, for example, the HDS or HDN reactions) as inorganic electrocatalysts for energy conversion suggests that particular attention should be paid to those catalysts carefully studied and developed for industrial applications. The similarity of certain electrochemical redox processes (such as HER) to those catalyzed with high efficiency in industrial chemical refining warrants further attention and suggests potential repurposing of these materials for electrocatalysis. Likewise, chemical or structural analogues of known high-performance (electro)catalysts could exhibit comparable (or even improved) activity and should therefore be explored. The study and development of catalytic materials stretching back several decades offers a wealth of knowledge to scientists seeking to develop earth-abundant electrocatalysts for energy conversion applications, which certainly should be leveraged. At the same time, the recent explosion in the number and variety of earth-abundant inorganic electrocatalysts suggests that we should expand even further into the periodic table, investigating new and increasingly complex materials that might enable more finely tuned electrocatalytic activity, perhaps beginning with the ternary compounds and alloys. The use of combinatorial techniques for screening new catalyst compositions appears to be a

very promising and effective approach, especially for compounds with complex stoichiometries.[150,224–227]

Until now, the discovery of earth-abundant inorganic electrocatalysts has remained largely Edisonian. Despite a recent uptick in theoretical and computational studies aimed at predicting promising candidates,[53,56,57,109] few emergent high-performance earth-abundant electrocatalysts have been rationally designed at a chemical and/or structural level based on the mechanism of the chemical transformation of interest. Instead, most recent reports of "new" earth-abundant electrocatalysts have focused on the controlled synthesis of materials (some with well-known catalytic activity) and characterization of their electrocatalytic activity and long-term stability, with little attention paid to the origin or fundamental nature of their activity. While such an approach certainly serves to advance the field in a practical sense, the lack of a basic understanding of such electrocatalytic activity could retard more directed and rational earth-abundant inorganic electrocatalyst development. As illustrated here, various classes of earth-abundant electrocatalysts are under rapid simultaneous screening, but *a priori* knowledge of the mechanism of catalysis and the relevant physical properties of potential earth-abundant electrocatalysts might enable more informed, in-depth studies of the most promising candidates, accelerating the rate of discovery and advance.

The progress of molybdenum sulfide-based electrocatalysts for the HER perhaps best illustrates how earth-abundant electrocatalyst development could proceed most efficiently. In this case, fundamental mechanistic studies of molecular systems,[64,112] supported by theory,[109] led to the identification of MoS_2 as a potential inorganic analogue. Then, careful analytical studies identified the edges of MoS_2 as being most active sites for HER electrocatalysis,[110] and

understanding of its layered structure inspired the study of well-defined molecular mimics that confirmed this edge-site activity.[112] With this knowledge, various synthetic and engineering strategies were employed to maximize the exposure of these edge sites, improving the HER electrocatalytic performance of MoS_2. Modification of the intrinsic activity and electrical transport properties of MoS_2 through a phase transformation has further increased its activity.[115] At the same time, MoS_2-based composite electrocatalysts have been prepared and shown to exhibit activities beyond those achieved with MoS_2 alone.[114] Still, unexpected discoveries, such as the high electrocatalytic activity of the amorphous molybdenum sulfides,[153] occurred along this path of development, but the combined efforts of theorists and experimentalists clearly helped to establish a roadmap for the development of high-performance MoS_2-based electrocatalysts. Only through a balanced combination of theoretical, fundamental, and performance-based studies will the development of earth-abundant inorganic electrocatalysts for energy conversion progress at the rapid rate necessary to address our growing energy demand.

1.9. References

(1) Lewis, N. S.; Nocera, D. G. Powering the planet: Chemical challenges in solar energy utilization. *Proc. Natl. Acad. Sci. U.S.A.* **2006**, *103*, 15729–15735.

(2) Saga, T. Advances in crystalline silicon solar cell technology for industrial mass production. *NPG Asia Mater.* **2010**, *2*, 96–102.

(3) Grätzel, M. Photoelectrochemical cells. *Nature* **2001**, *414*, 338–344.

(4) National Renewable Energy Laboratory: National Center for Photovoltaics. Best Research-Cell Efficiencies. http://www.nrel.gov/ncpv/images/efficiency_chart.jpg (accessed June 12, 2014).

(5) Lewis, N. S. Toward Cost-Effective Solar Energy Use. *Science* **2007**, *315*, 798–801.

(6) Wolden, C. A.; Kurtin, J.; Baxter, J. B.; Repins, I.; Shaheen, S. E.; Torvik, J. T.; Rockett, A. A.; Fthenakis, V. M.; Aydil, E. S. Photovoltaic manufacturing: Present status, future prospects, and research needs. *J. Vac. Sci. Technol. A* **2011**, *29*, 030801.

(7) Graetzel, M.; Janssen, R. A. J.; Mitzi, D. B.; Sargent, E. H. Materials interface engineering for solution-processed photovoltaics. *Nature* **2012**, *488*, 304–312.

(8) Hagfeldt, A.; Boschloo, G.; Sun, L. C.; Kloo, L.; Pettersson, H. Dye-Sensitized Solar Cells. *Chem. Rev.* **2010**, *110*, 6595–6663.

(9) Rühle, S.; Shalom, M.; Zaban, A. Quantum-Dot-Sensitized Solar Cells. *ChemPhysChem* **2010**, *11*, 2290–2304.

(10) Kamat, P. V. Quantum Dot Solar Cells. *The Next Big Thing* in Photovoltaics. *J. Phys. Chem. Lett.* **2013**, *4*, 908–918.

(11) Selinsky, R. S.; Ding, Q.; Faber, M. S.; Wright, J. C.; Jin, S. Quantum dot nanoscale heterostructures for solar energy conversion. *Chem. Soc. Rev.* **2013**, *42*, 2963–2985.

(12) Sargent, E. H. Colloidal quantum dot solar cells. *Nature Photon.* **2012**, *6*, 133–135.

(13) Nelson, J. Polymer:fullerene bulk heterojunction solar cells. *Mater. Today* **2011**, *14*, 462–470.

(14) Todorov, T.; Mitzi, D. B. Direct Liquid Coating of Chalcopyrite Light-Absorbing Layers for Photovoltaic Devices. *Eur. J. Inorg. Chem.* **2010**, 17–28.

(15) Snaith, H. J. Perovskites: The Emergence of a New Era for Low-Cost, High-Efficiency Solar Cells. *J. Phys. Chem. Lett.* **2013**, *4*, 3623–3630.

(16) Boix, P. P.; Nonomura, K.; Mathews, N.; Mhaisalkar, S. G. Current progress and future perspectives for organic/inorganic perovskite solar cells. *Mater. Today* **2014**, *17*, 16–23.

(17) Szczech, J. R.; Jin, S. Nanostructured silicon for high capacity lithium battery anodes. *Energy Environ. Sci.* **2011**, *4*, 56–72.

(18) Goodenough, J. B.; Kim, Y. Challenges for Rechargeable Li Batteries. *Chem. Mater.* **2010**, *22*, 587–603.

(19) Cook, T. R.; Dogutan, D. K.; Reece, S. Y.; Surendranath, Y.; Teets, T. S.; Nocera, D. G. Solar Energy Supply and Storage for the Legacy and Nonlegacy Worlds. *Chem. Rev.* **2010**, *110*, 6474–6502.

(20) Turner, J. A. Sustainable Hydrogen Production. *Science* **2004**, *305*, 972–974.

(21) Chen, X. B.; Shen, S. H.; Guo, L. J.; Mao, S. S. Semiconductor-based Photocatalytic Hydrogen Generation. *Chem. Rev.* **2010**, *110*, 6503–6570.

(22) McKone, J. R.; Lewis, N. S.; Gray, H. B. Will Solar-Driven Water-Splitting Devices See the Light of Day? *Chem. Mater.* **2014**, *26*, 407–414.

(23) Benson, E. E.; Kubiak, C. P.; Sathrum, A. J.; Smieja, J. M. Electrocatalytic and homogeneous approaches to conversion of CO_2 to liquid fuels. *Chem. Soc. Rev.* **2009**, *38*, 89–99.

(24) Roy, S. C.; Varghese, O. K.; Paulose, M.; Grimes, C. A. Toward Solar Fuels: Photocatalytic Conversion of Carbon Dioxide to Hydrocarbons. *ACS Nano* **2010**, *4*, 1259–1278.

(25) Appel, A. M.; Bercaw, J. E.; Bocarsly, A. B.; Dobbek, H.; DuBois, D. L.; Dupuis, M.; Ferry, J. G.; Fujita, E.; Hille, R.; Kenis, P. J. A.; Kerfeld, C. A.; Morris, R. H.; Peden, C. H. F.; Portis, A. R.; Ragsdale, S. W.; Rauchfuss, T. B.; Reek, J. N. H.; Seefeldt, L. C.; Thauer, R. K.; Waldrop, G. L. Frontiers, Opportunities, and Challenges in Biochemical and Chemical Catalysis of CO_2 Fixation. *Chem. Rev.* **2013**, *113*, 6621–6658.

(26) Srinivasan, S.; Mosdale, R.; Stevens, P.; Yang, C. Fuel Cells: Reaching the Era of Clean and Efficient Power Generation in the Twenty-First Century. *Annu. Rev. Energy Environ.* **1999**, *24*, 281–328.

(27) Gewirth, A. A.; Thorum, M. S. Electroreduction of Dioxygen for Fuel-Cell Applications: Materials and Challenges. *Inorg. Chem.* **2010**, *49*, 3557–3566.

(28) Walter, M. G.; Warren, E. L.; McKone, J. R.; Boettcher, S. W.; Mi, Q.; Santori, E. A.; Lewis, N. S. Solar Water Splitting Cells. *Chem. Rev.* **2010**, *110*, 6446–6473.

(29) Nocera, D. G. The Artificial Leaf. *Acc. Chem. Res.* **2012**, *45*, 767–776.

(30) Ran, J. R.; Zhang, J.; Yu, J. G.; Jaroniec, M.; Qiao, S. Z. Earth-abundant cocatalysts for semiconductor-based photocatalytic water splitting. *Chem. Soc. Rev.*, DOI: 10.1039/C1033CS60425J.

(31) Pinaud, B. A.; Benck, J. D.; Seitz, L. C.; Forman, A. J.; Chen, Z. B.; Deutsch, T. G.; James, B. D.; Baum, K. N.; Baum, G. N.; Ardo, S.; Wang, H. L.; Miller, E.; Jaramillo, T. F. Technical and economic feasibility of centralized facilities for solar hydrogen production *via* photocatalysis and photoelectrochemistry. *Energy Environ. Sci.* **2013**, *6*, 1983–2002.

(32) Pletcher, D. Electrocatalysis: present and future. *J. Appl. Electrochem.* **1984**, *14*, 403–415.

(33) Vesborg, P. C. K.; Jaramillo, T. F. Addressing the terawatt challenge: scalability in the supply of chemical elements for renewable energy. *RSC Adv.* **2012**, *2*, 7933–7947.

(34) McKone, J. R.; Marinescu, S. C.; Brunschwig, B. S.; Winkler, J. R.; Gray, H. B. Earth-abundant hydrogen evolution electrocatalysts. *Chem. Sci.* **2014**, *5*, 865–878.

(35) Zhu, C. Z.; Dong, S. J. Recent progress in graphene-based nanomaterials as advanced electrocatalysts towards oxygen reduction reaction. *Nanoscale* **2013**, *5*, 1753–1767.

(36) Gong, K. P.; Du, F.; Xia, Z. H.; Durstock, M.; Dai, L. M. Nitrogen-Doped Carbon Nanotube Arrays with High Electrocatalytic Activity for Oxygen Reduction. *Science* **2009**, *323*, 760–764.

(37) Cheng, Y. W.; Zhang, H. B.; Varanasi, C. V.; Liu, J. Highly Efficient Oxygen Reduction Electrocatalysts based on Winged Carbon Nanotubes. *Sci. Rep.* **2013**, *3*, DOI:10.1038/srep03195.

(38) Malinauskas, A. Electrocatalysis at conducting polymers. *Synthetic Met.* **1999**, *107*, 75–83.

(39) Chen, Z. W.; Higgins, D.; Yu, A. P.; Zhang, L.; Zhang, J. J. A review on non-precious metal electrocatalysts for PEM fuel cells. *Energy Environ. Sci.* **2011**, *4*, 3167–3192.

(40) Esswein, A. J.; Nocera, D. G. Hydrogen Production by Molecular Photocatalysis. *Chem. Rev.* **2007**, *107*, 4022–4047.

(41) Artero, V.; Fontecave, M. Some general principles for designing electrocatalysts with hydrogenase activity. *Coord. Chem. Rev.* **2005**, *249*, 1518–1535.

(42) Artero, V.; Chavarot-Kerlidou, M.; Fontecave, M. Splitting Water with Cobalt. *Angew. Chem. Int. Ed.* **2011**, *50*, 7238–7266.

(43) Dempsey, J. L.; Brunschwig, B. S.; Winkler, J. R.; Gray, H. B. Hydrogen Evolution Catalyzed by Cobaloximes. *Acc. Chem. Res.* **2009**, *42*, 1995–2004.

(44) Du, P. W.; Eisenberg, R. Catalysts made of earth-abundant elements (Co, Ni, Fe) for water splitting: Recent progress and future challenges. *Energy Environ. Sci.* **2012**, *5*, 6012–6021.

(45) Finn, C.; Schnittger, S.; Yellowlees, L. J.; Love, J. B. Molecular approaches to the electrochemical reduction of carbon dioxide. *Chem. Commun.* **2012**, *48*, 1392–1399.

(46) Thoi, V. S.; Sun, Y. J.; Long, J. R.; Chang, C. J. Complexes of earth-abundant metals for catalytic electrochemical hydrogen generation under aqueous conditions. *Chem. Soc. Rev.* **2013**, *42*, 2388–2400.

(47) Bockris, J. O. M.; Potter, E. C. The Mechanism of the Cathodic Hydrogen Evolution Reaction. *J. Electrochem. Soc.* **1952**, *99*, 169–186.

(48) Bard, A. J.; Faulkner, L. R. *Electrochemical Methods: Fundamentals and Applications*; Wiley: New York, 2001.

(49) Faber, M. S.; Dziedzic, R.; Lukowski, M. A.; Kaiser, N. S.; Ding, Q.; Jin, S. High-Performance Electrocatalysis Using Metallic Cobalt Pyrite (CoS_2) Micro- and Nanostructures. *J. Am. Chem. Soc.*, DOI: 10.1021/ja504099w.

(50) Lukowski, M. A.; Daniel, A. S.; English, C. R.; Meng, F.; Forticaux, A.; Hamers, R. J.; Jin, S. Highly Active Hydrogen Evolution Catalysis from Metallic WS_2 Nanosheets. *Energy Environ. Sci.*, DOI: 10.1039/C1034EE01329H.

(51) McCrory, C. C. L.; Jung, S. H.; Peters, J. C.; Jaramillo, T. F. Benchmarking Heterogeneous Electrocatalysts for the Oxygen Evolution Reaction. *J. Am. Chem. Soc.* **2013**, *135*, 16977–16987.

(52) Wu, M. X.; Ma, T. L. Platinum-Free Catalysts as Counter Electrodes in Dye-Sensitized Solar Cells. *ChemSusChem* **2012**, *5*, 1343–1357.

(53) Hou, Y.; Wang, D.; Yang, X. H.; Fang, W. Q.; Zhang, B.; Wang, H. F.; Lu, G. Z.; Hu, P.; Zhao, H. J.; Yang, H. G. Rational screening low-cost counter electrodes for dye-sensitized solar cells. *Nature Commun.* **2013**, *4*, DOI: 10.1038/Ncomms2547.

(54) Wu, M. X.; Ma, T. L. Recent Progress of Counter Electrode Catalysts in Dye-Sensitized Solar Cells. *J. Phys. Chem. C*, DOI: 10.1021/jp412713h.

(55) Parsons, R. The Rate of Electrolytic Hydrogen Evolution and the Heat of Adsorption of Hydrogen. *Trans. Faraday Soc.* **1958**, *54*, 1053–1063.

(56) Nørskov, J. K.; Bligaard, T.; Logadottir, A.; Kitchin, J. R.; Chen, J. G.; Pandelov, S.; Stimming, U. Trends in the Exchange Current for Hydrogen Evolution. *J. Electrochem. Soc.* **2005**, *152*, J23–J26.

(57) Nørskov, J. K.; Rossmeisl, J.; Logadottir, A.; Lindqvist, L.; Kitchin, J. R.; Bligaard, T.; Jónsson, H. Origin of the Overpotential for Oxygen Reduction at a Fuel-Cell Cathode. *J. Phys. Chem. B* **2004**, *108*, 17886–17892.

(58) *Transition Metal Sulphides: Chemistry and Catalysis*; Weber, T.; Prins, R.; van Santen, R. A., Eds.; Kluwer Academic Publishers: Dordrecht, 1998; Vol. 60.

(59) Alexander, A.-M.; Hargreaves, J. S. J. Alternative catalytic materials: carbides, nitrides, phosphides and amorphous boron alloys. *Chem. Soc. Rev.* **2010**, *39*, 4388–4401.

(60) Chianelli, R. R.; Berhault, G.; Raybaud, P.; Kasztelan, S.; Hafner, J.; Toulhoat, H. Periodic trends in hydrodesulfurization: in support of the Sabatier principle. *Appl. Catal. A* **2002**, *227*, 83–96.

(61) *Metal Oxide Catalysis*; Jackson, S. D.; Hargreaves, J. S. J., Eds.; Wiley-VCH: Weinheim, 2009; Vol. 2.

(62) Gregory, R. P. F. *Biochemistry of Photosynthesis*; Wiley-Interscience: New York, 1989.

(63) Andreiadis, E. S.; Jacques, P. A.; Tran, P. D.; Leyris, A.; Chavarot-Kerlidou, M.; Jousselme, B.; Matheron, M.; Pécaut, J.; Palacin, S.; Fontecave, M.; Artero, V. Molecular engineering of a cobalt-based electrocatalytic nanomaterial for H_2 evolution under fully aqueous conditions. *Nature Chem.* **2013**, *5*, 48–53.

(64) Jaramillo, T. F.; Bonde, J.; Zhang, J. D.; Ooi, B.-L.; Andersson, K.; Ulstrup, J.; Chorkendorff, I. Hydrogen Evolution on Supported Incomplete Cubane-type $[Mo_3S_4]^{4+}$ Electrocatalysts. *J. Phys. Chem. C* **2008**, *112*, 17492–17498.

(65) Hou, Y. D.; Abrams, B. L.; Vesborg, P. C. K.; Björketun, M. E.; Herbst, K.; Bech, L.; Setti, A. M.; Damsgaard, C. D.; Pedersen, T.; Hansen, O.; Rossmeisl, J.; Dahl, S.; Nørskov, J. K.; Chorkendorff, I. Bioinspired molecular co-catalysts bonded to a silicon photocathode for solar hydrogen evolution. *Nature Mater.* **2011**, *10*, 434–438.

(66) Hodes, G.; Manassen, J.; Cahen, D. Electrocatalytic Electrodes for the Polysulfide Redox System. *J. Electrochem. Soc.* **1980**, *127*, 544–549.

(67) Trasatti, S. Work Function, Electronegativity, and Electrochemical Behavior of Metals III. Electrolytic Hydrogen Evolution in Acid Solutions. *J. Electroanal. Chem.* **1972**, *39*, 163–184.

(68) Miles, M. H. Evaluation of Electrocatalysts for Water Electrolysis in Alkaline Solutions. *J. Electroanal. Chem.* **1975**, *60*, 89–96.

(69) Kuhn, A. T.; Mortimer, C. J.; Bond, G. C.; Lindley, J. A Critical Analysis of Correlations between the Rate of the Electrochemical Hydrogen Evolution Reaction and Physical Properties of the Elements. *J. Electroanal. Chem.* **1972**, *34*, 1–14.

(70) Highfield, J. G.; Claude, E.; Oguro, K. Electrocatalytic synergism in Ni/Mo cathodes for hydrogen evolution in acid medium: a new model. *Electrochim. Acta* **1999**, *44*, 2805–2814.

(71) Jaksic, M. M. Hypo–hyper-d-electronic interactive nature of interionic synergism in catalysis and electrocatalysis for hydrogen reactions. *Int. J. Hydrogen Energy* **2001**, *26*, 559–578.

(72) Greeley, J.; Nørskov, J. K.; Kibler, L. A.; El-Aziz, A. M.; Kolb, D. M. Hydrogen Evolution Over Bimetallic Systems: Understanding the Trends. *ChemPhysChem* **2006**, *7*, 1032–1035.

(73) Greeley, J.; Stephens, I. E. L.; Bondarenko, A. S.; Johansson, T. P.; Hansen, H. A.; Jaramillo, T. F.; Rossmeisl, J.; Chorkendorff, I.; Nørskov, J. K. Alloys of platinum and early transition metals as oxygen reduction electrocatalysts. *Nature Chem.* **2009**, *1*, 552–556.

(74) Brooman, E. W.; Kuhn, A. T. Correlations Between the Rate of the Hydrogen Electrode Reaction and the Properties of Alloys. *J. Electroanal. Chem.* **1974**, *49*, 325–353.

(75) Brown, D. E.; Mahmood, M. N.; Turner, A. K.; Hall, S. M.; Fogarty, P. O. Low Overvoltage Electrocatalysts for Hydrogen Evolving Electrodes. *Int. J. Hydrogen Energy* **1982**, *7*, 405–410.

(76) Brown, D. E.; Mahmood, M. N.; Man, M. C. M.; Turner, A. K. Preparation and Characterization of Low Overvoltage Transition Metal Alloy Electrocatalysts for Hydrogen Evolution in Alkaline Solutions. *Electrochim. Acta* **1984**, *29*, 1551–1556.

(77) Navarro-Flores, E.; Chong, Z. W.; Omanovic, S. Characterization of Ni, NiMo, NiW and NiFe electroactive coatings as electrocatalysts for hydrogen evolution in an acidic medium. *J. Mol. Catal. A: Chem.* **2005**, *226*, 179–197.

(78) McKone, J. R.; Sadtler, B. F.; Werlang, C. A.; Lewis, N. S.; Gray, H. B. Ni–Mo Nanopowders for Efficient Electrochemical Hydrogen Evolution. *ACS Catal.* **2013**, *3*, 166–169.

(79) McKone, J. R.; Warren, E. L.; Bierman, M. J.; Boettcher, S. W.; Brunschwig, B. S.; Lewis, N. S.; Gray, H. B. Evaluation of Pt, Ni, and Ni–Mo electrocatalysts for hydrogen evolution on crystalline Si electrodes. *Energy Environ. Sci.* **2011**, *4*, 3573–3583.

(80) Warren, E. L.; McKone, J. R.; Atwater, H. A.; Gray, H. B.; Lewis, N. S. Hydrogen-evolution characteristics of Ni–Mo-coated, radial junction, n^{+}p-silicon microwire array photocathodes. *Energy Environ. Sci.* **2012**, *5*, 9653–9661.

(81) Conway, B. E.; Bai, L. H_2 Evolution Kinetics at High Activity Ni–Mo–Cd Electrocoated Cathodes and Its Relation to Potential Dependence of Sorption of H*. *Int. J. Hydrogen Energy* **1986**, *11*, 533–540.

(82) Raj, I. A. Nickel Based Composite Electrolytic Surface Coatings as Electrocatalysts for the Cathodes in the Energy Efficient Industrial Production of Hydrogen from Alkaline Water Electrolytic Cells. *Int. J. Hydrogen Energy* **1992**, *17*, 413–421.

(83) Reece, S. Y.; Hamel, J. A.; Sung, K.; Jarvi, T. D.; Esswein, A. J.; Pijpers, J. J. H.; Nocera, D. G. Wireless Solar Water Splitting Using Silicon-Based Semiconductors and Earth-Abundant Catalysts. *Science* **2011**, *334*, 645–648.

(84) Trasatti, S. *Electrodes of Conductive Metallic Oxides*; Elsevier Scientific Pub. Co., 1980.

(85) Cheng, F. Y.; Su, Y.; Liang, J.; Tao, Z. L.; Chen, J. MnO_2-Based Nanostructures as Catalysts for Electrochemical Oxygen Reduction in Alkaline Media. *Chem. Mater.* **2010**, *22*, 898–905.

(86) Cheng, F. Y.; Shen, J. A.; Peng, B.; Pan, Y. D.; Tao, Z. L.; Chen, J. Rapid room-temperature synthesis of nanocrystalline spinels as oxygen reduction and evolution electrocatalysts. *Nature Chem.* **2011**, *3*, 79–84.

(87) Maiyalagan, T.; Jarvis, K. A.; Therese, S.; Ferreira, P. J.; Manthiram, A. Spinel-type lithium cobalt oxide as a bifunctional electrocatalyst for the oxygen evolution and oxygen reduction reactions. *Nature Commun.* **2014**, *5*, DOI: 10.1038/ncomms4949.

(88) Suntivich, J.; Gasteiger, H. A.; Yabuuchi, N.; Nakanishi, H.; Goodenough, J. B.; Shao-Horn, Y. Design principles for oxygen-reduction activity on perovskite oxide catalysts for fuel cells and metal-air batteries. *Nature Chem.* **2011**, *3*, 546–550.

(89) Liang, Y. Y.; Li, Y. G.; Wang, H. L.; Dai, H. J. Strongly Coupled lnorganic/Nanocarbon Hybrid Materials for Advanced Electrocatalysis. *J. Am. Chem. Soc.* **2013**, *135*, 2013–2036.

(90) Liang, Y. Y.; Li, Y. G.; Wang, H. L.; Zhou, J. G.; Wang, J.; Regier, T.; Dai, H. J. Co_3O_4 nanocrystals on graphene as a synergistic catalyst for oxygen reduction reaction. *Nature Mater.* **2011**, *10*, 780–786.

(91) Gao, M.-R.; Liu, S. A.; Jiang, J.; Cui, C.-H.; Yao, W.-T.; Yu, S.-H. *In situ* controllable synthesis of magnetite nanocrystals/$CoSe_2$ hybrid nanobelts and their enhanced catalytic performance. *J. Mater. Chem.* **2010**, *20*, 9355–9361.

(92) Xu, Y.-F.; Gao, M.-R.; Zheng, Y.-R.; Jiang, J.; Yu, S.-H. Nickel/Nickel(II) Oxide Nanoparticles Anchored onto Cobalt(IV) Diselenide Nanobelts for the Electrochemical Production of Hydrogen. *Angew. Chem. Int. Ed.* **2013**, *52*, 8546–8550.

(93) Ohnishi, R.; Takahashi, Y.; Takagaki, A.; Kubota, J.; Domen, K. Niobium Oxides as Cathode Electrocatalysts for Platinum-free Polymer Electrolyte Fuel Cells. *Chem. Lett.* **2008**, *37*, 838–839.

(94) Lin, X.; Wu, M. X.; Wang, Y. D.; Hagfeldt, A.; Ma, T. L. Novel counter electrode catalysts of niobium oxides supersede Pt for dye-sensitized solar cells. *Chem. Commun.* **2011**, *47*, 11489–11491.

(95) Wilson, J. A.; Yoffe, A. D. The Transition Metal Dichalcogenides: Discussion and Interpretation of the Observed Optical, Electrical and Structural Properties. *Adv. Phys.* **1969**, *18*, 193–335.

(96) Jaegermann, W.; Tributsch, H. Interfacial Properties of Semiconducting Transition Metal Chalcogenides. *Prog. Surf. Sci.* **1988**, *29*, 1–167.

(97) Gerischer, H. Electrochemical Photo and Solar Cells: Principles and Some Experiments. *J. Electroanal. Chem. Interfacial Electrochem.* **1975**, *58*, 263–274.

(98) Hodes, G.; Manassen, J.; Cahen, D. Photoelectrochemical energy conversion and storage using polycrystalline chalcogenide electrodes. *Nature* **1976**, *261*, 403–404.

(99) Miller, B.; Heller, A. Semiconductor liquid junction solar cells based on anodic sulfide films. *Nature* **1976**, *262*, 680–681.

(100) Ellis, A. B.; Kaiser, S. W.; Wrighton, M. S. Visible Light to Electrical Energy Conversion. Stable Cadmium Sulfide and Cadmium Selenide Photoelectrodes in Aqueous Electrolytes. *J. Am. Chem. Soc.* **1976**, *98*, 1635–1637.

(101) Allen, P. L.; Hickling, A. Electrochemistry of sulphur. Part 1.—Overpotential in the discharge of the sulphide ion. *Trans. Faraday Soc.* **1957**, *53*, 1626–1635.

(102) Loučka, T. The Adsorption of Sulphur and of Simple Organic Substances on Platinum Electrodes. *J. Electroanal. Chem.* **1972**, *36*, 369–381.

(103) Radich, J. G.; Dwyer, R.; Kamat, P. V. Cu_2S Reduced Graphene Oxide Composite for High-Efficiency Quantum Dot Solar Cells. Overcoming the Redox Limitations of S^{2-}/S_n^{2-} at the Counter Electrode. *J. Phys. Chem. Lett.* **2011**, *2*, 2453–2460.

(104) Radich, J. G.; Peeples, N. R.; Santra, P. K.; Kamat, P. V. Charge Transfer Mediation Through Cu_xS. The Hole Story of CdSe in Polysulfide. *J. Phys. Chem. C*, DOI: 10.1021/jp4113365.

(105) Chhowalla, M.; Shin, H. S.; Eda, G.; Li, L.-J.; Loh, K. P.; Zhang, H. The chemistry of two-dimensional layered transition metal dichalcogenide nanosheets. *Nature Chem.* **2013**, *5*, 263–275.

(106) Yang, J.; Shin, H. S. Recent advances in layered transition metal dichalcogenides for hydrogen evolution reaction. *J. Mater. Chem. A* **2014**, *2*, 5979–5985.

(107) Merki, D.; Hu, X. L. Recent developments of molybdenum and tungsten sulfides as hydrogen evolution catalysts. *Energy Environ. Sci.* **2011**, *4*, 3878–3888.

(108) Laursen, A. B.; Kegnæs, S.; Dahl, S.; Chorkendorff, I. Molybdenum sulfides—efficient and viable materials for electro- and photoelectrocatalytic hydrogen evolution. *Energy Environ. Sci.* **2012**, *5*, 5577–5591.

(109) Hinnemann, B.; Moses, P. G.; Bonde, J.; Jørgensen, K. P.; Nielsen, J. H.; Horch, S.; Chorkendorff, I.; Nørskov, J. K. Biomimetic Hydrogen Evolution: MoS_2 Nanoparticles as Catalyst for Hydrogen Evolution. *J. Am. Chem. Soc.* **2005**, *127*, 5308–5309.

(110) Jaramillo, T. F.; Jørgensen, K. P.; Bonde, J.; Nielsen, J. H.; Horch, S.; Chorkendorff, I. Identification of Active Edge Sites for Electrochemical H_2 Evolution from MoS_2 Nanocatalysts. *Science* **2007**, *317*, 100–102.

(111) Bonde, J.; Moses, P. G.; Jaramillo, T. F.; Nørskov, J. K.; Chorkendorff, I. Hydrogen evolution on nano-particulate transition metal sulfides. *Faraday Discuss.* **2008**, *140*, 219–231.

(112) Karunadasa, H. I.; Montalvo, E.; Sun, Y. J.; Majda, M.; Long, J. R.; Chang, C. J. A Molecular MoS_2 Edge Site Mimic for Catalytic Hydrogen Generation. *Science* **2012**, *335*, 698–702.

(113) Tenne, R.; Redlich, M. Recent progress in the research of inorganic fullerene-like nanoparticles and inorganic nanotubes. *Chem. Soc. Rev.* **2010**, *39*, 1423–1434.

(114) Li, Y. G.; Wang, H. L.; Xie, L. M.; Liang, Y. Y.; Hong, G. S.; Dai, H. J. MoS_2 Nanoparticles Grown on Graphene: An Advanced Catalyst for the Hydrogen Evolution Reaction. *J. Am. Chem. Soc.* **2011**, *133*, 7296–7299.

(115) Lukowski, M. A.; Daniel, A. S.; Meng, F.; Forticaux, A.; Li, L.; Jin, S. Enhanced Hydrogen Evolution Catalysis from Chemically Exfoliated Metallic MoS_2 Nanosheets. *J. Am. Chem. Soc.* **2013**, *135*, 10274–10277.

(116) Voiry, D.; Yamaguchi, H.; Li, J.; Silva, R.; Alves, D. C. B.; Fujita, T.; Chen, M.; Asefa, T.; Shenoy, V. B.; Eda, G.; Chhowalla, M. Enhanced catalytic activity in strained chemically exfoliated WS_2 nanosheets for hydrogen evolution. *Nature Mater.* **2013**, *12*, 850–855.

(117) Kong, D. S.; Wang, H. T.; Cha, J. J.; Pasta, M.; Koski, K. J.; Yao, J.; Cui, Y. Synthesis of MoS_2 and $MoSe_2$ Films with Vertically Aligned Layers. *Nano Lett.* **2013**, *13*, 1341–1347.

(118) Wang, H.; Lu, Z.; Xu, S.; Kong, D.; Cha, J. J.; Zheng, G.; Hsu, P.-C.; Yan, K.; Bradshaw, D.; Prinz, F. B.; Cui, Y. Electrochemical tuning of vertically aligned MoS_2 nanofilms and its application in improving hydrogen evolution reaction. *Proc. Natl. Acad. Sci. U.S.A.* **2013**, *110*, 19701–19706.

(119) Xie, J. F.; Zhang, H.; Li, S.; Wang, R. X.; Sun, X.; Zhou, M.; Zhou, J. F.; Lou, X. W.; Xie, Y. Defect-Rich MoS_2 Ultrathin Nanosheets with Additional Active Edge Sites for Enhanced Electrocatalytic Hydrogen Evolution. *Adv. Mater.* **2013**, *25*, 5807–5813.

(120) Xie, J. F.; Zhang, J. J.; Li, S.; Grote, F.; Zhang, X. D.; Zhang, H.; Wang, R. X.; Lei, Y.; Pan, B. C.; Xie, Y. Controllable Disorder Engineering in Oxygen-Incorporated MoS_2 Ultrathin Nanosheets for Efficient Hydrogen Evolution. *J. Am. Chem. Soc.* **2013**, *135*, 17881–17888.

(121) Chung, D. Y.; Park, S.-K.; Chung, Y.-H.; Yu, S.-H.; Lim, D.-H.; Jung, N.; Ham, H. C.; Park, H.-Y.; Piao, Y.; Yoo, S. J.; Sung, Y.-E. Edge-exposed MoS_2 nano-assembled

structures as efficient electrocatalysts for hydrogen evolution reaction. *Nanoscale* **2014**, *6*, 2131–2136.

(122) Zheng, X. L.; Xu, J. B.; Yan, K. Y.; Wang, H.; Wang, Z. L.; Yang, S. H. Space-Confined Growth of MoS_2 Nanosheets within Graphite: The Layered Hybrid of MoS_2 and Graphene as an Active Catalyst for Hydrogen Evolution Reaction. *Chem. Mater.* **2014**, *26*, 2344–2353.

(123) Lu, Z. Y.; Zhu, W.; Yu, X. Y.; Zhang, H. C.; Li, Y. J.; Sun, X. M.; Wang, X. W.; Wang, H.; Wang, J. M.; Luo, J.; Lei, X. D.; Jiang, L. Ultrahigh Hydrogen Evolution Performance of Under-Water "Superaerophobic" MoS_2 Nanostructured Electrodes. *Adv. Mater.* **2014**, *26*, 2683–2687.

(124) Kibsgaard, J.; Chen, Z.; Reinecke, B. N.; Jaramillo, T. F. Engineering the surface structure of MoS_2 to preferentially expose active edge sites for electrocatalysis. *Nature Mater.* **2012**, *11*, 963–969.

(125) Wang, D. Z.; Wang, Z. P.; Wang, C. L.; Zhou, P.; Wu, Z. Z.; Liu, Z. H. Distorted MoS_2 nanostructures: An efficient catalyst for the electrochemical hydrogen evolution reaction. *Electrochem. Commun.* **2013**, *34*, 219–222.

(126) Ding, Q.; Meng, F.; English, C. R.; Cabán-Acevedo, M.; Shearer, M. J.; Liang, D.; Daniel, A. S.; Hamers, R. J.; Jin, S. Efficient Photoelectrochemical Hydrogen Generation Using Heterostructures of Si and Chemically Exfoliated Metallic MoS_2. *J. Am. Chem. Soc.*, DOI: 10.1021/ja5025673.

(127) Wu, Z. Z.; Fang, B. Z.; Bonakdarpour, A.; Sun, A. K.; Wilkinson, D. P.; Wang, D. Z. WS_2 nanosheets as a highly efficient electrocatalyst for hydrogen evolution reaction. *Appl. Catal. B* **2012**, *125*, 59–66.

(128) Lin, J.; Peng, Z. W.; Wang, G.; Zakhidov, D.; Larios, E.; Yacaman, M. J.; Tour, J. M. Enhanced Electrocatalysis for Hydrogen Evolution Reactions from WS_2 Nanoribbons. *Adv. Energy Mater.*, DOI: 10.1002/aenm.201301875.

(129) Wang, H. T.; Kong, D. S.; Johanes, P.; Cha, J. J.; Zheng, G. Y.; Yan, K.; Liu, N. A.; Cui, Y. $MoSe_2$ and WSe_2 Nanofilms with Vertically Aligned Molecular Layers on Curved and Rough Surfaces. *Nano Lett.* **2013**, *13*, 3426–3433.

(130) Lai, C.-H.; Lu, M.-Y.; Chen, L.-J. Metal sulfide nanostructures: synthesis, properties and applications in energy conversion and storage. *J. Mater. Chem.* **2012**, *22*, 19–30.

(131) Gao, M.-R.; Xu, Y.-F.; Jiang, J.; Yu, S.-H. Nanostructured metal chalcogenides: synthesis, modification, and applications in energy conversion and storage devices. *Chem. Soc. Rev.* **2013**, *42*, 2986–3017.

(132) Huang, X.; Zeng, Z. Y.; Zhang, H. Metal dichalcogenide nanosheets: preparation, properties and applications. *Chem. Soc. Rev.* **2013**, *42*, 1934–1946.

(133) Morales-Guio, C. G.; Stern, L.-A.; Hu, X. L. Nanostructured hydrotreating catalysts for electrochemical hydrogen evolution. *Chem. Soc. Rev.*, DOI: 10.1039/C1033CS60468C.

(134) Guo, J. H.; Shi, Y. T.; Zhu, C.; Wang, L.; Wang, N.; Ma, T. L. Cost-effective and morphology-controllable niobium diselenides for highly efficient counter electrodes of dye-sensitized solar cells. *J. Mater. Chem. A* **2013**, *1*, 11874–11879.

(135) Ji, I. A.; Choi, H. M.; Bang, J. H. Metal selenide films as the counter electrode in dye-sensitized solar cell. *Mater. Lett.* **2014**, *123*, 51–54.

(136) Finn, S. T.; Macdonald, J. E. Petaled Molybdenum Disulfide Surfaces: Facile Synthesis of a Superior Cathode for QDSSCs. *Adv. Energy Mater.*, DOI: 10.1002/aenm.201400495.

(137) Faber, M. S.; Park, K.; Cabán-Acevedo, M.; Santra, P. K.; Jin, S. Earth-Abundant Cobalt Pyrite (CoS_2) Thin Film on Glass as a Robust, High-Performance Counter Electrode for Quantum Dot-Sensitized Solar Cells. *J. Phys. Chem. Lett.* **2013**, *4*, 1843–1849.

(138) Duan, X. L.; Gao, Z. Y.; Chang, J. L.; Wu, D. P.; Ma, P. F.; He, J. J.; Xu, F.; Gao, S. Y.; Jiang, K. CoS_2–graphene composite as efficient catalytic counter electrode for dye-sensitized solar cell. *Electrochim. Acta* **2013**, *114*, 173–179.

(139) Huang, Q.-H.; Ling, T.; Qiao, S.-Z.; Du, X.-W. Pyrite nanorod arrays as an efficient counter electrode for dye-sensitized solar cells. *J. Mater. Chem. A* **2013**, *1*, 11828–11833.

(140) Wang, Y.-C.; Wang, D.-Y.; Jiang, Y.-T.; Chen, H.-A.; Chen, C.-C.; Ho, K.-C.; Chou, H.-L.; Chen, C.-W. FeS_2 Nanocrystal Ink as a Catalytic Electrode for Dye-Sensitized Solar Cells. *Angew. Chem. Int. Ed.* **2013**, *52*, 6694–6698.

(141) Cabán-Acevedo, M.; Faber, M. S.; Tan, Y. Z.; Hamers, R. J.; Jin, S. Synthesis and Properties of Semiconducting Iron Pyrite (FeS_2) Nanowires. *Nano Lett.* **2012**, *12*, 1977–1982.

(142) Cabán-Acevedo, M.; Liang, D.; Chew, K. S.; DeGrave, J. P.; Kaiser, N. S.; Jin, S. Synthesis, Characterization, and Variable Range Hopping Transport of Pyrite (FeS_2) Nanorods, Nanobelts, and Nanoplates. *ACS Nano* **2013**, *7*, 1731–1739.

(143) Peng, S. J.; Li, L. L.; Tan, H. T.; Cai, R.; Shi, W. H.; Li, C. C.; Mhaisalkar, S. G.; Srinivasan, M.; Ramakrishna, S.; Yan, Q. Y. MS_2 (M = Co and Ni) Hollow Spheres with Tunable Interiors for High-Performance Supercapacitors and Photovoltaics. *Adv. Funct. Mater.* **2014**, *24*, 2155–2162.

(144) Baresel, D.; Sarholz, W.; Scharner, P.; Schmitz, J. Übergangs-Metallchalkogenide als Sauerstoff-Katalysatoren für Brennstoffzellen. *Berich. Bunsen Gesell.* **1974**, *78*, 608–611.

(145) Susac, D.; Zhu, L.; Teo, M.; Sode, A.; Wong, K. C.; Wong, P. C.; Parsons, R. R.; Bizzotto, D.; Mitchell, K. A. R.; Campbell, S. A. Characterization of FeS_2-Based Thin Films as Model Catalysts for the Oxygen Reduction Reaction. *J. Phys. Chem. C* **2007**, *111*, 18715–18723.

(146) Zhu, L.; Susac, D.; Teo, M.; Wong, K. C.; Wong, P. C.; Parsons, R. R.; Bizzotto, D.; Mitchell, K. A. R.; Campbell, S. A. Investigation of CoS_2-based thin films as model catalysts for the oxygen reduction reaction. *J. Catal.* **2008**, *258*, 235–242.

(147) Zhu, L.; Teo, M.; Wong, P. C.; Wong, K. C.; Narita, I.; Ernst, F.; Mitchell, K. A. R.; Campbell, S. A. Synthesis, characterization of a $CoSe_2$ catalyst for the oxygen reduction reaction. *Appl. Catal. A* **2010**, *386*, 157–165.

(148) Jirkovský, J. S.; Björling, A.; Ahlberg, E. Reduction of Oxygen on Dispersed Nanocrystalline CoS_2. *J. Phys. Chem. C* **2012**, *116*, 24436–24444.

(149) Zhao, C.; Li, D.; Feng, Y. Size-controlled hydrothermal synthesis and high electrocatalytic performance of CoS_2 nanocatalysts as non-precious metal cathode materials for fuel cells. *J. Mater. Chem. A* **2013**, *1*, 5741–5746.

(150) Ivanovskaya, A.; Singh, N.; Liu, R.-F.; Kreutzer, H.; Baltrusaitis, J.; Nguyen, T. V.; Metiu, H.; McFarland, E. Transition Metal Sulfide Hydrogen Evolution Catalysts for Hydrobromic Acid Electrolysis. *Langmuir* **2013**, *29*, 480–492.

(151) Kong, D. S.; Wang, H. T.; Lu, Z. Y.; Cui, Y. $CoSe_2$ Nanoparticles Grown on Carbon Fiber Paper: An Efficient and Stable Electrocatalyst for Hydrogen Evolution Reaction. *J. Am. Chem. Soc.* **2014**, *136*, 4897–4900.

(152) Kong, D. S.; Cha, J. J.; Wang, H. T.; Lee, H. R.; Cui, Y. First-row transition metal dichalcogenide catalysts for hydrogen evolution reaction. *Energy Environ. Sci.* **2013**, *6*, 3553–3558.

(153) Merki, D.; Fierro, S.; Vrubel, H.; Hu, X. L. Amorphous molybdenum sulfide films as catalysts for electrochemical hydrogen production in water. *Chem. Sci.* **2011**, *2*, 1262–1267.

(154) Seger, B.; Laursen, A. B.; Vesborg, P. C. K.; Pedersen, T.; Hansen, O.; Dahl, S.; Chorkendorff, I. Hydrogen Production Using a Molybdenum Sulfide Catalyst on a Titanium-Protected n^+p-Silicon Photocathode. *Angew. Chem. Int. Ed.* **2012**, *51*, 9128–9131.

(155) Wang, T. Y.; Zhuo, J. Q.; Du, K. Z.; Chen, B. B.; Zhu, Z. W.; Shao, Y. H.; Li, M. X. Electrochemically Fabricated Polypyrrole and MoS_x Copolymer Films as a Highly Active Hydrogen Evolution Electrocatalyst. *Adv. Mater.*, DOI: 10.1002/adma.201400265.

(156) Morales-Guio, C. G.; Tilley, S. D.; Vrubel, H.; Grätzel, M.; Hu, X. L. Hydrogen evolution from a copper(I) oxide photocathode coated with an amorphous molybdenum sulphide catalyst. *Nature Commun.* **2014**, *5*, DOI: 10.1038/ncomms4059.

(157) Benck, J. D.; Chen, Z. B.; Kuritzky, L. Y.; Forman, A. J.; Jaramillo, T. F. Amorphous Molybdenum Sulfide Catalysts for Electrochemical Hydrogen Production: Insights into the Origin of their Catalytic Activity. *ACS Catal.* **2012**, *2*, 1916–1923.

(158) Vrubel, H.; Merki, D.; Hu, X. L. Hydrogen evolution catalyzed by MoS_3 and MoS_2 particles. *Energy Environ. Sci.* **2012**, *5*, 6136–6144.

(159) Li, D. J.; Maiti, U. N.; Lim, J.; Choi, D. S.; Lee, W. J.; Oh, Y.; Lee, G. Y.; Kim, S. O. Molybdenum Sulfide/N-Doped CNT Forest Hybrid Catalysts for High-Performance Hydrogen Evolution Reaction. *Nano Lett.* **2014**, *14*, 1228–1233.

(160) Chang, Y.-H.; Lin, C.-T.; Chen, T.-Y.; Hsu, C.-L.; Lee, Y.-H.; Zhang, W. J.; Wei, K.-H.; Li, L.-J. Highly Efficient Electrocatalytic Hydrogen Production by MoS_x Grown on Graphene-Protected 3D Ni Foams. *Adv. Mater.* **2013**, *25*, 756–760.

(161) Zong, X.; Yan, H. J.; Wu, G. P.; Ma, G. J.; Wen, F. Y.; Wang, L.; Li, C. Enhancement of Photocatalytic H_2 Evolution on CdS by Loading MoS_2 as Cocatalyst under Visible Light Irradiation. *J. Am. Chem. Soc.* **2008**, *130*, 7176–7177.

(162) Laursen, A. B.; Pedersen, T.; Malacrida, P.; Seger, B.; Hansen, O.; Vesborg, P. C. K.; Chorkendorff, I. MoS_2–an integrated protective and active layer on n^+p-Si for solar H_2 evolution. *Phys. Chem. Chem. Phys.* **2013**, *15*, 20000–20004.

(163) Sun, Y.; Liu, C.; Grauer, D. C.; Yano, J.; Long, J. R.; Yang, P.; Chang, C. J. Electrodeposited Cobalt-Sulfide Catalyst for Electrochemical and Photoelectrochemical Hydrogen Generation from Water. *J. Am. Chem. Soc.* **2013**, *135*, 17699–17702.

(164) Gao, M.-R.; Lin, Z.-Y.; Zhuang, T.-T.; Jiang, J.; Xu, Y.-F.; Zheng, Y.-R.; Yu, S.-H. Mixed-solution synthesis of sea urchin-like NiSe nanofiber assemblies as economical Pt-

free catalysts for electrochemical H_2 production. *J. Mater. Chem.* **2012**, *22*, 13662–13668.

(165) Wang, M. K.; Anghel, A. M.; Marsan, B.; Ha, N.-L. C.; Pootrakulchote, N.; Zakeeruddin, S. M.; Grätzel, M. CoS Supersedes Pt as Efficient Electrocatalyst for Triiodide Reduction in Dye-Sensitized Solar Cells. *J. Am. Chem. Soc.* **2009**, *131*, 15976–15977.

(166) Kung, C.-W.; Chen, H.-W.; Lin, C.-Y.; Huang, K.-C.; Vittal, R.; Ho, K.-C. CoS Acicular Nanorod Arrays for the Counter Electrode of an Efficient Dye-Sensitized Solar Cell. *ACS Nano* **2012**, *6*, 7016–7025.

(167) Chang, S.-H.; Lu, M.-D.; Tung, Y.-L.; Tuan, H.-Y. Gram-Scale Synthesis of Catalytic Co_9S_8 Nanocrystal Ink as a Cathode Material for Spray-Deposited, Large-Area Dye-Sensitized Solar Cells. *ACS Nano* **2013**, *7*, 9443–9451.

(168) Sun, H. C.; Qin, D.; Huang, S. Q.; Guo, X. Z.; Li, D. M.; Luo, Y. H.; Meng, Q. B. Dye-sensitized solar cells with NiS counter electrodes electrodeposited by a potential reversal technique. *Energy Environ. Sci.* **2011**, *4*, 2630–2637.

(169) Choi, H. M.; Ji, I. A.; Bang, J. H. Metal Selenides as a New Class of Electrocatalysts for Quantum Dot-Sensitized Solar Cells: A Tale of $Cu_{1.8}Se$ and PbSe. *ACS Appl. Mater. Interfaces* **2014**, *6*, 2335–2343.

(170) Gong, F.; Wang, H.; Xu, X.; Zhou, G.; Wang, Z.-S. In Situ Growth of $Co_{0.85}Se$ and $Ni_{0.85}Se$ on Conductive Substrates as High-Performance Counter Electrodes for Dye-Sensitized Solar Cells. *J. Am. Chem. Soc.* **2012**, *134*, 10953–10958.

(171) Chen, J. G. G. Carbide and Nitride Overlayers on Early Transition Metal Surfaces: Preparation, Characterization, and Reactivities. *Chem. Rev.* **1996**, *96*, 1477–1498.

(172) Chen, W.-F.; Muckerman, J. T.; Fujita, E. Recent developments in transition metal carbides and nitrides as hydrogen evolution electrocatalysts. *Chem. Commun.* **2013**, *49*, 8896–8909.

(173) Chen, W.-F.; Sasaki, K.; Ma, C.; Frenkel, A. I.; Marinkovic, N.; Muckerman, J. T.; Zhu, Y. M.; Adzic, R. R. Hydrogen-Evolution Catalysts Based on Non-Noble Metal Nickel–Molybdenum Nitride Nanosheets. *Angew. Chem. Int. Ed.* **2012**, *51*, 6131–6135.

(174) Cao, B. F.; Veith, G. M.; Neuefeind, J. C.; Adzic, R. R.; Khalifah, P. G. Mixed Close-Packed Cobalt Molybdenum Nitrides as Non-noble Metal Electrocatalysts for the Hydrogen Evolution Reaction. *J. Am. Chem. Soc.* **2013**, *135*, 19186–19192.

(175) Liu, M. J.; Dong, Y. Z.; Wu, Y. M.; Feng, H. B.; Li, J. H. Titanium Nitride Nanocrystals on Nitrogen-Doped Graphene as an Efficient Electrocatalyst for Oxygen Reduction Reaction. *Chem. Eur. J.* **2013**, *19*, 14781–14786.

(176) Li, G. R.; Song, J.; Pan, G. L.; Gao, X. P. Highly Pt-like electrocatalytic activity of transition metal nitrides for dye-sensitized solar cells. *Energy Environ. Sci.* **2011**, *4*, 1680–1683.

(177) Zhang, X. Y.; Chen, X.; Zhang, K. J.; Pang, S. P.; Zhou, X. H.; Xu, H. X.; Dong, S. M.; Han, P. X.; Zhang, Z. Y.; Zhang, C. J.; Cui, G. L. Transition-metal nitride nanoparticles embedded in N-doped reduced graphene oxide: superior synergistic electrocatalytic materials for the counter electrodes of dye-sensitized solar cells. *J. Mater. Chem. A* **2013**, *1*, 3340–3346.

(178) Li, G.-R.; Wang, F.; Jiang, Q.-W.; Gao, X.-P.; Shen, P.-W. Carbon Nanotubes with Titanium Nitride as a Low-Cost Counter-Electrode Material for Dye-Sensitized Solar Cells. *Angew. Chem. Int. Ed.* **2010**, *49*, 3653–3656.

(179) Sweeny, N. P.; Rohrer, C. S.; Brown, O. W. Dinickel Phosphide as a Heterogeneous Catalyst for the Vapor Phase Reduction of Nitrobenzene with Hydrogen to Aniline and Water. *J. Am. Chem. Soc.* **1958**, *80*, 799–800.

(180) Oyama, S. T. Novel catalysts for advanced hydroprocessing: transition metal phosphides. *J. Catal.* **2003**, *216*, 343–352.

(181) Oyama, S. T.; Gott, T.; Zhao, H. Y.; Lee, Y.-K. Transition metal phosphide hydroprocessing catalysts: A review. *Catal. Today* **2009**, *143*, 94–107.

(182) Carenco, S.; Portehault, D.; Boissière, C.; Mézailles, N.; Sanchez, C. Nanoscaled Metal Borides and Phosphides: Recent Developments and Perspectives. *Chem. Rev.* **2013**, *113*, 7981–8065.

(183) Paseka, I. Evolution of Hydrogen and Its Sorption on Remarkable Active Amorphous Smooth Ni–P(x) Electrodes. *Electrochim. Acta* **1995**, *40*, 1633–1640.

(184) Deng, J.-F.; Li, H. X.; Wang, W. J. Progress in design of new amorphous alloy catalysts. *Catal. Today* **1999**, *51*, 113–125.

(185) Xu, Y.; Wu, R.; Zhang, J. F.; Shi, Y. M.; Zhang, B. Anion-exchange synthesis of nanoporous FeP nanosheets as electrocatalysts for hydrogen evolution reaction. *Chem. Commun.* **2013**, *49*, 6656–6658.

(186) Popczun, E. J.; McKone, J. R.; Read, C. G.; Biacchi, A. J.; Wiltrout, A. M.; Lewis, N. S.; Schaak, R. E. Nanostructured Nickel Phosphide as an Electrocatalyst for the Hydrogen Evolution Reaction. *J. Am. Chem. Soc.* **2013**, *135*, 9267–9270.

(187) Popczun, E. J.; Read, C. G.; Roske, C. W.; Lewis, N. S.; Schaak, R. E. Highly Active Electrocatalysis of the Hydrogen Evolution Reaction by Cobalt Phosphide Nanoparticles. *Angew. Chem. Int. Ed.* **2014**, *53*, 5427–5430.

(188) Tian, J. Q.; Liu, Q.; Asiri, A. M.; Sun, X. P. Self-Supported Nanoporous Cobalt Phosphide Nanowire Arrays: An Efficient 3D Hydrogen-Evolving Cathode over the Wide Range of pH 0–14. *J. Am. Chem. Soc.* **2014**, *136*, 7587–7590.

(189) Dou, Y. Y.; Li, G. R.; Song, J.; Gao, X. P. Nickel phosphide-embedded graphene as counter electrode for dye-sensitized solar cells. *Phys. Chem. Chem. Phys.* **2012**, *14*, 1339–1342.

(190) Wu, M. X.; Bai, J.; Wang, Y. D.; Wang, A. J.; Lin, X.; Wang, L.; Shen, Y. H.; Wang, Z. Q.; Hagfeldt, A.; Ma, T. L. High-performance phosphide/carbon counter electrode for both iodide and organic redox couples in dye-sensitized solar cells. *J. Mater. Chem.* **2012**, *22*, 11121–11127.

(191) Levy, R. B.; Boudart, M. Platinum-Like Behavior of Tungsten Carbide in Surface Catalysis. *Science* **1973**, *181*, 547–549.

(192) *The Chemistry of Transition Metal Carbides and Nitrides*; Oyama, S. T., Ed.; Chapman & Hall: London, 1996.

(193) Hwu, H. H.; Chen, J. G. G. Surface Chemistry of Transition Metal Carbides. *Chem. Rev.* **2005**, *105*, 185–212.

(194) Weidman, M. C.; Esposito, D. V.; Hsu, Y.-C.; Chen, J. G. G. Comparison of electrochemical stability of transition metal carbides (WC, W_2C, MO_2C) over a wide pH range. *J. Power Sources* **2012**, *202*, 11–17.

(195) Vrubel, H.; Hu, X. L. Molybdenum Boride and Carbide Catalyze Hydrogen Evolution in both Acidic and Basic Solutions. *Angew. Chem. Int. Ed.* **2012**, *51*, 12703–12706.

(196) Liao, L.; Wang, S. N.; Xiao, J. J.; Bian, X. J.; Zhang, Y. H.; Scanlon, M. D.; Hu, X. L.; Tang, Y.; Liu, B. H.; Girault, H. H. A nanoporous molybdenum carbide nanowire as an electrocatalyst for hydrogen evolution reaction. *Energy Environ. Sci.* **2014**, *7*, 387–392.

(197) Chen, W.-F.; Wang, C.-H.; Sasaki, K.; Marinkovic, N.; Xu, W.; Muckerman, J. T.; Zhu, Y.; Adzic, R. R. Highly active and durable nanostructured molybdenum carbide electrocatalysts for hydrogen production. *Energy Environ. Sci.* **2013**, *6*, 943–951.

(198) Wan, C.; Regmi, Y. N.; Leonard, B. M. Multiple Phases of Molybdenum Carbide as Electrocatalysts for the Hydrogen Evolution Reaction. *Angew. Chem. Int. Ed.*, DOI: 10.1002/anie.201402998.

(199) Berglund, S. P.; He, H. C.; Chemelewski, W. D.; Celio, H.; Dolocan, A.; Mullins, C. B. p-Si/W_2C and p-Si/W_2C/Pt Photocathodes for the Hydrogen Evolution Reaction. *J. Am. Chem. Soc.* **2014**, *136*, 1535–1544.

(200) Wu, M. X.; Lin, X. A.; Hagfeldt, A.; Ma, T. L. Low-Cost Molybdenum Carbide and Tungsten Carbide Counter Electrodes for Dye-Sensitized Solar Cells. *Angew. Chem. Int. Ed.* **2011**, *50*, 3520–3524.

(201) Jang, J. S.; Ham, D. J.; Ramasamy, E.; Lee, J.; Lee, J. S. Platinum-free tungsten carbides as an efficient counter electrode for dye sensitized solar cells. *Chem. Commun.* **2010**, *46*, 8600–8602.

(202) Guo, W.; Shen, Y. H.; Wu, M. X.; Wang, L.; Wang, L. L.; Ma, T. L. SnS-Quantum Dot Solar Cells Using Novel TiC Counter Electrode and Organic Redox Couples. *Chem. Eur. J.* **2012**, *18*, 7862–7868.

(203) Yeh, M.-H.; Lin, L.-Y.; Lee, C.-P.; Chou, C.-Y.; Tsai, K.-W.; Lin, J.-T.; Ho, K.-C. High performance CdS quantum-dot-sensitized solar cells with Ti-based ceramic materials as catalysts on the counter electrode. *J. Power Sources* **2013**, *237*, 141–148.

(204) Searcy, A. W. In *Chemical and mechanical behavior of inorganic materials*; Searcy, A. W., Ragone, D. V., Colombo, U., Eds.; Wiley-Interscience: New York, 1970.

(205) Chen, X.; Wang, X. K.; Xiu, J. H.; Williams, C. T.; Liang, C. H. Synthesis and Characterization of Ferromagnetic Nickel–Cobalt Silicide Catalysts with Good Sulfur Tolerance in Hydrodesulfurization of Dibenzothiophene. *J. Phys. Chem. C* **2012**, *116*, 24968–24976.

(206) Chen, X.; Liu, X.; Wang, L.; Li, M.; Williams, C. T.; Liang, C. H. High sulfur tolerance of Ni–Si intermetallics as hydrodesulfurization catalysts. *RSC Adv.* **2013**, *3*, 1728–1731.

(207) Chen, X.; Jin, J. H.; Sha, G. Y.; Li, C.; Zhang, B. S.; Su, D. S.; Williams, C. T.; Liang, C. H. Silicon–nickel intermetallic compounds supported on silica as a highly efficient catalyst for CO methanation. *Catal. Sci. Technol.* **2014**, *4*, 53–61.

(208) Vijh, A. K.; Bélanger, G.; Jacques, R. Electrochemical Activity of Silicides of Some Transition Metals for the Hydrogen Evolution Reaction in Acidic Solutions. *Int. J. Hydrogen Energy* **1990**, *15*, 789–794.

(209) Vijh, A. K.; Bélanger, G.; Jacques, R. Electrolysis of Water on Silicides of Some Transition Metals in Alkaline Solutions. *Int. J. Hydrogen Energy* **1992**, *17*, 479–483.

(210) Vijh, A. K.; Bélanger, G. Some trends in the electrocatalytic activities of metal silicides for the hydrogen evolution reaction. *J. Mater. Sci. Lett.* **1995**, *14*, 982–984.

(211) Wirth, S.; Harnisch, F.; Weinmann, M.; Schröder, U. Comparative study of IVB–VIB transition metal compound electrocatalysts for the hydrogen evolution reaction. *Appl. Catal. B* **2012**, *126*, 225–230.

(212) Schmitt, A. L.; Higgins, J. M.; Szczech, J. R.; Jin, S. Synthesis and applications of metal silicide nanowires. *J. Mater. Chem.* **2010**, *20*, 223–235.

(213) Estruga, M.; Girard, S. N.; Ding, Q.; Chen, L. Y.; Li, X. C.; Jin, S. Facile and scalable synthesis of Ti_5Si_3 nanoparticles in molten salts for metal-matrix nanocomposites. *Chem. Commun.* **2014**, *50*, 1454–1457.

(214) Szczech, J. R.; Jin, S. Epitaxially-hyperbranched FeSi nanowires exhibiting merohedral twinning. *J. Mater. Chem.* **2010**, *20*, 1375–1382.

(215) Los, P.; Lasia, A. Electrocatalytic properties of amorphous nickel boride electrodes for hydrogen evolution reaction in alkaline solution. *J. Electroanal. Chem.* **1992**, *333*, 115–125.

(216) Borodzínski, J. J.; Lasia, A. Electrocatalytic properties of doped nickel boride based electrodes for the hydrogen evolution reaction. *J. Appl. Electrochem.* **1994**, *24*, 1267–1275.

(217) Wu, G.; More, K. L.; Johnston, C. M.; Zelenay, P. High-Performance Electrocatalysts for Oxygen Reduction Derived from Polyaniline, Iron, and Cobalt. *Science* **2011**, *332*, 443–447.

(218) Zhao, Y.; Kamiya, K.; Hashimoto, K.; Nakanishi, S. Hydrogen Evolution by Tungsten Carbonitride Nanoelectrocatalysts Synthesized by the Formation of a Tungsten Acid/Polymer Hybrid In Situ. *Angew. Chem. Int. Ed.* **2013**, *52*, 13638–13641.

(219) Bierman, M. J.; Jin, S. Potential applications of hierarchical branching nanowires in solar energy conversion. *Energy Environ. Sci.* **2009**, *2*, 1050–1059.

(220) Meng, F.; Morin, S. A.; Forticaux, A.; Jin, S. Screw Dislocation Driven Growth of Nanomaterials. *Acc. Chem. Res.* **2013**, *46*, 1616–1626.

(221) Py, M. A.; Haering, R. R. Structural destabilization induced by lithium intercalation in MoS_2 and related compounds. *Can. J. Phys.* **1983**, *61*, 76–84.

(222) Tsai, C.; Abild-Pedersen, F.; Nørskov, J. K. Tuning the MoS_2 Edge-Site Activity for Hydrogen Evolution via Support Interactions. *Nano Lett.* **2014**, *14*, 1381–1387.

(223) Chen, W.-F.; Iyer, S.; Iyer, S.; Sasaki, K.; Wang, C.-H.; Zhu, Y. M.; Muckerman, J. T.; Fujita, E. Biomass-derived electrocatalytic composites for hydrogen evolution. *Energy Environ. Sci.* **2013**, *6*, 1818–1826.

(224) Woodhouse, M.; Parkinson, B. A. Combinatorial approaches for the identification and optimization of oxide semiconductors for efficient solar photoelectrolysis. *Chem. Soc. Rev.* **2009**, *38*, 197–210.

(225) Katz, J. E.; Gingrich, T. R.; Santori, E. A.; Lewis, N. S. Combinatorial synthesis and high-throughput photopotential and photocurrent screening of mixed-metal oxides for photoelectrochemical water splitting. *Energy Environ. Sci.* **2009**, *2*, 103–112.

(226) Xiang, C. X.; Suram, S. K.; Haber, J. A.; Guevarra, D. W.; Soedarmadji, E.; Jin, J.; Gregoire, J. M. High-Throughput Bubble Screening Method for Combinatorial Discovery of Electrocatalysts for Water Splitting. *ACS Comb. Sci.* **2014**, *16*, 47–52.

(227) Gerken, J. B.; Shaner, S. E.; Massé, R. C.; Porubsky, N. J.; Stahl, S. S. A survey of diverse earth abundant oxygen evolution electrocatalysts showing enhanced activity from Ni-Fe oxides containing a third metal. *Energy Environ. Sci.*, DOI: 10.1039/c1034ee00436a.

CHAPTER 2

Earth-Abundant Cobalt Pyrite (CoS_2) Thin Film on Glass as a Robust, High-Performance Counter Electrode for Quantum Dot-Sensitized Solar Cells †

2.1. Abstract

We report a cobalt pyrite (cobalt disulfide, CoS_2) thin film on glass as a robust, high-performance, low-cost, earth-abundant counter electrode for liquid-junction quantum dot-sensitized solar cells (QDSSCs) that employ the aqueous sulfide/polysulfide (S^{2-}/S_n^{2-}) redox electrolyte as the hole-transporting medium. The metallic CoS_2 thin film electrode is prepared via thermal sulfidation of a cobalt film deposited on glass, and has been characterized by powder X-ray diffraction and electron microscopy. Using the CoS_2 counter electrode, CdS/CdSe-sensitized QDSSCs display improved short-circuit photocurrent density and fill factor, achieving solar light-to-electricity conversion efficiencies as high as 4.16%, with an average efficiency

---

† This chapter was originally published as
Faber, M. S.; Park, K.; Cabán-Acevedo, M.; Santra, P. K.; Jin, S. Earth-Abundant Cobalt Pyrite (CoS_2) Thin Film on Glass as a Robust, High-Performance Counter Electrode for Quantum Dot-Sensitized Solar Cells. *J. Phys. Chem. Lett.* **2013**, *4*, 1843–1849
before being adapted here.

improvement of 54 (± 14)% over equivalent devices assembled with a traditional platinum counter electrode. Electrochemical measurements verify that CoS_2 shows high electrocatalytic activity toward polysulfide reduction, rationalizing the improved QDSSC performance. CoS_2 is also less susceptible to poisoning by the sulfide/polysulfide electrolyte, a problem that plagues platinum electrodes in this application; furthermore, CoS_2 exhibits excellent stability in sulfide/polysulfide electrolyte, resulting in highly reproducible performance.

2.2. Introduction

Quantum dot-sensitized solar cells (QDSSCs)[1–7] are promising new photovoltaic devices that could meet the requirements of third generation solar cells.[8] Specifically, quantum dots (QDs) are very attractive photon harvesters due to their high molar extinction coefficient (*e.g.*, exceeding 10^5 cm^{-1} M^{-1} at the first excitonic absorption of CdS and CdSe nanocrystals[9]) and the ability to tune their optical band gap through size control.[1,10] Furthermore, the potential to leverage nanoscale quantum mechanical effects capable of boosting solar light-to-electricity conversion efficiency, such as multiple exciton generation[11] and hot-carrier transfer,[12] grants QDs unique advantages as light absorbers. The QDSSC operates similarly to the dye-sensitized solar cell (DSSC),[13–15] with inorganic QD absorbers replacing the dye molecules that collect incident light in a DSSC. The QD sensitizer can be deposited on a wide-band-gap electron-transporting semiconductor, forming the donor–acceptor charge-separating heterojunction central to the QDSSC,[16] by proximal (or direct) adsorption[17] or chemical linking[18] of colloidal QDs, epitaxial growth,[19] electrodeposition,[20] chemical bath deposition,[21] or successive ionic layer adsorption and reaction (SILAR).[22] Among these, the SILAR method has gained popularity due

to its simplicity and, more importantly, the intimate contact between donor and acceptor that results.[23] Liquid-junction DSSCs have achieved high efficiencies using an iodide/triiodide (I^-/I_3^-)-based hole-transporting medium;[24] in QDSSCs, however, the common I^-/I_3^- electrolyte leads to photoanodic dissolution of the QD sensitizer.[15,25] On the other hand, the sulfide/polysulfide electrolyte (*i.e.*, the S^{2-}/S_n^{2-} redox couple in aqueous solution) has been shown to stabilize metal chalcogenide photoelectrochemical electrodes[26–28] and enable high solar energy conversion efficiencies in QDSSCs,[29] thereby making it the hole mediator of choice.

Despite their analogous designs, the performance of QDSSCs lags behind that of DSSCs due to inefficient charge separation and transfer at its various interfaces.[3,30] In particular, many common counter electrode (or cathode) materials, such as platinum, exhibit low electrocatalytic activity toward polysulfide reduction and result in low photocurrent density and fill factor (*FF*) in QDSSCs.[30] Moreover, sulfur species present in the sulfide/polysulfide electrolyte are known to chemisorb to platinum and further reduce its electrocatalytic activity toward polysulfide reduction,[31] which impedes electron flow through the QDSSC and promotes charge carrier recombination at the photoanode–electrolyte interface. Furthermore, the practical considerations of high materials cost and low elemental abundance discourage the use of platinum as an electrode material. The primary goal of the ongoing research into counter electrode materials for QDSSCs is to maximize the rate of polysulfide reduction at the counter electrode, which would suppress loss mechanisms elsewhere in the device. Many metal sulfides, including Cu_2S,[32] CoS,[33] and PbS[34] have been shown to surpass platinum in electrocatalytic activity toward polysulfide reduction, with Cu_2S showing the highest performance.[35] However, it has been observed that Cu_2S counter electrodes can poison the photoanode surface through both diffusion-

and field-assisted deposition of Cu_xS, resulting in gradual losses in short-circuit photocurrent density (J_{sc}), open-circuit voltage (V_{oc}), or both.[35] Furthermore, Cu_2S counter electrodes (often as sulfidized Cu or brass foils) suffer from mechanical instability, to the extent that such foils will completely disintegrate in the presence of sulfide/polysulfide electrolyte.[35] Progress has been made toward developing stable Cu_2S-based counter electrodes for QDSSCs, with reduced graphene oxide–cuprous sulfide (RGO–Cu_2S) composite counter electrodes prepared on a fluorine-doped tin oxide on glass (FTO/glass) substrate enabling high QDSSC efficiencies.[36] However, despite these advances, there exists a need for QDSSC counter electrode materials that exhibit high electrocatalytic activity, high stability, and consistent performance in sulfide/polysulfide electrolyte.

One such candidate material is cobalt pyrite (cobalt disulfide, CoS_2; cattierite), which has not been previously examined as an electrode material. We have been investigating iron pyrite (cubic β-FeS_2), an isostructural analogue of cobalt pyrite, as a promising light absorbing semiconductor for solar energy conversion.[37–39] Unlike iron pyrite, however, cobalt pyrite is a conductive metal, making it attractive for both electrode and electrocatalysis applications. For instance, CoS_2 has been previously investigated as a potential replacement for platinum in oxygen reduction electrocatalysis.[40] Furthermore, as the highest cobalt sulfide, CoS_2 benefits from the high natural abundance of its component elements, which translates to a low materials cost. In this Letter, we report the development and evaluation of a robust, high-performance CoS_2 counter electrode for QDSSCs that employ the sulfide/polysulfide electrolyte as the hole-transporting medium.

2.3. Experimental Methods

All chemicals were purchased from Sigma-Aldrich and used without further purification, unless otherwise noted. Additional experimental details can be found in Appendix 1.

2.3.1. CoS_2 Film Synthesis

A borosilicate plate glass substrate (3.3 mm thick) was first manually roughened on one side with SiC paper (Allied High Tech Products, 320 grit) for several minutes before it was ultrasonically cleaned at 100 W for 30 min in a detergent solution (Fisher Scientific, Versa-Clean, diluted 1:4 with deionized water) and then thoroughly rinsed with deionized water and ethanol. To further degrease the substrate, it was sonicated at 100 W for 10 min in ethanol and then rinsed with fresh ethanol and blown dry under a stream of nitrogen. Finally, the substrate was oxygen plasma cleaned (150 W RF, < 200 mTorr, 1 sccm O_2, 3 min) to remove any organic residues. A 5-nm thick Ti (Kurt J. Lesker Co., 99.995%) adhesion layer was then deposited on the substrate at a rate of 0.1 Å s^{-1} by *e*-beam evaporation, followed immediately by 100 nm of Co (Kurt J. Lesker Co., 99.95%) at 1 Å s^{-1}.

To synthesize the CoS_2 film, the metalized borosilicate glass substrate was transferred to the center of a fused silica tube on a home-built flow reactor equipped with both pressure and gas flow controllers. An alumina boat containing 2 g of S (99.5–100.5%) was loaded into the tube and placed at the farthest upstream position within the tube furnace. The tube was purged of air under a steady flow of Ar carrier gas at 25 sccm and 1 atm, and the furnace temperature was ramped from room temperature to 500 °C at a rate of approximately 60 °C min^{-1}. At the reaction temperature, the S precursor was evaporated upstream (T ≈ 250 °C) and carried downstream by the carrier gas where it reacted with the metal film at the hot zone of the furnace. After 1 h, all of

the S precursor had evaporated. The tube furnace was then opened to allow natural cooling of the sample back to room temperature under Ar flow. The sample of CoS_2 on borosilicate glass was then dipped in CS_2 (99.9%) for 30 s to remove any S residues, then thoroughly rinsed with ethanol and dried under a stream of nitrogen.

2.3.2. Materials Characterization

The as-synthesized CoS_2 film on borosilicate glass was characterized using a LEO SUPRA 55 VP field-emission scanning electron microscope operated at 2 kV and a Bruker D8 ADVANCE powder X-ray diffractometer using Cu Kα radiation. The PXRD pattern background (produced by the glass substrate) was fit to a cubic spline and subtracted using Jade® 5 (Materials Data, Inc.). The sheet resistance of the product and precursor films was measured using a custom Au-tip linear four-point probe and a Keithley 2400 SourceMeter.

2.3.3. Mesoscopic TiO_2 Photoanode Preparation and Sensitization by Successive Ionic Layer Adsorption and Reaction (SILAR)

The mesoscopic TiO_2 photoanodes were prepared and sensitized using published procedures[36,46,47] with minor modifications, as detailed in Appendix 1.

2.3.4. Thin-Layer Liquid-Junction QDSSC Fabrication

Prior to device fabrication, the CoS_2 counter electrode was soaked in 1 M HCl(*aq*) for > 2 min to ensure that a fresh CoS_2 surface was exposed; similarly, the Pt counter electrode was soaked in 1 M H_2SO_4(*aq*) for > 2 min to clean the Pt surface. Sandwich-style thin-layer liquid-junction QDSSCs were assembled by first placing a punched spacer (Bemis Flexible Packaging, Parafilm M) on the counter electrode (*i.e.*, CoS_2, Pt, or RGO–Cu_2S) and gently heating on a hot plate at 80 °C for 20 s to improve its adhesion to the counter electrode. Then, the counter

electrode–spacer assembly was removed from the hot plate and the punched active area was completely filled with several drops of aqueous sulfide/polysulfide electrolyte consisting of 2 M $Na_2S•9H_2O$ (≥ 99.99%) and 2 M S. The photoanode (*i.e.*, working electrode) was aligned with the punched area of the spacer and firmly pressed against the counter electrode to seal the cell. To fix the seal and prevent electrolyte leakage, two small binder clips were used to clamp the cell. The compact TiO_2 film over the FTO layer of the photoanode was removed with SiC paper, and contacts were deposited on the working and counter electrodes using Ag paint (Ted Pella, PELCO Colloidal Silver). To ensure comparable reflectivity of the different counter electrodes (and, hence, optical path length through the cell) a thin layer of reflective white paint (Sanford LP, Liquid Paper) was applied to the back of the counter electrode. Prior to characterization of the solar cells, an adhesive opaque matte black plastic mask (3M, Scotch® Super 33+ Tape) with a 1/8″ diameter aperture (defining a 0.0792 cm^2 device active area) was affixed to the glass side of the photoanode; additional strips of opaque black tape were used to mask the edges of the solar cell to limit the effects of light piping.[48]

The Pt counter electrodes were prepared by *e*-beam evaporating 10 nm of Pt (Kurt J. Lesker Co., 99.99%) at 1 Å s^{-1} onto a FTO/glass substrate (Hartford Glass Co. Inc., TEC 15, 15 Ω sq^{-1}, 2.2 mm thick) that was cleaned using the sonication and oxygen plasma cleaning procedures described above. The RGO–Cu_2S counter electrodes were prepared on FTO/glass (Pilkington North America Inc., NSG TEC A7, 7 Ω sq^{-1}, 2.2 mm thick) using the procedure of Radich *et al*.[36]

2.3.5. Electrochemical and Photoelectrochemical Characterization

All electrochemical and photoelectrochemical measurements were recorded in a two-electrode configuration using a Bio-Logic SP-200 potentiostat. A 1 kW Xe short arc lamp solar simulator (Newport Corp., Model 91191) with a AM1.5G filter was used to illuminate the QDSSCs at an intensity of 100 mW cm^{-2}, which was set prior to device characterization using a NREL-calibrated and NIST-traceable monocrystalline Si reference solar cell (Photo Emission Tech., Inc.; Model #60623). For each solar cell device, *J–V* curves were recorded between –0.2 V and 0.7 V at a scan rate of 20 mV s^{-1}, repeating the voltage scan a total of 5 times in both the forward and reverse directions to ensure stable device response.

The CoS_2 and Pt symmetrical cells were assembled using the same sandwich-style cell assembly procedure described above, using identical metallic working and counter electrodes and a Parafilm M spacer punched to give a 3/16″ diameter (0.178 cm^2) circular electrode area. Cyclic voltammetric measurements of the thin-layer symmetrical cells were performed at a scan rate of 50 mV s^{-1}, initially scanning cathodically from the open circuit potential and repeating the measurement for a total of 10 cycles. Electrochemical impedance spectroscopy was performed in potentiostatic mode at the open circuit potential, applying a sinusoidal voltage with an amplitude of 10 mV and scanning frequency from 200 kHz to 10 mHz. The EIS spectra were modeled using a simplified Randles equivalent circuit, with the fitting parameters obtained through application of the Levenberg-Marquardt minimization procedure.

2.4. Results and Discussion

Cobalt pyrite can be readily prepared in many different morphologies, including films via thermal sulfidation of cobalt foils with a sulfur precursor,[41] nanoparticles via hydrothermal synthesis,[42] and hollow spheres via solvothermal synthesis.[43] We prepared CoS_2 electrodes through the facile thermal sulfidation of a 100 nm thick cobalt film deposited over a 5-nm titanium adhesion layer on a manually roughened borosilicate glass substrate, as illustrated schematically in Scheme 2.1a. Argon carrier gas was used to transport elemental sulfur vapor to the metalized glass substrate, which was maintained at 500 °C for 1 h to ensure complete sulfidation. The opaque CoS_2 product film had a uniform, lustrous gray color and was well-adhered to the glass substrate (Figure 2.1a). Although the sulfidation synthesis can proceed normally on polished borosilicate glass, roughening the surface prior to metallization improves the adhesion of the CoS_2 product film to the substrate; similarly, CoS_2 thin films can be synthesized directly on roughened borosilicate glass with the titanium adhesion layer omitted, but we have found that the adhesion layer improves the mechanical stability of the product film in electrode applications. The sheet resistance of the as-synthesized CoS_2 film over a titanium adhesion layer was measured to be 15.7 ± 0.6 Ω sq^{-1} using the four-point probe method; for comparison, analogous CoS_2 films without the titanium adhesion layer exhibited a sheet resistance of 19.2 ± 0.3 Ω sq^{-1}, demonstrating that the contribution of the adhesion layer to the overall product film conductivity is minimal. To highlight the metallicity of the CoS_2 thin film, the sheet resistance of an unsulfidized 100-nm thick Co precursor thin film on roughened borosilicate glass was measured to be 13.1 ± 0.8 Ω sq^{-1}, which is less than 50% more conductive than the CoS_2 film directly on glass. Particularly for the CoS_2 films without the adhesion layer, it

is important to note that, because the CoS_2 film was prepared on an insulating glass substrate, this metallic conductivity results exclusively from the CoS_2 film itself. Moreover, the use of a conductive substrate, such as FTO/glass, is not necessary, as it would not substantially increase the CoS_2 film conductivity.

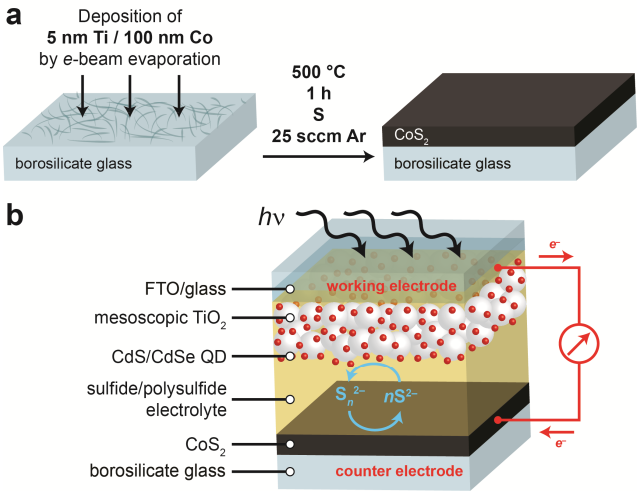

Scheme 2.1. Schematic depictions of (a) the preparation of a cobalt pyrite (CoS_2) film electrode via the thermal sulfidation of a 100 nm thick cobalt film deposited over a titanium adhesion layer on a roughened borosilicate glass substrate by electron-beam evaporation, and (b) the incorporation of an as-synthesized CoS_2 film on glass into a CdS/CdSe-sensitized thin-layer liquid-junction quantum dot-sensitized solar cell (QDSSC) filled with sulfide/polysulfide electrolyte to demonstrate the high QDSSC performance enabled by the CoS_2 counter electrode.

Scanning electron microscopy (SEM) revealed that the as-synthesized CoS_2 film consisted of nanoscale grains about 20–80 nm in diameter sintered to form a continuous polycrystalline film (Figure 2.1b). Cross-sectional SEM imaging showed that the CoS_2 film thickness was approximately 180 nm (Figure 2.1c), roughly commensurate with the volume expansion expected upon sulfidation of the cobalt precursor film. Powder X-ray diffraction (PXRD) was used to confirm the phase purity of the as-synthesized CoS_2 film (Figure 2.1d). All peaks in the PXRD pattern can be unequivocally indexed to cubic CoS_2 (JCPDS 41-1471; space group $Pa\overline{3}$, $a = 5.5376$ Å), shown structurally in the inset of Figure 2.1d. No impurity phases appear in the PXRD pattern; additionally, titanium sulfides resulting from sulfidation of the titanium adhesion layer were not detected. Therefore, we found this thermal sulfidation procedure to be a convenient method for preparing highly conductive, phase-pure CoS_2 thin films directly on glass.

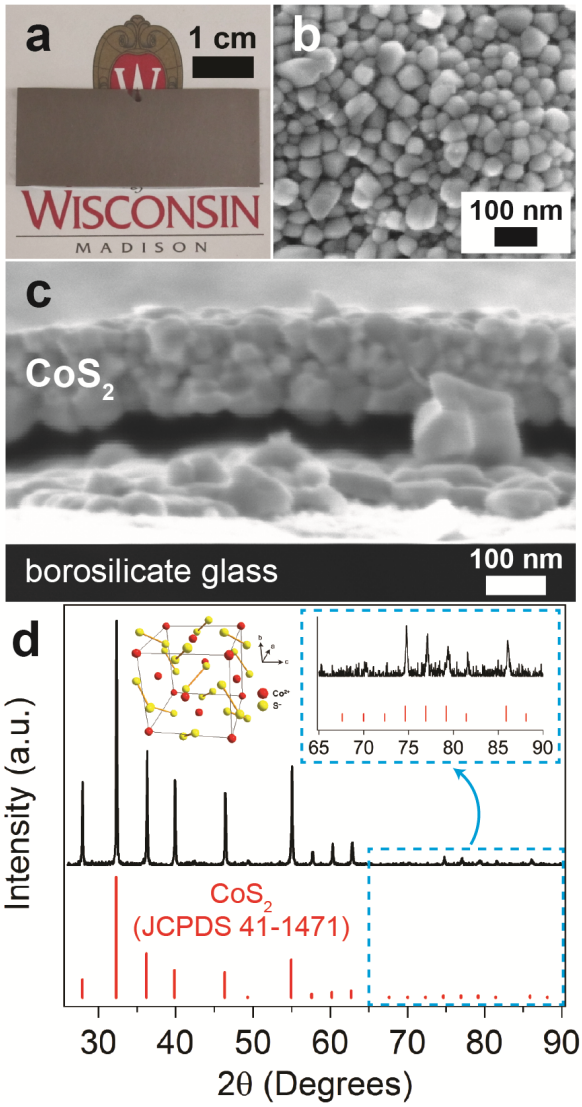

Figure 2.1. Structural characterization of the as-synthesized CoS_2 film on borosilicate glass. (a) Digital photograph showing the opaque CoS_2 film on the glass substrate. (b) SEM image depicting the small-grain polycrystalline texture of the CoS_2 film. (c) Cross-sectional SEM image of the CoS_2 film, slightly detached from the glass substrate due to sample preparation. (d) PXRD pattern of the as-synthesized CoS_2 film on glass compared with the standard pattern for

CoS_2 (JCPDS 41-1471). The high-angle portion of the pattern, highlighted by the dashed box, is magnified in the inset; the cubic pyrite crystal structure of CoS_2 is also shown in the inset.

We assembled sandwich-style thin-layer liquid-junction QDSSCs using an as-synthesized CoS_2 film on glass as the counter electrode, as depicted in Scheme 2.1b, in order to evaluate the electrochemical performance of CoS_2 in the presence of the sulfide/polysulfide electrolyte. The sulfide/polysulfide electrolyte filled into the QDSSCs consisted of 2 M S^{2-}/2 M S in aqueous solution—the optimal and, therefore, most commonly used composition[35,44,45]—and was free of methanol or other sacrificial hole scavengers that increase apparent performance but prevent fully regenerative device operation. The QDSSC photoanode was prepared by sequentially co-sensitizing a mesoscopic film of titanium dioxide (TiO_2) nanoparticles cast on an optically transparent, conductive FTO/glass substrate with CdS and CdSe QDs by the SILAR method (experimental details in Appendix 1).[22,36,46,47] After 5 SILAR cycles of CdS deposition and 8 SILAR cycles of CdSe deposition (a co-sensitization procedure recently shown to yield photoanodes with high photovoltaic solar energy conversion efficiency[46]), the CdS/CdSe sensitizer was capped with 2 SILAR cycles of ZnS deposition for enhanced photostability and decreased rate of carrier recombination.[3,5,32] The SILAR sensitization procedure resulted in greatly increased photoanode light absorption, as evidenced by the dark color of the sensitized mesoscopic TiO_2 film shown in the inset digital photograph of Figure 2.2. The sensitized photoanode was then assembled into a sandwich-style liquid-junction QDSSC with CoS_2 on glass as the counter electrode (henceforth denoted "CoS_2 CE"). To compare the performance of the CoS_2 CE to that of other counter electrode materials, QDSSCs were also assembled with platinum on FTO/glass and RGO–Cu_2S on FTO/glass counter electrodes (henceforth denoted "Pt CE" and "RGO–Cu_2S CE," respectively). The Pt CEs were prepared by depositing 10 nm of platinum onto a FTO/glass substrate by electron-beam (*e*-beam) evaporation, and the RGO–Cu_2S

CEs were prepared through the procedure of Radich *et al*.[36] The assembled QDSSCs were characterized under AM1.5G simulated solar irradiation (100 mW cm^{-2}) to assess device performance with each counter electrode material.

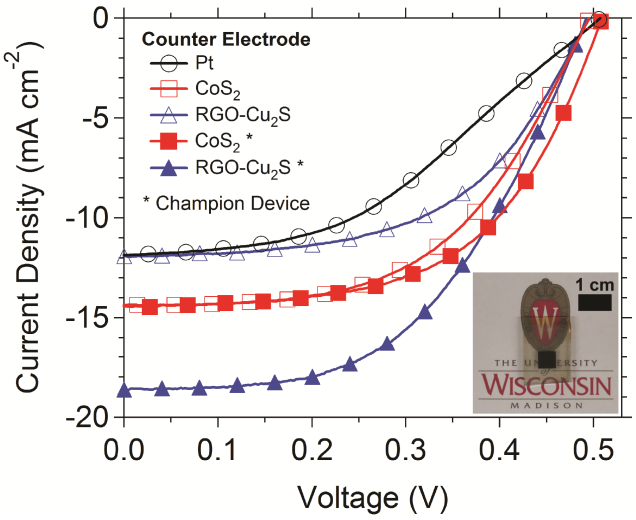

Figure 2.2. Current density–voltage (*J–V*) characterization of QDSSC devices assembled with CoS_2, Pt, and RGO–Cu_2S counter electrodes and filled with an aqueous sulfide/polysulfide (2 M S^{2-}/2 M S) electrolyte solution. The traces with open symbols were measured using a single photoanode in multiple QDSSC devices assembled with different counter electrodes, and the blue trace with filled triangles corresponds to the highest recorded champion device performance measured using a *different* photoanode and a RGO–Cu_2S counter electrode. The red trace with filled squares corresponds to the best device performance measured with a CoS_2 counter electrode among all QDSSCs tested. The inset shows a digital photograph of a typical CdS/CdSe-sensitized mesoscopic TiO_2 photoanode.

Through current density–voltage (*J–V*) characterization, we found that the CoS_2 CE outperformed the Pt CE in all of the QDSSCs measured. To make this direct comparison of CE performance, QDSSCs assembled with a CoS_2 or Pt CE were disassembled and then reassembled with the same CdS/CdSe-sensitized TiO_2 photoanode and a different counter electrode without causing significant losses in photoanode performance, as shown in Figure A1.1 (Appendix 1). The *J–V* curves of a set of representative high-performing QDSSCs fabricated using the same photoanode and CoS_2, Pt, and RGO–Cu_2S CEs are displayed in Figure 2.2 as traces with open symbols, and the photovoltaic device characteristics corresponding to these curves are summarized in Table 2.1. These data exemplify the poor electrocatalytic activity of platinum toward polysulfide reduction, as evidenced by the low J_{sc} and *FF* measured for QDSSCs using a Pt CE. In contrast, QDSSCs assembled with a CoS_2 CE exhibited consistently higher J_{sc} and *FF*, suggesting the high electrocatalytic activity of CoS_2 toward polysulfide reduction. As a result, the photovoltaic conversion efficiency (η) measured with the particular photoanode highlighted in Figure 2.2 increased from 2.53% to 3.83% when the Pt CE was replaced with a CoS_2 CE. The highest photovoltaic conversion efficiency was achieved with a different photoanode prepared using identical procedures and a RGO–Cu_2S CE (Figure 2.2, filled triangles, and Table 2.1), concordant with the very high electrocatalytic activity of Cu_2S toward polysulfide reduction; however, we found that the performance of QDSSCs using a RGO–Cu_2S CE was sometimes inconsistent, possibly due to the photoanode poisoning effects noted by Hodes *et al*.[35] On the other hand, we regularly observed that η steadily improved upon repeated *J–V* cycling when using the CoS_2 CE (Figure A1.1, Appendix 1). Highlighting the observed inconsistency of the RGO–Cu_2S CE, the conversion efficiency of the particular photoanode shown in the comparison

in Figure 2.2 was actually lower when measured with a RGO–Cu_2S CE (3.21%, open triangles) than when measured with the CoS_2 CE due to a lower J_{sc}. To illustrate the high reproducibility the CoS_2 CE, the photovoltaic device characteristics measured for many QDSSCs assembled with photoanodes from different batches and CoS_2 CEs are presented in Table A1.1 (Appendix 1) along with the conversion efficiencies measured for the same photoanodes when using a Pt CE. The highest conversion efficiency recorded with a CoS_2 CE was 4.16% (Figure 2.2, filled squares, and Table 2.1), measured for a QDSSC that had been assembled for the third time (Figure A1.1c, Appendix 1). We found an average efficiency improvement of 54 (± 14)% when replacing the Pt CE with a CoS_2 CE. Incident photon-to-electron conversion efficiency (IPCE) action spectra were measured for QDSSCs employing either a CoS_2 or Pt CE (Figure A1.2, Appendix) to confirm that this increase in η was not due to differences in the spectral response of the photoanodes. Furthermore, the J_{sc} produced by a photoanode paired with a CoS_2 CE was shown to remain constant for at least 2 h under continuous illumination, suggesting the long-term stability of the CoS_2 CE (Figure A1.3, Appendix 1). Similarly, QDSSCs assembled with the CoS_2 CE showed a rapid photocurrent response and excellent J_{sc} stability under chopped illumination (Figure A1.4, Appendix 1). Additionally, the V_{oc} of the QDSSCs rose sharply upon illumination and remained stable; when the illumination was removed, the V_{oc} decayed slowly, indicating few recombination pathways in the devices (Figure A1.5, Appendix 1).

Table 2.1. Photovoltaic Device Characteristics of Quantum Dot-Sensitized Solar Cells Measured with Different Counter Electrodes.

counter electrode	V_{oc} (V)	J_{sc} (mA cm^{-2})	*FF*	η (%)
CoS_2 [a]	0.496	14.37	0.537	3.83
Pt [a]	0.508	11.86	0.419	2.53
RGO–Cu_2S [a]	0.495	11.93	0.543	3.21
CoS_2 [b]	0.510	14.44	0.565	4.16
RGO–Cu_2S [c]	0.493	18.65	0.513	4.72

[a] Measured sequentially in the order displayed using the same CdS/CdSe-sensitized mesoscopic TiO_2 photoanode.

[b] Champion performance measured with a CoS_2 CE (with no titanium adhesion layer) in a QDSSC that had been disassembled and reassembled twice.

[c] The overall champion device shown here represents the highest performing QDSSC, which was measured with a RGO–Cu_2S CE. Note that the device parameters for this QDSSC rapidly decayed from these values upon repeated measurement of the device.

To further understand the high electrocatalytic activity and stability of CoS_2 toward polysulfide reduction relative to that of platinum, we performed cyclic voltammetry (CV) and other electrochemical studies using symmetrical sandwich-style thin-layer electrochemical cells assembled with both types of electrode and filled with 2 M S^{2-}/2 M S aqueous sulfide/polysulfide electrolyte (*i.e.*, Pt | 2 M S^{2-}(*aq*), 2 M S(*aq*) | Pt and CoS_2 | 2 M S^{2-}(*aq*), 2 M S(*aq*) | CoS_2). Figure 2.3a shows 10 complete CV cycles for both symmetrical cells. Although the cathodic and anodic current densities measured for the Pt symmetrical cell initially exceeded those for the CoS_2 symmetrical cell at high overpotential, the current density of the Pt symmetrical cell rapidly decayed upon repeated cycling to approximately half of its initial value after 10 cycles. This decay in current density is characteristic of the expected poisoning of the Pt surface by sulfur species adsorption. In contrast, the CoS_2 symmetrical cell showed perfectly reproducible cycling behavior, with no detectable decay in current density over the duration of the measurement. A plot of the tenth anodic voltage scan for each cell in Figure 2.3a at low overpotential, where the *J*–*V* response is nearly linear, clearly shows the lower polarization resistance of CoS_2 relative to Pt (Figure 2.3a, inset), suggesting the greater electrocatalytic activity of CoS_2 in sulfide/polysulfide electrolyte. If these same anodic voltage scans are plotted in the Tafel representation on a logarithmic scale versus overpotential (Figure 2.3b), the greater electrocatalytic activity of CoS_2 relative to Pt can be more clearly seen as a higher current density across the full range of applied overpotentials. Furthermore, extrapolation of the cathodic and anodic branches of each curve to the zero overpotential intercept shows that the exchange current density (J_0) is more than an order of magnitude greater for CoS_2 than for Pt, which is indicative of facile electrode kinetics for CoS_2 in sulfide/polysulfide electrolyte relative to Pt.

These trends in high stability and electrocatalytic activity for CoS_2 also hold true when diluted (0.1 M S^{2-}/0.1 M S) aqueous sulfide/polysulfide electrolyte is used (Figure A1.6, Appendix 1).

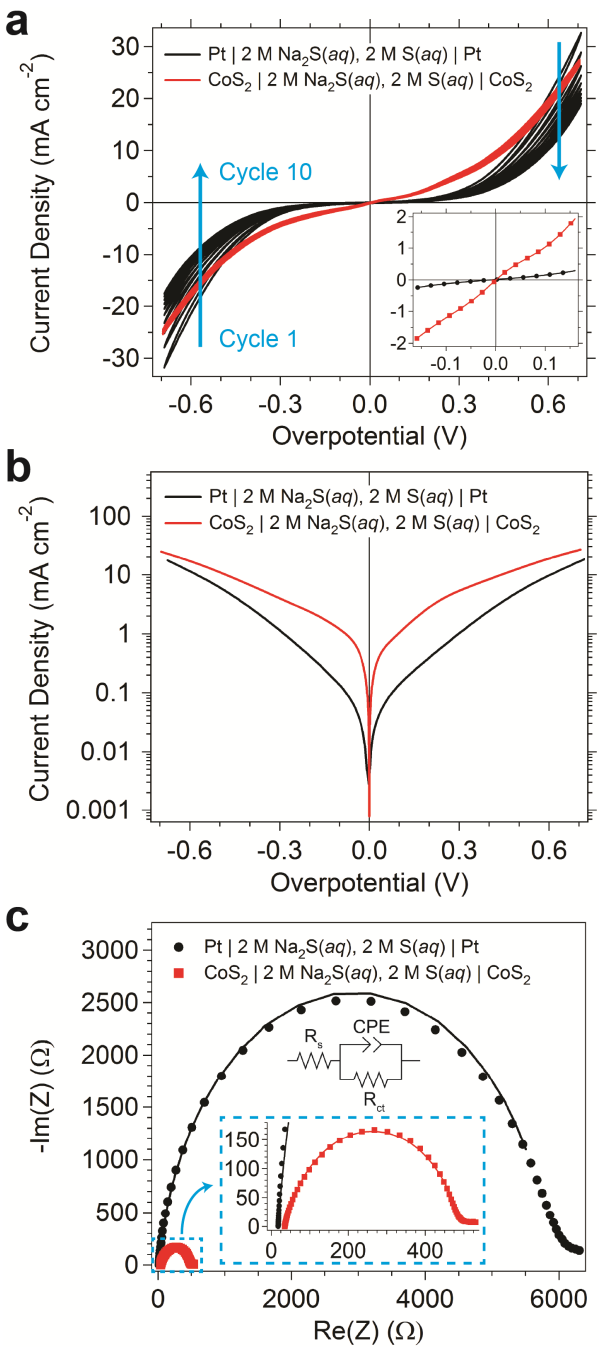

Figure 2.3. Electrochemical characterization of the CoS_2 on glass and Pt on FTO/glass electrodes in symmetrical sandwich-style thin-layer electrochemical cells filled with an aqueous sulfide/polysulfide (2 M S^{2-}/2 M S) electrolyte solution. (a) Cyclic voltammetric characterization

of the symmetrical cells for 10 complete cycles, showing the rapid deactivation of the Pt electrode surface due to sulfur species adsorption, which results in diminishing current density upon repeated cycling. The inset shows the linear (*i.e.*, low overpotential) region of the tenth anodic voltage scan for each cell, which highlights the low polarization resistance of the CoS_2 electrode relative to that of the Pt electrode, indicating the greater electrocatalytic activity of CoS_2 toward both oxidation and reduction of the sulfide/polysulfide redox couple. (b) The tenth anodic voltage scans from Figure 2.3a plotted on a logarithmic scale against applied overpotential to highlight the higher exchange current density of the CoS_2 electrode in sulfide/polysulfide electrolyte relative to that of the Pt electrode. (c) Electrochemical impedance spectra for both symmetrical cells, with that of the CoS_2 cell magnified in the inset. The inset circuit diagram shows the equivalent circuit used to fit the spectra and extract the charge-transfer resistance.

We further characterized the symmetrical thin-layer electrochemical cells using electrochemical impedance spectroscopy (EIS), as shown in Figure 2.3c. Both cells showed single-arc curves corresponding to the electrode–electrolyte interface in the Nyquist impedance plots of the EIS data. However, there is a dramatic difference in scale between the large impedances measured for the Pt cell and the much smaller impedances measured for the CoS_2 cell (magnified in the inset of Figure 2.3c). To extract the charge-transfer resistance (R_{ct}) for each electrode material from the EIS spectra, the data was modeled using the simplified Randles equivalent circuit shown as the inset of Figure 2.3c. The results of these fittings, shown as solid lines through the experimental data, yielded R_{ct} values of 521 Ω cm^2 and 40.6 Ω cm^2 for Pt and CoS_2, respectively. From these values of R_{ct}, the exchange current density (J_0) was calculated for both the Pt and CoS_2 electrodes using the Tafel equation,

$$J_0 = \frac{RT}{FR_{ct}},$$

where R is the gas constant, T is temperature, and F is the Faraday constant, to be 49.3 μA cm^{-2} and 633 μA cm^{-2}, respectively, which are roughly in agreement with the values of J_0 obtained by extrapolation of the Tafel curves shown in Figure 2.3b to the zero overpotential intercept. The fact that the R_{ct} of CoS_2 is more than an order of magnitude lower than that of Pt supports the conclusion that CoS_2 is highly electrocatalytic toward polysulfide reduction. Note that the R_{ct} for the RGO–Cu_2S CE has been reported to be 1.61 Ω cm^2 in 1 M S^{2-}/1 M S aqueous sulfide/polysulfide electrolyte,[36] still lower than that of CoS_2. This is perhaps consistent with the high reported electrocatalytic activity of Cu_2S toward the sulfide/polysulfide electrolyte and the large surface area of the RGO–Cu_2S composite, and supports the observation of high initial

QDSSC performance when using the RGO–Cu_2S CE.

2.5. Conclusions

In summary, we have shown that a CoS_2 thin film on borosilicate glass prepared by thermal sulfidation can serve as a high-performance counter electrode in a thin-layer liquid-junction QDSSC filled with sulfide/polysulfide electrolyte. When using a CoS_2 counter electrode, QDSSCs assembled with a CdS/CdSe co-sensitized mesoscopic TiO_2 film photoanode demonstrated light-to-electricity conversion efficiencies as high as 4.16%. This improved QDSSC conversion efficiency relative to that measured with a platinum counter electrode was enabled by the high electrocatalytic activity of CoS_2 toward the sulfide/polysulfide electrolyte. Furthermore, CoS_2 is not susceptible to poisoning in sulfide/polysulfide electrolyte, as is the case for platinum. Additionally, CoS_2 exhibits high reproducibility and stability in sulfide/polysulfide electrolyte. These advantages combined, CoS_2 represents a robust, high-performance, low-cost, earth-abundant counter electrode material for QDSSCs that employ the sulfide/polysulfide electrolyte.

2.6. References

(1) Kamat, P. V. Quantum Dot Solar Cells. Semiconductor Nanocrystals as Light Harvesters. *J. Phys. Chem. C* **2008**, *112*, 18737–18753.

(2) Kamat, P. V.; Tvrdy, K.; Baker, D. R.; Radich, J. G. Beyond Photovoltaics: Semiconductor Nanoarchitectures for Liquid-Junction Solar Cells. *Chem. Rev.* **2010**, *110*, 6664–6688.

(3) Kamat, P. V. Boosting the Efficiency of Quantum Dot Sensitized Solar Cells through Modulation of Interfacial Charge Transfer. *Acc. Chem. Res.* **2012**, *45*, 1906–1915.

(4) Nozik, A. J. Nanoscience and Nanostructures for Photovoltaics and Solar Fuels. *Nano Lett.* **2010**, *10*, 2735–2741.

(5) Mora-Seró, I.; Bisquert, J. Breakthroughs in the Development of Semiconductor-Sensitized Solar Cells. *J. Phys. Chem. Lett.* **2010**, *1*, 3046–3052.

(6) Nozik, A. J.; Beard, M. C.; Luther, J. M.; Law, M.; Ellingson, R. J.; Johnson, J. C. Semiconductor Quantum Dots and Quantum Dot Arrays and Applications of Multiple Exciton Generation to Third-Generation Photovoltaic Solar Cells. *Chem. Rev.* **2010**, *110*, 6873–6890.

(7) Kamat, P. V. Quantum Dot Solar Cells. *The Next Big Thing* in Photovoltaics. *J. Phys. Chem. Lett.* **2013**, *4*, 908–918.

(8) Green, M. A. *Third Generation Photovoltaics: Advanced Solar Energy Conversion*; Springer-Verlag: Berlin, 2003.

(9) Yu, W. W.; Qu, L. H.; Guo, W. Z.; Peng, X. G. Experimental Determination of the Extinction Coefficient of CdTe, CdSe, and CdS Nanocrystals. *Chem. Mater.* **2003**, *15*, 2854–2860.

(10) Alivisatos, A. P. Semiconductor Clusters, Nanocrystals, and Quantum Dots. *Science* **1996**, *271*, 933–937.

(11) Semonin, O. E.; Luther, J. M.; Choi, S.; Chen, H.-Y.; Gao, J.; Nozik, A. J.; Beard, M. C. Peak External Photocurrent Quantum Efficiency Exceeding 100% via MEG in a Quantum Dot Solar Cell. *Science* **2011**, *334*, 1530–1533.

(12) Tisdale, W. A.; Williams, K. J.; Timp, B. A.; Norris, D. J.; Aydil, E. S.; Zhu, X.-Y. Hot-Electron Transfer from Semiconductor Nanocrystals. *Science* **2010**, *328*, 1543–1547.

(13) Grätzel, M. Photoelectrochemical Cells. *Nature* **2001**, *414*, 338–344.

(14) Hagfeldt, A.; Boschloo, G.; Sun, L. C.; Kloo, L.; Pettersson, H. Dye-Sensitized Solar Cells. *Chem. Rev.* **2010**, *110*, 6595–6663.

(15) Hodes, G. Comparison of Dye- and Semiconductor-Sensitized Porous Nanocrystalline Liquid Junction Solar Cells. *J. Phys. Chem. C* **2008**, *112*, 17778–17787.

(16) Selinsky, R. S.; Ding, Q.; Faber, M. S.; Wright, J. C.; Jin, S. Quantum Dot Nanoscale Heterostructures for Solar Energy Conversion. *Chem. Soc. Rev.* **2013**, *42*, 2963–2985.

(17) Gopidas, K. R.; Bohorquez, M.; Kamat, P. V. Photophysical and Photochemical Aspects of Coupled Semiconductors. Charge-Transfer Processes in Colloidal CdS–TiO_2 and CdS–AgI Systems. *J. Phys. Chem.* **1990**, *94*, 6435–6440.

(18) Leschkies, K. S.; Divakar, R.; Basu, J.; Enache-Pommer, E.; Boercker, J. E.; Carter, C. B.; Kortshagen, U. R.; Norris, D. J.; Aydil, E. S. Photosensitization of ZnO Nanowires with CdSe Quantum Dots for Photovoltaic Devices. *Nano Lett.* **2007**, *7*, 1793–1798.

(19) Selinsky, R. S.; Shin, S.; Lukowski, M. A.; Jin, S. Epitaxial Heterostructures of Lead Selenide Quantum Dots on Hematite Nanowires. *J. Phys. Chem. Lett.* **2012**, *3*, 1649–1656.

(20) Liu, D.; Kamat, P. V. Photoelectrochemical Behavior of Thin CdSe and Coupled TiO_2/CdSe Semiconductor Films. *J. Phys. Chem.* **1993**, *97*, 10769–10773.

(21) Mane, R. S.; Lokhande, C. D. Chemical Deposition Method for Metal Chalcogenide Thin Films. *Mater. Chem. Phys.* **2000**, *65*, 1–31.

(22) Nicolau, Y. F. Solution Deposition of Thin Solid Compound Films by a Successive Ionic-Layer Adsorption and Reaction Process. *Appl. Surf. Sci.* **1985**, *22/23*, 1061–1074.

(23) Dibbell, R. S.; Watson, D. F. Distance-Dependent Electron Transfer in Tethered Assemblies of CdS Quantum Dots and TiO_2 Nanoparticles. *J. Phys. Chem. C* **2009**, *113*, 3139–3149.

(24) Boschloo, G.; Hagfeldt, A. Characteristics of the Iodide/Triiodide Redox Mediator in Dye-Sensitized Solar Cells. *Acc. Chem. Res.* **2009**, *42*, 1819–1826.

(25) Fujishima, A.; Sugiyama, E.; Honda, K. Photosensitized Electrolytic Oxidation of Iodide Ions on Cadmium Sulfide Single Crystal Electrode. *Bull. Chem. Soc. Jpn.* **1971**, *44*, 304.

(26) Miller, B.; Heller, A. Semiconductor Liquid Junction Solar Cells Based on Anodic Sulphide Films. *Nature* **1976**, *262*, 680–681.

(27) Ellis, A. B.; Kaiser, S. W.; Wrighton, M. S. Visible Light to Electrical Energy Conversion. Stable Cadmium Sulfide and Cadmium Selenide Photoelectrodes in Aqueous Electrolytes. *J. Am. Chem. Soc.* **1976**, *98*, 1635–1637.

(28) Ellis, A. B.; Kaiser, S. W.; Bolts, J. M.; Wrighton, M. S. Study of *n*-Type Semiconducting Cadmium Chalcogenide-Based Photoelectrochemical Cells Employing Polychalcogenide Electrolytes. *J. Am. Chem. Soc.* **1977**, *99*, 2839–2848.

(29) Lee, J.-W.; Son, D.-Y.; Ahn, T. K.; Shin, H.-W.; Kim, I. Y.; Hwang, S.-J.; Ko, M. J.; Sul, S.; Han, H.; Park, N.-G. Quantum-Dot-Sensitized Solar Cell with Unprecedentedly High Photocurrent. *Sci. Rep.* **2013**, *3*, DOI:10.1038/srep01050.

(30) Chakrapani, V.; Baker, D.; Kamat, P. V. Understanding the Role of the Sulfide Redox Couple (S^{2-}/S_n2-) in Quantum Dot-Sensitized Solar Cells. *J. Am. Chem. Soc.* **2011**, *133*, 9607–9615.

(31) Loučka, T. The Adsorption of Sulphur and of Simple Organic Substances on Platinum Electrodes. *J. Electroanal. Chem.* **1972**, *36*, 369–381.

(32) Giménez, S.; Mora-Seró, I.; Macor, L.; Guijarro, N.; Lana-Villarreal, T.; Gómez, R.; Diguna, L. J.; Shen, Q.; Toyoda, T.; Bisquert, J. Improving the Performance of Colloidal Quantum-Dot-Sensitized Solar Cells. *Nanotechnology* **2009**, *20*, 295204.

(33) Yang, Z. S.; Chen, C.-Y.; Liu, C.-W.; Chang, H.-T. Electrocatalytic Sulfur Electrodes for CdS/CdSe Quantum Dot-Sensitized Solar Cells. *Chem. Commun.* **2010**, *46*, 5485–5487.

(34) Tachan, Z.; Shalom, M.; Hod, I.; Rühle, S.; Tirosh, S.; Zaban, A. PbS as a Highly Catalytic Counter Electrode for Polysulfide-Based Quantum Dot Solar Cells. *J. Phys. Chem. C* **2011**, *115*, 6162–6166.

(35) Hodes, G.; Manassen, J.; Cahen, D. Electrocatalytic Electrodes for the Polysulfide Redox System. *J. Electrochem. Soc.* **1980**, *127*, 544–549.

(36) Radich, J. G.; Dwyer, R.; Kamat, P. V. Cu_2S Reduced Graphene Oxide Composite for High-Efficiency Quantum Dot Solar Cells. Overcoming the Redox Limitations of S^{2-}/S_n2- at the Counter Electrode. *J. Phys. Chem. Lett.* **2011**, *2*, 2453–2460.

(37) Ennaoui, A.; Fiechter, S.; Pettenkofer, C.; Alonso-Vante, N.; Büker, K.; Bronold, M.; Höpfner, C.; Tributsch, H. Iron Disulfide for Solar Energy Conversion. *Sol. Energy Mater. Sol. Cells* **1993**, *29*, 289–370.

(38) Cabán-Acevedo, M.; Faber, M. S.; Tan, Y. Z.; Hamers, R. J.; Jin, S. Synthesis and Properties of Semiconducting Iron Pyrite (FeS_2) Nanowires. *Nano Lett.* **2012**, *12*, 1977–1982.

(39) Cabán-Acevedo, M.; Liang, D.; Chew, K. S.; DeGrave, J. P.; Kaiser, N. S.; Jin, S. Synthesis, Characterization, and Variable Range Hopping Transport of Pyrite (FeS_2) Nanorods, Nanobelts, and Nanoplates. *ACS Nano* **2013**, *7*, 1731–1739.

(40) Jirkovský, J. S.; Björling, A.; Ahlberg, E. Reduction of Oxygen on Dispersed Nanocrystalline CoS_2. *J. Phys. Chem. C* **2012**, *116*, 24436–24444.

(41) Mrowec, S.; Danielewski, M.; Wójtowicz, A. Sulphidation of Cobalt at High Temperatures. *J. Mater. Sci.* **1998**, *33*, 2617–2628.

(42) Chen, X. H.; Fan, R. Low-Temperature Hydrothermal Synthesis of Transition Metal Dichalcogenides. *Chem. Mater.* **2001**, *13*, 802–805.

(43) Wang, Q. H.; Jiao, L. F.; Han, Y.; Du, H. M.; Peng, W. X.; Huan, Q. N.; Song, D. W.; Si, Y. C.; Wang, Y. J.; Yuan, H. T. CoS_2 Hollow Spheres: Fabrication and Their Application in Lithium-Ion Batteries. *J. Phys. Chem. C* **2011**, *115*, 8300–8304.

(44) Santra, P. K.; Nair, P. V.; Thomas, K. G.; Kamat, P. V. $CuInS_2$-Sensitized Quantum Dot Solar Cell. Electrophoretic Deposition, Excited-State Dynamics, and Photovoltaic Performance. *J. Phys. Chem. Lett.* **2013**, *4*, 722–729.

(45) Santra, P. K.; Kamat, P. V. Tandem-Layered Quantum Dot Solar Cells: Tuning the Photovoltaic Response with Luminescent Ternary Cadmium Chalcogenides. *J. Am. Chem. Soc.* **2013**, *135*, 877–885.

(46) Santra, P. K.; Kamat, P. V. Mn-Doped Quantum Dot Sensitized Solar Cells: A Strategy to Boost Efficiency over 5%. *J. Am. Chem. Soc.* **2012**, *134*, 2508–2511.

(47) Lee, H.; Wang, M. K.; Chen, P.; Gamelin, D. R.; Zakeeruddin, S. M.; Grätzel, M.; Nazeeruddin, M. K. Efficient CdSe Quantum Dot-Sensitized Solar Cells Prepared by an Improved Successive Ionic Layer Adsorption and Reaction Process. *Nano Lett.* **2009**, *9*, 4221–4227.

(48) Snaith, H. J. How Should You Measure Your Excitonic Solar Cells? *Energy Environ. Sci.* **2012**, *5*, 6513–6520.

CHAPTER 3

High-Performance Electrocatalysis Using Metallic Cobalt Pyrite (CoS_2) Micro- and Nanostructures †

3.1. Abstract

The development of efficient and robust earth-abundant electrocatalysts for the hydrogen evolution reaction (HER) is an ongoing challenge. We report metallic cobalt pyrite (cobalt disulfide, CoS_2) as one such high-activity candidate material, and demonstrate that its specific morphology—film, microwire, or nanowire, made available through controlled synthesis—plays a crucial role in determining its overall catalytic efficacy. The increase in effective electrode surface area that accompanies CoS_2 micro- and nanostructuring substantially boosts its performance, with CoS_2 nanowire electrodes achieving geometric current densities of −10 mA cm^{-2} at overpotentials as low as −145 mV vs. the reversible hydrogen electrode. Moreover, micro- and nanostructuring of the CoS_2 material has the synergistic effect of increasing its

---

† This chapter was originally published as
Faber, M. S.; Dziedzic, R.; Lukowski, M. A.; Kaiser, N. S.; Ding, Q.; Jin, S. High-Performance Electrocatalysis Using Metallic Cobalt Pyrite (CoS_2) Micro- and Nanostructures. *J. Am. Chem. Soc.* **2014**, DOI: 10.1021/ja504099w
before being adapted here.

operational stability, cyclability, and maximum achievable rate of hydrogen generation by promoting the release of evolved gas bubbles from the electrode surface. The benefits of catalyst micro- and nanostructuring are further demonstrated by the increased electrocatalytic activity of CoS_2 nanowire electrodes over planar film electrodes toward polysulfide and triiodide reduction, which suggests a straightforward way to improve the performance of quantum dot- and dye-sensitized solar cells, respectively. Extension of this micro- and nanostructuring strategy to other earth-abundant materials could similarly enable inexpensive electrocatalysts that lack the high intrinsic activity of the noble metals.

3.2. Introduction

The promise of hydrogen as a sustainable, secure, and clean alternative energy carrier that can satisfy the growing global energy demand will be realized only through its efficient, low-cost, and environmentally-friendly production.[1,2] Water electrolysis to give hydrogen fuel—preferably driven by solar energy—is a highly attractive means for meeting these requirements.[3–7] Among the many hydrogen evolution reaction (HER) electrocatalysts, noble metals such as platinum are the best,[8] but scarcity and high cost limit their applicability.[9] Identifying and developing high-performance earth-abundant substitutes for these precious metal electrocatalysts serves as one pathway toward enabling a hydrogen economy.[10–24] Expanding their anticipated scope of utility, such earth-abundant electrocatalysts may also serve as replacements for noble metals in catalyzing the electrochemical reactions central to other emerging renewable energy technologies, such as polysulfide and triiodide reduction in quantum dot-sensitized solar cells (QDSSCs)[25,26] and dye-sensitized solar cells (DSSCs),[27] respectively.

The pyrite-phase transition metal dichalcogenides (MX_2, where typically M = Fe, Co, or Ni and X = S or Se) are common minerals that have seldom been explored for electrocatalysis despite past suggestion that they could be efficient HER catalysts.[28] They are of particular interest due to their extremely low cost and expected long-term stability in both acidic and alkaline operating environments. Lately, there has been renewed activity in pyrite-phase electrocatalyst research.[23,24,29,30] When prepared as thin films on glassy carbon or as nanoparticles supported by carbon black, these pyrite-phase electrocatalysts exhibit encouraging HER activity.[23,30] This activity has been further enhanced by synthesizing nanoparticles on high surface area carbon fiber paper.[24] In particular, among these pyrite-phase transition metal dichalcogenides, cobalt pyrite (cobalt disulfide, CoS_2; cattierite) is intrinsically a conductive metal—in contrast to the semiconducting pyrites, such as nickel disulfide[31] or iron disulfide[32,33]—making it uniquely advantaged as an electrocatalyst material. Metallically conducting thin films of CoS_2 with a reported sheet resistance of 19.2 ± 0.3 Ω sq^{-1} prepared directly on insulating plate glass substrates have been previously demonstrated to be highly effective counter electrodes for QDSSCs that employ the aqueous sulfide/polysulfide redox electrolyte.[29] Similarly, CoS_2 has recently been identified as an efficient electrocatalyst for oxygen reduction.[34–36] Importantly, as a stable, intrinsically metallic mineral, CoS_2 possesses clear advantages over the more prominent layered transition metal dichalcogenide electrocatalysts, such as MoS_2[10–13] and WS_2,[16,17] that exhibit high activity toward the HER only after conversion from their thermodynamically-favored semiconducting phase to a metastable metallic polymorph.[10,12,13,16,17]

Furthermore, the performance of promising earth-abundant HER electrocatalysts could be

enhanced through nanostructuring, as recently shown for MoS_2,[10–13] amorphous MoS_x,[15] WS_2,[16,17] Ni_2P,[18] CoP,[19] and Ni–Mo alloys.[20,21] With the increasing roughness (*i.e.*, the total surface area relative to the geometric surface area) that accompanies decreasing structure size, the number of available catalytic sites is expected to increase, thereby relaxing the stringent requirements of intrinsic catalytic activity required to achieve a specified level of performance. Moreover, compared with the common high surface area nanoparticle and nanostructured film morphologies, arrays of catalytic micro- and nanowires (MWs and NWs, respectively) directly integrated with a conducting electrode could enjoy the additional advantages of further enhanced performance and improved stability by facilitating both charge carrier transport[10] and the release of evolved hydrogen gas from the electrode surface.[37] In this work, we establish CoS_2 as a high-performance, earth-abundant electrocatalyst material for the HER. We further develop facile routes for CoS_2 MW and NW growth in high density directly on graphite substrates and show their dramatically improved performance and stability (particularly for the MW electrodes) during HER electrocatalysis. The generality of these syntheses also permits the preparation of CoS_2 MWs and NWs on glass substrates and the demonstration of their increased activity toward polysulfide and triiodide reduction, which could boost QDSSC and DSSC performance, respectively, without using noble metal electrodes.

3.3. Materials and Methods

Full synthesis and characterization details appear in Appendix 2.

3.3.1. Materials Synthesis

CoS_2 Films. The CoS_2 films were synthesized on graphite and glass substrates by

electron-beam evaporating 100 nm of Co (Kurt J. Lesker, 99.95%) onto the substrate at 1 Å s^{-1} and then thermally sulfidizing the Co film.

CoS_2 Microwires. Cobalt hydroxide (β-$Co(OH)_2$) MWs were synthesized on graphite and glass substrates using a published procedure with minor modifications.[38,39] In a typical synthesis, 10 mmol of $Co(NO_3)_2$•$6H_2O$ (Sigma-Aldrich, ≥ 98%) was dissolved in 10 mL of 18.2 MΩ cm distilled water. Then, 40 mL of concentrated $NH_4OH(aq)$ solution (Sigma-Aldrich, 28.0–30.0%) was added dropwise to the stirred solution. The solution was stirred in ambient air for 30 min before adding 16 mL to a 23-mL Teflon (PTFE) autoclave liner containing the substrate. The reaction vessel was loosely covered with a watch glass and heated at 85 °C for 14 h in a ventilated forced-air convection oven. After 14 h, the substrate was removed, rinsed, and dried under a stream of nitrogen. The β-$Co(OH)_2$ MWs were then thermally sulfidized to give CoS_2 MWs.

CoS_2 Nanowires. Cobalt hydroxide carbonate hydrate ($Co(OH)(CO_3)_{0.5}$•xH_2O, "CHCH") NWs were synthesized on graphite and glass substrates by following a published procedure with minor modifications.[40] In a typical synthesis, 1.5 mmol of $Co(NO_3)_2$•$6H_2O$, 3 mmol of NH_4F (Sigma-Aldrich, ≥ 98.0%), and 7.5 mmol of $(NH_2)_2CO$ (Riedel-de Haën, 99.5–100.5%) were dissolved in 50 mL of distilled water. Then, 16 mL of this solution was transferred to a 23-mL PTFE-lined stainless steel autoclave containing the substrate, which was sealed and heated at 110 °C for 5 h. After cooling, the substrate was removed, rinsed, and dried under a stream of nitrogen. The CHCH NWs were then thermally sulfidized to give CoS_2 NWs.

Thermal Sulfidation. The as-prepared Co films, β-$Co(OH)_2$ MWs, and CHCH NWs on graphite or glass were thermally sulfidized to CoS_2 using a previously described procedure.[29]

Briefly, the substrates covered with precursor material were placed in the center of a fused silica tube on a reactor equipped with both pressure and gas flow controllers. An alumina boat containing 2 g of S powder (Sigma-Aldrich, 99.5–100.5%) was placed in the tube at the farthest upstream position within the tube furnace. The tube was purged of air and maintained at 780 Torr under a steady flow of Ar carrier gas (99.999%) at 25 sccm. The furnace temperature was ramped to 500 °C and held for 1 h. After cooling under Ar flow, the samples were rinsed with CS_2 (Sigma-Aldrich, 99.9%) and dried with nitrogen.

3.3.2. Materials Characterization

The as-prepared films, MWs, and NWs on graphite or glass were characterized using a LEO SUPRA 55 VP field-emission scanning electron microscope (SEM) operated at 2 kV and a Bruker D8 ADVANCE powder X-ray diffractometer (XRD) using Cu Kα radiation. The XRD pattern background was fit to a cubic spline and subtracted using Jade 5 (Materials Data, Inc.). Transmission electron microscopy (TEM) samples were prepared by dispersing as-prepared MWs on graphite in isopropyl alcohol by ultrasonication (100 W, 10 s) and drop casting the suspended MWs onto the lacey carbon support of a Cu grid (Ted Pella, #01890-F). High-resolution TEM images of the β-$Co(OH)_2$ and CoS_2 MWs were obtained on an aberration-corrected FEI Titan scanning transmission electron microscope operated at an accelerating voltage of 200 kV in TEM mode. Raman spectra of the as-prepared and as-measured CoS_2 film on graphite were collected on a Thermo Scientific DXR Raman microscope fitted with 532 nm excitation laser. X-ray photoelectron spectroscopy (XPS) was performed on as-synthesized and as-measured CoS_2 films on graphite using a Thermo Scientific K-Alpha XPS system with an Al Kα source.

3.3.3. Electrochemical Characterization of Catalytic Activity Toward the HER

All electrochemical measurements were performed in a three-electrode configuration using a rotating disk electrode (RDE) setup (Bioanalytical Systems, Inc.; RDE-2) and recorded using a Bio-Logic SP-200 potentiostat. Each measurement was performed in room-temperature 0.5 M $H_2SO_4(aq)$ electrolyte continuously purged with $H_2(g)$ (99.999%) using a saturated calomel reference electrode (SCE) (CH Instruments), a graphite rod (National Carbon Co., AGKSP Spectroscopic Electrode) as the counter electrode, and a graphite-supported CoS_2 film, MW array, or NW array affixed to a glassy carbon RDE tip using silver paint (Ted Pella, PELCO Colloidal Silver) as the working electrode. Linear sweep or cyclic voltammograms were measured a minimum of five times from +0.25 V to −0.45 V vs. the reversible hydrogen electrode (RHE) (+0.25 V to −0.24 V vs. RHE for film electrodes) at a scan rate of 3 mV s^{-1} in both the forward and reverse directions while rotating the working electrode at 2000 RPM, with the final sweep always used for analysis. The SCE was calibrated against the reversible hydrogen potential using platinum wire (Kurt J. Lesker, 99.99%; 0.50 mm diameter) as both the working and counter electrodes after each measurement. The Pt reference trace was recorded using a Pt wire as the working electrode. All polarization curves were corrected for background current and *IR* losses, as detailed in Appendix 2, unless otherwise noted. Electrochemical impedance spectroscopy was performed in potentiostatic mode at −0.24 V vs. RHE, applying a sinusoidal voltage with an amplitude of 10 mV and scanning frequency from 200 kHz to 50 mHz.

3.3.4. Symmetrical Cell Fabrication and Measurement

The electrochemical symmetrical cells were fabricated and characterized by following a published procedure with minor modifications.[29] The sulfide/polysulfide electrolyte consisted of

2 M $Na_2S•9H_2O$ (Sigma-Aldrich, ≥ 99.99%) and 2 M S in aqueous solution. The iodide/triiodide electrolyte consisted of 0.6 M 1-methyl-3-propylimidazolium iodide (Solaronix SA; "PMII")/0.03 M I_2 (Sigma-Aldrich, ≥ 99.8 %)/0.1 M guanidinium thiocyanate (Sigma-Aldrich, ≥ 97%; "GSCN")/0.5 M 4-*tert*-butylpyridine (Fluka, > 98%; "TBP") in 85:15 (v/v) acetonitrile (Sigma-Aldrich, anhydrous, 99.8%; "ACN"):valeronitrile (Sigma-Aldrich, 99.5%; "VN").

3.4. Results and Discussion

The different routes for preparing CoS_2 film, MW array, and NW array electrodes are summarized in Scheme 3.1. CoS_2 films are synthesized directly on graphite (or glass) substrates via thermal sulfidation of a cobalt metal precursor film, as illustrated in Scheme 3.1A. To prepare CoS_2 MWs and NWs, we first grow β-$Co(OH)_2$ MWs[38,39] or CHCH NWs[40] from solution directly on graphite (or glass) substrates, as shown schematically in Scheme 3.1B and C, respectively. Then, these intermediate structures are converted to CoS_2 with complete retention of their one-dimensional morphology. The thermal sulfidation conditions are identical in all preparations (Scheme 3.1), regardless of the intermediate material. Prior to thermal sulfidation, the β-$Co(OH)_2$ MWs and CHCH NWs can both be optionally converted to a cobalt oxide (Co_3O_4) intermediate by dehydration in air or inert atmosphere at 350 °C for 2 h, but this additional step was not found to impact the final CoS_2 MW or NW morphology or performance. The graphite disk substrate was selected as a convenient, low-cost, chemically inert, electrically conductive support that has negligible activity toward the HER and is insensitive to the harsh conditions of the thermal sulfidation. The direct growth of CoS_2 on graphite substrates ensures a low-resistance electrical contact between the substrate and the electrocatalyst to minimize *IR*

losses.[10] Note that metallically conducting CoS_2 films, MW arrays, and NW arrays can also be prepared directly on insulating glass substrates using the same synthetic procedures (Figure A2.1, Appendix 2).

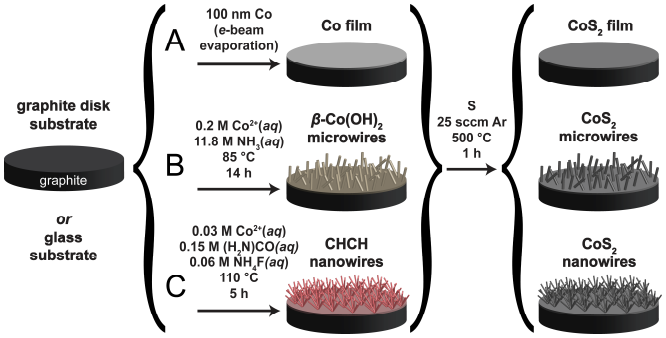

Scheme 3.1. Schematic depictions of the preparation of a cobalt pyrite (CoS_2) film, microwire (MW) array, or nanowire (NW) array on a graphite disk (or glass) substrate. (A) The CoS_2 film is synthesized via the thermal sulfidation of a 100 nm thick cobalt film deposited on the substrate by electron-beam evaporation. (B) Cobalt hydroxide (β-$Co(OH)_2$) MWs are grown directly on the substrate from aqueous solution and then thermally sulfidized to give vertically-oriented CoS_2 MWs. (C) Vertically-oriented cobalt hydroxide carbonate hydrate ($Co(OH)(CO_3)_{0.5}\bullet xH_2O$, "CHCH") NWs are grown via hydrothermal synthesis directly on the substrate and then thermally sulfidized to give CoS_2 NWs in high density. The thermal sulfidation conditions are identical in each synthesis.

Scanning electron microscopy (SEM) shows that, upon thermal sulfidation, the 100 nm thick evaporated Co film on graphite (Figure 3.1A) converts to a polycrystalline CoS_2 film with grain sizes of approximately 20–80 nm (Figure 3.1B). While this preparation yields a film that completely covers the graphite surface, large pits and imperfections in the graphite disk itself typically remain visible (Figure A2.2, Appendix 2). On the other hand, the solution synthesis of the β-$Co(OH)_2$ MWs and CHCH NWs tends to fill in these imperfections, resulting in a surface topography that is dominated by the MW or NW products (Figure 3.1C–F). In these syntheses, the early formation of a conformal particulate β-$Co(OH)_2$ or CHCH film over the graphite substrate is observed (inset cross-sectional SEM images of Figure 3.1C and E, respectively), and especially in the case of β-$Co(OH)_2$, this defective film likely seeds one-dimensional screw dislocation-driven MW or NW growth.[39,41] The intimate integration of the β-$Co(OH)_2$ and CHCH products with the graphite surface could also impart enhanced mechanical stability. The β-$Co(OH)_2$ MWs vary in diameter over approximately 5–30 μm, and their lengths generally exceed 100 μm (Figure 3.1C). The β-$Co(OH)_2$ synthesis strongly favors the formation of long, thick MWs, particularly on graphite substrates; however, we very occasionally observed the growth of shorter, thinner β-$Co(OH)_2$ MWs or NWs, which is actually the more common product morphology on glass substrates (Figure A2.1, Appendix 2). The CHCH NWs have a fairly consistent diameter of approximately 100 nm, and they densely grow in radial sea urchin-like structures with lengths around 10 μm (Figure 3.1E). The phase and phase purity of these as-synthesized intermediate products has been confirmed by XRD analysis (Figure A2.3, Appendix 2). Upon thermal sulfidation, the β-$Co(OH)_2$ MWs and CHCH NWs are fully converted to CoS_2 with retention of their one-dimensional morphology, albeit with an apparent increase in surface

roughness likely owing to grain growth (Figure 3.1D and F). High-resolution TEM further confirmed the crystallinity and phase of the as-synthesized β-$Co(OH)_2$ and CoS_2 MW products (Figure 3.1G and H, respectively). The fast Fourier transform (FFT) inset in Figure 3.1H is indexed to the [110] zone axis of CoS_2. XRD analysis of the as-prepared CoS_2 film, MW, and NW products on graphite confirms the overall phase purity of the conversion products (Figure 3.1I), with all peaks corresponding to CoS_2 (JCPDS 41-1471; space group $Pa\bar{3}$; a = 5.5376 Å) with no preferred orientation, perhaps consistent with the coarsening observed in the SEM images. Note that, in the XRD pattern for the CoS_2 MWs, reflections from graphite are not visible due to heavy product coverage on the substrate.

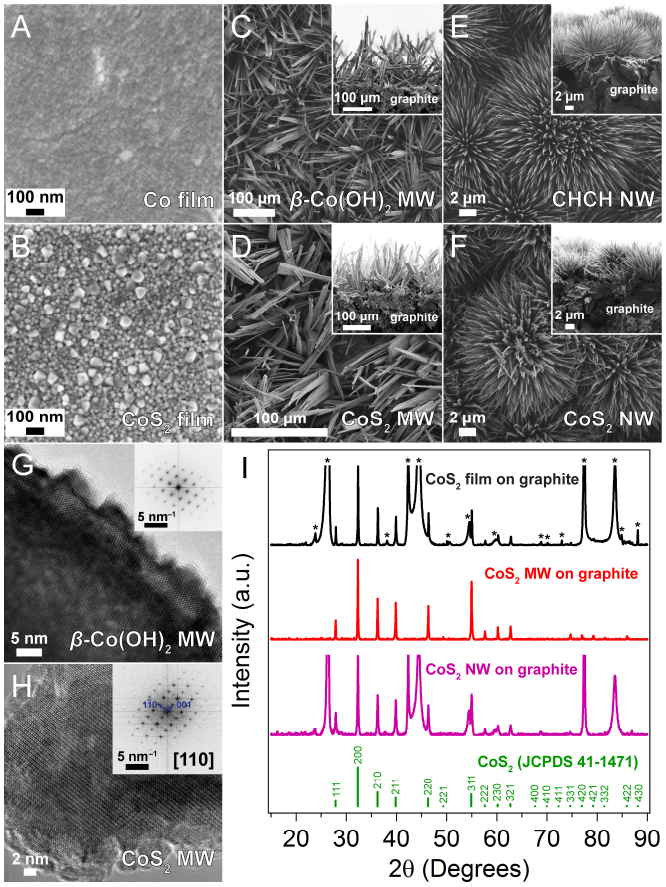

Figure 3.1. Structural characterization of an as-synthesized CoS_2 film, MW array, and NW array on graphite and their corresponding precursors. SEM images of (A) an evaporated Co film, (B) a polycrystalline CoS_2 film, (C) cobalt hydroxide (β-$Co(OH)_2$) MWs, (D) CoS_2 MWs, (E) cobalt hydroxide carbonate hydrate ($Co(OH)(CO_3)_{0.5}\bullet xH_2O$, "CHCH") NWs, and (F) CoS_2 NWs on graphite (with cross-sectional SEM images inset in the corresponding panels). High-resolution TEM images of the as-synthesized (G) β-$Co(OH)_2$ and (H) CoS_2 MW products and the corresponding fast Fourier transforms (inset) confirm their crystallinity and phase. (I) XRD patterns of the as-synthesized CoS_2 film (black trace), MW array (red trace), and NW array (violet trace) products on graphite compared with the standard pattern for CoS_2 (JCPDS 41-

1471). The high-intensity reflections from the graphite substrate are truncated and indicated by asterisks above the CoS_2 film pattern.

The direct preparation of the CoS_2 films, MWs, and NWs on graphite allows for convenient evaluation of their electrocatalytic activity toward the HER by mounting the graphite disk on the glassy carbon working electrode of a standard RDE apparatus. All measurements of HER activity were performed in 0.5 M $H_2SO_4(aq)$ electrolyte continuously purged with $H_2(g)$ and were corrected for background current and *IR* losses unless otherwise indicated (Figure A2.4, Appendix 2). The origin of the background current (which has been previously observed for pyrite-phase HER electrocatalysts[23]) is complex, but it most likely results primarily from capacitive charging of the CoS_2 surface (Appendix 2). Polarization curves showing the geometric current density (J) plotted against the applied potential appear in Figure 3.2A for representative samples of the different CoS_2 morphologies, along with that of a Pt wire standard. It is important to note that the CoS_2 film electrodes were measured over a narrowed range of applied potentials as compared to the MW and NW electrodes. This is because at elevated cathodic overpotentials (η) and high current densities, rapid $H_2(g)$ evolution damages the CoS_2 film and causes its delamination, as evidenced by SEM, XRD, and Raman analysis (Figure A2.5A–D, Appendix 2). Such CoS_2 film instability could be exacerbated by the stresses formed at the CoS_2–graphite interface during thermal sulfidation. Therefore, the high electrocatalytic performance of the CoS_2 film electrodes toward the HER cannot be maintained upon repeated cycling when applying $\eta < -0.25$ V vs. RHE (Figure A2.5E, Appendix 2) due the damage caused by the rapid evolution of $H_2(g)$ bubbles. Limiting η to permit only modest current densities, however, greatly improves the cyclability of the CoS_2 film electrodes.

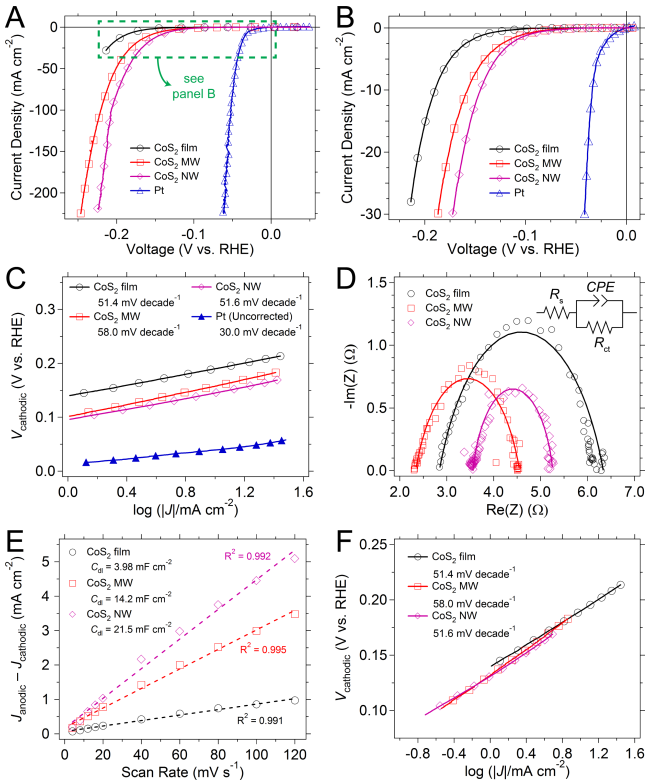

Figure 3.2. Electrochemical characterization of CoS_2 film, MW array, and NW array electrodes for HER electrocatalysis. Polarization curves at (A) higher and (B) lower applied overpotentials show the relative performance of the CoS_2 electrodes (film, open circles; MW, open squares; NW, open diamonds) in comparison to a Pt wire standard (open triangles). (C) Tafel analysis of the data presented in panels A and B. (D) Electrochemical impedance spectroscopy (EIS) Nyquist plots showing the similar series and operating charge transfer resistances of the different CoS_2 electrodes. The data was fit to the simplified Randles equivalent circuit shown in the inset, and the fitting results are shown as solid traces. (E) Plot showing the extraction of the double layer capacitance (C_{dl}) for each CoS_2 electrode. (F) Tafel data from panel C normalized by relative electrode surface area to highlight the similar intrinsic activity of the CoS_2 electrodes.

Importantly, the comparison in Figure 3.2A shows that the CoS_2 catalyst morphology clearly plays a key role in its performance, with high current densities (*i.e.*, $J_{cathodic} > 200$ mA cm^{-2}) achievable only with the MW and NW samples. Figure 3.2B highlights this comparison over a range of moderate current densities and clearly shows the trend of decreasing overpotential required to achieve a target current density with increasing surface texture, in the order of film to MWs to NWs. Specifically, the CoS_2 film sample requires an applied overpotential of −190 mV vs. RHE for significant $H_2(g)$ evolution ($J_{cathodic} = 10$ mA cm^{-2}), while the CoS_2 MW and NW array samples require only −158 mV and −145 mV vs. RHE, respectively. These low overpotentials are among the best observed for non-noble metal HER electrocatalysts.[10–12,14–24] Moreover, the different CoS_2 electrodes all have a very low onset of cathodic current at around −75 mV vs. RHE, which also compares favorably with that of other earth-abundant HER electrocatalysts.[10–12,14–24] This common onset potential suggests that, as expected for polycrystalline, phase-pure materials, there are no dramatic differences in the intrinsic activity of the different CoS_2 samples.

The Tafel slopes of the CoS_2 film, MW, and NW electrodes near the onset of substantial cathodic current are all in the approximate range of 50–60 mV $decade^{-1}$, with that of the film sample the lowest at 51.4 mV $decade^{-1}$ (Figure 3.2C). While higher than the 30.0 mV $decade^{-1}$ characteristic of Pt, these values compare quite favorably with the Tafel slopes of other recently reported high-performance earth-abundant HER electrocatalysts.[10–12,14–24] In particular, the similar Tafel slopes of the CoS_2 film, MW, and NW electrodes are roughly commensurate with a recent report on CoS_2 films, as are the geometric exchange current densities ($J_{0,geometric}$) calculated from these data (Table 3.1),[23] and again suggest that the disparity in performance is

not due to variations in the intrinsic activity of the CoS_2 materials prepared through the different synthetic routes. Similarly, electrochemical impedance spectroscopy (EIS) analysis of these electrodes under operating conditions (*i.e.*, at a cathodic bias that drives rapid hydrogen evolution) shows that the difference in their performance is likely not fully attributable to differences in the charge transfer resistance (R_{ct}) associated with $H_2(g)$ evolution (Figure 3.2D). The R_{ct} for each electrode was extracted by modeling the EIS data using a simplified Randles equivalent circuit (Figure 3.2D, inset). These fittings, shown as solid line traces through the measured data, yield geometric R_{ct} values of 0.99 Ω cm^2, 0.62 Ω cm^2, and 0.48 Ω cm^2 for the film, MW, and NW samples, respectively. Even though these R_{ct} values do follow the trend of increasing activity (Table 3.1), it is unlikely that a small variation in R_{ct} of ~0.5 Ω cm^2 fully accounts for the dramatic differences in observed performance. Additionally, the performance trend does not track with the amount of CoS_2 catalyst present, as the typical mass loading of the MW samples (25 ± 2 mg cm^{-2}) is much higher than that of the NW samples (1.7 ± 0.3 mg cm^{-2}) (Appendix 2). In an attempt to resolve this apparent discrepancy, we measured the capacitive current for the same CoS_2 samples as a function of scan rate in order to extract the double layer capacitance (C_{dl}) of each electrode (Figure 3.2E), which serves as an estimate of the effective electrochemically active surface area of the solid–liquid interface (Figure A2.6, Appendix 2). By comparing these values of C_{dl}, the increase in relative effective surface area that results from micro- or nanostructuring of the CoS_2 material can be estimated, as shown in Table 3.1. This comparison reveals that the introduction of microstructuring to the CoS_2 material more than triples the effective surface area as compared to the CoS_2 film, while nanostructuring increases the effective surface area by over five times. It is likely this huge change in effective surface area

that primarily accounts for the differences in performance, as evidenced by the fact that the current densities measured for the MW and NW samples similarly scale with their increased effective surface area over the range of low to moderate applied overpotentials. Indeed, when normalized by relative surface area, the Tafel data in Figure 3.2C are shifted such that they all fall on essentially the same Tafel line (Figure 3.2F) and yield similar normalized exchange current densities ($J_{0,\text{normalized}}$, Table 3.1), further suggesting the comparable intrinsic activity of the CoS_2 materials, regardless of synthesis pathway.

Table 3.1. Summary of the Electrochemical Properties of CoS_2 Electrodes with Different Morphologies.

sample	η (mV vs. RHE) for $J = -10$ mA cm^{-2}	R_{ct} (Ω cm^2)	Tafel slope (mV decade^{-1})	$J_{0,geometric}$ (μA cm^{-2})	C_{dl} (mF cm^{-2})	relative surface area	$J_{0,normalized}$ (μA cm^{-2})
CoS_2 film	−190	0.99	51.4	1.97	3.98	1.00	1.97
CoS_2 MW	−158	0.62	58.0	18.8	14.2	3.57	5.27
CoS_2 NW	−145	0.48	51.6	15.1	21.5	5.40	2.80

In contrast to the limited performance of the CoS_2 films toward HER electrocatalysis, the CoS_2 MW and NW electrodes can be repeatedly cycled to pass extremely high cathodic currents with no losses and, in fact, often even improvements in their performance (Figure A2.7, Appendix 2), possibly due to the removal of surface contaminants or inactive surface species upon $H_2(g)$ evolution. Furthermore, the CoS_2 MW electrodes can maintain constant $H_2(g)$ evolution at $J_{cathodic}$ = 10 mA cm^{-2} with minimal change in the applied overpotential, as shown in Figure 3.3A (red trace). Over the duration of a 41-h stability measurement, the cathodic overpotential required for the CoS_2 MW electrode to maintain $J_{cathodic}$ = 10 mA cm^{-2} was very stable, increasing by only about 20 mV. SEM images of the CoS_2 film, MW, and NW electrodes after typical electrochemical characterization (Figure 3.3B–D) were also obtained to assess possible morphological and surface changes as a result of HER electrocatalysis. No noticeable changes in the appearance of the MW electrode can be detected (Figure 3.3C). On the other hand, the corresponding overpotential for the CoS_2 film electrode rapidly increased (Figure 3.3A, black trace), with a large jump occurring within 1 h, likely caused by the delamination and physical loss of electrocatalyst material, as shown in Figure 3.3B and further illustrated in Figure A2.5 of Appendix 2. The CoS_2 NW electrodes showed improved stability relative to the film electrodes during conditions of continuous hydrogen evolution, but they eventually also suffered from the physical loss of CoS_2 material, as indicated by the sharp increase in overpotential after approximately 3 h (Figure 3.3A, violet trace). The CoS_2 NWs collapse and bundle up due to surface tension (Figure 3.3D, left), and tend to crack, break, and eventually separate from the graphite support after prolonged continuous operation (Figure 3.3D, right), leading to a drop in electrode performance after several hours. However, aside from the mechanical delamination of

the films and eventual cracking of the NW arrays, at the nanoscale, the CoS_2 materials after typical HER electrochemical testing have essentially the same appearance (Figure 3.3B, right) as the as-synthesized products (Figure 3.1), suggesting the chemical robustness of the CoS_2 electrocatalyst. To further assess the chemical stability and oxidation states of CoS_2 under HER electrocatalysis conditions, X-ray photoelectron spectroscopy (XPS) was performed on CoS_2 films on graphite before and after electrochemical characterization (Figure 3.3E and F). The positions and relative intensities of the Co 2p (Figure 3.3E) and S 2p (Figure 3.3F) peaks, which are in good agreement with previous reports,[34,42] remain essentially unchanged as a result of HER electrocatalysis, suggesting the high chemical stability of CoS_2. The satellite peaks at 780.9 and 797.8 eV in the Co 2p spectrum (Figure 3.3E), as well as the sulfate peak at 168.7 eV in the S 2p spectrum (Figure 3.3F), indicate that CoS_2 is susceptible to oxidation in air, but these oxide products are removed upon exposure to the 0.5 M $H_2SO_4(aq)$ electrolyte.

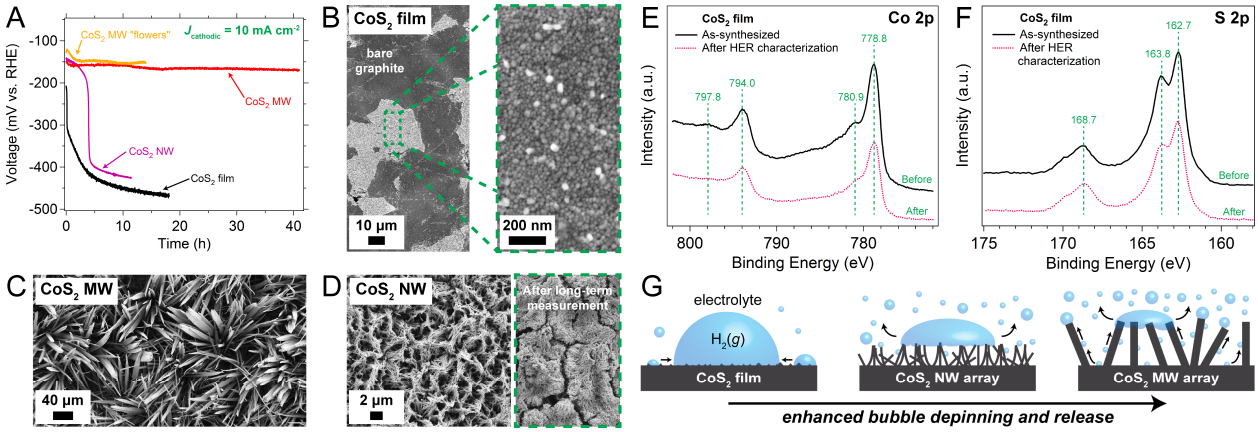

Figure 3.3. Characterization of CoS_2 stability during HER electrocatalysis and scheme illustrating enhanced hydrogen gas bubble release from CoS_2 nano- and microstructures. (A) Long-term stability measurements for representative CoS_2 film, NW, MW, and MW "flower" electrodes illustrating the greatly enhanced stability of the MW electrodes relative to the film and NW electrodes. SEM images of measured (B) CoS_2 film, (C) MW, and (D) NW electrodes. In the case of film electrodes (panel B), rapid $H_2(g)$ evolution can damage the film (left), but the remaining portions (magnified and highlighted by the dashed green box on the right) are relatively unchanged at the smaller length scale. Similarly, prolonged continuous measurement (> 3 h) of the CoS_2 NW electrodes can result in NW breakage, cracking, and overall loss of the nanostructured morphology (dashed green box on the right of panel D). X-ray photoelectron spectra of the (E) Co 2p and (F) S 2p regions for as-synthesized (upper black traces) and electrochemically characterized (lower magenta traces) CoS_2 film electrodes. (G) Schematic depictions of CoS_2 NWs and MWs bursting the larger $H_2(g)$ bubbles that commonly pin at the CoS_2 film surface, with the MWs most effectively wicking the evolved bubbles and maintaining the solid–liquid interface.

We believe that both the enhanced catalytic performance and stability when passing high current densities derive from the micro- or nanostructuring of the CoS_2 material. This is because when the production of $H_2(g)$ bubbles is vigorous ($J_{cathodic}$ > 10 mA cm^{-2}), the MWs and, to a lesser degree, NWs are superior in facilitating bubble convection away from the electrode surface (Figure 3.3G). Such behavior prevents the $H_2(g)$ bubbles from accumulating and damaging the catalyst, as commonly occurs for the CoS_2 films (Figure A2.5, Appendix 2, and earlier discussion), enabling the improved cyclability and long-term stability of the MW and NW electrodes. The improved integration of the MW and NW products with the graphite support may also contribute to their increased stability. Furthermore, for the CoS_2 films, large bubbles commonly pin at the electrode surface, reducing the effective electrode surface area;[37] on the other hand, we found that the CoS_2 NWs and, in particular, MWs tend to burst these larger bubbles and wick them away from the electrode surface (Figure 3.3G), much like air bubbles at the microstructured surface of a lotus leaf.[43] Still photographs of a CoS_2 MW electrode operating at $J_{cathodic}$ > 200 mA cm^{-2} reveal the efficiency with which the MWs suppress $H_2(g)$ bubble pinning, resulting in an electrolyte solution that is effectively turbid with numerous small bubbles cast off of the MW electrode (Figure A2.8, Appendix 2). Consistent with air bubble behavior at micro- and nanostructured silicon surfaces,[43] we have observed that the CoS_2 MW electrodes are most effective in promoting gas bubble release. Most importantly, conveyance of the $H_2(g)$ bubbles away from the electrode surface maintains the integrity of the solid–liquid interface necessary for HER electrocatalysis,[37] which, in addition to the concomitant increase in surface area that accompanies micro- and nanostructuring, may also be responsible for the improved performance of the MW and NW electrodes. In contrast, nanoparticulate or

mesoporous electrocatalyst films can also enable increased effective electrode surface area, but they lack a mechanism to promote gas bubble release, which could result in mechanical instability and decreased performance at high current densities, as has been observed for the CoS_2 film electrodes.

The synergistic effects of a large electrode surface area and a microstructured morphology to promote $H_2(g)$ bubble release is best demonstrated by the hierarchical CoS_2 MW "flower" samples that we sometimes obtained on graphite via the β-$Co(OH)_2$ MW synthesis route (Figure 3.4A and additional details in Appendix 2). For such a morphology, a high effective electrode surface area leads to high performance ($\eta = -147$ mV vs. RHE for $J_{cathodic} = 10$ mA cm^{-2}, which is comparable with the best CoS_2 NW samples), while the MW structures lead to rapid bubble bursting and release from the electrode surface, enabling very high current densities (Figure 3.4B) and good long-term stability (Figure 3.3A, orange trace). The uncorrected data in Figure 3.4B (filled squares) show that cathodic current densities in excess of 300 mA cm^{-2} can be achieved for $\eta_{uncorrected} < -420$ mV vs. RHE, which is practically valuable for the rapid electrocatalytic generation of pure $H_2(g)$. The magnified view of these data in Figure 3.4C highlights the fact that deviation from the equilibrium potential can result in substantial background current for such high surface area electrodes, and that proper treatment of this background is necessary for fair and honest representation of electrode performance (Figure A2.4, Appendix 2). The EIS data (Figure 3.4D) show that the operational R_{ct} of this very high performing CoS_2 MW "flower" sample (0.40 Ω cm^2) is consistent with that of the representative CoS_2 film, MW, and NW samples shown in Figure 3.2D, suggesting that the high overall performance is indeed due to its unique hierarchical morphology.

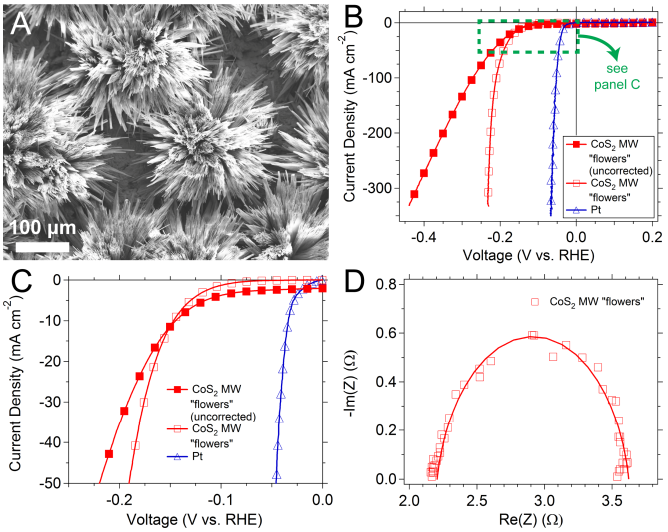

Figure 3.4. Electrochemical characterization of a hierarchical CoS_2 MW "flower" sample that exhibits high overall catalytic performance toward the HER. (A) SEM image of the CoS_2 MW "flower" electrode. Polarization curves over (B) wider and (C) narrower ranges of applied overpotentials show the high activity of the CoS_2 MW "flower" electrode. (D) Nyquist plot showing the low series and charge transfer resistances of the CoS_2 MW "flower" electrode, with the solid line trace indicating the result of fitting the experimental data to the simplified Randles equivalent circuit inset in Figure 3.2D.

The significant improvement in the HER catalytic activity of CoS_2 that can be achieved through micro- and nanostructuring suggests that increases in effective surface area could similarly improve CoS_2 as an electrocatalyst for other applications. The convenience with which metallically conducting CoS_2 films, MWs, and NWs can be prepared on glass substrates (Figures 1 and S1, Appendix 2) allows for their facile incorporation into sandwich-style thin-layer liquid-junction solar cells, such as QDSSCs and DSSCs, as the counter electrode. It has recently been shown that CoS_2 films on glass exhibit higher electrocatalytic activity toward polysulfide reduction than Pt films on fluorine-doped tin oxide/glass (FTO/glass) in QDSSCs, enabling improved device performance and stability.[29] Increasing the effective counter electrode surface area through nanostructuring could serve as one pathway for further improving device performance. Figure 3.5A compares cyclic voltammetry (CV) measurements for sandwich-style thin-layer liquid-junction symmetrical cells assembled with either CoS_2 film or NW electrodes (on glass) and filled with the 2 M $Na_2S(aq)$/2 M $S(aq)$ sulfide/polysulfide redox electrolyte most commonly used in liquid-junction QDSSCs. The CoS_2 NW electrodes enable vastly increased current densities, and slight shifts in the equilibrium potential even in this highly concentrated electrolyte indicate facile electrode kinetics toward the sulfide/polysulfide redox couple. Additionally, the CoS_2 NW electrodes show good cyclability in the sulfide/polysulfide electrolyte, which suggests long-term stability. The Nyquist impedance plots of these symmetrical cells (Figure 3.5B) reveal that the CoS_2 NW electrodes exhibit a substantially reduced R_{ct} of 1.72 Ω cm^2 as compared to that of the CoS_2 film electrodes (21.7 Ω cm^2), which is competitive with the 1.61 Ω cm^2 reported for state-of-the-art, high-performance reduced graphene oxide–Cu_2S QDSSC counter electrodes.[44] Interestingly, the CoS_2 NW electrodes also

show a lower series resistance (R_s) than the CoS_2 film electrodes (3.74 Ω and 25.3 Ω, respectively), likely owing to the thick conductive CoS_2 film that forms below the NW array (Figure A2.1, Appendix 2).

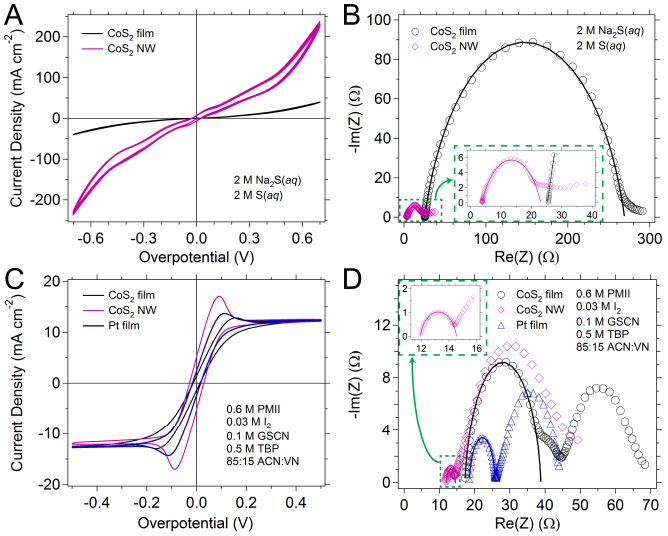

Figure 3.5. Electrochemical characterization of the activity of CoS_2 film and NW electrodes (on glass) in sandwich-style thin-layer liquid-junction symmetrical cells filled with either (A, B) sulfide/polysulfide or (C, D) iodide/triiodide redox electrolyte. Symmetrical cells were fabricated in parallel using CoS_2 film (black traces and open circle markers) or CoS_2 NW (violet traces and open diamond markers) electrodes (both on glass), and, in the case of the iodide/triiodide symmetrical cells, Pt film on FTO/glass electrodes (blue traces and open triangle markers). The cyclic voltammograms in panel A show ten complete cycles for each cell, while those in panel C show only the tenth cycle for improved clarity. The main arc of each electrochemical impedance spectrum shown in panels B and D (corresponding to the electrode–electrolyte interface) was fit to the simplified Randles equivalent circuit shown in the inset of Figure 3.2D, with the results of these fittings indicated as solid traces. The main arc of the CoS_2 NW electrode data, highlighted by a dashed box, is magnified in the insets of panels B and D.

Interestingly, we also found metallic CoS_2 to be a highly active electrocatalyst for triiodide reduction, and that its performance can be further enhanced by electrode nanostructuring. To our knowledge, CoS_2 has not been explored as a catalyst for triiodide reduction in DSSCs, even though other cobalt sulfide phases[45-47] and pyrites[48] have been shown to be reasonably effective. The CV characterization of symmetrical cells filled with iodide/triiodide electrolyte shown in Figure 3.5C reveals that CoS_2 film electrodes do catalyze triiodide reduction, but their performance lags behind that of the Pt on FTO/glass electrodes commonly employed in DSSCs, as indicated by their higher polarization resistance at low overpotential and lower peak current density. The CoS_2 NW electrodes, however, actually surpass the performance of the Pt electrodes, achieving both a lower polarization resistance and higher peak current density. Note that only the tenth CV cycle is shown for each symmetrical cell in Figure 3.5C for enhanced clarity, but the performance of the CoS_2 electrodes actually increases upon repeated cycling, suggesting high stability in the iodide/triiodide electrolyte (Figure A2.9, Appendix 2). Furthermore, the EIS Nyquist impedance plots for these symmetrical cells support this performance trend, with the R_{ct} of the CoS_2 NW electrodes (0.232 Ω cm^2) substantially lower than that of the Pt/FTO/glass (0.650 Ω cm^2) and CoS_2 film (1.92 Ω cm^2) electrodes (Figure 3.5D). Again, the CoS_2 NW on glass electrodes exhibit a lower R_s (11.9 Ω) than the CoS_2 film on glass (17.3 Ω) and Pt/FTO/glass electrodes (18.6 Ω) due to the thick conductive CoS_2 layer that forms below the NW array. These electrochemical measurements suggest that not only is CoS_2 a promising replacement for Pt as the cathode material in DSSCs, reducing device cost while maintaining performance, but also that nanostructuring of the CoS_2 counter electrode may enable improved performance.

3.5. Conclusions

In summary, we have shown that metallic CoS_2 catalyzes the HER, polysulfide reduction, and triiodide reduction with high efficiency. Further, micro- and nanostructuring of CoS_2 significantly increases its catalytic performance in a synergistic manner: the effective electrode surface area is increased, enabling high current densities at low cathodic overpotentials; simultaneously, micro- and nanostructures facilitate the release of hydrogen gas bubbles from the electrode surface, promoting mechanical stability of the catalyst. Realization of optimized CoS_2 micro- and nanostructuring yields robust electrodes capable of continuously sustaining very high current densities for HER without causing catalyst degradation. These concepts have been further extended to the use of CoS_2 as the catalytic counter electrode material for polysulfide reduction in QDSSCs and triiodide reduction in DSSCs, where nanostructuring of the CoS_2 electrode drastically improves its activity. This has the potential to substantially increase the performance of both QDSSCs and DSSCs while simultaneously eliminating their reliance on precious platinum, increasing their viability as emerging technologies. This work establishes CoS_2 as a general high-performance electrocatalyst for the reduction reactions central to several renewable energy applications, and demonstrates the effective strategies of micro- and nanostructuring for improving earth-abundant catalyst materials that may not have the high intrinsic activity of the noble metals.

3.6. References

(1) Lewis, N. S.; Nocera, D. G. Powering the planet: Chemical challenges in solar energy utilization. *Proc. Natl. Acad. Sci. U.S.A.* **2006**, *103*, 15729–15735.

(2) Turner, J. A. Sustainable Hydrogen Production. *Science* **2004**, *305*, 972–974.

(3) Gray, H. B. Powering the planet with solar fuel. *Nature Chem.* **2009**, *1*, 7–7.

(4) Walter, M. G.; Warren, E. L.; McKone, J. R.; Boettcher, S. W.; Mi, Q.; Santori, E. A.; Lewis, N. S. Solar Water Splitting Cells. *Chem. Rev.* **2010**, *110*, 6446–6473.

(5) Cook, T. R.; Dogutan, D. K.; Reece, S. Y.; Surendranath, Y.; Teets, T. S.; Nocera, D. G. Solar Energy Supply and Storage for the Legacy and Nonlegacy Worlds. *Chem. Rev.* **2010**, *110*, 6474–6502.

(6) Nocera, D. G. The Artificial Leaf. *Acc. Chem. Res.* **2012**, *45*, 767–776.

(7) McKone, J. R.; Lewis, N. S.; Gray, H. B. Will Solar-Driven Water-Splitting Devices See the Light of Day? *Chem. Mater.* **2014**, *26*, 407–414.

(8) Nørskov, J. K.; Bligaard, T.; Logadottir, A.; Kitchin, J. R.; Chen, J. G.; Pandelov, S.; Stimming, U. Trends in the Exchange Current for Hydrogen Evolution. *J. Electrochem. Soc.* **2005**, *152*, J23–J26.

(9) Vesborg, P. C. K.; Jaramillo, T. F. Addressing the terawatt challenge: scalability in the supply of chemical elements for renewable energy. *RSC Adv.* **2012**, *2*, 7933–7947.

(10) Lukowski, M. A.; Daniel, A. S.; Meng, F.; Forticaux, A.; Li, L.; Jin, S. Enhanced Hydrogen Evolution Catalysis from Chemically Exfoliated Metallic MoS_2 Nanosheets. *J. Am. Chem. Soc.* **2013**, *135*, 10274–10277.

(11) Kibsgaard, J.; Chen, Z.; Reinecke, B. N.; Jaramillo, T. F. Engineering the surface structure of MoS_2 to preferentially expose active edge sites for electrocatalysis. *Nature Mater.* **2012**, *11*, 963–969.

(12) Wang, H. T.; Lu, Z. Y.; Xu, S. C.; Kong, D. S.; Cha, J. J.; Zheng, G. Y.; Hsu, P.-C.; Yan, K.; Bradshaw, D.; Prinz, F. B.; Cui, Y. Electrochemical tuning of vertically aligned MoS_2 nanofilms and its application in improving hydrogen evolution reaction. *Proc. Natl. Acad. Sci. U.S.A.* **2013**, *110*, 19701–19706.

(13) Ding, Q.; Meng, F.; English, C. R.; Cabán-Acevedo, M.; Shearer, M. J.; Liang, D.; Daniel, A. S.; Hamers, R. J.; Jin, S. Efficient Photoelectrochemical Hydrogen Generation Using Heterostructures of Si and Chemically Exfoliated Metallic MoS_2. *J. Am. Chem. Soc.*, DOI: 10.1021/ja5025673.

(14) Merki, D.; Fierro, S.; Vrubel, H.; Hu, X. Amorphous molybdenum sulfide films as catalysts for electrochemical hydrogen production in water. *Chem. Sci.* **2011**, *2*, 1262–1267.

(15) Benck, J. D.; Chen, Z. B.; Kuritzky, L. Y.; Forman, A. J.; Jaramillo, T. F. Amorphous Molybdenum Sulfide Catalysts for Electrochemical Hydrogen Production: Insights into the Origin of their Catalytic Activity. *ACS Catal.* **2012**, *2*, 1916–1923.

(16) Voiry, D.; Yamaguchi, H.; Li, J.; Silva, R.; Alves, D. C. B.; Fujita, T.; Chen, M.; Asefa, T.; Shenoy, V. B.; Eda, G.; Chhowalla, M. Enhanced catalytic activity in strained chemically exfoliated WS_2 nanosheets for hydrogen evolution. *Nature Mater.* **2013**, *12*, 850–855.

(17) Lukowski, M. A.; Daniel, A. S.; English, C. R.; Meng, F.; Forticaux, A.; Hamers, R. J.; Jin, S. Highly Active Hydrogen Evolution Catalysis from Metallic WS_2 Nanosheets. *Energy Environ. Sci.*, DOI: 10.1039/C1034EE01329H.

(18) Popczun, E. J.; McKone, J. R.; Read, C. G.; Biacchi, A. J.; Wiltrout, A. M.; Lewis, N. S.; Schaak, R. E. Nanostructured Nickel Phosphide as an Electrocatalyst for the Hydrogen Evolution Reaction. *J. Am. Chem. Soc.* **2013**, *135*, 9267–9270.

(19) Popczun, E. J.; Read, C. G.; Roske, C. W.; Lewis, N. S.; Schaak, R. E. Highly Active Electrocatalysis of the Hydrogen Evolution Reaction by Cobalt Phosphide Nanoparticles. *Angew. Chem. Int. Ed.* **2014**, *53*, 5427–5430.

(20) McKone, J. R.; Warren, E. L.; Bierman, M. J.; Boettcher, S. W.; Brunschwig, B. S.; Lewis, N. S.; Gray, H. B. Evaluation of Pt, Ni, and Ni–Mo electrocatalysts for hydrogen evolution on crystalline Si electrodes. *Energy Environ. Sci.* **2011**, *4*, 3573–3583.

(21) McKone, J. R.; Sadtler, B. F.; Werlang, C. A.; Lewis, N. S.; Gray, H. B. Ni–Mo Nanopowders for Efficient Electrochemical Hydrogen Evolution. *ACS Catal.* **2013**, *3*, 166–169.

(22) Sun, Y.; Liu, C.; Grauer, D. C.; Yano, J.; Long, J. R.; Yang, P.; Chang, C. J. Electrodeposited Cobalt-Sulfide Catalyst for Electrochemical and Photoelectrochemical Hydrogen Generation from Water. *J. Am. Chem. Soc.* **2013**, *135*, 17699–17702.

(23) Kong, D. S.; Cha, J. J.; Wang, H. T.; Lee, H. R.; Cui, Y. First-row transition metal dichalcogenide catalysts for hydrogen evolution reaction. *Energy Environ. Sci.* **2013**, *6*, 3553–3558.

(24) Kong, D. S.; Wang, H. T.; Lu, Z. Y.; Cui, Y. $CoSe_2$ Nanoparticles Grown on Carbon Fiber Paper: An Efficient and Stable Electrocatalyst for Hydrogen Evolution Reaction. *J. Am. Chem. Soc.* **2014**, *136*, 4897–4900.

(25) Kamat, P. V. Quantum Dot Solar Cells. *The Next Big Thing* in Photovoltaics. *J. Phys. Chem. Lett.* **2013**, *4*, 908–918.

(26) Selinsky, R. S.; Ding, Q.; Faber, M. S.; Wright, J. C.; Jin, S. Quantum dot nanoscale heterostructures for solar energy conversion. *Chem. Soc. Rev.* **2013**, *42*, 2963–2985.

(27) Hagfeldt, A.; Boschloo, G.; Sun, L. C.; Kloo, L.; Pettersson, H. Dye-Sensitized Solar Cells. *Chem. Rev.* **2010**, *110*, 6595–6663.

(28) Jaegermann, W.; Tributsch, H. Interfacial Properties of Semiconducting Transition Metal Chalcogenides. *Prog. Surf. Sci.* **1988**, *29*, 1–167.

(29) Faber, M. S.; Park, K.; Cabán-Acevedo, M.; Santra, P. K.; Jin, S. Earth-Abundant Cobalt Pyrite (CoS_2) Thin Film on Glass as a Robust, High-Performance Counter Electrode for Quantum Dot-Sensitized Solar Cells. *J. Phys. Chem. Lett.* **2013**, *4*, 1843–1849.

(30) Ivanovskaya, A.; Singh, N.; Liu, R.-F.; Kreutzer, H.; Baltrusaitis, J.; Nguyen, T. V.; Metiu, H.; McFarland, E. Transition Metal Sulfide Hydrogen Evolution Catalysts for Hydrobromic Acid Electrolysis. *Langmuir* **2013**, *29*, 480–492.

(31) Thio, T.; Bennett, J. W. Hall effect and conductivity in pyrite NiS_2. *Phys. Rev. B* **1994**, *50*, 10574–10577.

(32) Cabán-Acevedo, M.; Faber, M. S.; Tan, Y. Z.; Hamers, R. J.; Jin, S. Synthesis and Properties of Semiconducting Iron Pyrite (FeS_2) Nanowires. *Nano Lett.* **2012**, *12*, 1977–1982.

(33) Cabán-Acevedo, M.; Liang, D.; Chew, K. S.; DeGrave, J. P.; Kaiser, N. S.; Jin, S. Synthesis, Characterization, and Variable Range Hopping Transport of Pyrite (FeS_2) Nanorods, Nanobelts, and Nanoplates. *ACS Nano* **2013**, *7*, 1731–1739.

(34) Zhu, L.; Susac, D.; Teo, M.; Wong, K. C.; Wong, P. C.; Parsons, R. R.; Bizzotto, D.; Mitchell, K. A. R.; Campbell, S. A. Investigation of CoS_2-based thin films as model catalysts for the oxygen reduction reaction. *J. Catal.* **2008**, *258*, 235–242.

(35) Jirkovský, J. S.; Björling, A.; Ahlberg, E. Reduction of Oxygen on Dispersed Nanocrystalline CoS_2. *J. Phys. Chem. C* **2012**, *116*, 24436–24444.

(36) Zhao, C.; Li, D. Q.; Feng, Y. J. Size-controlled hydrothermal synthesis and high electrocatalytic performance of CoS_2 nanocatalysts as non-precious metal cathode materials for fuel cells. *J. Mater. Chem. A* **2013**, *1*, 5741–5746.

(37) Harrison, J. A.; Kuhn, A. T. The Role of Gas Bubble Formation in the Electrocatalysis of the Hydrogen Evolution Reaction. *Surf. Technol.* **1983**, *19*, 249–259.

(38) Li, Y.; Tan, B.; Wu, Y. Freestanding Mesoporous Quasi-Single-Crystalline Co_3O_4 Nanowire Arrays. *J. Am. Chem. Soc.* **2006**, *128*, 14258–14259.

(39) Li, Y.; Wu, Y. Critical Role of Screw Dislocation in the Growth of $Co(OH)_2$ Nanowires as Intermediates for Co_3O_4 Nanowire Growth. *Chem. Mater.* **2010**, *22*, 5537–5542.

(40) Xia, X. H.; Chao, D. L.; Qi, X. Y.; Xiong, Q. Q.; Zhang, Y. Q.; Tu, J. P.; Zhang, H.; Fan, H. J. Controllable Growth of Conducting Polymers Shell for Constructing High-Quality Organic/Inorganic Core/Shell Nanostructures and Their Optical-Electrochemical Properties. *Nano Lett.* **2013**, *13*, 4562–4568.

(41) Meng, F.; Morin, S. A.; Forticaux, A.; Jin, S. Screw Dislocation Driven Growth of Nanomaterials. *Acc. Chem. Res.* **2013**, *46*, 1616–1626.

(42) van der Heide, H.; Hemmel, R.; van Bruggen, C. F.; Haas, C. X-Ray Photoelectron Spectra of *3d* Transition Metal Pyrites. *J. Solid State Chem.* **1980**, *33*, 17–25.

(43) Wang, J. M.; Zheng, Y. M.; Nie, F.-Q.; Zhai, J.; Jiang, L. Air Bubble Bursting Effect of Lotus Leaf. *Langmuir* **2009**, *25*, 14129–14134.

(44) Radich, J. G.; Dwyer, R.; Kamat, P. V. Cu_2S Reduced Graphene Oxide Composite for High-Efficiency Quantum Dot Solar Cells. Overcoming the Redox Limitations of S^{2-}/S_n^{2-} at the Counter Electrode. *J. Phys. Chem. Lett.* **2011**, *2*, 2453–2460.

(45) Wang, M. K.; Anghel, A. M.; Marsan, B.; Ha, N.-L. C.; Pootrakulchote, N.; Zakeeruddin, S. M.; Grätzel, M. CoS Supersedes Pt as Efficient Electrocatalyst for Triiodide Reduction in Dye-Sensitized Solar Cells. *J. Am. Chem. Soc.* **2009**, *131*, 15976–15977.

(46) Kung, C.-W.; Chen, H.-W.; Lin, C.-Y.; Huang, K.-C.; Vittal, R.; Ho, K.-C. CoS Acicular Nanorod Arrays for the Counter Electrode of an Efficient Dye-Sensitized Solar Cell. *ACS Nano* **2012**, *6*, 7016–7025.

(47) Chang, S.-H.; Lu, M.-D.; Tung, Y.-L.; Tuan, H.-Y. Gram-Scale Synthesis of Catalytic Co_9S_8 Nanocrystal Ink as a Cathode Material for Spray-Deposited, Large-Area Dye-Sensitized Solar Cells. *ACS Nano* **2013**, *7*, 9443–9451.

(48) Huang, Q.-H.; Ling, T.; Qiao, S.-Z.; Du, X.-W. Pyrite nanorod arrays as an efficient counter electrode for dye-sensitized solar cells. *J. Mater. Chem. A* **2013**, *1*, 11828–11833.

CHAPTER 4

Earth-Abundant Metal Pyrites (FeS_2, CoS_2, NiS_2, and Their Alloys) for Highly Efficient Hydrogen Evolution and Polysulfide Reduction Electrocatalysis †

4.1. Abstract

Many materials have been explored as potential hydrogen evolution reaction (HER) electrocatalysts to generate clean hydrogen fuel via water electrolysis, but none so far compete with the highly efficient and stable—but cost prohibitive—noble metals. Similarly, noble metals often excel as electrocatalytic counter electrode materials in regenerative liquid-junction photoelectrochemical solar cells, such as quantum dot-sensitized solar cells (QDSSCs) that employ the sulfide/polysulfide redox electrolyte as the hole mediator. Here, we systematically investigate thin films of the earth-abundant pyrite-phase transition metal disulfides (FeS_2, CoS_2, NiS_2, and their alloys) as promising alternative electrocatalysts for both the HER and polysulfide

† This chapter was prepared in collaboration with M. A. Lukowski, N. S. Kaiser, Q. Ding, and S. Jin and submitted for publication before being adapted here.

reduction. Their electrocatalytic activity toward the HER is correlated to their composition and morphology. The emergent trends in their performance suggest that cobalt plays an important role in facilitating the HER, with CoS_2 exhibiting highest overall performance. Additionally, we demonstrate the high activity of the transition metal pyrites toward polysulfide reduction and highlight the particularly high intrinsic activity of NiS_2, which could enable improved QDSSC performance. Furthermore, structural disorder introduced by alloying different transition metal pyrites could increase their areal density of active sites for catalysis, leading to enhanced performance.

4.2. Introduction

The ability to efficiently and inexpensively generate hydrogen gas is essential to its proposed adoption as a sustainable, secure, and clean next-generation alternative energy carrier.[1,2] Various methods exist for producing hydrogen fuel,[2] but among these, water electrolysis (ideally driven by solar energy[3–7]) is most attractive. By electrocatalytically splitting water to give clean hydrogen fuel, no harmful byproducts are released; then, upon its consumption in the presence of air, only energy and water are produced.[7] Numerous inorganic materials have been investigated as potential hydrogen evolution reaction (HER) electrocatalysts,[8] but none so far match both the performance and stability of the noble metals, particularly platinum.[9] However, the scarcity and high cost of the noble metals inhibits the large-scale deployment of energy conversion technologies that utilize noble metal electrocatalysts.[10] By replacing such precious metal electrocatalysts with high-performance substitutes composed entirely of earth-abundant elements,[8,11–27] though, the cost of electrochemical and

photoelectrochemical hydrogen production could be considerably reduced.

Through substantial (and ongoing) research efforts, a number of earth-abundant materials have been identified as promising candidate HER electrocatalysts,[8] including MoS_2,[11–13] WS_2,[14,15] amorphous MoS_x,[16,17] amorphous Co–S,[18] FeP,[19] CoP,[20] Ni_2P,[21] $Co_{0.6}Mo_{1.4}N_2$,[22] and the Ni–Mo alloys,[23,24] among others. The cubic pyrite-phase transition metal dichalcogenides (with the general formula MX_2, where typically M = Fe, Co, or Ni and X = S or Se) have only recently emerged as efficient HER electrocatalysts,[25–28] despite the suggestion over twenty years ago that they could catalyze the HER.[29] Within the family of transition metal pyrites, iron disulfide (iron pyrite, FeS_2; "fool's gold"), cobalt disulfide (cobalt pyrite, CoS_2; cattierite), and nickel disulfide (nickel pyrite, NiS_2; vaesite) are common and well-studied minerals. Composed of first-row transition metals and rock-forming chalcogens, the transition metal pyrites are very abundant and inexpensive, making them particularly interesting as materials for energy conversion applications. For example, semiconducting FeS_2 is presently under intense investigation as a potential earth-abundant solar light absorber.[30–32] The electrocatalytic properties of FeS_2 have also been leveraged in dye-sensitized solar cells (DSSCs),[33] with nanorod arrays[34] and thin film electrodes prepared from a nanocrystal ink[35] enabling device performance competitive with that achieved using platinum counter electrodes. Similarly, both FeS_2 and $(Fe,Co)S_2$ alloys have been investigated as oxygen reduction reaction (ORR) electrocatalysts.[36] Both FeS_2[37] and CoS_2[38] are also promising electrode materials for lithium-ion batteries. Unlike the semiconducting pyrites, though, CoS_2 is intrinsically a conductive metal, allowing it to be used directly as an electrode material. This has been demonstrated through the use of CoS_2 thin films synthesized directly on glass as highly effective counter electrodes[39] in quantum dot-sensitized solar cells (QDSSCs)[40,41]

that employ the sulfide/polysulfide redox electrolyte as the hole-transporting medium. Graphene-based composite electrodes incorporating CoS_2 nanoparticles have also proven effective in reducing triiodide in DSSCs, exhibiting performance superior to that of platinum.[42] Recently, we employed nanostructuring strategies to further increase the activity of CoS_2 electrodes toward both polysulfide and triiodide reduction.[26] In this same work, thin films, microwires, and nanowires of CoS_2 prepared directly on conducting graphite supports were shown to exhibit excellent electrocatalytic activity toward the HER, with micro- and nanostructuring of the CoS_2 material synergistically enhancing both performance and stability.[26] As with FeS_2, CoS_2 thin films and nanocrystals have also been investigated as ORR electrocatalysts,[43–45] further establishing its generality as a high-performance electrocatalyst. More recently, hollow spheres of CoS_2 and NiS_2 have been used in supercapacitors,[46] as have NiS_2 nanocubes.[47] These NiS_2 nanocubes were also demonstrated as efficient cocatalysts for the photocatalytic production of hydrogen.[47]

Here, we report the systematic investigation of the HER and polysulfide reduction electrocatalytic activity of various pyrite-phase transition metal disulfides, namely, FeS_2, CoS_2, NiS_2, and their alloys. While each of transition metal pyrites characterized here exhibits activity toward the HER, confirming the general electrocatalytic properties of the pyrites, we show that their performance (as measured by their ability to enable high catalytic current densities at low overpotentials) tends to increase with increasing cobalt content, with CoS_2 being superior, suggesting a special role for cobalt in facilitating the HER. We have similarly compared the polysulfide reduction activity of FeS_2, NiS_2, and an alloy thereof to that of CoS_2 and identified NiS_2 as possessing particularly high activity. Furthermore, we suggest that alloying may be an

effective and general method for enhancing the electrocatalytic activity of the transition metal pyrites due to the introduction of structural disorder, which could increase their areal density of active sites for catalysis.

4.3. Experimental Methods

All chemicals were purchased from Sigma-Aldrich and used without further purification, unless otherwise noted.

4.3.1. Materials Synthesis

Substrate Preparation. Graphite disk substrates (6.0 mm diameter; < 1 mm thick) were prepared by cutting and mechanically thinning slices of a graphite rod (Ultra Carbon Corp., Ultra "F" Purity). Each slice of the graphite rod was abraded on both sides with SiC paper (Allied High Tech Products, Inc.; 320 grit) until a thin disk was obtained. Then, one side of each graphite disk substrate was polished to a specular finish using 1200 grit SiC paper. The polished graphite disks were cleaned by sequential sonication (100 W) in neutral distilled water (Thermo Scientific, Barnstead Nanopure, 18.2 MΩ cm) for 10 min, then in aqua regia (3:1 HCl(*aq*):HNO_3(*aq*)) for 10 min, and again in fresh distilled water for 10 min to remove loose graphite dust and any metal impurities. Finally, the clean graphite disks were dried in a forced-air convection oven at 120 °C.

Borosilicate plate glass substrates (1.5 cm × 3.0 cm; 3.3 mm thick) were manually roughened on one side with SiC paper (320 grit) for several minutes and then ultrasonically cleaned (100 W) for 30 min in a detergent solution (Fisher Scientific, Versa-Clean, diluted 1:4 with deionized water). The glass substrates were then thoroughly rinsed with distilled water and

ethanol and then blown dry under a stream of nitrogen. Finally, the substrates were oxygen plasma cleaned (150 W RF, < 200 mTorr, 1 sccm O_2, 3 min) to remove any organic residues.

Transition Metal Pyrite Thin Film Synthesis. For the binary transition metal pyrite thin films on graphite, a 30 nm thick film of the corresponding high-purity metal (Kurt J. Lesker, ≥ 99.95%) was deposited onto the polished side of clean graphite disk substrates at a rate of 0.3 Å s^{-1} by electron-beam evaporation. An alloy film consisting mostly of Ni and Fe was deposited by electron-beam evaporating 30 nm of Permalloy ("Py," HyMu 80 alloy: 80.00 Ni, 4.20 Mo, 0.50 Mn, 0.35 Si, 0.02 C, balance Fe) onto graphite disk substrates. To prepare iron/cobalt and nickel/cobalt pyrite alloy films, metal bilayers consisting of 15 nm of Fe over 15 nm of Co or 15 nm of Ni over 15 nm of Co, respectively, were sequentially electron-beam evaporated onto graphite disk substrates.

To convert the metal films to their corresponding disulfide, a simple thermal sulfidation procedure was used.[26,39] Briefly, the metalized substrates were loaded into the center of a fused silica tube on a home-built flow reactor equipped with both pressure and gas flow controllers. An alumina boat containing 2 g of S powder (99.5–100.5%) was placed in the tube at the farthest upstream position within the tube furnace (Lindberg/Blue M, TF55035A-1). The tube reactor was then purged of air and maintained at a slight positive pressure of 780 Torr under a steady flow of Ar carrier gas (99.999%) at 25 sccm. To initiate the conversion, the furnace temperature was ramped from room temperature to 500 °C at a rate of approximately 60 °C min^{-1} and held for 1 h. Then, the tube furnace was opened to allow natural cooling of the sample back to room temperature under Ar flow.

Electrodes for the fabrication of symmetrical electrochemical cells were prepared by

electron-beam evaporating 50 nm of Fe, Co, Ni, or Py onto borosilicate glass substrates coated with a ~180 nm thick conducting CoS_2 film (prepared by thermally sulfidizing a 100 nm thick Co film[39]). Then, these metal films were thermally sulfidized (using the same procedures described above) to yield FeS_2, CoS_2, NiS_2, or Permalloy pyrite ("PyS_2") thin films, respectively, electrically contacted directly by the underlying metallic CoS_2 film.

4.3.2. Materials Characterization

The as-synthesized pyrite films on graphite were characterized using a LEO SUPRA 55 VP field-emission scanning electron microscope operated at 5 kV and a Thermo Scientific DXR Raman microscope fitted with 532 nm excitation laser. X-ray photoelectron spectroscopy (XPS) was performed on the as-synthesized pyrite films on graphite using a Thermo Scientific K-Alpha XPS system with an Al Kα source. X-ray diffraction (XRD) patterns of the thicker pyrite films on glass were acquired on a Bruker D8 ADVANCE powder XRD using Cu Kα radiation. The XRD pattern background was fit to a cubic spline and subtracted using the Jade 5 software (Materials Data, Inc.).

4.3.3. Electrochemical Characterization of Electrocatalytic Activity Toward the HER

All electrochemical characterizations of HER activity were performed in a three-electrode configuration and recorded using a Bio-Logic SP-200 potentiostat. Each measurement was performed in 0.5 M $H_2SO_4(aq)$ electrolyte continuously purged with $H_2(g)$ (99.999%) using a saturated calomel reference electrode (SCE) (CH Instruments) and a graphite rod (National Carbon Co., AGKSP Spectroscopic Electrode) as the counter electrode. After characterization of pyrite film electrocatalytic activity toward the HER, the SCE was calibrated against the reversible hydrogen electrode (RHE) using platinum wire (Kurt J. Lesker, 99.99%; 0.50 mm

diameter) as both the working and counter electrodes. The working electrode in each measurement was a pyrite thin film-coated graphite disk sample mounted on a fluoropolymer (PCTFE)-encased glassy carbon disk electrode using silver paint (Ted Pella, PELCO Colloidal Silver). Cyclic voltammograms (CVs) were recorded for each electrode from approximately +0.10 V to −0.24 V vs. RHE at a scan rate of 2 mV s^{-1}, repeating this scan at least twice. Then, electrochemical impedance spectroscopy (EIS) was performed in potentiostatic mode at −0.19 V vs. RHE, applying a sinusoidal voltage with an amplitude of 10 mV and scanning frequency from 200 kHz to 50 mHz. The EIS spectra were modeled using a simplified Randles equivalent circuit consisting of a resistor in series with a parallel arrangement of a constant phase element and a second resistor for the purpose of extracting the series resistance associated with each electrode. All polarization curves were corrected for background current and *IR* losses, as described in detail previously,[26] and those presented here depict representative electrode behavior.

4.3.4. Symmetrical Cell Fabrication and Electrochemical Characterization

Symmetrical electrochemical cells were fabricated using freshly-prepared pyrite film electrodes on glass and characterized in a two-electrode configuration using procedures described elsewhere.[26,39] The sulfide/polysulfide electrolyte filled into the symmetrical cells consisted of 2 M $Na_2S•9H_2O$ ($\geq$ 99.99%) and 2 M S in aqueous solution. To ensure good electrical contact to the pyrite-phase electrocatalyst film on each electrode, the top pyrite film was lightly scratched using SiC paper and electrical contacts were applied directly to the underlying CoS_2 film using silver paint.

4.4. Results and Discussion

4.4.1. Pyrite Thin Film Synthesis and Structural Characterization

The simplicity and generality of the thermal sulfidation procedure described here allows metallic thin films of iron, cobalt, nickel, and Permalloy (which primarily consists of nickel and iron), as well as bilayer iron/cobalt and nickel/cobalt films, to all be converted to their corresponding pyrite-phase disulfides using the same synthesis conditions (Experimental Methods). The resulting transition metal pyrite thin films adhere well to and uniformly cover the substrate surface (either graphite or glass). Two types of samples were prepared: thin pyrite films (less than 50 nm in thickness) on conductive graphite substrates for direct characterization of their HER electrocatalytic activity, and thick bilayer pyrite films on glass substrates for the assessment of their activity toward polysulfide reduction in symmetrical electrochemical cells (Experimental Methods). The thin pyrite-phase electrocatalyst films on graphite do not permit direct phase identification by X-ray diffraction (XRD) due to the low-signal pyrite diffraction peaks being overwhelmed by the reflections from the graphite support; however, the thicker films on glass clearly establish the formation of pyrite-phase products via thermal sulfidation (Figure 4.1). In these diffraction patterns, the most intense peaks result from the underlying CoS_2 film on glass (which provides electrical contact to the uppermost pyrite-phase electrocatalyst layers). Peak broadening and/or the appearance additional peaks adjacent to the primary CoS_2 peaks results from the presence of a FeS_2, NiS_2, or PyS_2 overlayer (Figure 4.1b–d). Because the pyrite phases are isostructural with one another and possess very similar lattice constants, XRD reaches its resolution limit and cannot effectively differentiate the pyrite-phase products, particularly in the case of FeS_2 and CoS_2 (Figure 4.1b).

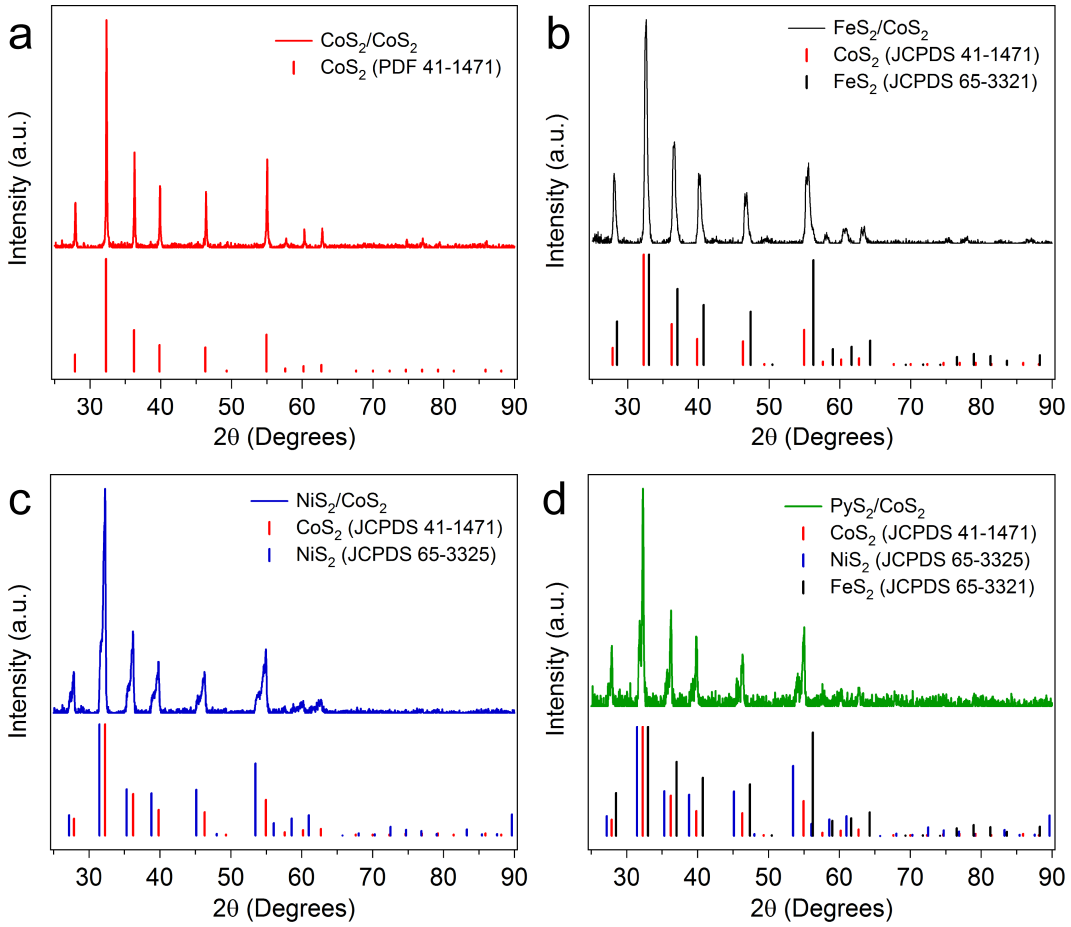

Figure 4.1. X-ray diffraction (XRD) patterns of as-prepared pyrite-phase (a) CoS_2, (b) FeS_2, (c) NiS_2, and (d) PyS_2 electrocatalyst thin films over a CoS_2 film on glass. In each panel, the standard diffraction patterns for CoS_2 (JCPDS 41-1471), FeS_2 (JCPDS 65-3321), and/or NiS_2 (JCPDS 65-3325) appear below the experimental pattern.

Moreover, in the case of the Permalloy and bilayer metal precursor films on graphite, pyrite-phase alloy thin films are obtained upon thermal sulfidation due to mixing of the metal species, further complicating their structural characterization by XRD. To effectively differentiate the different transition metal disulfide thin films on graphite, we instead used Raman spectroscopy to both verify the formation of pyrite-phase products and to qualitatively evaluate their composition and crystallinity. The Raman spectra of the thinner transition metal pyrite and pyrite alloy films on graphite are shown in Figure 4.2. The Raman spectra for the FeS_2, CoS_2, and NiS_2 thin films are in strong agreement with previous reports on the corresponding phase-pure pyrites,[31,43] with the sharp peaks associated with the distinct vibrational modes of the pyrite structure indicating long-range crystalline ordering. In contrast, the Raman peaks of the PyS_2 thin film are very broad, possibly owing to the alloying of multiple metal sulfides upon thermal sulfidation of Permalloy; however, the primary peaks at 464 and 480 cm^{-1} likely result from a composition consisting primarily of NiS_2, while the peak at 382 cm^{-1} might indicate the presence of FeS_2. More importantly, the peaks are substantially broadened and reduced in intensity as compared to those of the binary pyrites, indicating greater structural disorder in the alloy film. Similarly, the Raman spectrum for the $(Fe,Co)S_2$ thin film shows a broad peak centered around 371 cm^{-1} which is likely the result of approximately equal contributions from the primary CoS_2 peak at 393 cm^{-1} and the most intense FeS_2 peaks at 377 and 342 cm^{-1}. Likewise, a very broad peak centered at 433 cm^{-1} appears in the Raman spectrum of the $(Co,Ni)S_2$ thin film owing to contributions from both CoS_2 and NiS_2 in an randomly mixed alloy. The increased full width at half maximum of this primary Raman feature suggests that the $(Co,Ni)S_2$ films might possess even greater structural disorder than the $(Fe,Co)S_2$ films. Had

these pyrite-phase alloys thin films instead consisted of a bilayer (or mixture) of two distinct pyrite phases, we would have observed a simple superposition of the Raman spectra corresponding to the two phase-pure binary pyrites.

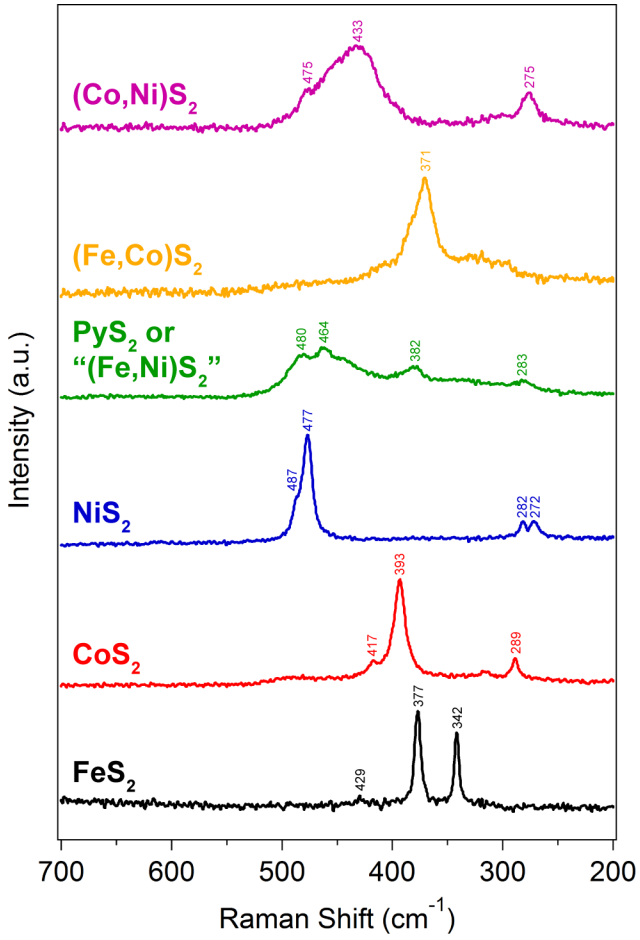

Figure 4.2. Raman spectra for iron pyrite (FeS_2, black trace), cobalt pyrite (CoS_2, red trace), nickel pyrite (NiS_2, blue trace), "Permalloy pyrite" ["PyS_2" or "$(Fe,Ni)S_2$," green trace], iron/cobalt pyrite [$(Fe,Co)S_2$, orange trace], and cobalt/nickel pyrite [$(Co,Ni)S_2$, violet trace] thin films prepared on graphite disk substrates.

The Raman spectra confirm the formation of pyrite-phase products for the binary disulfides and strongly suggest the presence of pyrite-phase alloys for the other thin films, but they do not permit quantification of the surface composition of the alloys, which is particularly relevant in electrocatalysis. For the pyrite-phase alloy thin films on graphite, the exact ratio of transition metals at the film surface was determined using X-ray photoelectron spectroscopy (XPS) (Figure 4.3). Integration and comparison of the Fe 2p and Co 2p or Ni 2p and Co 2p signals revealed alloy compositions of $(Fe_{0.48}Co_{0.52})S_2$ and $(Co_{0.59}Ni_{0.41})S_2$, respectively, for the thin films prepared by thermal sulfidation of the corresponding metal bilayers, confirming that there is substantial mixing of the metal films upon thermal sulfidation. Similarly, comparing the Ni 2p and Fe 2p peaks in the PyS_2 XPS spectrum revealed an approximate surface composition of "$(Fe_{0.07}Ni_{0.93})S_2$" (not accounting for other minor species that may be present), consistent with the nickel-rich composition of Permalloy.

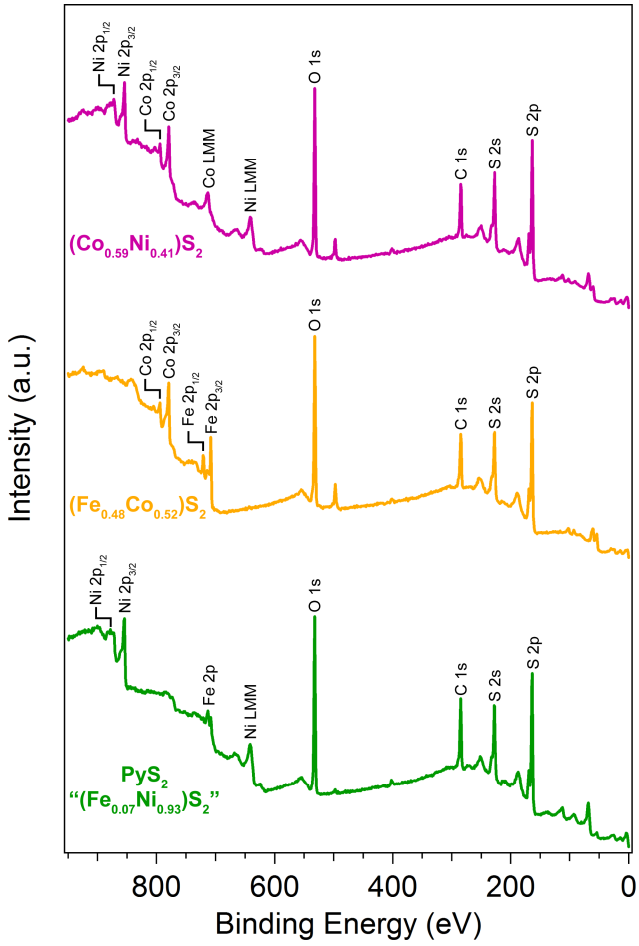

Figure 4.3. X-ray photoelectron spectroscopy (XPS) survey spectra of the pyrite-phase transition metal disulfide alloy thin films formed by thermally sulfidizing a Permalloy film (bottom green trace), an iron/cobalt metal bilayer (middle orange trace), or a nickel/cobalt metal bilayer (top violet trace), which yield alloy compositions of "$(Fe_{0.07}Ni_{0.93})S_2$" (which is roughly commensurate with the composition of Permalloy, not accounting for minor species), $(Fe_{0.48}Co_{0.52})S_2$, and $(Co_{0.59}Ni_{0.41})S_2$, respectively.

Scanning electron microscopy (SEM) of the pyrite-phase thin films on graphite reveals that the as-sulfidized films generally consist of uniform nanocrystalline grains sintered together to cover the substrate surface (Figure 4.4), as previously reported.[26,39] The morphologies of the pyrite-phase thin films prepared on glass are very similar. While the polycrystalline pyrite-phase thin films all exhibit essentially the same appearance, there are important morphological differences that distinguish them from one another. In particular, the NiS_2 grains, which are typically 80–200 nm in diameter and sintered into clusters to form a porous film, are substantially larger than those of FeS_2 or CoS_2. Consistent with this observation, the other pyrite-phase films that contain a substantial amount of nickel—namely, PyS_2 and $(Co_{0.59}Ni_{0.41})S_2$—also show the clustering of grains to give a more open film structure. Similarly, the $(Fe_{0.48}Co_{0.52})S_2$ films feature both the compact morphology of the CoS_2 films and the larger grain size of the FeS_2 films.

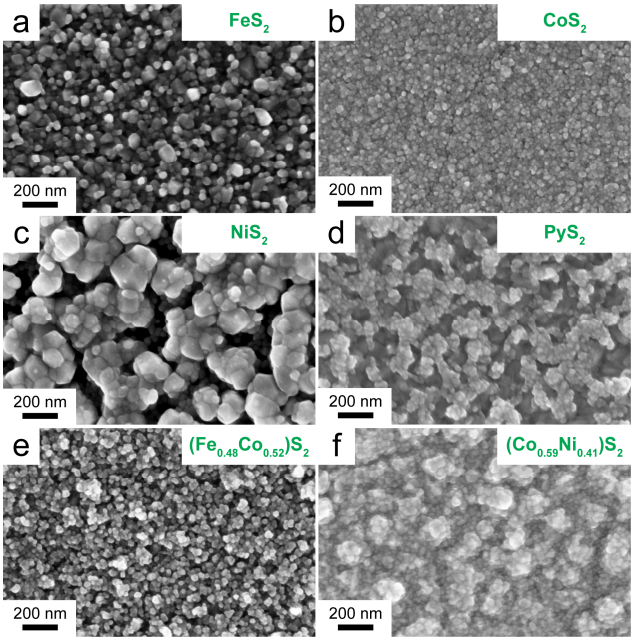

Figure 4.4. Scanning electron microscopy images of representative (a) FeS_2, (b) CoS_2, (c) NiS_2, (d) PyS_2, (e) $(Fe_{0.48}Co_{0.52})S_2$, and (f) $(Co_{0.59}Ni_{0.41})S_2$ thin films prepared on graphite disk substrates depicting their small-grain polycrystalline texture.

4.4.2. Electrocatalytic Performance of Pyrite Thin Films Toward the HER

By directly synthesizing the pyrite-phase electrocatalyst thin films on conducting graphite disk substrates, their electrocatalytic activity toward the HER can be easily assessed using standard electrochemical techniques. These characterizations were performed by interfacing the graphite-supported thin films with a glassy carbon disk electrode and measuring their voltammetric behavior in 0.5 M $H_2SO_4(aq)$ electrolyte continuously purged with $H_2(g)$ in a three-electrode electrochemical measurement (Experimental Methods). Linear sweep voltammetric polarization curves showing the electrocatalytic current density (J) produced by each of the pyrite-phase electrocatalyst thin film electrodes plotted against the applied potential appear in Figure 4.5a–b.

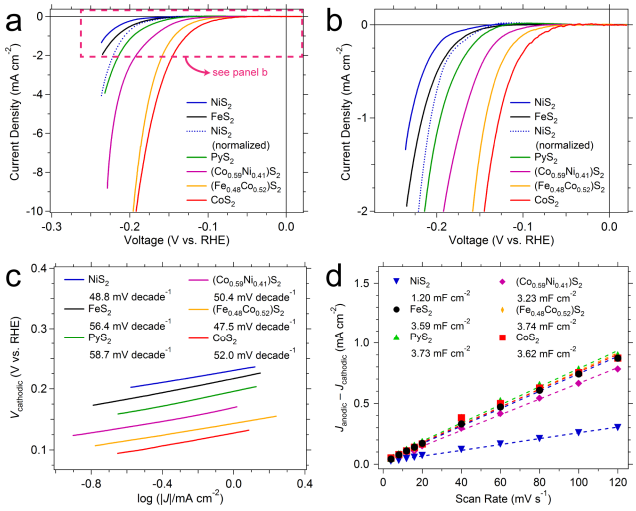

Figure 4.5. Electrochemical characterization of the catalytic activity of FeS_2 (black traces and circle markers), CoS_2 (red traces and square markers), NiS_2 (blue traces and down-pointing triangles), PyS_2 (green traces and up-pointing triangles), $(Fe_{0.48}Co_{0.52})S_2$ (orange traces and thin diamond markers), and $(Co_{0.59}Ni_{0.41})S_2$ (violet traces and diamond markers) thin films prepared on graphite disk substrates toward the HER. Polarization curves (corrected for background currents and *IR* losses) over (a) wider and (b) narrower ranges of current density comparing the performance of the pyrite-phase electrocatalyst thin films. The dashed trace presents the NiS_2 data normalized by its relative surface area. (c) Tafel analysis of the data presented in panel a, with the specific Tafel slopes given in the figure legend. (d) Plot showing the method of extracting the double layer capacitance (C_{dl}) for each electrode.

Figure 4.5a illustrates that all of the pyrite-phase thin films enable the electrocatalytic evolution of hydrogen gas, as indicated by the onset of current and the formation of bubbles at the electrode surface under cathodic bias. However, there is a marked difference in performance among the electrocatalysts, as highlighted in Figure 4.5b. If we measure the cathodic overpotential (η) required for the different electrocatalysts to drive the HER at 1 mA cm^{-2}, we notice that it steady decreases in the order of NiS_2 (η = 230 mV) to FeS_2 (η = 217 mV) to PyS_2 (η = 196 mV) to $(Co_{0.59}Ni_{0.41})S_2$ (η = 170 mV) to $(Fe_{0.48}Co_{0.52})S_2$ (η = 143 mV) to CoS_2 (η = 128 mV), as summarized in Table 4.1. These overpotentials are roughly consistent with the apparent shifts in the onset of catalytic current for the different electrocatalysts, which compare favorably with those previously reported in the literature for both pyrite-phase HER electrocatalysts[25–27] and other earth-abundant HER electrocatalysts.[11–24] While the $(Fe_{0.48}Co_{0.52})S_2$ and CoS_2 thin films are able to achieve $J = -10$ mA cm^{-2} (at $\eta = -196$ mV and -192 mV, respectively), as shown in Figure 4.5a, the lower performing electrocatalysts do not reach this current density over the range of applied overpotentials. As we have shown previously, transition metal pyrite thin films on graphite tend to delaminate under the conditions of rapid hydrogen evolution that accompanies high current densities,[26] so we intentionally limited our characterizations to permit only modest current densities.

Tafel analysis of the data presented in Figure 4.5a–b reveals that the Tafel slopes of all of the pyrite-phase electrocatalysts lie in the approximate range of 50–60 mV $decade^{-1}$ (Figure 4.5c and Table 4.1), consistent with previous reports.[25–27] Interestingly, the highest-performing CoS_2 film does not exhibit the highest intrinsic activity toward the HER, as indicated by its Tafel slope; it does, however, possess the highest geometric exchange current density ($J_{0,geometric}$),

which is characteristic of high electrocatalytic activity. The lowest-performing NiS_2 film actually shows a lower Tafel slope, consistent with a previous report,[25] suggesting that NiS_2 may in fact possess higher intrinsic activity toward the HER than CoS_2. The $J_{0,\text{geometric}}$ of NiS_2 is the lowest among those measured, though, which rationalizes its relatively poor performance among these pyrite-phase electrocatalysts. To better resolve these trends in performance and intrinsic activity, we must also consider the effective electrochemically active surface area of each pyrite-phase electrocatalyst film, since it is known to affect overall HER performance.[26] The double-layer capacitance (C_{dl}) of each pyrite-phase electrocatalyst film, which is proportional to its effective surface area, was extracted using cyclic voltammetry (Experimental Methods), as shown in Figure 4.5d. All of the pyrite-phase electrocatalyst thin films exhibit similar values of C_{dl}, indicating comparable surface area, except NiS_2, for which the C_{dl} was approximately one-third that of the other electrocatalyst films. When these values of C_{dl} are compared against that of the CoS_2 film (the highest performing electrocatalyst), we see that the relative surface area of the NiS_2 film is indeed about one-third that of the other pyrite films (Table 4.1). This observation is consistent with their respective film morphologies as revealed by SEM (Figure 4.4), where the NiS_2 film grains are substantially larger, likely resulting in a lower overall effective surface area. If the polarization data corresponding to the NiS_2 film are normalized by the relative electrode surface area, the trace (Figure 4.5a–b, dashed blue line) is shifted closer to that of the PyS_2 electrode (green line), consistent with the nickel-rich composition of the PyS_2 film. The results of these electrochemical characterizations are summarized in Table 4.1.

Table 4.1. Summary of the Electrochemical Properties of the Different Pyrite-Phase Thin Film Electrocatalysts for the Hydrogen Evolution Reaction.

electrocatalyst	η (mV vs. RHE) for $J = -1$ mA cm^{-2}	η (mV vs. RHE) for $J = -10$ mA cm^{-2}	Tafel slope (mV decade^{-1})	$J_{0,\text{geometric}}$ (μA cm^{-2})	C_{dl} (mF cm^{-2})	relative surface area
FeS_2	−217	N/A	56.4	0.144	3.59	0.99
CoS_2	−128	−192	52.0	3.53	3.62	1.00
NiS_2	−230	N/A	48.8	0.0191	1.20	0.33
PyS_2 ["$(Fe_{0.07}Ni_{0.93})S_2$"]	−196	N/A	58.7	0.0469	3.73	1.03
$(Fe_{0.48}Co_{0.52})S_2$	−143	−196	47.5	0.959	3.74	1.03
$(Co_{0.59}Ni_{0.41})S_2$	−170	N/A	50.4	0.0476	3.23	0.89

The electrochemical characterizations of the pyrite-phase electrocatalysts shown in Figure 4.5 indicate that their performance tends to increase with the introduction of cobalt, with CoS_2 exhibiting the highest overall performance, suggesting that cobalt may energetically modify the active sites for catalysis (perhaps like a "promoter" species in the MoS_2 system[48]) to facilitate the HER more effectively than iron or nickel. This is perhaps consistent with previous implications of the under-coordinated metal centers at low-index pyrite crystal faces, which resemble the active site of hydrogenase,[49] as being the active sites for HER electrocatalysis.[25] Interestingly, among the transition metal phosphide HER electrocatalysts, CoP[20] also exhibits superior performance as compared to Ni_2P[21] and FeP.[19] Similarly, the controlled introduction of cobalt to δ-MoN to form the $Co_{0.6}Mo_{1.4}N_2$ phase substantially boosts its electrocatalytic activity toward the HER.[22] These examples echo our observations of improved performance for HER electrocatalysts that contain cobalt. Additionally, the improved performance of PyS_2 and $(Ni_{0.41}Co_{0.59})S_2$ (relative to that of NiS_2) and $(Fe_{0.48}Co_{0.52})S_2$ (relative to that of FeS_2) suggests that alloying may also be an effective method for enhancing electrocatalytic activity. The structural disorder introduced through alloying could lead to a proliferation of active sites for catalysis, and the electronic interaction of multiple metal species may synergistically enhance intrinsic activity,[8] perhaps in the same way that amorphous MoS_x can exhibit intrinsic electrocatalytic activity toward the HER rivaling or even surpassing that of crystalline MoS_2.[16,17] Together, these conclusions suggest simple pathways toward improving the performance of the pyrite-phase transition metal disulfide electrocatalysts, and have implications for other families of transition metal compound electrocatalysts.[8]

4.4.3. Electrocatalytic Performance of Pyrite Thin Films Toward Polysulfide Reduction

Considering the high electrocatalytic activity of CoS_2 toward polysulfide reduction[26,39] and the demonstrations here of the HER activity of other pyrite-phase transition metal disulfides, we probed the electrocatalytic activity of FeS_2, NiS_2, and PyS_2 thin films toward polysulfide reduction and compared their performance to that of CoS_2. The electrocatalyst thin films used in these characterizations were prepared on glass supports coated with a ~180 nm thick film of conducting CoS_2 (Experimental Methods). Cobalt pyrite was selected as the conductive electrocatalyst thin film support due to both its insensitivity to the thermal sulfidation conditions necessary to synthesize the FeS_2, NiS_2, and PyS_2 thin films as well as its known chemical compatibility with the sulfide/polysulfide electrolyte.

Using these thin film electrodes, symmetrical electrochemical cells were assembled and filled with sulfide/polysulfide electrolyte (Experimental Methods). The performance of each electrocatalyst thin film was assessed in the symmetrical cell configuration using both cyclic voltammetry (CV) and electrochemical impedance spectroscopy (EIS) techniques (Experimental Methods). Remarkably, all of the pyrite-phase transition metal disulfide thin films show both good stability and high activity toward polysulfide reduction (Figure 4.6a). Moreover, both the PyS_2 and, to a lesser extent, NiS_2 films exhibit performance superior to that of CoS_2, as indicated by higher current densities across the full range of applied overpotentials. The FeS_2 films, however, show performance inferior to that of the CoS_2 films.

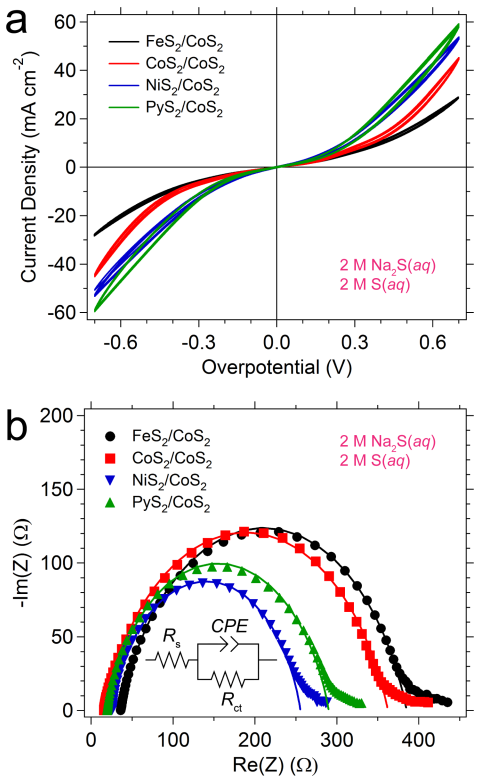

Figure 4.6. Electrochemical characterization of the pyrite-phase FeS_2 (black traces and circle markers), CoS_2 (red traces and square markers), NiS_2 (blue traces and down-pointing trianges), and PyS_2 (green traces and up-pointing triangles) electrocatalyst thin films prepared on CoS_2/glass electrodes toward polysulfide reduction in symmetrical electrochemical cells. (a) Cyclic voltammetry and (b) electrochemical impedance spectroscopy characterization of the symmetrical cells. The inset circuit diagram in panel b shows the equivalent circuit model used to fit the experimental data, with the results of these fittings shown a solid line traces.

To understand the performance trends observed in the CV measurements, EIS was performed at the open circuit potential for each symmetrical cell device. The Nyquist plots shown in Figure 4.6b permit extraction of the series resistance (R_s) and charge-transfer resistance (R_{ct}) associated with each symmetrical cell device by fitting the experimental data to an equivalent circuit model (inset). The results of these fittings are displayed in Table 4.2. The R_s extracted for each electrode provides information about the electrical transport properties of each pyrite-phase electrocatalyst. Owing to its metallic conductivity, CoS_2 shows the lowest R_s; conversely, semiconducting FeS_2 shows the highest R_s, which supports the observation of lower current densities at high overpotentials in Figure 4.6a. NiS_2 exhibits an intermediate R_s that is slightly higher than that of PyS_2, which may have higher conductivity than NiS_2 due to the minor presence of other metal sulfide species. More importantly, the values of R_{ct} provide information about the relative activity of the different pyrites toward polysulfide reduction. The CoS_2 thin films show a value of R_{ct} similar to what has been previously reported,[26,39] and remarkably, the R_{ct} for FeS_2 is quite comparable, indicating nearly equivalent levels of intrinsic activity toward polysulfide reduction. The R_{ct} of NiS_2, however, is the lowest, suggesting its superior activity toward polysulfide reduction. This observation is perhaps consistent with the low Tafel slope of NiS_2 associated with HER electrocatalysis. This R_{ct} is still higher than that of the state-of-the-art reduced graphene oxide–cuprous sulfide (RGO–Cu_2S) composite electrocatalyst that enables the highest QDSSC solar light-to-electricity conversion efficiencies.[50] The R_{ct} of PyS_2 is higher than that of NiS_2, perhaps due to iron alloying, but still lower than that of CoS_2. Coupled with its low R_s, then, PyS_2 enables the highest performance seen in the CV characterizations. These results indicate that, as in the case of HER electrocatalysis, multiple pyrite-phase transition metal

disulfide compounds exhibit high activity toward polysulfide reduction. Furthermore, NiS_2 possesses the highest intrinsic activity—even higher than that of CoS_2—suggesting that its incorporation into QDSSC devices as the counter electrode electrocatalyst (perhaps as a composite with a conductive support, such as RGO, that facilitates electron transport) could enable improved solar light-to-electricity conversion efficiencies. Similarly, with the high activity of FeS_2, CoS_2, NiS_2, and other transition metal sulfide phases toward triiodide reduction already documented,[26,34,35,42,46,47,51,52] the trends observed here could potentially inform the development of improved pyrite-phase electrocatalysts for DSSC counter electrodes.

Table 4.2. Summary of the Electrochemical Properties of the Different Pyrite-Phase Thin Film Electrocatalysts for Polysulfide Reduction.

electrode	R_s (Ω)	R_{ct} (Ω cm^2)
FeS_2/CoS_2	35.7	31.1
CoS_2/CoS_2	15.0	30.9
NiS_2/CoS_2	25.2	20.5
PyS_2/CoS_2	19.4	24.1

4.5. Summary and Perspectives

In conclusion, we have demonstrated that both binary and alloyed pyrite-phase transition metal disulfide thin films can be prepared directly on graphite or glass substrates through the facile thermal sulfidation of metal precursor films, and that these transition metal pyrite thin films are highly efficient HER and polysulfide reduction electrocatalysts. Current density–voltage characterizations of these pyrite-phase electrocatalyst thin films show the onset of $H_2(g)$ evolution at low overpotentials competitive with other earth-abundant electrocatalysts. The trends in their performance suggest that cobalt might play a special role in enhancing HER electrocatalytic performance. Additionally, Raman characterization of the alloy thin films confirms their increased structural disorder, which may contribute to their improved electrocatalytic performance. Furthermore, thin films of FeS_2, NiS_2, and PyS_2 were found to efficiently catalyze polysulfide reduction, with the intrinsic activity of NiS_2 exceeding that of CoS_2. The general electrocatalytic activity of the pyrite-phase transition metal disulfides implies that a common feature might impart such activity. In addition to the effects of the transition metal cation on electrocatalytic activity reported here, the disulfide anions (S_2^{2-}) present in all pyrite structures could be important for their high electrocatalytic activity toward the HER. Indeed, the disulfide-terminated edges of MoS_2 and other layered transition metal dichalcogenides have been identified experimentally[53] and pursued in molecular mimics[54,55] as the active sites for HER electrocatalysis, again suggesting a catalytic role for disulfide. The abundance of disulfide-terminated surface sites in the pyrite crystal structure, then, could contribute to the superb and general electrocatalytic activity of the pyrite-phase transition metal

disulfides; however, additional mechanistic studies are required to establish such a relationship. Nevertheless, the trends observed in the electrocatalytic activity of these pyrite-phase thin films toward both the HER and polysulfide reduction suggest potential strategies for further boosting their performance in these and potentially other electrocatalytic and renewable energy applications.

4.6. References

(1) Lewis, N. S.; Nocera, D. G. Powering the planet: Chemical challenges in solar energy utilization. *Proc. Natl. Acad. Sci. U.S.A.* **2006**, *103*, 15729–15735.

(2) Turner, J. A. Sustainable Hydrogen Production. *Science* **2004**, *305*, 972–974.

(3) Gray, H. B. Powering the planet with solar fuel. *Nature Chem.* **2009**, *1*, 7–7.

(4) Chen, X. B.; Shen, S. H.; Guo, L. J.; Mao, S. S. Semiconductor-based Photocatalytic Hydrogen Generation. *Chem. Rev.* **2010**, *110*, 6503–6570.

(5) Walter, M. G.; Warren, E. L.; McKone, J. R.; Boettcher, S. W.; Mi, Q.; Santori, E. A.; Lewis, N. S. Solar Water Splitting Cells. *Chem. Rev.* **2010**, *110*, 6446–6473.

(6) Nocera, D. G. The Artificial Leaf. *Acc. Chem. Res.* **2012**, *45*, 767–776.

(7) Cook, T. R.; Dogutan, D. K.; Reece, S. Y.; Surendranath, Y.; Teets, T. S.; Nocera, D. G. Solar Energy Supply and Storage for the Legacy and Nonlegacy Worlds. *Chem. Rev.* **2010**, *110*, 6474–6502.

(8) Faber, M. S. Earth-abundant inorganic electrocatalysts and their nanostructures for energy conversion applications. PhD Dissertation, University of Wisconsin–Madison, Madison, WI, 2014.

(9) Nørskov, J. K.; Bligaard, T.; Logadottir, A.; Kitchin, J. R.; Chen, J. G.; Pandelov, S.; Stimming, U. Trends in the Exchange Current for Hydrogen Evolution. *J. Electrochem. Soc.* **2005**, *152*, J23–J26.

(10) Vesborg, P. C. K.; Jaramillo, T. F. Addressing the terawatt challenge: scalability in the supply of chemical elements for renewable energy. *RSC Adv.* **2012**, *2*, 7933–7947.

(11) Lukowski, M. A.; Daniel, A. S.; Meng, F.; Forticaux, A.; Li, L. S.; Jin, S. Enhanced Hydrogen Evolution Catalysis from Chemically Exfoliated Metallic MoS_2 Nanosheets. *J. Am. Chem. Soc.* **2013**, *135*, 10274–10277.

(12) Wang, H. T.; Lu, Z. Y.; Xu, S. C.; Kong, D. S.; Cha, J. J.; Zheng, G. Y.; Hsu, P.-C.; Yan, K.; Bradshaw, D.; Prinz, F. B.; Cui, Y. Electrochemical tuning of vertically aligned MoS_2 nanofilms and its application in improving hydrogen evolution reaction. *Proc. Natl. Acad. Sci. U.S.A.* **2013**, *110*, 19701–19706.

(13) Ding, Q.; Meng, F.; English, C. R.; Cabán-Acevedo, M.; Shearer, M. J.; Liang, D.; Daniel, A. S.; Hamers, R. J.; Jin, S. Efficient Photoelectrochemical Hydrogen Generation Using Heterostructures of Si and Chemically Exfoliated Metallic MoS_2. *J. Am. Chem. Soc.*, DOI: 10.1021/ja5025673.

(14) Voiry, D.; Yamaguchi, H.; Li, J. W.; Silva, R.; Alves, D. C. B.; Fujita, T.; Chen, M. W.; Asefa, T.; Shenoy, V. B.; Eda, G.; Chhowalla, M. Enhanced catalytic activity in strained chemically exfoliated WS_2 nanosheets for hydrogen evolution. *Nature Mater.* **2013**, *12*, 850–855.

(15) Lukowski, M. A.; Daniel, A. S.; English, C. R.; Meng, F.; Forticaux, A.; Hamers, R. J.; Jin, S. Highly Active Hydrogen Evolution Catalysis from Metallic WS_2 Nanosheets. *Energy Environ. Sci.*, DOI: 10.1039/C1034EE01329H.

(16) Merki, D.; Fierro, S.; Vrubel, H.; Hu, X. L. Amorphous molybdenum sulfide films as catalysts for electrochemical hydrogen production in water. *Chem. Sci.* **2011**, *2*, 1262–1267.

(17) Benck, J. D.; Chen, Z. B.; Kuritzky, L. Y.; Forman, A. J.; Jaramillo, T. F. Amorphous Molybdenum Sulfide Catalysts for Electrochemical Hydrogen Production: Insights into the Origin of their Catalytic Activity. *ACS Catal.* **2012**, *2*, 1916–1923.

(18) Sun, Y. J.; Liu, C.; Grauer, D. C.; Yano, J.; Long, J. R.; Yang, P.; Chang, C. J. Electrodeposited Cobalt-Sulfide Catalyst for Electrochemical and Photoelectrochemical Hydrogen Generation from Water. *J. Am. Chem. Soc.* **2013**, *135*, 17699–17702.

(19) Xu, Y.; Wu, R.; Zhang, J. F.; Shi, Y. M.; Zhang, B. Anion-exchange synthesis of nanoporous FeP nanosheets as electrocatalysts for hydrogen evolution reaction. *Chem. Commun.* **2013**, *49*, 6656–6658.

(20) Popczun, E. J.; Read, C. G.; Roske, C. W.; Lewis, N. S.; Schaak, R. E. Highly Active Electrocatalysis of the Hydrogen Evolution Reaction by Cobalt Phosphide Nanoparticles. *Angew. Chem. Int. Ed.* **2014**, *53*, 5427–5430.

(21) Popczun, E. J.; McKone, J. R.; Read, C. G.; Biacchi, A. J.; Wiltrout, A. M.; Lewis, N. S.; Schaak, R. E. Nanostructured Nickel Phosphide as an Electrocatalyst for the Hydrogen Evolution Reaction. *J. Am. Chem. Soc.* **2013**, *135*, 9267–9270.

(22) Cao, B. F.; Veith, G. M.; Neuefeind, J. C.; Adzic, R. R.; Khalifah, P. G. Mixed Close-Packed Cobalt Molybdenum Nitrides as Non-noble Metal Electrocatalysts for the Hydrogen Evolution Reaction. *J. Am. Chem. Soc.* **2013**, *135*, 19186–19192.

(23) McKone, J. R.; Warren, E. L.; Bierman, M. J.; Boettcher, S. W.; Brunschwig, B. S.; Lewis, N. S.; Gray, H. B. Evaluation of Pt, Ni, and Ni–Mo electrocatalysts for hydrogen evolution on crystalline Si electrodes. *Energy Environ. Sci.* **2011**, *4*, 3573–3583.

(24) McKone, J. R.; Sadtler, B. F.; Werlang, C. A.; Lewis, N. S.; Gray, H. B. Ni–Mo Nanopowders for Efficient Electrochemical Hydrogen Evolution. *ACS Catal.* **2013**, *3*, 166–169.

(25) Kong, D. S.; Cha, J. J.; Wang, H. T.; Lee, H. R.; Cui, Y. First-row transition metal dichalcogenide catalysts for hydrogen evolution reaction. *Energy Environ. Sci.* **2013**, *6*, 3553–3558.

(26) Faber, M. S.; Dziedzic, R.; Lukowski, M. A.; Kaiser, N. S.; Ding, Q.; Jin, S. High-Performance Electrocatalysis Using Metallic Cobalt Pyrite (CoS_2) Micro- and Nanostructures. *J. Am. Chem. Soc.*, DOI: 10.1021/ja504099w.

(27) Kong, D. S.; Wang, H. T.; Lu, Z. Y.; Cui, Y. $CoSe_2$ Nanoparticles Grown on Carbon Fiber Paper: An Efficient and Stable Electrocatalyst for Hydrogen Evolution Reaction. *J. Am. Chem. Soc.* **2014**, *136*, 4897–4900.

(28) Ivanovskaya, A.; Singh, N.; Liu, R.-F.; Kreutzer, H.; Baltrusaitis, J.; Nguyen, T. V.; Metiu, H.; McFarland, E. Transition Metal Sulfide Hydrogen Evolution Catalysts for Hydrobromic Acid Electrolysis. *Langmuir* **2013**, *29*, 480–492.

(29) Jaegermann, W.; Tributsch, H. Interfacial Properties of Semiconducting Transition Metal Chalcogenides. *Prog. Surf. Sci.* **1988**, *29*, 1–167.

(30) Cabán-Acevedo, M.; Faber, M. S.; Tan, Y. Z.; Hamers, R. J.; Jin, S. Synthesis and Properties of Semiconducting Iron Pyrite (FeS_2) Nanowires. *Nano Lett.* **2012**, *12*, 1977–1982.

(31) Cabán-Acevedo, M.; Liang, D.; Chew, K. S.; DeGrave, J. P.; Kaiser, N. S.; Jin, S. Synthesis, Characterization, and Variable Range Hopping Transport of Pyrite (FeS_2) Nanorods, Nanobelts, and Nanoplates. *ACS Nano* **2013**, *7*, 1731–1739.

(32) Seefeld, S.; Limpinsel, M.; Liu, Y.; Farhi, N.; Weber, A.; Zhang, Y. N.; Berry, N.; Kwon, Y. J.; Perkins, C. L.; Hemminger, J. C.; Wu, R. Q.; Law, M. Iron Pyrite Thin Films Synthesized from an $Fe(acac)_3$ Ink. *J. Am. Chem. Soc.* **2013**, *135*, 4412–4424.

(33) Hagfeldt, A.; Boschloo, G.; Sun, L. C.; Kloo, L.; Pettersson, H. Dye-Sensitized Solar Cells. *Chem. Rev.* **2010**, *110*, 6595–6663.

(34) Huang, Q.-H.; Ling, T.; Qiao, S.-Z.; Du, X.-W. Pyrite nanorod arrays as an efficient counter electrode for dye-sensitized solar cells. *J. Mater. Chem. A* **2013**, *1*, 11828–11833.

(35) Wang, Y.-C.; Wang, D.-Y.; Jiang, Y.-T.; Chen, H.-A.; Chen, C.-C.; Ho, K.-C.; Chou, H.-L.; Chen, C.-W. FeS_2 Nanocrystal Ink as a Catalytic Electrode for Dye-Sensitized Solar Cells. *Angew. Chem. Int. Ed.* **2013**, *52*, 6694–6698.

(36) Susac, D.; Zhu, L.; Teo, M.; Sode, A.; Wong, K. C.; Wong, P. C.; Parsons, R. R.; Bizzotto, D.; Mitchell, K. A. R.; Campbell, S. A. Characterization of FeS_2-Based Thin Films as Model Catalysts for the Oxygen Reduction Reaction. *J. Phys. Chem. C* **2007**, *111*, 18715–18723.

(37) Li, L. S.; Cabán-Acevedo, M.; Girard, S. N.; Jin, S. High-purity iron pyrite (FeS_2) nanowires as high-capacity nanostructured cathodes for lithium-ion batteries. *Nanoscale* **2014**, *6*, 2112–2118.

(38) Wang, Q. H.; Jiao, L. F.; Han, Y.; Du, H. M.; Peng, W. X.; Huan, Q. N.; Song, D. W.; Si, Y. C.; Wang, Y. J.; Yuan, H. T. CoS_2 Hollow Spheres: Fabrication and Their Application in Lithium-Ion Batteries. *J. Phys. Chem. C* **2011**, *115*, 8300–8304.

(39) Faber, M. S.; Park, K.; Cabán-Acevedo, M.; Santra, P. K.; Jin, S. Earth-Abundant Cobalt Pyrite (CoS_2) Thin Film on Glass as a Robust, High-Performance Counter Electrode for Quantum Dot-Sensitized Solar Cells. *J. Phys. Chem. Lett.* **2013**, *4*, 1843–1849.

(40) Selinsky, R. S.; Ding, Q.; Faber, M. S.; Wright, J. C.; Jin, S. Quantum dot nanoscale heterostructures for solar energy conversion. *Chem. Soc. Rev.* **2013**, *42*, 2963–2985.

(41) Kamat, P. V. Quantum Dot Solar Cells. *The Next Big Thing* in Photovoltaics. *J. Phys. Chem. Lett.* **2013**, *4*, 908–918.

(42) Duan, X. L.; Gao, Z. Y.; Chang, J. L.; Wu, D. P.; Ma, P. F.; He, J. J.; Xu, F.; Gao, S. Y.; Jiang, K. CoS_2–graphene composite as efficient catalytic counter electrode for dye-sensitized solar cell. *Electrochim. Acta* **2013**, *114*, 173–179.

(43) Zhu, L.; Susac, D.; Teo, M.; Wong, K. C.; Wong, P. C.; Parsons, R. R.; Bizzotto, D.; Mitchell, K. A. R.; Campbell, S. A. Investigation of CoS_2-based thin films as model catalysts for the oxygen reduction reaction. *J. Catal.* **2008**, *258*, 235–242.

(44) Jirkovský, J. S.; Björling, A.; Ahlberg, E. Reduction of Oxygen on Dispersed Nanocrystalline CoS_2. *J. Phys. Chem. C* **2012**, *116*, 24436–24444.

(45) Zhao, C.; Li, D. Q.; Feng, Y. J. Size-controlled hydrothermal synthesis and high electrocatalytic performance of CoS_2 nanocatalysts as non-precious metal cathode materials for fuel cells. *J. Mater. Chem. A* **2013**, *1*, 5741–5746.

(46) Peng, S. J.; Li, L. L.; Tan, H. T.; Cai, R.; Shi, W. H.; Li, C. C.; Mhaisalkar, S. G.; Srinivasan, M.; Ramakrishna, S.; Yan, Q. Y. MS_2 (M = Co and Ni) Hollow Spheres with Tunable Interiors for High-Performance Supercapacitors and Photovoltaics. *Adv. Funct. Mater.* **2014**, *24*, 2155–2162.

(47) Pang, H.; Wei, C. Z.; Li, X. X.; Li, G. C.; Ma, Y. H.; Li, S. J.; Chen, J.; Zhang, J. S. Microwave-assisted synthesis of NiS_2 nanostructures for supercapacitors and cocatalytic enhancing photocatalytic H_2 production. *Sci. Rep.* **2014**, *4*, DOI: 10.1038/srep03577.

(48) Bonde, J.; Moses, P. G.; Jaramillo, T. F.; Nørskov, J. K.; Chorkendorff, I. Hydrogen evolution on nano-particulate transition metal sulfides. *Faraday Discuss.* **2008**, *140*, 219–231.

(49) Du, P. W.; Eisenberg, R. Catalysts made of earth-abundant elements (Co, Ni, Fe) for water splitting: Recent progress and future challenges. *Energy Environ. Sci.* **2012**, *5*, 6012–6021.

(50) Radich, J. G.; Dwyer, R.; Kamat, P. V. Cu_2S Reduced Graphene Oxide Composite for High-Efficiency Quantum Dot Solar Cells. Overcoming the Redox Limitations of S^{2-}/S_n^{2-} at the Counter Electrode. *J. Phys. Chem. Lett.* **2011**, *2*, 2453–2460.

(51) Chang, S.-H.; Lu, M.-D.; Tung, Y.-L.; Tuan, H.-Y. Gram-Scale Synthesis of Catalytic Co_9S_8 Nanocrystal Ink as a Cathode Material for Spray-Deposited, Large-Area Dye-Sensitized Solar Cells. *ACS Nano* **2013**, *7*, 9443–9451.

(52) Wang, M. K.; Anghel, A. M.; Marsan, B.; Ha, N.-L. C.; Pootrakulchote, N.; Zakeeruddin, S. M.; Grätzel, M. CoS Supersedes Pt as Efficient Electrocatalyst for Triiodide Reduction in Dye-Sensitized Solar Cells. *J. Am. Chem. Soc.* **2009**, *131*, 15976–15977.

(53) Jaramillo, T. F.; Jørgensen, K. P.; Bonde, J.; Nielsen, J. H.; Horch, S.; Chorkendorff, I. Identification of Active Edge Sites for Electrochemical H_2 Evolution from MoS_2 Nanocatalysts. *Science* **2007**, *317*, 100–102.

(54) Karunadasa, H. I.; Montalvo, E.; Sun, Y. J.; Majda, M.; Long, J. R.; Chang, C. J. A Molecular MoS_2 Edge Site Mimic for Catalytic Hydrogen Generation. *Science* **2012**, *335*, 698–702.

(55) Kibsgaard, J.; Jaramillo, T. F.; Besenbacher, F. Building an appropriate active-site motif into a hydrogen-evolution catalyst with thiomolybdate $[Mo_3S_{13}]^{2-}$ clusters. *Nature Chem.* **2014**, *6*, 248–253.

APPENDIX 1

Supporting Information for CHAPTER 2: Earth-Abundant Cobalt Pyrite (CoS_2) Thin Film on Glass as a Robust, High-Performance Counter Electrode for Quantum Dot-Sensitized Solar Cells †

A1.1. Experimental Details

A1.1.1. Mesoscopic TiO_2 Photoanode Preparation

The mesoscopic TiO_2 photoanodes were prepared by following a published procedure with minor modifications.[1] A fluorine-doped tin oxide on soda lime glass (FTO/glass) substrate (Hartford Glass Co. Inc., TEC 8, 8 Ω sq^{-1}, 2.2 mm thick) was first patterned by etching with Zn powder (Alfa Aesar, median 6–9 micron, 97.5%) and hydrochloric acid (Sigma-Aldrich, 37%) around a mask formed by strips of adhesive tape (3M, Scotch® Magic™ Tape). Next, the FTO/glass substrate was ultrasonically cleaned in a detergent solution (Fisher Scientific, Versa-

† This appendix was originally made available online as the Supporting Information for Faber, M. S.; Park, K.; Cabán-Acevedo, M.; Santra, P. K.; Jin, S. *J. Phys. Chem. Lett.* Earth-Abundant Cobalt Pyrite (CoS_2) Thin Film on Glass as a Robust, High-Performance Counter Electrode for Quantum Dot-Sensitized Solar Cells **2013**, *4*, 1843–1849 before being adapted here.

Clean, diluted 1:4 with deionized water), then thoroughly rinsed with deionized water and ethanol. The substrate was then sonicated at 100 W for 10 min in ethanol, rinsed with fresh ethanol, and blown dry with nitrogen before cleaning with oxygen plasma (150 W RF, 1 sccm O_2, < 200 mTorr, 3 min) to remove any organic residues. The FTO/glass substrate was immersed in a 40 mM $TiCl_4(aq)$ solution at 70 °C for 30 min and then rinsed with deionized water and ethanol and blown dry under a stream of nitrogen. A transparent nanocrystalline mesoscopic anatase TiO_2 film was cast onto the clean FTO/glass substrate by doctor blading a TiO_2 nanoparticle paste (Solaronix, Ti-Nanoxide T/SP, ~18 wt%, 15–20 nm diameter particles) through a mask formed by strips of adhesive tape. The typical area of the TiO_2 film was approximately 0.25 cm^2. This film was allowed to dry in ambient air for 1 h before drying at 80 °C for 1 h. Then, the TiO_2 photoanodes were transferred to a muffle furnace and the temperature was ramped from 100 °C to 500 °C at 10 °C min^{-1}, holding at 500 °C for 1 h to remove any organic binders and sinter the particles of the mesoscopic TiO_2 film. After cooling to room temperature, a scattering layer of anatase TiO_2 particles was cast over the mesoscopic TiO_2 film by doctor blading a TiO_2 particle paste (Solaronix, Ti-Nanoxide R/SP, ~18 wt%, > 100 nm diameter particles), as described above. The scattering layer was then allowed to dry in ambient air, then at 80 °C, and finally sintered at 500 °C, all using the same procedures described above for the mesoscopic TiO_2 film. Finally, the TiO_2 photoanodes were again treated with a 40 mM $TiCl_4(aq)$ solution at 70 °C for 30 min, as described above, and then sintered at 500 °C (10 °C min^{-1} ramp rate from 100 °C) for 30 min.

A1.1.2. TiO_2 Film Sensitization by Successive Ionic Layer Adsorption and Reaction (SILAR)

The TiO_2 films were sensitized through the sequential SILAR deposition of CdS, CdSe, and ZnS, following procedures previously described.[2,3] Briefly, the TiO_2 photoanode was first treated with oxygen plasma, as described above, and then further cleaned by exposure to short wave ultraviolet light for 30 min immediately before SILAR deposition. CdS was first deposited over the TiO_2 film by alternately dipping the photoanode in room-temperature cation and anion precursor solutions of 0.1 M $Cd(NO_3)_2 \bullet 4H_2O$ (Fluka, 98%) in methanol and 0.1 M $Na_2S \bullet 9H_2O$ (Sigma-Aldrich, ≥ 99.99%) in 1:1 deionized water/methanol, respectively, for 1 min, with a 30 s dip rinse in methanol followed by rinsing with flowing methanol and blowing dry with nitrogen after each precursor solution dip. This sequence was repeated for a total of 5 CdS SILAR cycles. The CdS-sensitized photoanode was immediately transferred to a nitrogen-filled glove box for CdSe SILAR using the procedure of Lee *et al*.[4] CdSe SILAR precursor solutions of 30 mM $Cd(NO_3)_2 \bullet 4H_2O$ and 30 mM Se^{2-} in ethanol (Sigma-Aldrich, 200 proof, anhydrous, ≥ 99.5%) were first prepared in the glove box. The Se^{2-} precursor solution was prepared through the *in situ* reduction of SeO_2 (Sigma-Aldrich, ≥ 99.9%) with excess $NaBH_4$ (Fluka, ≥ 99%). The CdS-sensitized photoanode was then alternately dipped in these room-temperature precursor solutions for 30 s inside the glove box, with a 30 s dip rinse in ethanol followed by rinsing with flowing ethanol and blowing dry with nitrogen after each precursor solution dip. This sequence was repeated for a total of 8 CdSe SILAR cycles. Finally, the CdS/CdSe-sensitized photoanode was removed from the glove box and immediately coated with 2 SILAR cycles of ZnS deposition using room-temperature precursor solutions of 0.1 M $Zn(CH_3CO_2)_2 \bullet 2H_2O(aq)$ (Sigma-Aldrich,

98+%) and 0.1 M $Na_2S•9H_2O$ in 1:1 deionized water/methanol with the same cycle sequence as that used for CdS SILAR. The photoanodes were generally characterized in a sandwich-style thin-layer liquid-junction quantum dot-sensitized solar cell (QDSSC) configuration immediately after SILAR sensitization; photoanodes not immediately characterized were stored in the dark in a nitrogen-filled glove box.

A1.1.3. Long-Term Measurement of Short-Circuit Photocurrent Density Stability

In both measurements of short-circuit photocurrent density (J_{sc}) stability, AM1.5G (100 mW cm^{-2}) simulated sunlight was supplied by 1 kW Xe short arc lamp solar simulator (Newport Corp., Model 91191; AM1.5G filter) and the photocurrent was recorded at the short-circuit condition using a Bio-Logic SP-200 potentiostat. Before starting each 2-h J_{sc} stability measurement, the light intensity at the position of the photoanode was verified using an NREL-calibrated and NIST-traceable monocrystalline Si reference solar cell (Photo Emission Tech., Inc.; Model #60623).

The long-term J_{sc} stability under continuous 1 sun illumination was measured with a cobalt pyrite (CoS_2) counter electrode (CE) in both the sandwich-style thin-layer QDSSC and two-electrode open cell configurations. The QDSSC devices were assembled with a CoS_2 CE using the procedures described in Chapter 2. To set up the two-electrode open cell measurement of J_{sc} stability, a custom electrochemical cell was filled with approximately 15 mL of 2 M $Na_2S(aq)$/2 M S(*aq*) sulfide/polysulfide electrolyte. The sulfide/polysulfide solution was sparged with Ar for 1 h and then blanketed with Ar for the duration of the stability measurement to suppress electrolyte oxidation. A CdS/CdSe-sensitized mesoscopic TiO_2 photoanode (geometrical area = 0.137 cm^2, measured using a calibrated digital image and ImageJ) was

positioned near the flat quartz window of the electrochemical cell, and a CoS_2 CE (geometrical area = 3.42 cm^2) was positioned opposite the photoanode, with an electrode spacing of approximately 1.5 cm. The photoanode was illuminated from the glass side, and since the photoanode was not apertured, the full geometrical area of the photoanode was used to convert the measured current to a current density. The electrolyte was not stirred or otherwise perturbed during the stability measurement. Immediately after the stability measurement, the current density–voltage (*J*–*V*) characteristics of the photoanode were recorded using the procedure given in Chapter 2. In the calculation of solar light-to-electricity conversion efficiency (η), light absorption by the sulfide/polysulfide electrolyte (approximately 3 mm path length), which likely altered the spectral irradiance distribution of the incident light and attenuated its intensity, was not taken into account.

A1.1.4. Measurement of Incident Photon-to-Electron Conversion Efficiency Action Spectra

The incident photon-to-electron conversion efficiency (IPCE) action spectra were measured for sandwich-style thin-layer QDSSCs with either a Pt or CoS_2 CE assembled using the procedures described in Chapter 2. In these measurements, light from a 250-W quartz tungsten halogen lamp (Newport Corp., Model 67011) was passed through a monochromator (Princeton Instruments/Acton, Model MS-2300i) and focused into a custom optical fiber (Newport Corp.) that was used to direct the monochromated light to a dark measurement chamber. The monochromated light emitted from the optical fiber was passed through a 400-nm longpass filter (Thorlabs Inc., FGL400M) to eliminate second-order diffraction lines (and, only when measuring the spectral intensity of the monochromated light source, a TEC 8 FTO/glass

filter to account for intensity attenuation due to absorption, reflection, or scattering by the optically transparent electrode of the photoanode). The spectral intensity of the monochromated light source was measured from 750 to 400 nm with a step size of 5 nm using a NIST-traceable calibrated Si photodiode power sensor (Thorlabs Inc., S120C; masked with a 0.0792 cm^2 aperture) connected to a digital power meter (Thorlabs Inc., PM100D). Before measuring their response under monochromated light, *J–V* curves for each QDSSC under AM1.5G (100 mW cm^{-2}) illumination were recorded using the procedure given in Chapter 2. Then, the current produced by the QDSSCs under the monochromated illumination was recorded over the same wavelength range using a Bio-Logic SP-200 potentiostat.

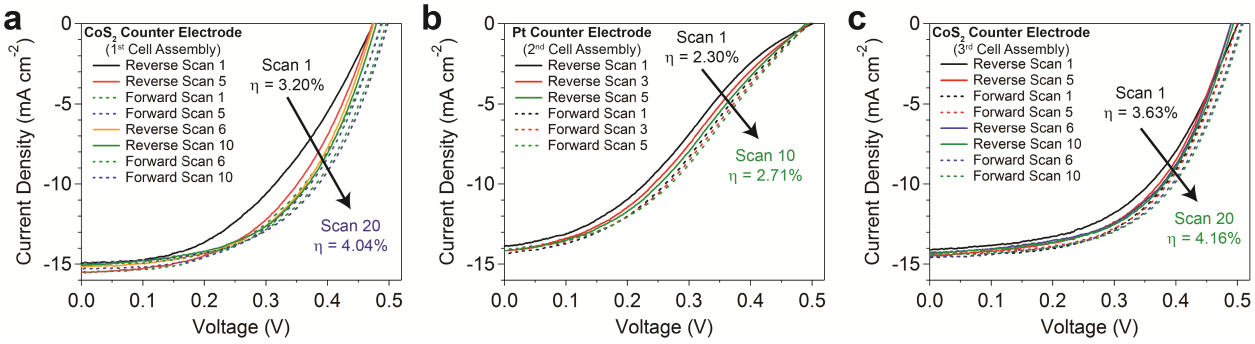

Figure A1.1. Demonstration of the stability of a single CdS/CdSe-sensitized mesoscopic TiO_2 photoanode assembled into sandwich-style thin-layer quantum dot-sensitized solar cells (QDSSCs) with either (a, c) a cobalt pyrite (CoS_2) thin film counter electrode (CE) or (b) a Pt CE and filled with 2 M $Na_2S(aq)$/2 M $S(aq)$ sulfide/polysulfide electrolyte, carried out in the sequence shown. (a) Repeated current density–voltage (*J–V*) measurement of a QDSSC assembled with a CoS_2 CE (first cell assembly) in both the forward and reverse scanning directions to highlight the CoS_2 CE stability, with a 26.3% increase in solar light-to-electricity conversion efficiency (η) (from 3.20% to 4.04%) observed after 20 consecutive *J–V* measurements. (b) Forward and reverse *J–V* measurements of the same photoanode from (a) reassembled into a QDSSC with a Pt CE and fresh electrolyte (second cell assembly), with a 17.8% increase in η (from 2.30% to 2.71%) observed after 10 consecutive *J–V* measurements. (c) Forward and reverse *J–V* measurements of the same photoanode from (b) reassembled into a QDSSC with a CoS_2 CE and fresh electrolyte (third cell assembly), with a 14.6% increase in η (from 3.63% to 4.16%) observed after 20 consecutive *J–V* measurements.

Table A1.1. Comparison of the Photovoltaic Device Characteristics Measured with Representative Photoanodes from Different Batches Assembled with a CoS_2 (or Pt) Counter Electrode.

Sample	V_{oc} (V)	J_{sc} (mA cm^{-2})	*FF*	η (CoS_2) (%)	η (Pt) (%) [a]
1	0.517	14.62	0.458	3.01 [b]	2.34 [b]
2	0.490	14.62	0.539	3.40 [b]	1.98 [b]
3	0.486	12.80	0.550	3.01 [b]	1.85 [b]
4	0.508	14.12	0.528	3.79	2.43
5	0.510	14.44	0.565	4.16 [c]	2.71
6	0.506	15.32	0.510	3.96	N/A [d]
7	0.508	13.60	0.561	3.88	N/A [d]
8	0.490	13.57	0.563	3.74	N/A [d]
9	0.476	14.28	0.528	3.59	N/A [d]

[a] Photovoltaic conversion efficiency measured for the same photoanode with a Pt counter electrode.

[b] Incident AM1.5G light intensity deviated slightly from the standard 100 mW cm^{-2}; however, this difference in illumination intensity was taken into account when calculating photovoltaic conversion efficiency.

[c] Measured in a QDSSC that had been disassembled and reassembled twice using a CoS_2 CE with no Ti adhesion layer.

[d] Not measured.

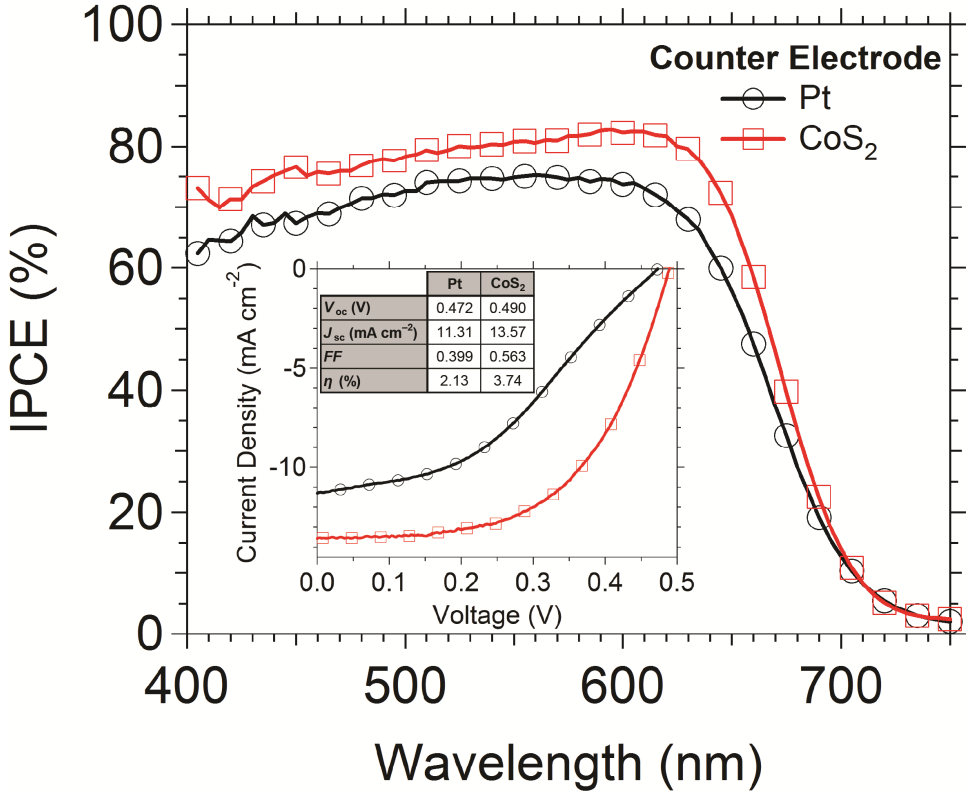

Figure A1.2. Incident photon-to-electron conversion efficiency (IPCE) action spectra for two quantum dot-sensitized solar cells (QDSSCs), one employing a CoS_2 counter electrode (CE) and the other a Pt CE. The inset current density–voltage (*J*–*V*) curves were recorded for the two QDSSCs immediately before IPCE measurement, and the photovoltaic device characteristics corresponding to these *J*–*V* curves are summarized in the inset table.

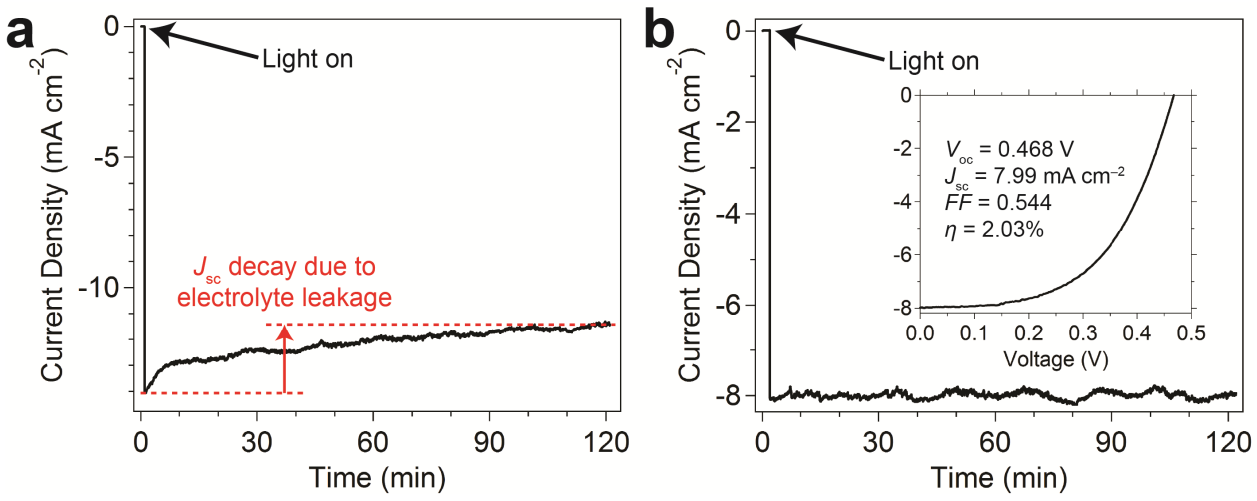

Figure A1.3. Long-term measurement of the short-circuit photocurrent density (J_{sc}) produced by a CdS/CdSe-sensitized mesoscopic TiO_2 photoanode under continuous illumination with AM1.5G (100 mW cm^{-2}) simulated sunlight for 2 h in (a) a sandwich-style thin-layer quantum dot-sensitized solar cell and (b) a two-electrode open cell configuration, both using a CoS_2 thin film counter electrode. The gradual decrease in J_{sc} over the course of the measurement in (a) resulted from electrolyte leakage, visible as bubbles in the cell after the stability measurement. The inset current density–voltage (J–V) curve in (b) was recorded immediately after the 2-h stability measurement and corroborates the magnitude of the stable J_{sc} measured in the long-term measurement. The J–V curve was exactly reproducible upon repeated cycling. Note that the two-electrode open cell measurement configuration was not optimized for high performance and consequently exhibited low J_{sc}.

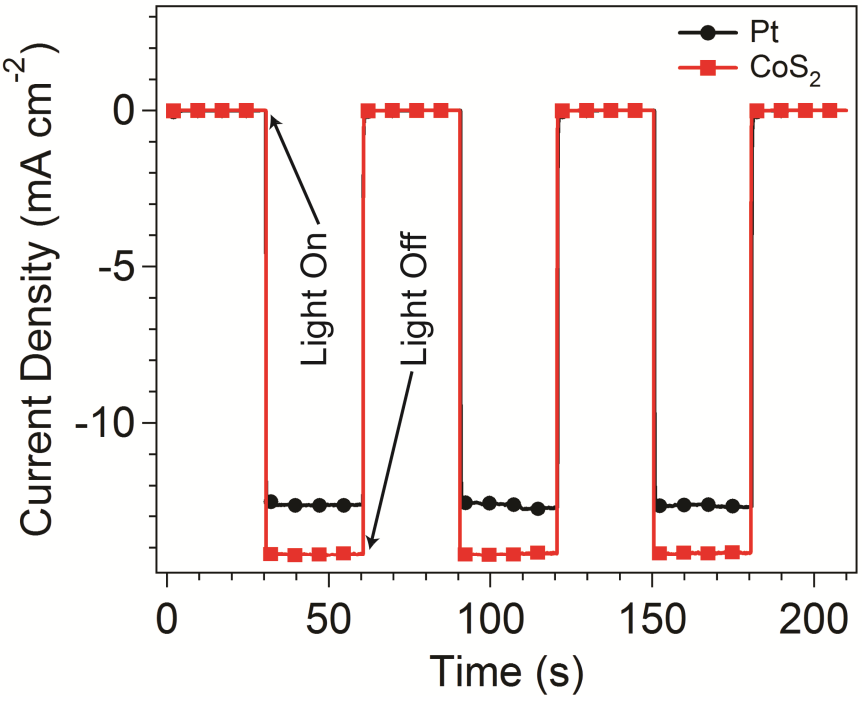

Figure A1.4. Measurement of the short-circuit photocurrent density (J_{sc}) response and stability under chopped simulated AM1.5G (100 mW cm^{-2}) illumination for a quantum dot-sensitized solar cell (QDSSC) that incorporated either a cobalt pyrite (CoS_2) or Pt counter electrode (CE). The sharp and stable photocurrent response indicates the stability of the CoS_2 CE (red trace, square markers). Comparison to the response of the same photoanode assembled with a Pt CE (black trace, circle markers) highlights the greater J_{sc} achievable with the CoS_2 CE.

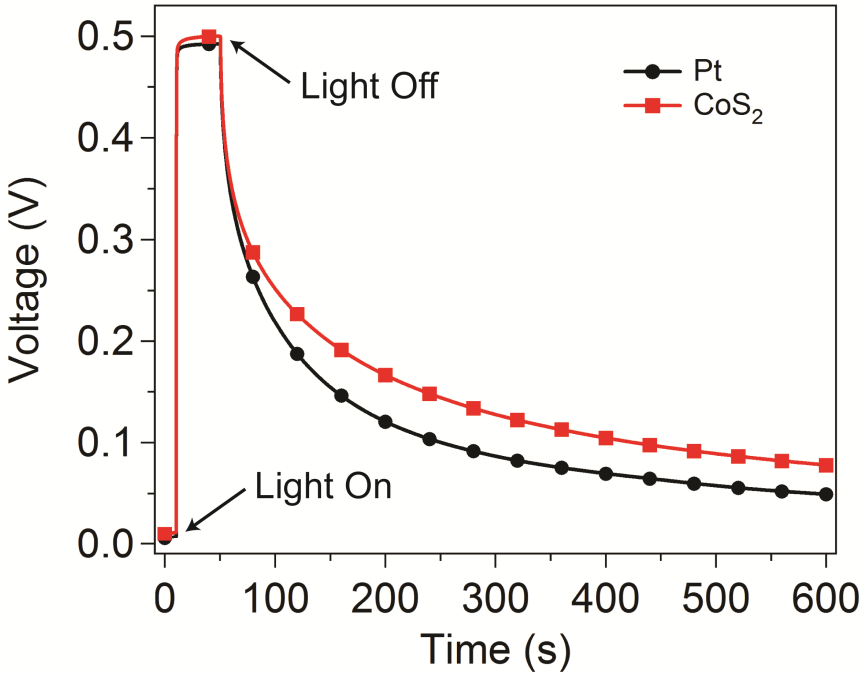

Figure A1.5. Measurement of the open-circuit voltage (V_{oc}) rise and decay under application and subsequent removal of simulated AM1.5G (100 mW cm^{-2}) illumination for a quantum dot-sensitized solar cell (QDSSC) that incorporated either a cobalt pyrite (CoS_2) or Pt counter electrode (CE). For both the CoS_2 (red trace, square markers) and Pt (black trace, circle markers) CEs, V_{oc} rose sharply and remained stable. Upon removal of illumination, the V_{oc} decay for both counter electrodes was slow, indicating that there were few charge recombination pathways in the photoanode.

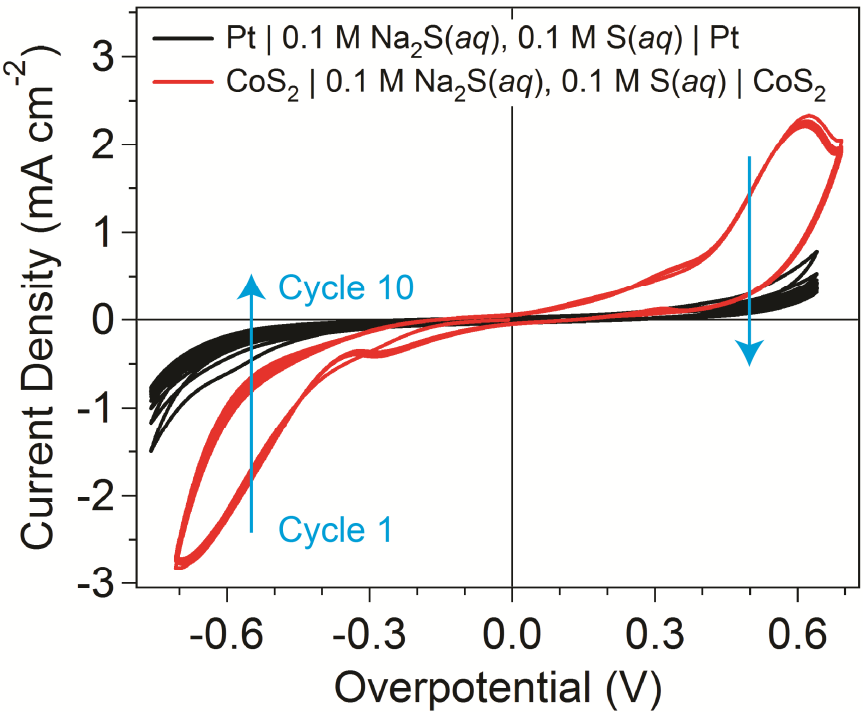

Figure A1.6. Cyclic voltammetry of cobalt pyrite (CoS_2) and Pt symmetrical sandwich-style thin-layer electrochemical cells filled with a 0.1 M S^{2-}/0.1 M S aqueous sulfide/polysulfide electrolyte, with a total of 10 complete cycles shown. The cyclic voltammograms were recorded at a rate of 50 mV s^{-1}, initially scanning cathodically from the open circuit potential. Rapid deactivation of the Pt electrodes due to sulfur species adsorption, resulting in diminishing current density upon repeated cycling, is evident (black trace). The high and reproducible current density of the CoS_2 electrode (red trace) upon repeated cycling confirms the stability of CoS_2 in sulfide/polysulfide electrolyte. The improved kinetics of the CoS_2 electrode over the Pt electrode can also be seen in the slight diffusion-limited shifts in electrolyte equilibrium potential for the CoS_2 cell, which result from local changes in the concentrations of the oxidized and reduced species at the CoS_2 electrode surface during cycling.

A1.2. References

(1) Choi, H.; Nicolaescu, R.; Paek, S.; Ko, J.; Kamat, P. V. Supersensitization of CdS Quantum Dots with a Near-Infrared Organic Dye: Toward the Design of Panchromatic Hybrid-Sensitized Solar Cells. *ACS Nano* **2011**, *5*, 9238–9245.

(2) Radich, J. G.; Dwyer, R.; Kamat, P. V. Cu_2S Reduced Graphene Oxide Composite for High-Efficiency Quantum Dot Solar Cells. Overcoming the Redox Limitations of S^{2-}/S_n^{2-} at the Counter Electrode. *J. Phys. Chem. Lett.* **2011**, *2*, 2453–2460.

(3) Santra, P. K.; Kamat, P. V. Mn-Doped Quantum Dot Sensitized Solar Cells: A Strategy to Boost Efficiency over 5%. *J. Am. Chem. Soc.* **2012**, *134*, 2508–2511.

(4) Lee, H.; Wang, M. K.; Chen, P.; Gamelin, D. R.; Zakeeruddin, S. M.; Grätzel, M.; Nazeeruddin, M. K. Efficient CdSe Quantum Dot-Sensitized Solar Cells Prepared by an Improved Successive Ionic Layer Adsorption and Reaction Process. *Nano Lett.* **2009**, *9*, 4221–4227.

APPENDIX 2

Supporting Information for CHAPTER 3: High-Performance Electrocatalysis Using Metallic Cobalt Pyrite (CoS_2) Micro- and Nanostructures [†]

A2.1. Experimental Details

A2.1.1. Glass and Graphite Substrate Preparation

A borosilicate plate glass substrate (1.5 cm × 3.0 cm; 3.3 mm thick) was first manually roughened on one side with SiC paper (Allied High Tech Products, Inc.; 320 grit) for several minutes before it was ultrasonically cleaned at 100 W for 30 min in a detergent solution (Fisher Scientific, Versa-Clean, diluted 1:4 with deionized water) and then thoroughly rinsed with deionized water and ethanol. To further degrease the substrate, it was sonicated at 100 W for 10 min in 200-proof ethanol and then rinsed with fresh ethanol and blown dry under a stream of nitrogen. Finally, the substrate was oxygen plasma cleaned (150 W RF, < 200 mTorr, 1 sccm O_2,

---

[†] This appendix was originally made available online as the Supporting Information for Faber, M. S.; Dziedzic, R.; Lukowski, M. A.; Kaiser, N. S.; Ding, Q.; Jin, S. High-Performance Electrocatalysis Using Metallic Cobalt Pyrite (CoS_2) Micro- and Nanostructures. *J. Am. Chem. Soc.* **2014**, DOI: 10.1021/ja504099w before being adapted here.

3 min) to remove any organic residues.

Graphite disk substrates (6.0 mm diameter; < 1 mm thick) were prepared by cutting and mechanically thinning slices of a graphite rod (Ultra Carbon Corp., Ultra "F" Purity). Slices of the graphite rod were thinned by abrading both sides with SiC paper. The graphite disks were cleaned by sequentially sonicating (100 W) in deionized water for 10 min, then in aqua regia (*i.e.*, 3:1 HCl(*aq*) (Sigma-Aldrich, 37%):HNO_3(*aq*) (Sigma-Aldrich, 68.0–70.0%)) for 10 min, and finally in fresh deionized water for 10 min to remove loose graphite dust and any metal impurities. Finally, the clean graphite disks were dried in a forced-air oven at 120 °C.

A2.1.2. Cobalt Film Preparation

The cobalt film was deposited on the graphite and roughened borosilicate glass substrates by following a published procedure with minor modifications.[1] Specifically, 100 nm of Co (Kurt J. Lesker, 99.95%) was deposited on the rotated substrates at a rate of 1 Å s^{-1} using an electron-beam evaporation system (Angstrom Engineering).

A2.1.3. *β*-$Co(OH)_2$ Microwire Synthesis

The cobalt hydroxide (*β*-$Co(OH)_2$; brucite structure type) microwires (MWs) were synthesized on graphite and roughened borosilicate glass substrates by refining a published procedure.[2,3] In a typical synthesis, 10 mmol of $Co(NO_3)_2$•$6H_2O$ (Sigma-Aldrich, ≥ 98%) was dissolved in 10 mL of neutral distilled water (Thermo Scientific, Barnstead Nanopure, 18.2 MΩ cm) in ambient air with vigorous magnetic stirring, yielding a clear, light pink $Co(H_2O)_6^{2+}$(*aq*) solution. Then, 40 mL of concentrated NH_4OH(*aq*) solution (Sigma-Aldrich, 28.0–30.0%) was added dropwise to the stirred $Co(H_2O)_6^{2+}$(*aq*) solution over several minutes, which resulted in a series of color changes concordant with the relative $Co(H_2O)_6^{2+}$(*aq*) and $Co(NH_3)_6^{2+}$(*aq*)

complex acidities and stabilities. After adding approximately 5 mL of $NH_4OH(aq)$, blue $Co(H_2O)_4(OH)_2$ solid begins to precipitate, consistent with the expected acid–base chemistry between the $Co(H_2O)_6^{2+}$ complex and free ammonia in solution, giving a turbid blue suspension. Upon further ammonia addition, the $Co(H_2O)_4(OH)_2$ precipitate further reacts to give soluble anionic complexes. Ammonia eventually displaces the original aqua ligands, yielding a clear, deep red solution of $Co(NH_3)_6^{2+}(aq)$ upon complete addition of the $NH_4OH(aq)$ solution. The reaction solution was then rapidly stirred in ambient air for 30 min. During this time, the solution color gradually transitioned from deep red to dark brown, owing to the oxidation of Co^{2+} to Co^{3+} in air and the concomitant formation of $[(NH_3)_5Co^{III}O_2Co^{III}(NH_3)_5]^{4+}$, a μ-peroxo-bridged binuclear complex ion.[4] Then, 16 mL of the reaction solution was added to a 23-mL polytetrafluoroethylene (Teflon, PTFE) autoclave liner (Parr Instrument Co., No. A280AC) containing the substrate (either roughened borosilicate glass or graphite disks mounted on roughened borosilicate glass using double-sided carbon tape) angled against the liner wall with the side of interest facing down. The reaction vessel was loosely covered with a watch glass (3 inch diameter, concave side up) and heated at 85 °C for 14 h in a ventilated forced-air convection oven. During heating, $[(NH_3)_5Co^{III}O_2Co^{III}(NH_3)_5]^{4+}$ slowly decomposes, releasing O_2; at the same time, ammonia rapidly evaporates from the reaction solution, reducing the ammine ligand concentration and lowering the solution pH enough to favor $Co(OH)_2$ precipitation, consistent with the cobalt Pourbaix diagram. In this way, the supersaturation of free Co^{2+} is controlled to promote one-dimensional growth driven by axial screw dislocations.[2,5] After the 14-h reaction, ~9 mL of reaction solution remained in the PTFE vessel, indicating substantial evaporation of solvent. The substrate and the walls of the reaction vessel were coated with pink precipitate.

Occasionally the MW precipitate was black in color, indicating the minor presence of Co_3O_4, but this was not found to impact their subsequent thermal sulfidation. The substrate was thoroughly washed rinsed with excess distilled H_2O, then with 200-proof ethanol, and dried under a stream of nitrogen.

A2.1.3.1. β-Co(OH)$_2$ Microwire "Flower" Synthesis

The β-$Co(OH)_2$ synthesis detailed in Section A2.1.3 usually yields MWs on graphite like those shown in Figure 3.1C of Chapter 3; however, in approximately 10% of our reactions, alternate β-$Co(OH)_2$ morphologies have been obtained on graphite, including sparse microwires, nanowire bundles, and, in some cases, hierarchical microwire "flowers" like those shown in Figure 3.4A of Chapter 3. Because this synthesis is conducted in open reaction vessels, the rate of ammonia evaporation—which subsequently dictates the rate of $Co(OH)_2$ precipitation—is not precisely controlled, sometimes leading to unusual product morphologies. With proper control of the ammonia evaporation rate, however, this synthesis could be optimized to more consistently yield the hierarchical MW "flower" morphology.

A2.1.4. $Co(OH)(CO_3)_{0.5}$•xH_2O ("CHCH") Nanowire Synthesis

The cobalt hydroxide carbonate hydrate ($Co(OH)(CO_3)_{0.5}$•xH_2O; "CHCH") nanowires (NWs) were synthesized on graphite and roughened borosilicate glass substrates by following a published procedure with minor modifications.[6] In a typical synthesis, 1.5 mmol of $Co(NO_3)_2$•$6H_2O$, 3 mmol NH_4F (Sigma-Aldrich, ≥ 98.0%), and 7.5 mmol $(NH_2)_2CO$ (Riedel-de Haën, 99.5–100.5%) were dissolved in 50 mL of distilled water in ambient air, yielding a clear, light pink solution. Then, 16 mL of this solution was transferred to a 23-mL PTFE autoclave liner containing the substrate (either roughened borosilicate glass or graphite disks mounted on

roughened borosilicate glass) angled against the liner wall with the side of interest facing down. The stainless steel autoclave was sealed and heated at 110 °C for 5 h and then cooled to room temperature under flowing water. The substrate was removed from the autoclave liner and thoroughly washed rinsed with excess distilled H_2O, then with 200-proof ethanol, and dried under a stream of nitrogen.

A2.1.5. Thermal Sulfidation of Co Films, β-$Co(OH)_2$ Microwires, and CHCH Nanowires

The as-prepared Co films, β-$Co(OH)_2$ MWs, and CHCH NWs on graphite or glass were thermally sulfidized to CoS_2 (cobalt disulfide, CoS_2; cattierite) using a previously described procedure.[1] Briefly, the substrates covered with precursor material were placed in the center of a fused silica tube in a home-built reactor equipped with both pressure and gas flow controllers. An alumina boat containing 2 g of S powder (Sigma-Aldrich, 99.5–100.5%) was placed in the tube at the farthest upstream position within the tube furnace (Lindberg/Blue M, TF55035A-1). The tube was purged of air and maintained at a slight positive pressure of 780 Torr under a steady flow of Ar carrier gas (99.999%) at 25 sccm. The furnace temperature was ramped from room temperature to 500 °C at a rate of approximately 60 °C min^{-1} and held for 1 h. The tube furnace was then opened to allow natural cooling of the sample back to room temperature under Ar flow. The as-sulfidized samples were dipped in CS_2 (Sigma-Aldrich, 99.9%) for 30 s to remove any S residues, then thoroughly rinsed with fresh CS_2 and 200-proof ethanol and dried under a stream of nitrogen.

A2.1.6. Determination of CoS_2 Micro- or Nanowire Mass Loading on Graphite Disk Substrates

In order to determine the amount of CoS_2 MW or NW catalyst material that was

synthesized on the graphite disk substrates, the mass of the electrode was recorded using a Mettler-Toledo XS105 DualRange balance both before beginning the respective CoS_2 preparation and after completing the thermal sulfidation and rinsing procedures. Prior to weighing the clean graphite disk substrates, they were dehydrated in a forced-air oven at 120 °C for at least 30 min.

A2.1.7. Electrochemical Characterization of Catalytic Activity Toward the Hydrogen Evolution Reaction (HER)

All electrochemical measurements were performed in a three-electrode configuration using a rotating disk electrode (RDE) setup (Bioanalytical Systems, Inc.; RDE-2) and recorded using a Bio-Logic SP-200 potentiostat. Each measurement was performed in room-temperature 0.5 M $H_2SO_4(aq)$ electrolyte (prepared using 18.2 MΩ distilled water) continuously purged with $H_2(g)$ (99.999%) using a saturated calomel reference electrode (SCE) (CH Instruments) and a graphite rod (National Carbon Co., AGKSP Spectroscopic Electrode) as the counter electrode. The working electrode in each measurement was a graphite-supported CoS_2 film, MW array, or NW array (used without any further cleaning or etching) affixed to a glassy carbon RDE tip using silver paint (Ted Pella, PELCO Colloidal Silver). The CoS_2 samples were typically measured within 24 h of preparation to prevent any potential surface oxidation in air, though longer air exposure was not found to be deleterious to performance. To allow potentials to be referenced against the reversible hydrogen electrode (RHE), the SCE was calibrated against the reversible hydrogen potential using platinum wire (Kurt J. Lesker, 99.99%; 0.50 mm diameter) as both the working and counter electrodes after each measurement. Linear sweep or cyclic voltammograms of the CoS_2 MW and NW samples were measured from +0.25 V to −0.45 V vs.

RHE at a scan rate of 3 mV s^{-1} in both the forward and reverse directions while rotating the working electrode at 2000 RPM. The CoS_2 film samples were measured in the narrowed voltage window of +0.25 V to −0.24 V vs. RHE to minimize film damage during hydrogen evolution. The current response of each sample was measured across the respective voltage window a minimum of five times, and the final sweep was always used for analysis. The Pt reference trace was recorded using an electrochemically cleaned Pt wire that was masked to a calculated geometric surface area of 0.452 cm^2 using paraffin wax as the working electrode. After voltammetric characterization, electrochemical impedance spectroscopy (EIS) was performed in potentiostatic mode at −0.24 V vs. RHE, applying a sinusoidal voltage with an amplitude of 10 mV and scanning frequency from 200 kHz to 50 mHz. The main arc in each EIS spectrum was modeled using a simplified Randles equivalent circuit (shown in the inset of Figure 3.2D of Chapter 3), which consisted of a resistor (R_s) in series with a parallel arrangement of a resistor (R_{ct}) and a constant phase element (CPE), with the fitting parameters obtained through application of the Levenberg-Marquardt minimization procedure.

A2.1.8. *IR* and Background Correction of Current Density–Voltage (*J–V*) Data

In order to fairly and accurately compare the apparent catalytic activity of the different CoS_2 morphologies, it is necessary correct the measurements of current density (J) vs. applied voltage (V) for all ohmic losses throughout the system, which include the wiring, substrate, catalyst material, and solution resistances. Together, these resistances constitute the series resistance (R_s) of the measurement, which can be obtained from an EIS Nyquist plot as the first intercept of the main arc (corresponding to the electrode–electrolyte interface) with the real axis. Then, for each measured value of current, the potential loss can be calculated using R_s and

Ohm's Law and subtracted from the raw data (Figure A2.4, filled squares) to give the *IR*-corrected data (Figure A2.4, open squares with crosses). The values of R_s in the various measurements of CoS_2 activity are low, consistent, and similar to one another, which helps ensure that no one data set has been over- or under-corrected relative to the others.

Furthermore, it is consistently observed that the CoS_2 electrodes—particularly the high surface area MW and NW electrodes—produce a substantial background current, as seen in the uncorrected data in Figure A2.4. In fact, we even observe this background current when using inert bare graphite electrodes, suggesting that it is primarily capacitive in origin. However, we cannot rule out the possibility of slow cathodic dissolution of the CoS_2 material contributing to this background current. The background current is stable, and electrode rotation significantly increases its magnitude. Its effect is to artificially shift the polarization curves to higher current densities. Subtraction of this background current permits more clear and true analysis of catalytic activity toward the faradaic process of interest (in this case, the HER). In order to achieve accurate background current correction, the background current was fit to a line in a region prior to the onset of hydrogen evolution (typically in the voltage range of approximately −20 to +100 mV vs. RHE). Then, as seen in Figure A2.4, this background current fit (black line) was subtracted from the *IR*-corrected data to give the fully *IR*- and background-corrected data (open squares). To illustrate the importance of treating this background current, failure to correct the data in Figure A2.4 for the background current gives $J_{cathodic}$ = 10 mA cm^{-2} at an overpotential (η) of −139 mV vs. RHE, while after background correction $J_{cathodic}$ = 10 mA cm^{-2} is observed at η = −147 mV vs. RHE. In spite of the relatively minor difference, proper data correction ensures that the catalytic performance is accurately and consistently represented.

A2.1.9. Estimate of Effective Electrode Surface Area

Cyclic voltammetry (CV) can be used to probe the electrochemical double layer at non-faradaic overpotentials as a means for estimating the effective electrode surface area. By plotting the difference in current density (J) between the anodic and cathodic sweeps (*i.e.*, $J_{anodic} - J_{cathodic}$, or ΔJ) at a set overpotential against the CV scan rate, a linear trend is observed. Fitting this data to a line permits the extraction of the geometric double layer capacitance (C_{dl}), which is linearly proportional to the effective electrode surface area (see Figure 3.2E of Chapter 3). These values of C_{dl} permit comparison of relative surface areas for electrodes of different textures (*e.g.*, micro- or nanowires), as discussed in Chapter 3, particularly when these electrodes consist of the same material (in this case, CoS_2).

To determine C_{dl} for each CoS_2 electrode, two CV cycles were recorded from −60 mV to −160 mV vs. SCE in the standard measurement configuration described in Section A2.1.7 at scan rates of 4, 8, 12, 16, 20, 40, 60, 80, 100, and 120 mV s^{-1} (these applied potentials were later corrected to the true RHE scale, as described in Section A2.1.7). The two CV cycles at each scan rate were compared to ensure consistency, and the second cycle was always used for C_{dl} determination. The example in Figure A2.6 shows the CVs at different scan rates for the specific CoS_2 NW sample characterized in Figure 3.2 of Chapter 3 (no corrections applied). Then, for each scan rate, ΔJ was measured at −0.15 V vs. RHE and plotted against the scan rate (as shown in Figure 3.2E of Chapter 3). These data were then fit to a line, the slope of which is equal to twice the geometric C_{dl}. The C_{dl} of the other CoS_2 electrodes was determined in a similar fashion (Figure 3.2E of Chapter 3) and summarized in Table 3.1 of Chapter 3.

A2.1.10. Fabrication and Electrochemical Characterization of Symmetrical Cells

The electrochemical symmetrical cells used to assess the activity of the CoS_2 film and NW electrodes toward polysulfide and triiodide reduction were fabricated and characterized by following a published procedure with minor modifications.[1] The Pt electrodes were prepared by electron-beam evaporating 10 nm of Pt (Kurt J. Lesker Co., 99.99%) at 1 Å s^{-1} onto a fluorine-doped tin oxide on glass (FTO/glass) substrate (Hartford Glass Co. Inc., TEC 15, 15 Ω sq^{-1}, 2.2 mm thick) that was cleaned using the sonication and oxygen plasma cleaning procedures described in Section A2.1.1. The Pt electrodes were soaked in 1 M H_2SO_4(*aq*) for at least 2 min, then rinsed with deionized water and dried under a stream of nitrogen, to clean the Pt surface prior to iodide/triiodide symmetrical cell fabrication. All CoS_2 electrodes were used for symmetrical cell fabrication immediately following their preparation to obviate the need for acid etching to remove potential surface oxides that can form in air. Furthermore, all symmetrical cells were fabricated using electrodes from the same synthesis (*i.e.*, by breaking the sample in half to give two electrodes) to ensure that both electrodes in the symmetrical cell were truly identical.

The sandwich-style thin-layer liquid-junction symmetrical cells were assembled by first placing a spacer (Bemis Flexible Packaging, Parafilm M) punched to give a 3/16″ diameter (0.178 cm^2) circular electrode area on one electrode (*i.e.*, CoS_2 film/glass, CoS_2 NW/glass, or Pt film/FTO/glass) and gently heating on a hot plate at 80 °C for 20 s to improve its adhesion to the electrode surface. For the CoS_2 NW electrodes, regions near the edge of the electrode were cleared of NWs using a cotton swab to improve spacer adhesion to the electrode and reduce electrolyte leakage. Then, the electrode–spacer assembly was removed from the hot plate and the

punched active area was completely filled with several drops of either the aqueous sulfide/polysulfide redox electrolyte (used in quantum dot-sensitized solar cells) or the iodide/triiodide redox electrolyte (used in dye-sensitized solar cells). The preparations of these electrolyte solutions are described below:

- Sulfide/polysulfide electrolyte: An aqueous solution consisting of 2 M $Na_2S•9H_2O$ (Sigma-Aldrich, ≥ 99.99%) and 2 M S was prepared by dissolving appropriate amounts of each solid in distilled water under ambient atmospheric conditions. The sulfide/polysulfide electrolyte was stored in a tightly-sealed glass bottle in ambient air.
- Iodide/triiodide electrolyte: A solution consisting of 0.6 M 1-methyl-3-propylimidazolium iodide (Solaronix SA, Aubonne, Switzerland; "PMII"), 0.03 M I_2 (Sigma-Aldrich, ≥ 99.8%), 0.1 M guanadinium thiocyanate (Sigma-Aldrich, ≥ 97%; "GSCN"), and 0.5 M 4-*tert*-butylpyridine (Fluka, > 98%; "TBP") was prepared by dissolving appropriate amounts of each solute in 85:15 (v/v) acetonitrile (Sigma-Aldrich, anhydrous, 99.8%; "ACN"):valeronitrile (Sigma-Aldrich, 99.5%; "VN") in a $N_2(g)$-filled dry box maintained at 35% relative humidity. The iodide/triiodide electrolyte was stored in an opaque, tightly-sealed glass bottle in the dry box.

The symmetrical cells filled with the aqueous sulfide/polysulfide electrolyte solution were assembled in ambient air, while those filled with the iodide/triiodide electrolyte solution were assembled in a $N_2(g)$-filled dry box maintained at 35% relative humidity to minimize water contamination of the electrolyte. The corresponding counter electrode was then aligned with the punched area of the spacer and firmly pressed against the electrolyte-filled electrode–spacer assembly to seal the cell. To fix the seal and prevent electrolyte leakage, two small binder clips

were used to clamp the cell. Lastly, electrical contacts were deposited on the two electrodes of the symmetrical cell using silver paint.

Cyclic voltammetric (CV) measurements of the symmetrical cells were performed at a scan rate of 50 mV s^{-1}, initially scanning cathodically from the open circuit potential and repeating the measurement for a total of 10 cycles. The symmetrical cells filled with the sulfide/polysulfide solution were cycled between +0.7 V and −0.7 V vs. the open circuit potential, while those filled with the iodide/triiodide solution were cycled between +0.5 V and −0.5 V vs. the open circuit potential. EIS was performed in potentiostatic mode at the open circuit potential, applying a sinusoidal voltage with an amplitude of 10 mV and scanning frequency from 200 kHz to 10 mHz. The main arcs of EIS data were modeled using the simplified Randles equivalent circuit shown in Figure 3.2D of Chapter 3, with the fitting parameters obtained through application of the Levenberg-Marquardt minimization procedure.

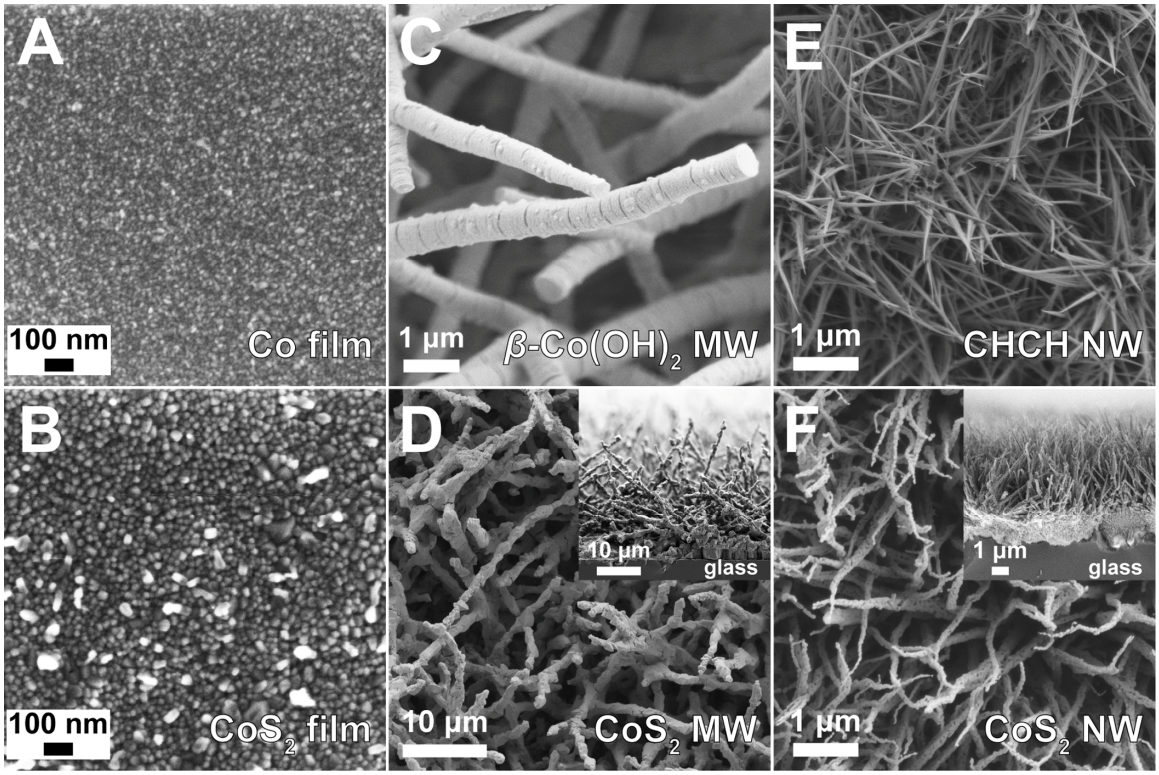

Figure A2.1. Scanning electron microscopy (SEM) images of representative film, microwire (MW), and nanowire (NW) samples prepared on roughened borosilicate glass substrates before and after thermal sulfidation to phase-pure cobalt pyrite (CoS_2). The (A) evaporated Co film and (B) CoS_2 film on glass have essentially the same texture and morphology as the corresponding films prepared on graphite. (C) The cobalt hydroxide (β-$Co(OH)_2$) MWs prepared on glass tend to be thinner and shorter than those prepared on graphite; high-magnification SEM images show that for these thinner MWs the layered brucite crystal structure is visible. (D) The CoS_2 MWs show a substantial increase in surface roughness after thermal sulfidation due to grain coarsening, and the inset cross-sectional SEM image shows that the MWs generally retain their vertical orientation. The cross-sectional SEM image also shows the microns thick CoS_2 layer that forms at the base of the MWs and provides high electrical conductivity. (E) The cobalt hydroxide

carbonate hydrate ($Co(OH)(CO_3)_{0.5}•xH_2O$; "CHCH") NWs prepared on roughened borosilicate glass have essentially the same length (about 10 μm) and diameter (about 100 nm) as those prepared on graphite, but they tend to form a more regular vertically-oriented array rather than the sea urchin-like structures observed on graphite. (F) After thermal sulfidation, the CoS_2 NWs also show a substantial increase in surface roughness, to the extent that some of the NWs appear porous, which may contribute to their high surface area. The inset cross-sectional SEM image confirms that the CoS_2 NWs retain their vertical orientation and shows that a microns thick CoS_2 layer also forms at the base of the NWs.

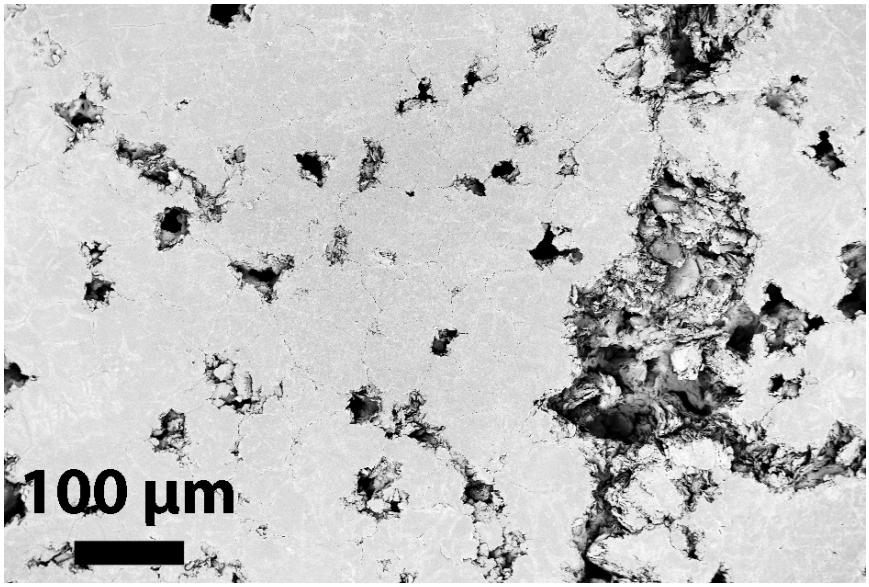

Figure A2.2. Low-magnification SEM image of a CoS_2 film prepared on graphite, highlighting the large pits and imperfections in the graphite surface that remain despite polishing of the graphite disk substrate surface.

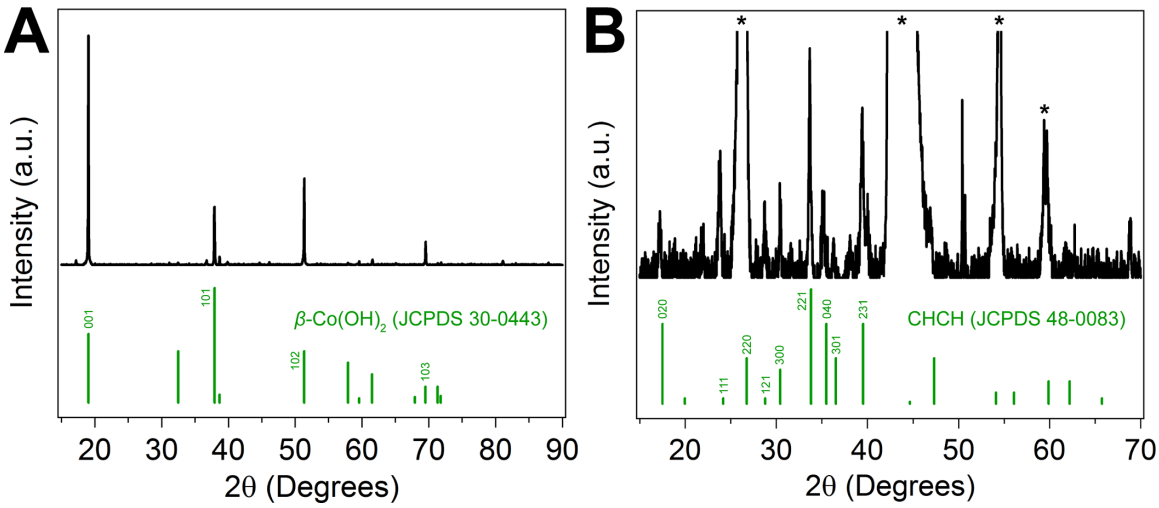

Figure A2.3. X-ray diffraction (XRD) patterns for the as-prepared intermediate (A) cobalt hydroxide (β-$Co(OH)_2$) microwire (MW) and (B) cobalt hydroxide carbonate hydrate ($Co(OH)(CO_3)_{0.5}\bullet xH_2O$; "CHCH") nanowire (NW) products prepared directly on graphite disk substrates. (A) The β-$Co(OH)_2$ MW XRD pattern corresponds to [001]-oriented β-$Co(OH)_2$ (JCPDS 30-0443; space group $P\bar{3}m1$; a = 3.183 Å, c = 4.652 Å), consistent with the growth direction of the vertically-oriented MWs. Note that the extent of product coverage for these samples was typically large enough to mask the XRD peaks from the graphite substrate. (B) The CHCH NW XRD pattern corresponds to CHCH (JCPDS 48-0083) with an orthorhombic crystal structure with no preferred orientation. In this pattern, the intense XRD peaks from the graphite substrate are truncated and marked with asterisks.

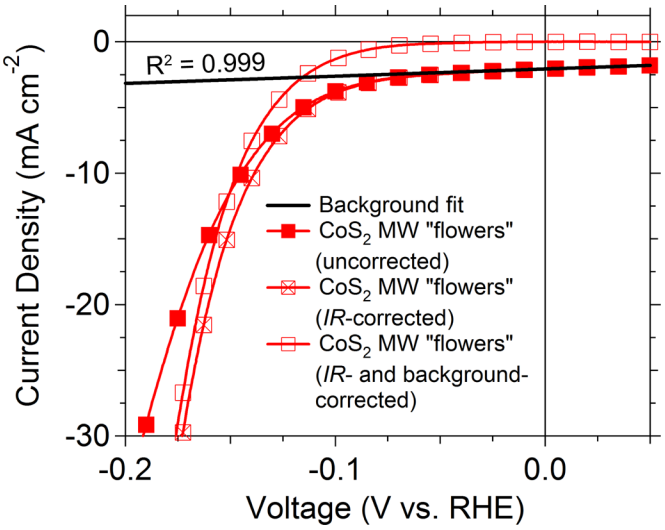

Figure A2.4. Illustration of the method of *IR* and background correction that has been applied to all corrected current density–voltage measurements. In this example (using the data from the CoS_2 MW "flower" sample presented in Figure 3.4 from Chapter 3), it can be seen that *IR* correction has the effect of shifting the raw data (filled squares) to lower overpotentials (open squares with crosses, *IR*-corrected data), with the magnitude of this voltage shift dependent on the amount of current passed at that particular overpotential. The background current was fit to a line in a region prior to the onset of hydrogen evolution (black line) and subtracted from the *IR*-corrected data to give the fully *IR*- and background-corrected data (open squares) presented in Figure 3.4 of Chapter 3.

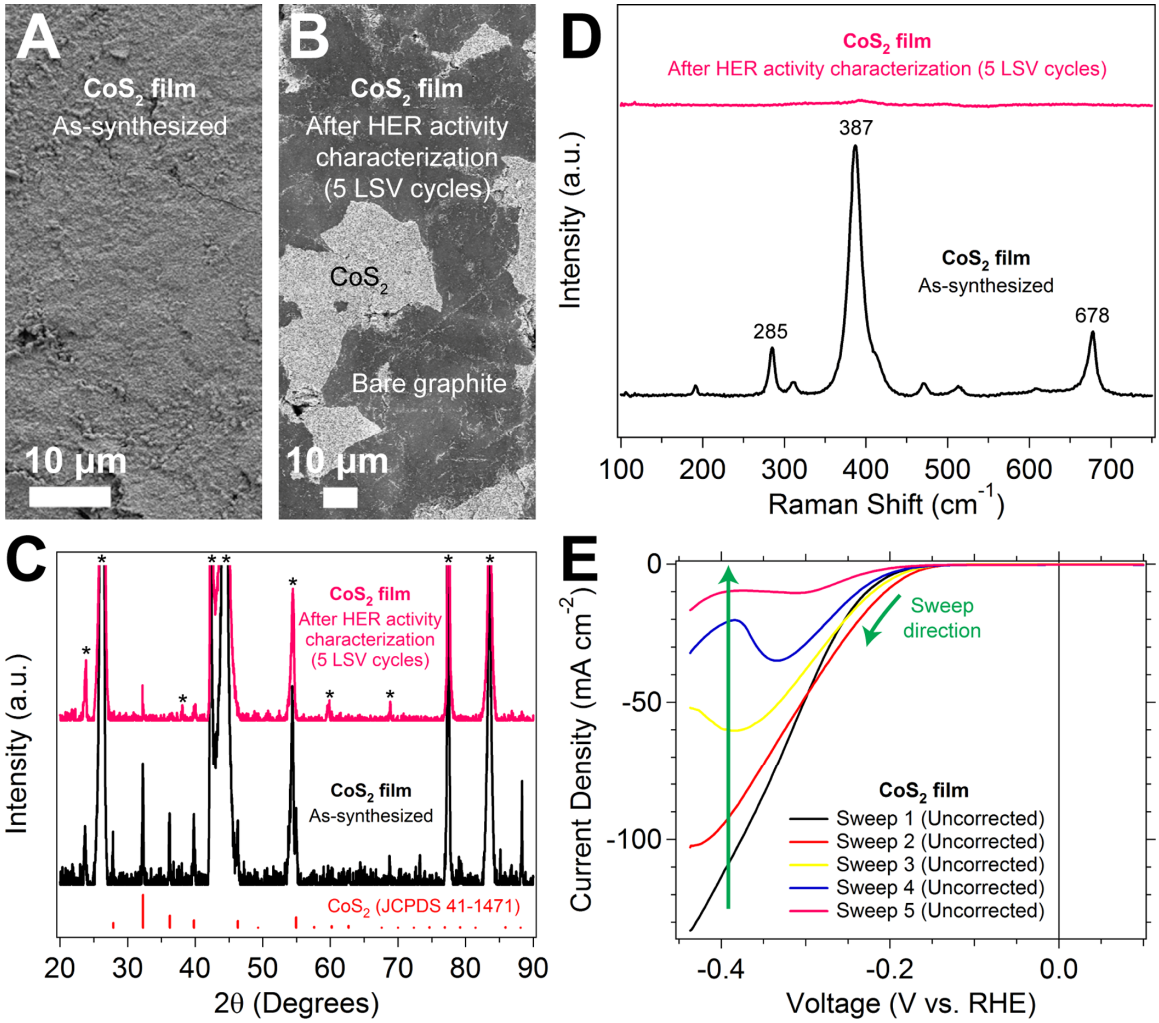

Figure A2.5. Structural, spectroscopic, and electrochemical characterization of a representative CoS_2 film on graphite electrode before and after electrochemical testing for HER catalytic activity, as described in Section A2.1.7. Scanning electron microscopy (SEM) images of the CoS_2 film electrode surface (A) before and (B) after electrochemical testing show that large patches of the CoS_2 film were physically delaminated from the graphite substrate surface. The loss of CoS_2 material as a result of electrocatalytic hydrogen evolution was confirmed by acquiring (C) XRD patterns and (D) Raman spectra before (black traces) and after (violet traces)

the electrochemical testing, both of which show vastly decreased signal from CoS_2 after measurement, corroborating the SEM observations. (E) The five linear sweep voltammetry (LSV) measurements recorded for the CoS_2 film electrode characterized in panels A–D reveal poor cyclability as a result of the loss of CoS_2 material during rapid $H_2(g)$ evolution. In the first LSV sweep (black trace), the inflection point observed at a current density of around −80 mA cm^{-2} suggests the beginning of active CoS_2 material loss.

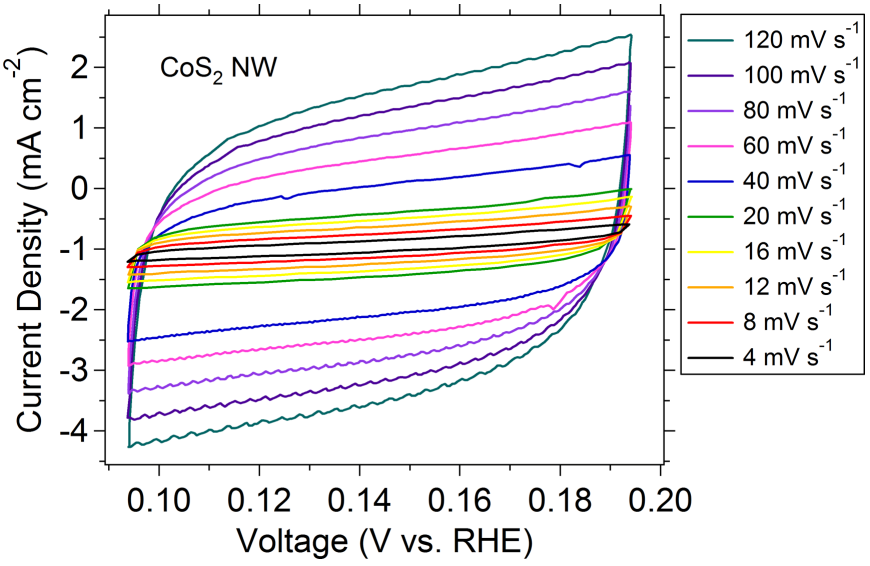

Figure A2.6. Cyclic voltammograms recorded for a CoS_2 NW electrode in the approximate region of 0.1–0.2 V vs. RHE at various scan rates for the purpose of determining the double layer capacitance.

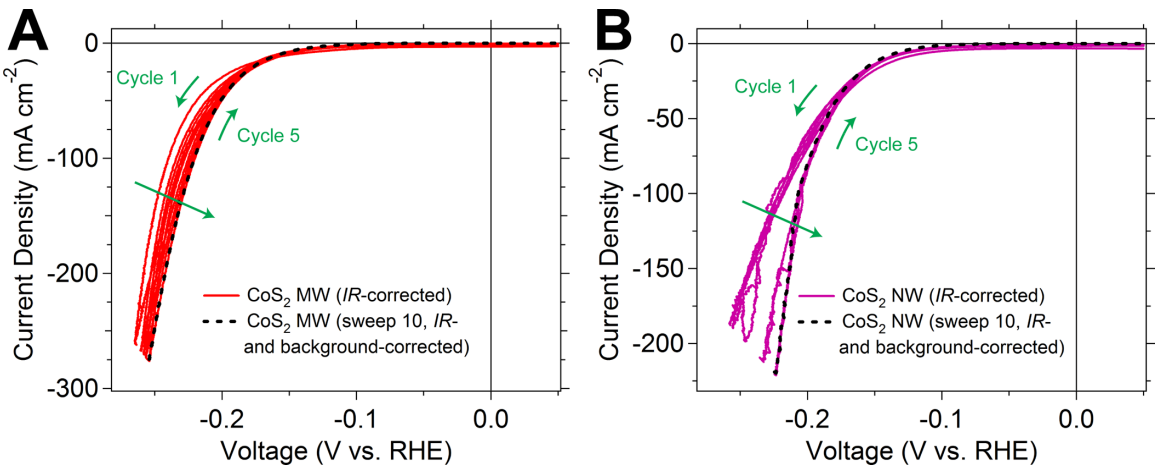

Figure A2.7. Full cyclic voltammetric (CV) characterization of the HER electrocatalytic performance of the representative (A) CoS_2 MW and (B) NW electrodes analyzed in Figure 3.2 of Chapter 3 shows improved performance upon repeated cycling. Five complete CV cycles were recorded for each sample as described in Section A2.1.7, and the data has been corrected for *IR* losses (solid traces) as described in Section A2.1.8. The final, tenth anodic sweep for each sample (dashed traces) have been both *IR*- and background-corrected, and these are the same traces that appear in Figure 3.2A and B of Chapter 3. Note that the noise observed in the CVs for the CoS_2 NW sample in panel B at cathodic current densities exceeding 100 mA cm^{-2} could be due to $H_2(g)$ bubble pinning and depinning at the electrode surface that was observed during measurement. Furthermore, the increase in electrode performance upon repeated cycling could be due to the removal of inactive surface species or contaminants (such as interfacial sulfur residues) upon $H_2(g)$ evolution.

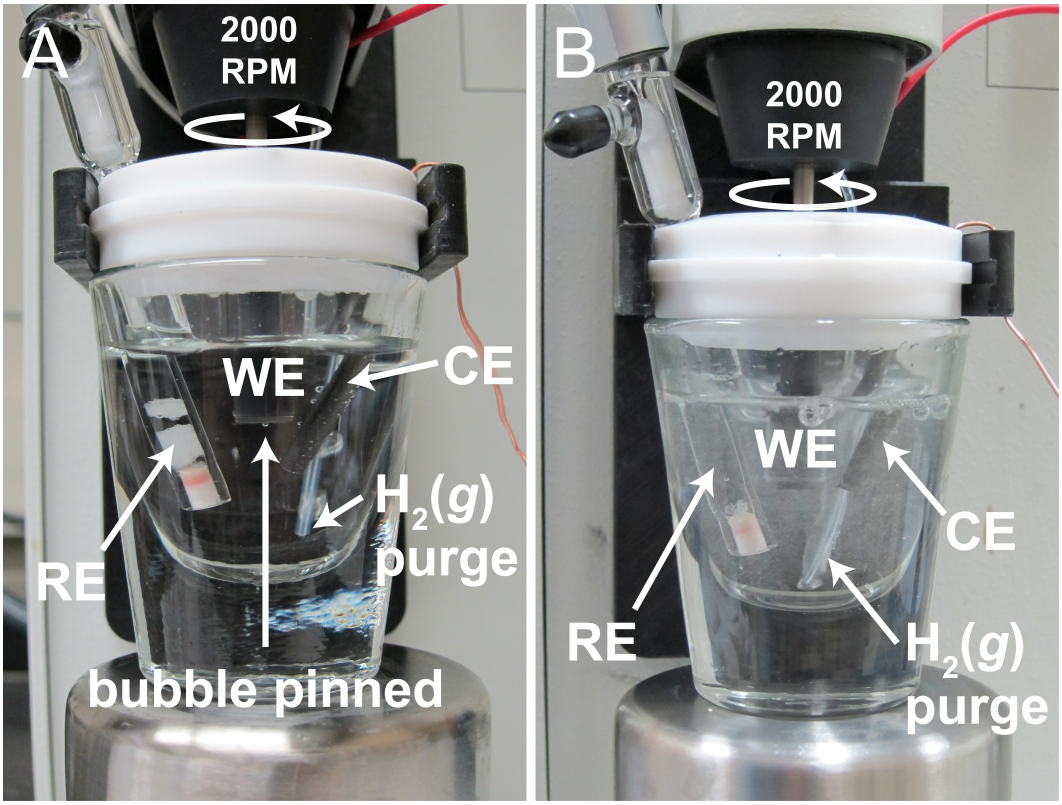

Figure A2.8. Digital photographs of operating cobalt pyrite (CoS_2) (A) film and (B) microwire (MW) array electrodes evolving $H_2(g)$ at geometric cathodic current densities exceeding 80 and 250 mA cm^{-2}, respectively. In each measurement, a graphite disk covered with CoS_2 material is mounted on a glassy carbon rotating disk electrode (rotated at 2000 RPM) as the working electrode (WE). The graphite rod counter electrode (CE), saturated calomel reference electrode (RE), and $H_2(g)$ purge line are also indicated in the photographs. (A) For the CoS_2 film electrodes, large $H_2(g)$ bubbles commonly pin at the electrode surface, as indicated. (B) Due to the MW morphology of the catalyst material, the 0.5 M $H_2SO_4(aq)$ electrolyte becomes turbid with many small $H_2(g)$ bubbles that rapidly form at and escape from the CoS_2 MW electrode surface.

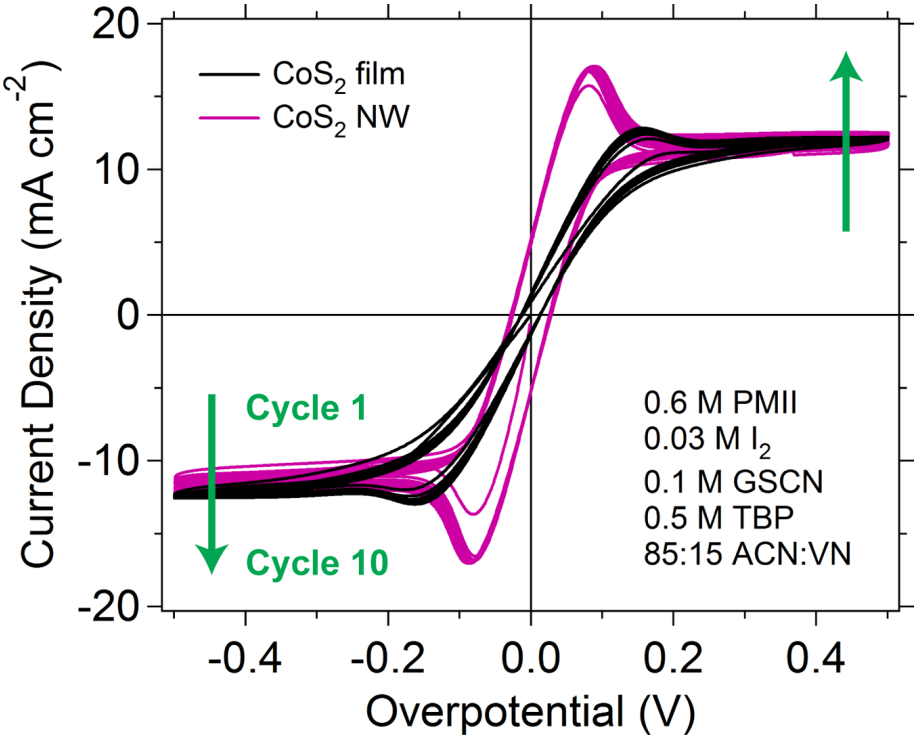

Figure A2.9. Full cyclic voltammetric (CV) characterization of sandwich-style thin-layer liquid-junction symmetrical cells filled with the 0.6 M 1-methyl-3-propylimidazolium iodide ("PMII")/0.03 M I_2/0.1 M guanidinium thiocyanate ("GSCN")/0.5 M 4-*tert*-butylpyridine ("TBP") in 85:15 (v/v) acetonitrile ("ACN"):valeronitrile ("VN") iodide/triiodide redox electrolyte used in dye-sensitized solar cells. The symmetrical cells were fabricated using either CoS_2 film (black trace) or CoS_2 NW (violet trace) electrodes (on glass substrates). The CVs show ten complete cycles for each symmetrical cell, with the current density increasing upon repeated cycling for both cells, confirming the high stability of CoS_2 in the presence of the iodide/triiodide redox electrolyte.

A2.2. References

(1) Faber, M. S.; Park, K.; Cabán-Acevedo, M.; Santra, P. K.; Jin, S. Earth-Abundant Cobalt Pyrite (CoS_2) Thin Film on Glass as a Robust, High-Performance Counter Electrode for Quantum Dot-Sensitized Solar Cells. *J. Phys. Chem. Lett.* **2013**, *4*, 1843–1849.

(2) Li, Y. G.; Tan, B.; Wu, Y. Y. Freestanding Mesoporous Quasi-Single-Crystalline Co_3O_4 Nanowire Arrays. *J. Am. Chem. Soc.* **2006**, *128*, 14258–14259.

(3) Li, Y. G.; Wu, Y. Y. Critical Role of Screw Dislocations in the Growth of $Co(OH)_2$ Nanowires as Intermediates for Co_3O_4 Nanowire Growth. *Chem. Mater.* **2010**, *22*, 5537–5542.

(4) Schaefer, W. P. The Structure of Decaammine-μ-peroxo-dicobalt Disulfate Tetrahydrate. *Inorg. Chem.* **1968**, *7*, 725–731.

(5) Meng, F.; Morin, S. A.; Forticaux, A.; Jin, S. Screw Dislocation Driven Growth of Nanomaterials. *Acc. Chem. Res.* **2013**, *46*, 1616–1626.

(6) Xia, X. H.; Chao, D. L.; Qi, X. Y.; Xiong, Q. Q.; Zhang, Y. Q.; Tu, J. P.; Zhang, H.; Fan, H. J. Controllable Growth of Conducting Polymer Shell for Constructing High-Quality Organic/Inorganic Core/Shell Nanostructures and Their Optical-Electrochemical Properties. *Nano Lett.* **2013**, *13*, 4562–4568.

APPENDIX 3

Vapor Phase Synthesis of the Cobalt Dichalcogenides and Characterization of their Activity toward the Hydrogen Evolution Reaction †

A3.1. Introduction

Despite their high cost and low terrestrial abundance, high-activity noble metal electrocatalysts such as platinum continue to play prominent roles in emerging energy conversion technologies, including the water electrolysis and proton exchange membrane fuel cell units that generate and consume, respectively, clean hydrogen fuel.[1] Recently, there have been intense research efforts to identify low-cost, earth-abundant alternatives to these precious metal electrocatalysts. Among the many candidate compounds that have been characterized so far, the pyrite-phase cobalt dichalcogenides, including cobalt disulfide (CoS_2; cobalt pyrite, cattierite) and cobalt diselenide ($CoSe_2$), exhibit promising intrinsic activity and stability.[2–11] Furthermore, CoS_2 and $CoSe_2$ are intrinsically conductive metals, unlike their semiconducting

† This appendix contains the preliminary results of work conducted in collaboration with M. L. Stone under the supervision of S. Jin.

isostructural analogues iron pyrite (FeS_2)[12,13] and nickel pyrite (NiS_2),[14] making them ideally suited for use as electrocatalysts in a variety of electrochemical energy conversion applications. For example, in liquid-junction quantum dot-sensitized solar cells that employ the sulfide/polysulfide redox electrolyte, CoS_2-based counter electrodes enable more efficient polysulfide reduction than those employing platinum; furthermore, device stability is increased due to the high chemical stability of the CoS_2 material.[2,3] Similarly, CoS_2 has been used as an efficient electrocatalyst for the reduction of both the triiodide[3,10] and disulfide[11] species used in liquid-junction dye-sensitized solar cell redox electrolytes. The demonstration of CoS_2 as an oxygen reduction reaction (ORR) electrocatalyst[7–9] and previous suggestion of the pyrites as electrocatalytic materials[15] inspired the use of CoS_2 and $CoSe_2$ use as hydrogen evolution reaction (HER) electrocatalysts,[3–6] where they exhibit exceptional intrinsic activity among the earth-abundant electrocatalysts.

Despite the well-established electrocatalytic activity of CoS_2 and $CoSe_2$, the origin of this activity remains understudied and poorly understood. In the case of the HER, though, analogy to biological systems suggests that there could be facet-dependent activity.[4] However, most pyrite-phase electrocatalysts characterized so far have been prepared as polycrystalline films, nanostructures, or nanoparticles and therefore offer no opportunity to resolve variations in the intrinsic activity of the different crystalline facets. By preparing transition metal pyrite structures with strong preferential faceting, the activity of different crystal facets toward a specific electrocatalytic conversion reaction of interest could be electrochemically assessed and compared. With the structural knowledge of the specific surface bonding arrangements at each crystal facet, then, the mechanism of the electrocatalytic reaction could potentially be resolved.

Furthermore, the synthesis of the electrocatalyst material could be tuned to favor exposure of these high-activity facets, thereby maximizing its overall electrocatalytic activity. To this end, we report the vapor phase synthesis of faceted CoS_2 and $CoSe_2$ particles directly on graphite supports and the characterization of their electrocatalytic activity toward the HER.

A3.2. Experimental Methods

All chemicals were purchased from Sigma-Aldrich and used without further purification, unless otherwise noted.

A3.2.1. Graphite Substrate Preparation

Graphite disk substrates (6.0 mm diameter; < 1 mm thick) were prepared using procedures described elsewhere.[3] Briefly, slices of a graphite rod (Ultra Carbon Corp., Ultra "F" Purity) were cut and mechanically thinned by abrading both sides with SiC paper (Allied High Tech Products, 320 grit). The graphite disks were cleaned by sequentially sonicating (100 W) in neutral distilled water (Thermo Scientific, Barnstead Nanopure, 18.2 MΩ cm) for 10 min, then in aqua regia (3:1 HCl(*aq*):HNO_3(*aq*)) for 10 min, and finally in fresh distilled water for 10 min to remove loose graphite dust and any metal impurities. The clean graphite disks were then dried in a forced-air oven at 120 °C for at least 30 min.

A3.2.2. Direct Synthesis of CoS_2 and $CoSe_2$

Cobalt disulfide (CoS_2; cobalt pyrite) was synthesized directly on graphite disk supports through modification of a published procedure for preparing iron pyrite (FeS_2) nanorods, nanobelts, and nanoplates.[13] All syntheses were performed on a home-built flow reactor consisting of a 1-in. outer diameter fused silica tube placed inside a single-zone tube furnace

(Lindberg/Blue M, TF55035A-1) and equipped with both pressure and gas flow controllers. To prepare the CoS_2 material directly on the graphite disk substrate, cobalt bromide ($CoBr_2$, 99%) precursor was loaded onto the graphite disk substrate by either directly adding $CoBr_2$ powder or by drop casting a concentrated slurry of $CoBr_2$ in methanol (Macron, anhydrous). When using the powder precursor, 10 mg of loose $CoBr_2$ powder was spread evenly across the surface of the graphite disk; when drop casting the precursor, the graphite disk was placed on a hot plate at 70 °C and four 10-μL drops of the $CoBr_2$ slurry were added to the heated substrate, allowing complete solvent evaporation between drops. The graphite disk substrates coated with $CoBr_2$ precursor material were then loaded into the center of the flow reactor. An alumina boat containing 2 g of sulfur powder (99.5–100.5%) was also loaded into the tube upstream of the samples and positioned outside of the furnace. The tube was evacuated and flushed with argon (Airgas, 99.999%) three times to exclude air from the reactor. Then, with the system under vacuum, the samples were heated at 100 °C for 30 min to dehydrate the $CoBr_2$ precursor. During this step, pink, hydrated $CoBr_2$ was converted to vibrant green, anhydrous $CoBr_2$. Then, the argon flow rate was set to 25 sccm and the pressure was adjusted to 780 Torr. The furnace temperature was ramped to 500 °C (at a rate of approximately 60 °C min^{-1}) and the sulfur boat was pushed into the furnace. (Note that the synthesis is relatively insensitive to the reaction temperature, with similar products obtained over the range of 425–650 °C.) After 1 h, the furnace was opened and the samples were allowed to cool naturally to room temperature under argon flow before being removed. Excess precursor material and cobalt pyrite product not well attached to the graphite substrate was removed with a gentle stream of nitrogen gas.

The above procedure can also be used to prepare pyrite-phase cobalt diselenide ($CoSe_2$)

simply by replacing the sulfur precursor with selenium. In this reaction, an alumina boat containing 100 mg of selenium powder (99.99+%) was placed upstream of the samples and approximately 7 cm inside the tube furnace opening (T ≈ 450 °C). Additionally, in the above syntheses, $CoBr_2$ can be replaced with $CoCl_2$ (≥ 98.0%) or CoI_2 (Alfa Aesar, 99.5%) with no significant changes in product purity or morphology; however, we observed the most consistent results when using $CoBr_2$ as the cobalt precursor.

A3.2.3. Chemical Vapor Deposition of CoS_2 and $CoSe_2$

The procedure for the direct synthesis of CoS_2 (or $CoSe_2$) can also be used to achieve the chemical vapor deposition of these pyrite-phase products. Clean graphite substrates placed downstream of those covered with precursor material accumulate CoS_2 (or $CoSe_2$) as the precursors react in the vapor phase and are transported downstream. The exact position of the downstream graphite substrates within the reactor does not strongly impact the size, crystal habit, or growth density of the deposited pyrite products.

A3.2.4. Materials Characterization

The as-synthesized CoS_2 (and $CoSe_2$) products on graphite were characterized using a LEO SUPRA 55 VP field-emission scanning electron microscope operated at 2 kV and a Bruker D8 ADVANCE powder X-ray diffractometer using Cu Kα radiation.

A3.2.5. Electrochemical Characterization

All electrochemical measurements were performed in a three-electrode configuration using a rotating-disk electrode (RDE) setup (Bioanalytical Systems, Inc.; RDE-2) and recorded using a Bio-Logic SP-200 potentiostat. Each measurement was performed in 0.5 M $H_2SO_4(aq)$ electrolyte (prepared using distilled water) continuously purged with $H_2(g)$ (Airgas, 99.999%)

using a saturated calomel reference electrode (SCE) (CH Instruments) and a graphite rod (National Carbon Co., AGKSP Spectroscopic Electrode) as the counter electrode. The working electrode in each measurement was a graphite disk sample covered with CoS_2 (or $CoSe_2$) product material that was mounted on the tip of a glassy carbon RDE electrode using silver paint (Ted Pella, PELCO Colloidal Silver). The SCE was calibrated against the reversible hydrogen electrode (RHE) using platinum wire (Kurt J. Lesker, 99.99%) as both the working and counter electrodes. Cyclic voltammograms were measured from +0.26 V to –0.25 V vs. RHE at a scan rate of 3 mV s^{-1} while rotating the working electrode at 2000 RPM, repeating this scan a minimum of five times to ensure stability. Traces representing the stable voltammetric response for the sample were used for analysis. Electrochemical impedance spectroscopy was performed in potentiostatic mode at –0.25 V vs. RHE, applying a sinusoidal voltage with an amplitude of 10 mV and scanning frequency from 200 kHz to 50 mHz. The EIS spectra were modeled using a simplified Randles equivalent circuit, with the fitting parameters obtained through application of the Levenberg-Marquardt minimization procedure.

A3.3. Results and Discussion

The reaction of sulfur vapor with cobalt halide precursor at the surface of a graphite substrate results in the growth of microscale, multifaceted CoS_2 particles, as depicted in Figure A3.1. A similar procedure has been used to grow iron pyrite (FeS_2) nanorods, nanobelts, and nanoplates on alumina supports.[13] Although lacking an obvious preferred crystal habit, the CoS_2 particles reported here exhibit much more clear faceting than CoS_2 products obtained through the thermal sulfidation of cobalt films[2,4] or cobalt-containing hard template structures.[3] Figure

A3.1a shows that large, faceted CoS_2 particles can be obtained through the direct reaction of sulfur vapor with $CoBr_2$ powder, but poor integration of the CoS_2 product with the graphite substrate often leaves large areas of bare graphite. On the other hand, $CoBr_2$ precursor films formed by drop casting a $CoBr_2$ slurry on the graphite surface can be reacted to give more uniform coverage of faceted CoS_2 particles (Figure A3.1b). In contrast, the downstream deposition of CoS_2 particles on graphite through the vapor-phase reaction of sulfur with evaporated $CoBr_2$ leads to the formation of larger CoS_2 particles with improved faceting, but their areal coverage on the substrate is very low (Figure A3.1c). In each of these cases, the deposited product material is phase-pure CoS_2, as shown in the representative X-ray diffraction (XRD) pattern of Figure A3.1d in comparison with that of a CoS_2 standard (JCPDS 41-1471). Note that the most intense peaks in this XRD pattern correspond to graphite (Graphite-2H, JCPDS 41-1487) and have been truncated for improved clarity.

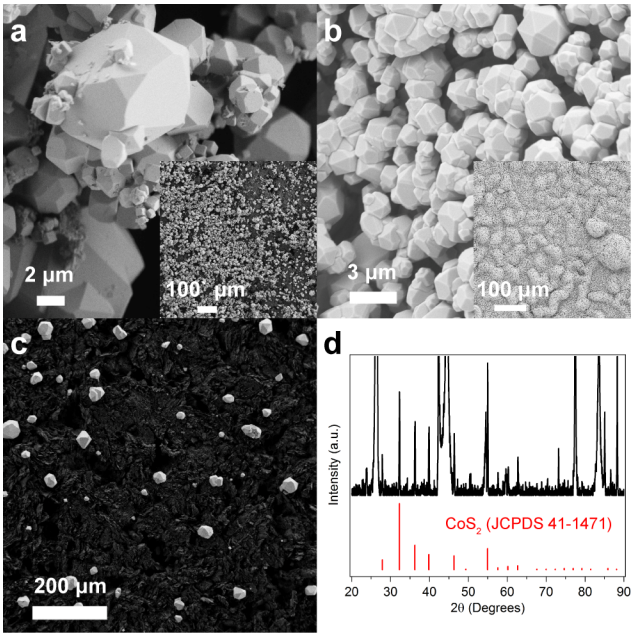

Figure A3.1. Structural characterization of representative cobalt disulfide (CoS_2) products prepared directly on a graphite disk substrate. Scanning electron microscopy (SEM) characterization of the size, morphology, and growth density of CoS_2 products obtained through (a) the direct sulfidation of cobalt bromide ($CoBr_2$) powder, (b) the direct sulfidation of drop-casted $CoBr_2$ films, and (c) the vapor-phase reaction of evaporated $CoBr_2$ and sulfur, all at 500 °C and 780 Torr under 25 sccm Ar flow, reveals that the specific method of introducing the cobalt precursor most strongly impacts the extent of product coverage on the substrate. In each case, the microscale CoS_2 particles are multifaceted. The inset SEM images in panels a and b show a large-area view of the sample surface to highlight the improved coverage of CoS_2 product that can be achieved by uniformly drop casting the cobalt halide precursor on the graphite substrate. (d) X-ray diffraction (XRD) pattern of a typical sample of particulate CoS_2 on graphite confirms both the phase and phase purity of the product (note that the unidentified

reflections correspond to graphite, and the most intense peaks have been truncated for enhanced clarity).

By replacing the sulfur precursor with selenium and making only minor modifications to the experimental procedure (see Experimental Methods), microscale, multifaceted $CoSe_2$ particles can be obtained in high yield (Figure A3.2). The trends observed in the synthesis of CoS_2 also hold for the synthesis of $CoSe_2$, establishing the generality of the synthesis strategy.

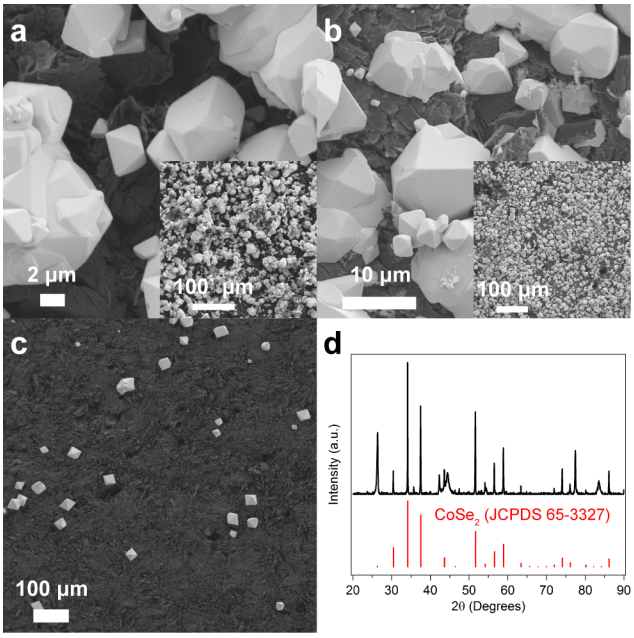

Figure A3.2. Structural characterization of representative cobalt diselenide ($CoSe_2$) products prepared directly on a graphite disk substrate. SEM characterization of the size, morphology, and growth density of $CoSe_2$ products obtained through (a) the direct selenization of $CoBr_2$ powder, (b) the direct selenization of drop-casted $CoBr_2$ films, and (c) the vapor-phase reaction of evaporated $CoBr_2$ and selenium, all at 500 °C and 780 Torr under 25 sccm Ar flow, reveals that the specific method of introducing the cobalt precursor most strongly impacts the extent of product coverage on the substrate. In each case, the microscale $CoSe_2$ particles are multifaceted. The inset SEM images in panels a and b show a large-area view of the sample surface to highlight the improved coverage of $CoSe_2$ product that can be achieved by uniformly drop casting the cobalt halide precursor on the graphite substrate. (d) X-ray diffraction (XRD) pattern of a typical sample of particulate $CoSe_2$ on graphite confirms both the phase and phase purity of the product (note that the unidentified reflections correspond to graphite).

The preparation of the faceted pyrite-phase CoS_2 and $CoSe_2$ products directly on graphite disk substrates allows for the convenient evaluation of their electrocatalytic activity toward the HER by interfacing the substrate with an RDE apparatus and measuring their voltammetric behavior in 0.5 M $H_2SO_4(aq)$ electrolyte continuously purged with $H_2(g)$ in a three-electrode electrochemical measurement (Experimental Methods). Polarization curves showing the current density (J) plotted against the applied potential (V) vs. the RHE for representative CoS_2 and $CoSe_2$ electrodes prepared using the drop-casting procedure (with electrocatalyst mass loadings of 19.3 and 27.1 mg cm^{-2}, respectively) appear in Figure A3.3a.

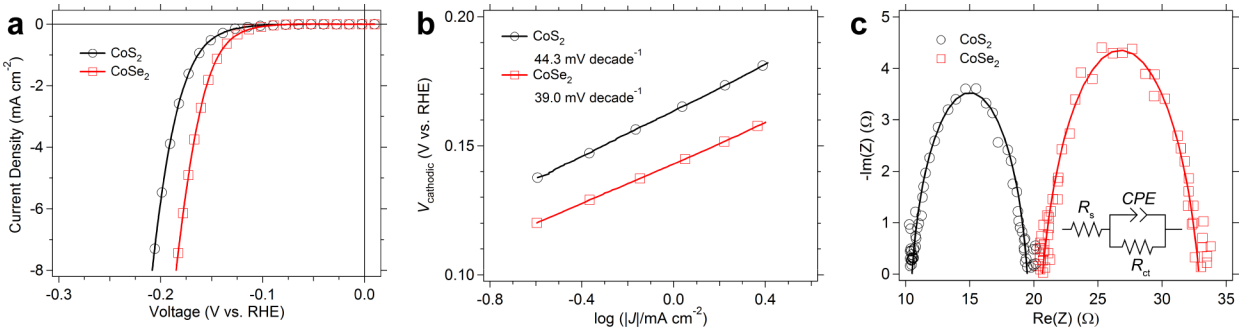

Figure A3.3. Electrochemical characterization of representative CoS_2 and $CoSe_2$ electrodes for HER electrocatalysis. (a) Polarization curves show the relative activity of the CoS_2 (black trace, circle markers) and $CoSe_2$ (red trace, square markers) electrodes. (b) Tafel analysis of the data presented in panel a. (c) Electrochemical impedance spectroscopy (EIS) Nyquist plots showing the series and operating charge transfer resistances of the CoS_2 and $CoSe_2$ electrodes. The data was fit to the simplified Randles equivalent circuit shown in the inset, and the fitting results are shown as solid traces.

The *J*–*V* data presented in Figure A3.3 has been corrected for both ohmic *IR* losses and non-faradaic background current using procedures documented elsewhere.[3] Both the CoS_2 and $CoSe_2$ electrocatalyst particles enable onset potentials for the HER around −100 mV vs. RHE, which compare well with other reports on pyrite-phase HER electrocatalysts.[3–6] In general, the *J*–*V* response of the CoS_2 and $CoSe_2$ electrodes was stable upon repeated cycling, but there was occasionally some performance decay, possibly owing to the physical loss of electrocatalyst material during $H_2(g)$ evolution, which has been reported in the literature for similar electrodes.[3] Both the CoS_2 and $CoSe_2$ electrocatalyst particles enable significant $H_2(g)$ evolution at low applied overpotential, achieving $J_{cathodic} = 8$ mA cm^{-2} at −208 mV and −185 mV vs. RHE for the CoS_2 and $CoSe_2$ electrodes, respectively. For both materials, this level of performance is competitive with what has been previously reported.[3–6]

To elucidate the reason for the difference in CoS_2 and $CoSe_2$ electrocatalyst performance, the *J*–*V* data presented in Figure A3.3a was subjected to Tafel analysis (Figure A3.3b). In the region of modest current density close to the onset of $H_2(g)$ evolution, the CoS_2 electrode exhibits a Tafel slope of 44.3 mV decade^{-1}, while the $CoSe_2$ electrode possesses a Tafel slope of 39.0 mV decade^{-1}. Interestingly, these values are the lowest that have appeared in the literature for the respective materials,[3–5] suggesting that the faceting of these CoS_2 and $CoSe_2$ particles might enable enhanced intrinsic electrocatalytic activity. Furthermore, electrochemical impedance spectroscopy (EIS) was used to probe the kinetics of both the CoS_2 and $CoSe_2$ electrocatalyst particles under HER operating conditions (Figure A3.3c). The EIS data were fit to the simplified Randles equivalent circuit shown in the inset of Figure A3.3c to extract the series and charge transfer resistances (R_s and R_{ct}, respectively) for each electrocatalyst. The CoS_2

electrode exhibits a R_{ct} of 2.54 Ω cm^2, while the $CoSe_2$ electrode shows a R_{ct} of 3.45 Ω cm^2. The similarity of these values suggests that the difference in HER electrocatalytic performance between CoS_2 and $CoSe_2$ results from the difference in their intrinsic activity, as determined from Tafel analysis.

A3.4. Preliminary Conclusions and Future Work

In conclusion, we have demonstrated that faceted CoS_2 and $CoSe_2$ particles can be directly synthesized on graphite disk substrates through the vapor-phase reaction of a cobalt halide precursor with the corresponding chalcogenide. Additionally, these faceted cobalt dichalcogenide particles exhibit improved intrinsic electrocatalytic activity toward the HER. Polarization measurements show a low onset potential for $H_2(g)$ evolution using these pyrite-phase electrocatalysts, and that significant $H_2(g)$ evolution can be achieved at overpotentials competitive with previous reports. However, the reduced Tafel slopes that have been achieved here suggest that the synthesis of preferentially faceted electrocatalyst structures could, upon further optimization, enable improved electrocatalytic performance. Characterization of facet-specific electrocatalytic activity toward the HER could guide the synthesis of graphite-supported CoS_2 and $CoSe_2$ particles that are exclusively bounded by the most active facet for electrocatalysis, which should substantially boost their performance. This could be achieved by growing large, faceted single crystals of CoS_2 from a sodium sulfide–sulfur flux and characterizing the intrinsic activity of the dominant low-index facets of the pyrite crystal structure. Similar flux reactions in the presence of a graphite substrate could enable the high-yield synthesis of supported, faceted micro- or nanostructures, as have been observed in

preliminary experiments (Figure A3.4).

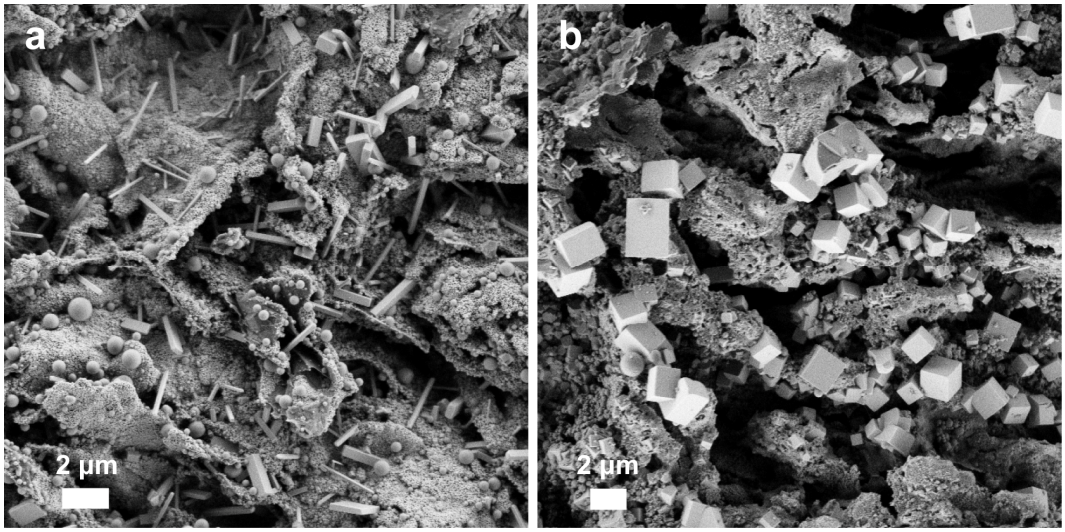

Figure A3.4. SEM images of faceted (a) microrods and (b) particles of CoS_2 prepared directly on a graphite support from a sodium sulfide–sulfur flux. (Results obtained in collaboration with M. Cabán-Acevedo.)

Such methods could also be extended to the Co–Se system to enable the flux growth of faceted $CoSe_2$ particles and potentially micro- and nanostructures. Only through careful characterization of the facet-specific electrocatalytic activity of CoS_2 and $CoSe_2$ toward the HER can their synthesis be tuned to yield products with maximized intrinsic activity, further increasing the potential for these low-cost, earth-abundant materials to replace expensive noble metal electrocatalysts.

A3.5. References

(1) Walter, M. G.; Warren, E. L.; McKone, J. R.; Boettcher, S. W.; Mi, Q.; Santori, E. A.; Lewis, N. S. Solar Water Splitting Cells. *Chem. Rev.* **2010**, *110*, 6446–6473.

(2) Faber, M. S.; Park, K.; Cabán-Acevedo, M.; Santra, P. K.; Jin, S. Earth-Abundant Cobalt Pyrite (CoS_2) Thin Film on Glass as a Robust, High-Performance Counter Electrode for Quantum Dot-Sensitized Solar Cells. *J. Phys. Chem. Lett.* **2013**, *4*, 1843–1849.

(3) Faber, M. S.; Dziedzic, R.; Lukowski, M. A.; Ding, Q.; Jin, S. High-Performance Electrocatalysis Using Metallic Cobalt Pyrite (CoS_2) Micro- and Nanostructures. **2014**.

(4) Kong, D. S.; Cha, J. J.; Wang, H. T.; Lee, H. R.; Cui, Y. First-row transition metal dichalcogenide catalysts for hydrogen evolution reaction. *Energy Environ. Sci.* **2013**, *6*, 3553–3558.

(5) Kong, D. S.; Wang, H. T.; Lu, Z. Y.; Cui, Y. $CoSe_2$ Nanoparticles Grown on Carbon Fiber Paper: An Efficient and Stable Electrocatalyst for Hydrogen Evolution Reaction. *J. Am. Chem. Soc.* **2014**, *136*, 4897–4900.

(6) Ivanovskaya, A.; Singh, N.; Liu, R.-F.; Kreutzer, H.; Baltrusaitis, J.; Nguyen, T. V.; Metiu, H.; McFarland, E. Transition Metal Sulfide Hydrogen Evolution Catalysts for Hydrobromic Acid Electrolysis. *Langmuir* **2013**, *29*, 480–492.

(7) Zhu, L.; Susac, D.; Teo, M.; Wong, K. C.; Wong, P. C.; Parsons, R. R.; Bizzotto, D.; Mitchell, K. A. R.; Campbell, S. A. Investigation of CoS_2-based thin films as model catalysts for the oxygen reduction reaction. *J. Catal.* **2008**, *258*, 235–242.

(8) Jirkovský, J. S.; Björling, A.; Ahlberg, E. Reduction of Oxygen on Dispersed Nanocrystalline CoS_2. *J. Phys. Chem. C* **2012**, *116*, 24436–24444.

(9) Zhao, C.; Li, D. Q.; Feng, Y. J. Size-controlled hydrothermal synthesis and high electrocatalytic performance of CoS_2 nanocatalysts as non-precious metal cathode materials for fuel cells. *J. Mater. Chem. A* **2013**, *1*, 5741–5746.

(10) Duan, X. L.; Gao, Z. Y.; Chang, J. L.; Wu, D. P.; Ma, P. F.; He, J. J.; Xu, F.; Gao, S. Y.; Jiang, K. CoS_2–graphene composite as efficient catalytic counter electrode for dye-sensitized solar cell. *Electrochim. Acta* **2013**, *114*, 173–179.

(11) Peng, S. J.; Li, L. L.; Tan, H. T.; Cai, R.; Shi, W. H.; Li, C. C.; Mhaisalkar, S. G.; Srinivasan, M.; Ramakrishna, S.; Yan, Q. Y. MS_2 (M = Co and Ni) Hollow Spheres with Tunable Interiors for High-Performance Supercapacitors and Photovoltaics. *Adv. Funct. Mater.* **2014**, *24*, 2155–2162.

(12) Cabán-Acevedo, M.; Faber, M. S.; Tan, Y. Z.; Hamers, R. J.; Jin, S. Synthesis and Properties of Semiconducting Iron Pyrite (FeS_2) Nanowires. *Nano Lett.* **2012**, *12*, 1977–1982.

(13) Cabán-Acevedo, M.; Liang, D.; Chew, K. S.; DeGrave, J. P.; Kaiser, N. S.; Jin, S. Synthesis, Characterization, and Variable Range Hopping Transport of Pyrite (FeS_2) Nanorods, Nanobelts, and Nanoplates. *ACS Nano* **2013**, *7*, 1731–1739.

(14) Yao, X.; Honig, J. M.; Hogan, T.; Kannewurf, C.; Spałek, J. Electrical properties of $NiS_{2-x}Se_x$ single crystals: From Mott insulator to paramagnetic metal. *Phys. Rev. B* **1996**, *54*, 17469–17475.

(15) Jaegermann, W.; Tributsch, H. Interfacial Properties of Semiconducting Transition Metal Chalcogenides. *Prog. Surf. Sci.* **1988**, *29*, 1–167.

APPENDIX 4

Metallic 1T Layered Transition Metal Dichalcogenide Electrocatalysts for Enhanced Polysulfide Reduction in Quantum Dot-Sensitized Solar Cells †

A4.1. Introduction

The two-dimensional layered transition metal dichalcogenides (TMDs),[1] which have the general chemical formula MX_2 (where M is a transition metal and X is typically S or Se),[2,3] have recently emerged as a new class of promising earth-abundant electrocatalysts for alternative energy conversion applications.[4,5] Although their catalytic properties for industrial hydrotreating and reforming processes, such as the hydrodesulfurization and hydrodenitrogenation of petroleum, have been known for decades,[6–8] only in the last few years have the layered TMDs been investigated as electrocatalysts. The recognition that molybdenum disulfide (MoS_2) could have activity toward the hydrogen evolution reaction (HER), realized through computational analogy to natural systems,[9] led to a series of careful fundamental studies that identified the edge

† This appendix contains the preliminary results of work conducted in collaboration with M. A. Lukowski under the supervision of S. Jin. It has been prepared for submission as part of a full report on the synthesis, characterization, and electrocatalytic properties of the metallic 1T polymorph of various layered transition metal dichalcogenides.

sites of MoS_2 as possessing particularly high electrocatalytic activity toward the HER.[9–11] Upon finding that this activity approaches that of the superior—but prohibitively scarce and expensive[12]—noble metals, it was quickly realized that MoS_2 could serve as a low-cost, earth-abundant alternative electrocatalyst for the HER. Rapid progress has revealed that several other members of the layered TMD family, including tungsten disulfide (WS_2), possess promising electrocatalytic activity.

Subsequently, great efforts have been made to optimize the synthesis of the layered TMDs for maximum electrocatalytic activity. One of the most important recent advances was the discovery that the specific phase of the layered TMD material substantially impacts its electrocatalytic activity. Specifically, conversion of a layered TMD material from its thermodynamically-favored semiconducting 2H polymorph to its metallic 1T polymorph results in a significant enhancement of its electrocatalytic activity toward the HER.[13–16] At the same time, this phase conversion—typically achieved by intercalating lithium ions into the interstices of the layered crystal structure and then rapidly removing them through reaction with water—leads to the exfoliation of the layered material, maximizing the availability of the edge sites known to possess the highest catalytic activity. Given that the catalytic activity of the layered TMDs is not limited to only the HER, one might expect that conversion to the 1T phase may enhance their electrocatalytic activity toward other electrochemical reactions relevant to energy conversion. Specifically, in quantum dot-sensitized solar cells (QDSSCs),[17,18] the sulfide/polysulfide redox couple is used as the hole mediator to enable regenerative operation. Several metal sulfide materials, including cobalt pyrite (CoS_2)[19] and edge-oriented petaled MoS_2,[20] have recently been shown to be effective electrocatalysts for polysulfide reduction in

QDSSCs. Further increasing the electrocatalytic activity of MoS_2 and other layered TMDs toward polysulfide reduction could boost QDSSC performance while simultaneously eliminating their need for expensive noble metal electrocatalysts at the counter electrode. Here, we first investigate 1T-MoS_2 and 1T-WS_2 nanosheets as potential low-cost, earth-abundant electrocatalysts for polysulfide reduction before incorporating 1T-MoS_2 as the electrocatalyst at the counter electrode in functional QDSSC devices.

A4.2. Experimental Methods

All chemicals were purchased from Sigma–Aldrich and used without further purification, unless otherwise noted.

A4.2.1. Materials Synthesis

Substrate Preparation. Borosilicate plate glass (3.3 mm thick) and fluorine-doped tin oxide on glass (FTO/glass) substrates (Hartford Glass, TEC 15, 15 Ω sq^{-1}, 2.2 mm thick) were cleaned using procedures that appear in the literature.[19] Graphite planchets (Ted Pella, #16505; 15 mm diameter; 1.6 mm thick) were cleaned using procedures described elsewhere.[14] Glassy carbon plate substrates (Alfa Aesar, 2 mm thick) were polished to a mirror finish using alumina slurries and cleaned by first sonicating (100 W) in neutral distilled water (Thermo Scientific, Barnstead Nanopure, 18.2 MΩ cm) for 10 min and then using the same procedures used to clean the glass and FTO/glass substrates. Molybdenum and tungsten foils (0.1 mm thick, 1 cm^2) were cleaned by sequential sonication in acetone, isopropanol, and distilled water for 10 min each before drying under a stream of nitrogen.

Synthesis of Cobalt Pyrite (CoS_2) Thin Films on Glass. Cobalt disulfide (CoS_2; cobalt

pyrite) thin films were synthesized directly on roughened borosilicate plate glass substrates using a procedure described in the literature.[19] Briefly, 100 nm of Co (Kurt J. Lesker, 99.95%) was electron-beam evaporated onto the glass substrates at 1 Å s^{-1} and then thermally sulfidized at 500 °C for 1 h under an argon atmosphere at 780 Torr. Before using these electrodes for electrochemical studies, they were cleaned of surface residues by soaking in 1 M HCl(*aq*).[19]

Chemical Vapor Deposition of MoS_2 Nanosheets. In a home-built chemical vapor deposition (CVD) reactor consisting of a 1-in. outer diameter fused silica tube equipped with both pressure and gas flow controllers inside a single-zone tube furnace (Lindberg/Blue M, TF55035A-1), alumina combustion boats containing 50 mg of molybdenum chloride ($MoCl_5$, 95%) and 200 mg of sulfur (99.5–100.5%) were placed outside of the furnace, upstream of the prepared substrates (graphite, glassy carbon, and/or molybdenum foil), which were positioned at the center of the furnace. The reactor was evacuated and flushed with argon (Airgas, 99.999%) three times before it was pressurized to 770 Torr under a constant argon flow of 125 sccm. The furnace temperature was then ramped to 525 °C (at a rate of approximately 60 °C min^{-1}). Once at the reaction temperature, the $MoCl_5$ and sulfur boats were pushed into the furnace (1.5 cm inside the furnace insulation for the $MoCl_5$ boat, and 4.5 cm for the sulfur boat) with the aid of a Teflon-coated magnet to initiate the reaction. The synthesis was allowed to proceed for 20 min, before allowing the furnace to cool naturally to room temperature under argon flow.

Chemical Vapor Deposition of WS_2 Nanosheets. The CVD synthesis of the WS_2 nanosheets is similar to that used to prepare the MoS_2 nanosheets, with the key differences noted below. In this reaction, a single alumina combustion boat containing both 50 mg of tungsten chloride (WCl_6, 99.9%) and 200 mg of sulfur was placed outside of the furnace, upstream of the

prepared tungsten foil substrates, which were positioned at the center of the furnace. The reactor was flushed argon, as described above, and pressurized to 770 Torr under a constant argon flow of 125 sccm. The furnace temperature was then ramped to 550 °C (at a rate of approximately 60 °C min^{-1}). Once at the reaction temperature, the combustion boat was pushed 1.5 cm inside the furnace insulation with the aid of a Teflon-coated magnet to initiate the reaction. The synthesis was allowed to proceed for 20 min, before allowing the furnace to cool naturally to room temperature under argon flow.

Lithium Intercalation and Chemical Exfoliation of As-Synthesized MoS_2 and WS_2 Nanosheets. Inside an argon-filled glove box, substrates covered with as-synthesized MoS_2 or WS_2 nanosheets were transferred to tightly sealed vials containing 3 mL of *n*-butyllithium solution (2.7 M in heptane). These vials were then removed from the glove box and heated in a forced-air convection oven at 80 °C for 48 h. After this lithium intercalation step, the samples were removed from the vials and excess *n*-butyllithium solution was removed by rinsing the samples with heptane (99%, anhydrous). Then, the samples were reacted with excess distilled water to complete the chemical exfoliation. The MoS_2 nanosheets prepared on graphite and glassy carbon were electrochemically characterized immediately after gently rinsing with distilled water and drying under a stream of nitrogen. The MoS_2 and WS_2 nanosheets prepared on molybdenum and tungsten foil substrates (respectively) readily delaminate from their substrates upon chemical exfoliation treatment, forming a nanosheet suspension in water. To isolate these exfoliated 1T-MoS_2 and 1T-WS_2 nanosheet products, the suspensions were centrifuged at 13,200 RPM for 15 min in an Eppendorf 5415D centrifuge. The supernatant was removed, and the nanosheet precipitate was twice washed with distilled water (centrifuging

between washes) to ensure complete removal of the intercalated lithium. Lastly, the 1T-MoS_2 and 1T-WS_2 nanosheets were suspended in 1 mL of isopropanol. While the exact weight percent of 1T-MX_2 material in these suspensions was not determined, the similar yields of the 1T-MoS_2 and 1T-WS_2 suggest that they should likewise be similar.

A4.2.2. Materials Characterization

The as-synthesized 1T-MoS_2 products on graphite and glassy carbon were characterized using a LEO SUPRA 55 VP field-emission scanning electron microscope operated at 2 kV.

A4.2.3. Electrochemical Characterization

Electrode Preparation. The electrodes consisting of 1T-MoS_2 nanosheets directly synthesized and chemically exfoliated on graphite or glassy carbon were used as-prepared. For the other electrodes, 1T-MoS_2 or 1T-WS_2 nanosheets suspended in isopropanol (harvested from molybdenum or tungsten foil, respectively) were drop cast onto masked secondary electrodes (CoS_2 films on glass for the electrochemical studies, or FTO/glass for the QDSSC device studies) to give a coating of electrocatalytic 1T-MX_2 material. To give a well-defined area of 1T-MX_2 nanosheet deposition, the electrodes were first masked with strips of adhesive tape (3M, Scotch Magic Tape) to give an approximately 5 mm × 5 mm drop casting area. Typically, a total of five 3-μL drops of the 1T-MX_2 nanosheet suspension were added to the masked area of the electrode, allowing complete solvent evaporation between drops. Then, the strips of adhesive tape were removed, leaving a rectangular area of 1T-MX_2 nanosheet deposition on the electrode surface.

QDSSC Photoanode Preparation. Cadmium sulfide/cadmium selenide (CdS/CdSe) quantum dot-sensitized mesoscopic titanium dioxide (TiO_2) films were prepared on FTO/glass

by following a published procedure[19] and used as the light-absorbing QDSSC photoanodes.

Thin-Layer Liquid-Junction QDSSC and Symmetrical Electrochemical Cell Fabrication. Sandwich-style thin-layer liquid-junction QDSSCs were assembled by following a published procedure.[19] The symmetrical electrochemical cells were assembled using the same cell assembly procedure,[19] using identical working and counter electrodes and a spacer (Bemis Flexible Packaging, Parafilm M) punched to give a 3/16″ diameter (0.178 cm^2) circular electrode area. In all device fabrications, the electrodes were carefully aligned to ensure that the active portion (*e.g.*, the area with the drop-cast 1T-MX_2 electrocatalyst) was probed. In all devices, the sulfide/polysulfide electrolyte consisted of 2 M $Na_2S•9H_2O$ (≥ 99.99%) and 2 M S in aqueous solution. After QDSSC or symmetrical electrochemical cell assembly, two small binder clips were used to clamp the device, fixing the seal and preventing electrolyte leakage. Before measurement, electrical contacts were deposited on the working and counter electrodes using silver paint (Ted Pella, PELCO Colloidal Silver). Prior to characterization of the QDSSCs, an adhesive opaque matte black plastic mask (3M, Scotch Super 33+ Tape) with a 1/8″ diameter aperture (defining a 0.0792 cm^2 device active area) was affixed to the glass side of the photoanode; additional strips of opaque black tape were used to mask the edges of the solar cell.

Electrochemical and Photoelectrochemical Characterization. All electrochemical and photoelectrochemical measurements were recorded in a two-electrode configuration using a Bio-Logic SP-200 potentiostat. Cyclic voltammetric (CV) measurements of the symmetrical cells were performed at a scan rate of 50 mV s^{-1}, initially scanning cathodically from the open circuit potential and repeating the measurement for a total of 10 cycles. Electrochemical impedance spectroscopy (EIS) was performed in potentiostatic mode at the open circuit potential, applying a

sinusoidal voltage with an amplitude of 10 mV and scanning frequency from 200 kHz to 10 mHz. The EIS spectra were modeled using a Randles equivalent circuit consisting of a resistor (R_s) in series with a parallel arrangement of a constant phase element (CPE) and a resistor (R_{ct}) and a Warburg element (Z_W) in series, with the fitting parameters obtained through application of the Levenberg-Marquardt minimization procedure.

A 1 kW Xe short arc lamp solar simulator (Newport Corp., Model 91191) with a AM1.5G filter was used to illuminate the QDSSCs at an intensity of 100 mW cm^{-2}, which was set prior to device characterization using a NREL-calibrated and NIST-traceable monocrystalline Si reference solar cell (Photo Emission Tech., Model #60623). For each solar cell device, current density–voltage (*J*–*V*) curves were recorded between −0.2 V and 0.7 V at a scan rate of 20 mV s^{-1}.

A4.3. Results and Discussion

To assess the electrocatalytic activity of the 1T-MoS_2 and 1T-WS_2 nanosheets toward polysulfide reduction and evaluate their potential to enable highly efficient QDSSCs, these materials were first incorporated into thin-layer liquid-junction symmetrical electrochemical cells filled with the sulfide/polysulfide electrolyte used in QDSSCs. To enable such characterizations, the 1T-MX_2 electrocatalyst materials must be dispersed on conductive electrodes possessing high chemical compatibility with the sulfide/polysulfide electrolyte. Thin films of CoS_2 on insulating borosilicate plate glass substrates (Experimental Methods), which were recently shown to serve as a highly robust and efficient counter electrodes for QDSSCs,[19] were selected as the ideal electrode supports to enable these comparisons. Additionally, being

itself an effective polysulfide reduction electrocatalyst, the CoS_2 thin film electrodes would enable the convenient comparison of the 1T-MX_2-modified electrodes to a proven QDSSC counter electrode material. To this end, suspended 1T-MoS_2 and 1T-WS_2 nanosheets were drop cast onto CoS_2 thin film electrodes to give "1T-MoS_2/CoS_2" and "1T-WS_2/CoS_2" electrodes, respectively (Experimental Methods). These electrodes were then used to assemble symmetrical electrochemical cells, and their performance was characterized using cyclic voltammetry (CV) and electrochemical impedance spectroscopy (EIS) and compared to that of a symmetrical cell assembled with CoS_2 electrodes that were not modified with 1T-MX_2 nanosheets (Experimental Methods). Figure A4.1a shows ten complete CV cycles for the three symmetrical cells.

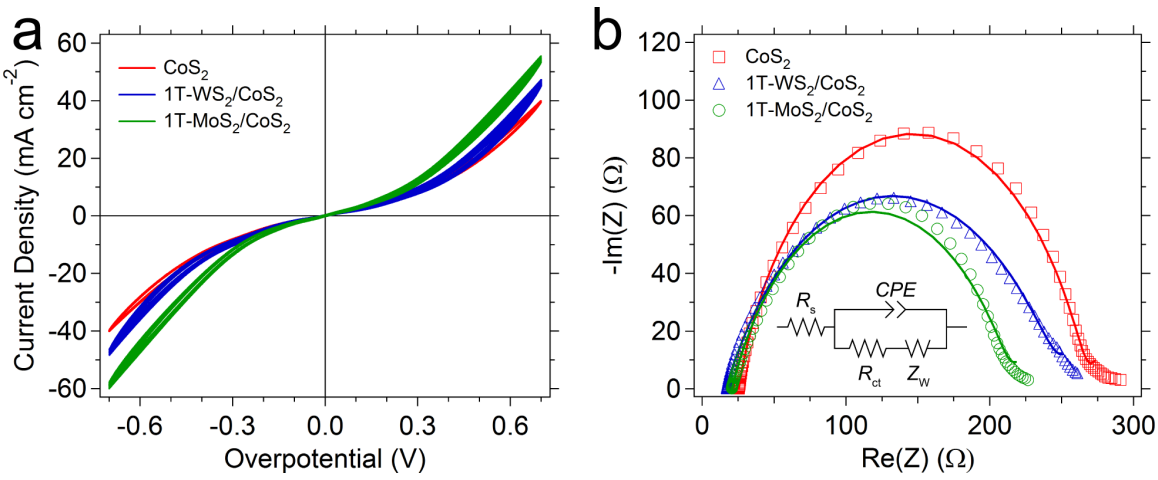

Figure A4.1. Electrochemical characterization of the CoS_2 (red traces and square markers), 1T-WS_2/CoS_2 (blue traces and triangle markers), and 1T-MoS_2/CoS_2 (green traces with circle markers) electrodes in sandwich-style thin-layer symmetrical electrochemical cells filled with an aqueous sulfide/polysulfide (2 M S^{2-}/2 M S) electrolyte solution. (a) Cyclic voltammetric characterization of the symmetrical cells for ten complete cycles. (b) Electrochemical impedance spectra for the symmetrical cells. The inset circuit diagram shows the equivalent circuit model used to fit each spectrum and extract the charge-transfer resistance (R_{ct}).

As expected, bare CoS_2 electrodes (red traces and square markers) enable high performance (indicated by high current densities at large applied overpotentials) and stability in sulfide/polysulfide electrolyte. By modifying the CoS_2 electrode surface with 1T-WS_2 nanosheets, however, higher current densities can be achieved while still maintaining good electrode cyclability. Similarly, the addition of 1T-MoS_2 nanosheets to the CoS_2 electrode surface enhances electrode performance, but to a greater extent, without sacrificing electrode stability.

To understand the origin of this apparent increase in performance, the EIS spectra for these same symmetrical cells were compared (Figure A4.1b). To extract the series resistance (R_s) and charge-transfer resistance (R_{ct}) of each symmetrical cell, the EIS data in Figure A4.1b were fit to a Randles equivalent circuit model (shown in the inset), with the results of these fittings shown as solid line traces through the experimental data points. Owing to the common CoS_2 electrode, the three symmetrical cells all show similar values of R_s; more importantly, though, the R_{ct} decreases for the 1T-WS_2/CoS_2 electrodes and further yet for the 1T-MoS_2/CoS_2 electrodes (Table A4.1).

Table A4.1. Summary of the Electrochemical Properties of CoS_2, 1T-WS_2/CoS_2, and 1T-MoS_2/CoS_2 Symmetrical Electrochemical Cells.

electrode	R_s (Ω)	R_{ct} (Ω cm^2)	J_0 (μA cm^{-2})
CoS_2	25.5	21.4	1.20
1T-WS_2/CoS_2	16.5	20.5	1.25
1T-MoS_2/CoS_2	20.8	17.2	1.49

This trend in decreasing R_{ct} is commensurate with the symmetrical cell performance observed in Figure A4.1a. Using these values of R_{ct}, the exchange current density (J_0) for each electrode was calculated using the Tafel equation

$$J_0 = \frac{RT}{FR_{ct}}$$

where R is the gas constant, T is the temperature (room temperature, in this case), and F is the Faraday constant. These values of J_0, collected in Table A4.1, compare favorably with a previous report on CoS_2 for polysulfide reduction,[19] as well as to other high-performance QDSSC counter electrode materials.[21] Together, these symmetrical cell measurements indicate that both 1T-WS_2 and 1T-MoS_2 exhibit activity toward polysulfide reduction exceeding that of CoS_2, with 1T-MoS_2 being the best among these, implying that the 1T-MX_2 materials could enable highly efficient QDSSCs.

To explore the performance of counter electrodes incorporating 1T-MX_2 nanosheets in complete QDSSC devices, we prepared several different counter electrodes containing 1T-MoS_2 (Experimental Methods), which was determined in the initial electrochemical studies to exhibit superior activity toward polysulfide reduction. Both direct synthesis and secondary deposition strategies were employed to incorporate the 1T-MoS_2 nanosheets with current-collecting electrodes that could be assembled into thin-layer liquid-junction QDSSC devices (Experimental Methods). Drop casting 1T-MoS_2 nanosheets suspended in isopropanol onto FTO/glass electrodes gave "1T-MoS_2/FTO" electrodes, while the direct synthesis of 1T-MoS_2 nanosheets on glassy carbon and graphite substrates gave "1T-MoS_2/glassy carbon" and "1T-MoS_2/graphite" electrodes, respectively. Scanning electron microscopy imaging of these latter two electrodes

shows that the as-prepared 1T-MoS_2 materials are effectively integrated with the conductive substrate (Figure A4.2).

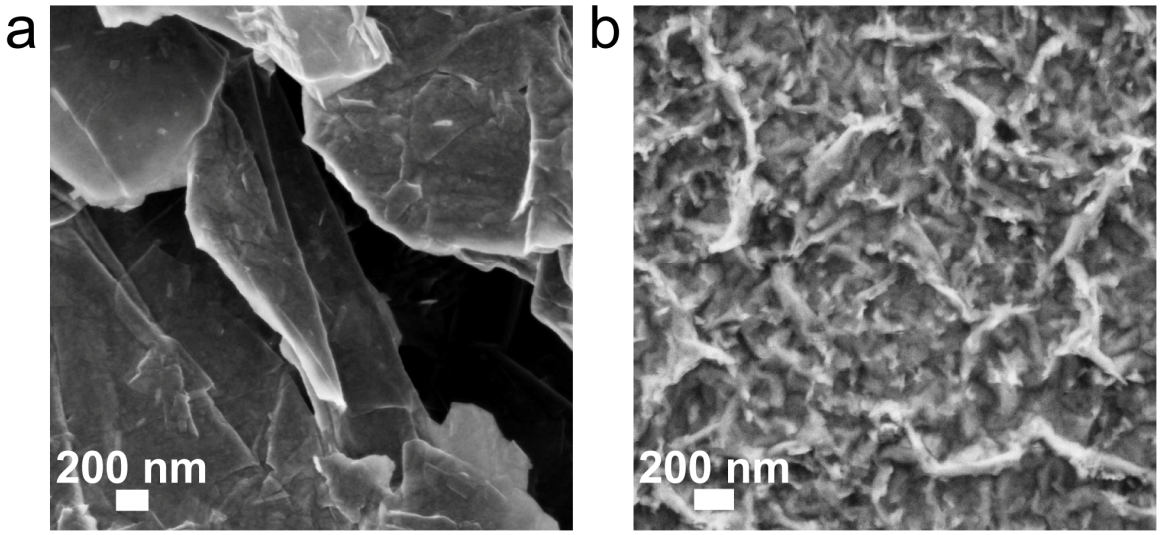

Figure A4.2. Representative scanning electron microscopy images of 1T-MoS_2 nanosheets prepared directly on (a) graphite and (b) glassy carbon supports.

It is important to note that glassy carbon and graphite were selected as direct synthesis substrates mostly for their ability to withstand the MoS_2 synthesis conditions and chemical exfoliation treatment, since most other conductive substrates (such as FTO/glass) would either sulfidize during the MoS_2 synthesis or dissolve during the chemical exfoliation treatment. Additionally, the conductive substrates used here exhibit relatively low activity toward polysulfide reduction, so any apparent activity can be attributed to the 1T-MoS_2 electrocatalyst.

When incorporated into QDSSC devices (Experimental Methods), each of these electrodes enables efficient photovoltaic operation, as indicated by the *J*–*V* curves presented in Figure A4.3.

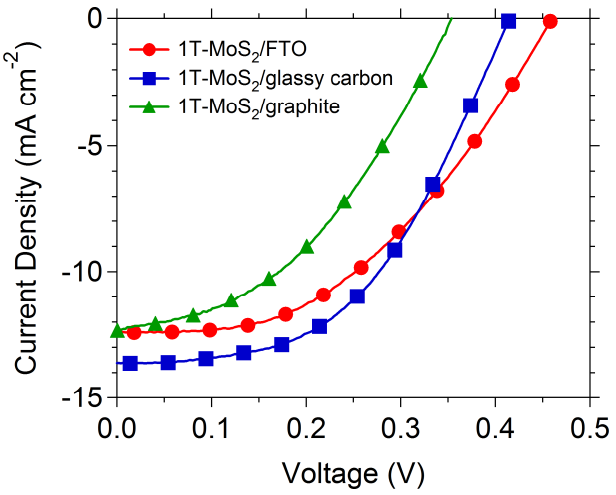

Figure A4.3. Current density−voltage (*J*−*V*) characterization of QDSSC devices assembled with 1T-MoS_2/FTO (red trace with circle markers), 1T-MoS_2/glassy carbon (blue trace with square markers), and 1T-MoS_2/FTO (green trace with triangle markers) counter electrodes and filled with an aqueous sulfide/polysulfide (2 M S^{2-}/2 M S) electrolyte solution.

While the overall conversion efficiencies (η) of the devices characterized in Figure A4.3 are relatively low compared to state-of-the-art QDSSCs,[22] they have not been optimized for high performance. Nevertheless, each device exhibits an open-circuit voltage (V_{oc}), short-circuit current density (J_{sc}), and fill factor (FF) comparable to analogous QDSSCs assembled with high-performance counter electrodes.[19,20] The specific photovoltaic device characteristics of the QDSSCs characterized in Figure A4.3 are summarized in Table A4.2.

Table A4.2. Photovoltaic Device Characteristics of Quantum Dot-Sensitized Solar Cells Measured with Different Counter Electrodes.

counter electrode	V_{oc} (V)	J_{sc} (mA cm^{-2})	FF	η (%)
1T-MoS_2/FTO	0.460	12.4	0.447	2.55
1T-MoS_2/glassy carbon	0.416	13.6	0.494	2.80
1T-MoS_2/graphite	0.355	12.3	0.414	1.82

Remarkably, η = 2.80% for the device assembled with the 1T-MoS_2/glassy carbon counter electrode exceeds that previously reported for QDSSCs employing an as-synthesized petaled MoS_2 counter electrode by more than a factor of two,[20] suggesting that the 2H to 1T polymorph transition indeed boosts activity toward polysulfide reduction. The performance of the QDSSCs characterized in Figure A4.3 was relatively stable upon repeated cycling, but the decay could be attributed to electrolyte leakage (particularly for the 1T-MoS_2/graphite electrode, which did not form a complete seal due to the rough graphite surface). Additionally, the 1T-MoS_2 nanosheets could have delaminated from the counter electrode over time, reducing the amount of electrocatalyst material at the counter electrode surface and, worse yet, potentially poisoning the photoanode. Nevertheless, these potential stability issues could be addressed through further development of the 1T-MX_2-based counter electrode preparation. Most importantly, the substantial photovoltaic activity observed in Figure A4.3 indicates that 1T-MoS_2 is indeed an effective polysulfide reduction electrocatalyst. Along with the electrochemical characterization shown in Figure A4.1, this suggests that 1T-WS_2 (and potentially other metallic layered TMDs) could also be an effective polysulfide reduction electrocatalyst.

A4.4. Conclusions

In summary, we have demonstrated that the metallic 1T polymorph of the layered TMDs, particularly 1T-WS_2 and 1T-MoS_2, can serve as effective electrocatalysts for polysulfide reduction, enabling efficient QDSSC operation. When drop cast onto current-collecting CoS_2 film electrodes and assembled into symmetrical electrochemical cells filled with sulfide/polysulfide redox electrolyte, these 1T-phase layered TMD electrocatalysts enable

enhanced performance as compared to the CoS_2 electrodes alone while maintaining high electrode stability. Thorough EIS analysis reveals that 1T-WS_2 and 1T-MoS_2 possess higher intrinsic activity toward polysulfide reduction, owing to lower values of R_{ct} (and, consequently, higher values of J_0). To demonstrate this activity in working devices, various counter electrodes employing 1T-MoS_2 nanosheet electrocatalysts were incorporated into QDSSCs and characterized, with the highest-performing device exhibiting an overall conversion efficiency of 2.80%, more than double that previously reported for QDSSCs employing a MoS_2-based counter electrode. Collectively, these data confirm that the metallic 1T-phase layered TMDs are efficient polysulfide reduction electrocatalysts, and that, with proper optimization, they could enable further enhanced QDSSC performance.

A4.5. References

(1) Chhowalla, M.; Shin, H. S.; Eda, G.; Li, L.-J.; Loh, K. P.; Zhang, H. The chemistry of two-dimensional layered transition metal dichalcogenide nanosheets. *Nature Chem.* **2013**, *5*, 263–275.

(2) Wilson, J. A.; Yoffe, A. D. The Transition Metal Dichalcogenides: Discussion and Interpretation of the Observed Optical, Electrical and Structural Properties. *Adv. Phys.* **1969**, *18*, 193–335.

(3) Jaegermann, W.; Tributsch, H. Interfacial Properties of Semiconducting Transition Metal Chalcogenides. *Prog. Surf. Sci.* **1988**, *29*, 1–167.

(4) Yang, J.; Shin, H. S. Recent advances in layered transition metal dichalcogenides for hydrogen evolution reaction. *J. Mater. Chem. A* **2014**, *2*, 5979–5985.

(5) Merki, D.; Hu, X. L. Recent developments of molybdenum and tungsten sulfides as hydrogen evolution catalysts. *Energy Environ. Sci.* **2011**, *4*, 3878–3888.

(6) *Transition Metal Sulphides: Chemistry and Catalysis*; Weber, T.; Prins, R.; van Santen, R. A., Eds.; Kluwer Academic Publishers: Dordrecht, 1998; Vol. 60.

(7) Chianelli, R. R.; Berhault, G.; Raybaud, P.; Kasztelan, S.; Hafner, J.; Toulhoat, H. Periodic trends in hydrodesulfurization: in support of the Sabatier principle. *Appl. Catal. A* **2002**, *227*, 83–96.

(8) Alexander, A.-M.; Hargreaves, J. S. J. Alternative catalytic materials: carbides, nitrides, phosphides and amorphous boron alloys. *Chem. Soc. Rev.* **2010**, *39*, 4388–4401.

(9) Hinnemann, B.; Moses, P. G.; Bonde, J.; Jørgensen, K. P.; Nielsen, J. H.; Horch, S.; Chorkendorff, I.; Nørskov, J. K. Biomimetic Hydrogen Evolution: MoS_2 Nanoparticles as Catalyst for Hydrogen Evolution. *J. Am. Chem. Soc.* **2005**, *127*, 5308–5309.

(10) Jaramillo, T. F.; Jørgensen, K. P.; Bonde, J.; Nielsen, J. H.; Horch, S.; Chorkendorff, I. Identification of Active Edge Sites for Electrochemical H_2 Evolution from MoS_2 Nanocatalysts. *Science* **2007**, *317*, 100–102.

(11) Karunadasa, H. I.; Montalvo, E.; Sun, Y. J.; Majda, M.; Long, J. R.; Chang, C. J. A Molecular MoS_2 Edge Site Mimic for Catalytic Hydrogen Generation. *Science* **2012**, *335*, 698–702.

(12) Vesborg, P. C. K.; Jaramillo, T. F. Addressing the terawatt challenge: scalability in the supply of chemical elements for renewable energy. *RSC Adv.* **2012**, *2*, 7933–7947.

(13) Voiry, D.; Yamaguchi, H.; Li, J.; Silva, R.; Alves, D. C. B.; Fujita, T.; Chen, M.; Asefa, T.; Shenoy, V. B.; Eda, G.; Chhowalla, M. Enhanced catalytic activity in strained

chemically exfoliated WS_2 nanosheets for hydrogen evolution. *Nature Mater.* **2013**, *12*, 850–855.

(14) Lukowski, M. A.; Daniel, A. S.; Meng, F.; Forticaux, A.; Li, L.; Jin, S. Enhanced Hydrogen Evolution Catalysis from Chemically Exfoliated Metallic MoS_2 Nanosheets. *J. Am. Chem. Soc.* **2013**, *135*, 10274–10277.

(15) Lukowski, M. A.; Daniel, A. S.; English, C. R.; Meng, F.; Forticaux, A.; Hamers, R. J.; Jin, S. Highly Active Hydrogen Evolution Catalysis from Metallic WS_2 Nanosheets. *Energy Environ. Sci.*, DOI: 10.1039/c1034ee01329h.

(16) Ding, Q.; Meng, F.; English, C. R.; Cabán-Acevedo, M.; Shearer, M. J.; Liang, D.; Daniel, A. S.; Hamers, R. J.; Jin, S. Efficient Photoelectrochemical Hydrogen Generation Using Heterostructures of Si and Chemically Exfoliated Metallic MoS_2. *J. Am. Chem. Soc.*, DOI: 10.1021/ja5025673.

(17) Selinsky, R. S.; Ding, Q.; Faber, M. S.; Wright, J. C.; Jin, S. Quantum dot nanoscale heterostructures for solar energy conversion. *Chem. Soc. Rev.* **2013**, *42*, 2963–2985.

(18) Kamat, P. V. Quantum Dot Solar Cells. *The Next Big Thing* in Photovoltaics. *J. Phys. Chem. Lett.* **2013**, *4*, 908–918.

(19) Faber, M. S.; Park, K.; Cabán-Acevedo, M.; Santra, P. K.; Jin, S. Earth-Abundant Cobalt Pyrite (CoS_2) Thin Film on Glass as a Robust, High-Performance Counter Electrode for Quantum Dot-Sensitized Solar Cells. *J. Phys. Chem. Lett.* **2013**, *4*, 1843–1849.

(20) Finn, S. T.; Macdonald, J. E. Petaled Molybdenum Disulfide Surfaces: Facile Synthesis of a Superior Cathode for QDSSCs. *Adv. Energy Mater.*, DOI: 10.1002/aenm.201400495.

(21) Radich, J. G.; Dwyer, R.; Kamat, P. V. Cu_2S Reduced Graphene Oxide Composite for High-Efficiency Quantum Dot Solar Cells. Overcoming the Redox Limitations of S^{2-}/S_n^{2-} at the Counter Electrode. *J. Phys. Chem. Lett.* **2011**, *2*, 2453–2460.

(22) Radich, J. G.; Peeples, N. R.; Santra, P. K.; Kamat, P. V. Charge Transfer Mediation Through Cu_xS. The Hole Story of CdSe in Polysulfide. *J. Phys. Chem. C*, DOI: 10.1021/jp4113365.

(This page is intentionally left blank.)

POSTFACE

The attentive reader will notice that there's no mention of a "Postface" in the Table of Contents, and that was intentional. But I'll get to that in a second.

First, let me thank you—and possibly commend you, depending on your opinion of my work—for making it through to the end. If you're hoping for more illuminating scientific insights, though, I'll go ahead and stop you now: there's no new data here, no new discussion, no further analysis. Only a brief moment of reflection.

Frankly, it just didn't seem appropriate for me to let a document like this abruptly end with a list of references. Don't get me wrong, there are some great papers in that list, so make sure you check 'em out… but on a personal level, it doesn't necessarily make for a fitting conclusion to something so meaningful to me. But perhaps this little bit of candid discourse will do the trick.

So anyway, there it is: my PhD dissertation. Nobody said it would be easy, and for good reason: it wasn't. I'll admit that. But it was totally worth it.

Without a doubt, this document cumulatively represents the most rewarding experience of my life.

On the heels of that, I suppose all I can really say is:

"This ends the story."

Matthew J. Faber JUNE 12, 2014